Investigating the properties of brown dwarfs using intermediate resolution spectroscopy

— James Ignatius Canty —

Centre for Astrophysics Research
Science and Technology Research Institute
— University of Hertfordshire —

Submitted to the University of Hertfordshire in partial fulfilment of the requirements of the degree of Ph.D.

Principal Supervisor: Dr. Philip W. Lucas

— October 2014 —

Declaration

I certify that the content presented in this thesis is my own work. Any results, diagrams and tables used from other published works have been properly cited.

James I. Canty

Preface

In the course of my PhD studentship, I have attended three conferences:

- CoolStars 17 (17th Cambridge Workshop on Cool Stars, Stellar Systems and the Sun) in Barcelona, Spain, between 24-29th June, 2012
- Brown Dwarfs Come of Age, Fuerteventura, Canary Islands, Spain, between 20-24th May, 2013
- National Astronomical Meeting (NAM), University of St. Andrews, Scotland, UK, between 1-5th July, 2013

The poster I presented at the Brown Dwarfs Come of Age conference was a synopsis of the analysis of spectral features in the K-band spectra of brown dwarfs which I describe in Chapter 2 and has been published in the conference proceedings (Canty et al., 2013a).

I have had one paper published in which I was the first author (Canty et al., 2013b). At the time of writing this paper has received four refereed citations (Currie et al. 2014; Schneider et al. 2014; Currie, Burrows & Daemgen 2014; Pinfield et al. 2014). In addition, I have been a co-author of three other papers. I reduced the L band spectrum of the T9 standard UGPS 0722-0540 which appeared in Leggett et al. (2012). I also reduced the spectra of several candidate T dwarfs from the the VISTA Hemisphere Survey (Lodieu et al., 2012), and the UKIDSS Large Area Survey (Burningham et al., 2013).

Burningham B. et al., 2013, MNRAS, 433, 457

Canty J. I., Lucas P. W., Roche P. F., Pinfield D. J., 2013a, Mem. Soc. Astron. Italiana, 84, 1110

Canty J. I., Lucas P. W., Roche P. F., Pinfield D. J., 2013b, MNRAS, 435, 2650

Currie T., Burrows A., Daemgen S., 2014, ApJ, 787, 104

Currie T., Daemgen S., Debes J., Lafreniere D., Itoh Y., Jayawardhana R., Ratzka T., Correia S., 2014, ApJ, 780, L30

Leggett S. K. et al., 2012, ApJ, 748, 74

Lodieu N., Deacon N. R., Hambly N. C., Boudreault S., 2012, MNRAS, 426, 3403

Pinfield D. J. et al., 2014, MNRAS, 444, 1931

Schneider A. C., Cushing M. C., Kirkpatrick J. D., Mace G. N., Gelino C. R., Faherty J. K., Fajardo-Acosta S., Sheppard S. S., 2014, AJ, 147, 34

Acknowledgements

My thanks go first and foremost to Phil Lucas, my Supervisor. This thesis would not have existed but for Phil's patience, guidance and depth of knowledge. Phil was a co-author of my paper, described in Chapter 2. My thanks also go to the other co-authors, David Pinfield[1] and Pat Roche[2]

I also wish to thank Didier Saumon[3] and Mark Marley[4]. Didier's and Mark's model spectra provide the theoretical underpinning for the $H_2(K)$ spectral index which I derive in Chapter 2 of this thesis, and my analysis of NH_3 opacity in the near-infrared spectra of late T dwarfs, which I describe in Chapter 3. I am particularly grateful to Didier for his prompt responses to my many queries about the chemistry and evolution of brown dwarf atmospheres.

My thanks also go to Katelyn Allers[5], the referee of my paper which forms Chapter 2 of this thesis. Katelyn's insightful and comprehensive comments hugely improved the quality of my paper, and this thesis.

My special thanks also to Sergey Yurchenko[6] and Jonathan Tennyson[6]. Sergey and Jonathan are members of the ExoMol team at University College London, whose molecular line lists are used in the spectral analyses in Chapter 3 of this thesis. I am also grateful to Sergey for elucidating the molecular/quantum physics of the rotational-vibrational line transitions responsible for the absorption features I describe in this chapter.

Finally, I also thank those researchers who gave me access to their data in order for me to develop this thesis. I particularly thank Kerstin Geißler[7], Kevin Luhman[8], Ralph Neuhaüser[9], and Tomas Schmidt[9].

---

[1] Centre for Astrophysics Research, Science and Technology Research Institute, University of Hertfordshire, Hatfield AL10 9AB, UK

[2] Astrophysics Department, University of Oxford, 1 Keble Road, Oxford OX1 3RH, UK

[3] Los Alamos National Laboratory, P.O. Box 1663, Los Alamos, NM 87545, USA

[4] NASA Ames Research Center, MS-245-3, Moffett Field, CA 94035, USA

[5] Department of Physics and Astronomy, Bucknell University, Lewisburg, PA 17837, USA

[6] Department of Physics and Astronomy, University College London, London WC1E 6BT, UK

[7] Department of Physics and Astronomy, Stony Brook University, Stony Brook, NY 11794-3800, USA

[8] Department of Astronomy and Astrophysics, The Pennsylvania State University, University Park, PA 16802, USA

[9] Astrophysikalisches Institut, University Jena, Schillergäßchen 2-3, D-07745 Jena, Germany

Abstract

This thesis is an investigation into some properties of brown dwarfs using medium-resolution spectroscopy. In the first part of the thesis, I address the issue of parameter degeneracy in brown dwarfs. In the course of my analysis, I derive a gravity-sensitive spectral index which can be used, statistically at least, to differentiate populations of young objects from field dwarfs. The index is also capable of finding the difference between a population of $\sim$1 Myr objects and a population of $\sim$10 Myr objects and may be used to separate low-mass members from foreground and background objects in young clusters and associations. The second part of my thesis is an investigation into the major opacity sources in the atmospheres of late T dwarfs. I look particularly at CH_4 and NH_3 absorption features in the near-infrared spectra of these objects. In my analysis, I identify new absorption features produced by these molecules. I also correct features which had previously been wrongly identifed. This has been made possible by the use of high quality data, together with a new CH_4 synthetic line list, which is more complete at these temperatures than any previously available list.

Contents

List of Figures

List of Tables

List of Symbols and Units

Å	angstrom (10^{-10} m)
CaH	Calcium Hydride
CH_4	Methane
CrH	Chromium Hydride
G	gravitational constant (currently measured to be $6.673 \times 10^{-8}\,\mathrm{cm}^3\,\mathrm{g}^{-1}\,\mathrm{s}^{-2}$)
Gyr	10^9 years
H_2	Molecular Hydrogen
κ	absorption coefficient
$\log g$	logarithm (base 10) of the surface gravity of a star (usually quoted in cgs units)
$M_\odot$	Solar mass
Myr	10^6 years
μm	micron (10^{-6} m)
MOL^{-1}	per molecule
mol^{-1}	per mole
r	radius
T_{eff}	Effective temperature
NH_3	Ammonia
TiO	Titanium Oxide
VO	Vanadium Oxide
$v \sin i$	projected rotational velocity of a star
yr	year

List of Abbreviations

1D	1 dimensional
2D	2 dimensional
2MASS	Two Micron All-Sky Survey
CIA	collision-induced absorption
EW	equivalent width
FWHM	full-width at half-maximum
GNIRS	Gemini North Infrared Spectrograph
HITRAN	HIgh-resolution TRANsmission molecular absorption database
HR	Hertzsprung-Russell
HRD	Hertzsprung-Russell Diagram
IMF	initial mass function
IRAF	Image Reduction and Analysis Facility
IRCS	Infrared Camera and Spectrograph
IRTF	NASA Infrared Telescope Facility
KPNO	Kitt Peak National Observatory
MS	main-sequence
NIFS	Near-infrared Integral Field Spectrometer
NIR	Near-infrared
ONC	Orion Nebula Cluster
pEW	pseudo-equivalent width
PMO	planetary mass object
SED	spectral energy distribution
S/N	signal-to-noise ratio

T-ReCS	Thermal-Region Camera Spectrograph
TWA	TW Hydrae Association

Chapter 1

Introduction

Brown dwarfs are objects with insufficient mass to sustain stable hydrogen burning in their cores (Kumar 1962; Hayashi & Nakano 1963). How these objects form is still uncertain. They may form in the same way as stars, through the gravitational collapse of molecular clouds. Or they may form through the interruption of the accretion process due to dynamical interaction among protostars, or radiation from nearby OB star(s) causing photoionisation of the protostar envelope and disc. Other possible formation mechanisms include the fragmentation of massive circumstellar discs, and turbulence in molecular clouds. Excellent reviews of current theories of the formation and early evolution of low-mass stars and brown dwarfs may be found in Luhman (2012) and Stamatellos (2014), and references therein.

While the minimum mass for sustained hydrogen burning is calculated to be ∼0.75 $M_\odot$ (Hayashi & Nakano, 1963), brown dwarfs with masses near this limit may undergo lithium and/or deuterium burning (Chabrier & Baraffe 1997; Chabrier et al. 2000) for $\sim 10^8$ years after formation, during which time the gravitational force is balanced by gas pressure. With largely stable radii and energy radiated from the photosphere replaced with energy released at the core, for a time the T_{eff} of these objects is approximately constant. Once nuclear burning at the core ends, however, these more massive brown dwarfs evolve like all other brown dwarfs. As radiated energy is no longer being replaced, they start to cool, and since the gravitational force is now unbalanced, their radii contract. As brown dwarfs increase in density, free electrons in their cores become

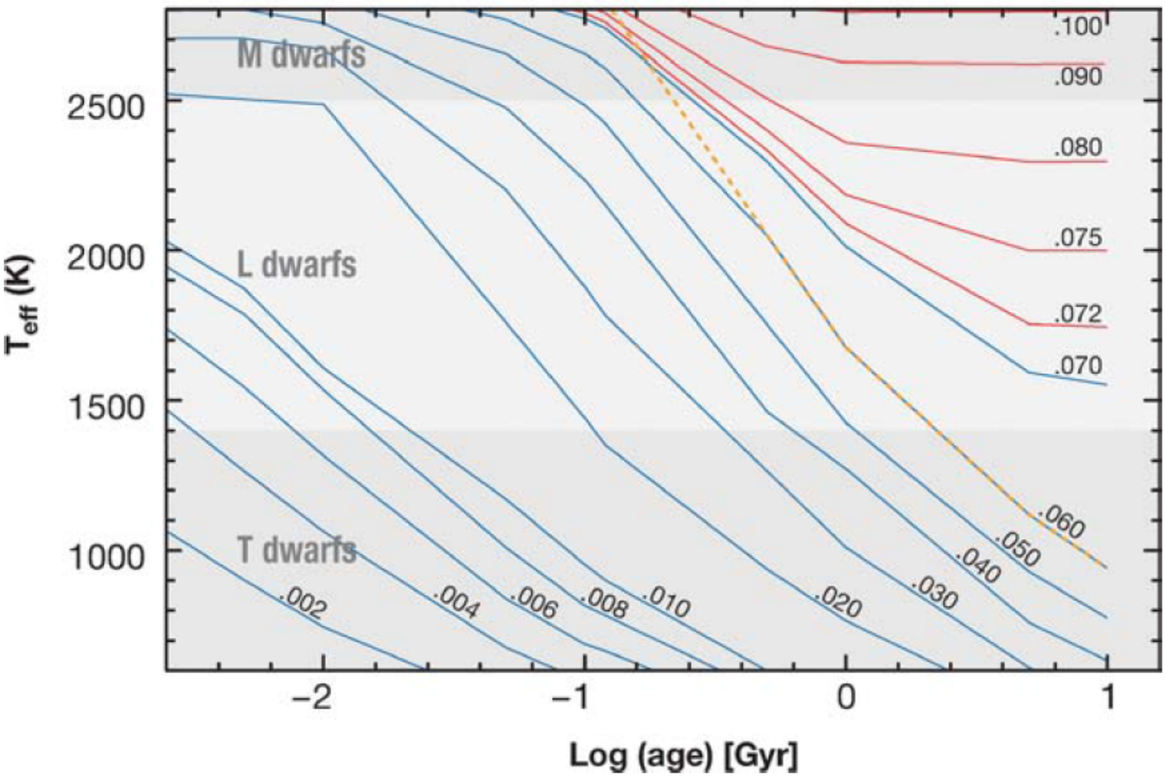

Fig. 1.1: Theoretical tracks showing the evolution of T_{eff} with age for low-mass stars (red) and brown dwarfs (blue). Notice how an initial episode of core nuclear burning in the most massive brown dwarfs delays the cooling of these objects. The orange dotted line marks the boundary at which lithium is 50% depleted. Objects to the right of this line have burned their primordial stock of lithium. Plot from Kirkpatrick (2005).

degenerate and this degeneracy pressure eventually halts any further contraction. Although the brown dwarf is in hydrostatic equilibrium, it is not in thermal equilibrium. It continues to cool, its peak flux moving to longer and longer wavelengths. Figure 1.1 shows the evolutionary tracks of low-mass stars and brown dwarfs.

The first detected brown dwarf was a companion to the white dwarf GD 165 (Becklin & Zuckerman, 1988). GD 165B was known to be low mass, but wasn't confirmed as a brown dwarf at the time it was discovered. The first confirmed discovery of a brown dwarf was a companion to an early-type M red dwarf star, Gl 229 (Oppenheimer et al., 1995). The methane features observed in the near-infrared spectrum of Gl 229B are similar to features in the atmosphere of Jupiter. In particular, a methane absorption edge at ∼1.6 μm, and methane absorption bands at 2.17 μm and 2.20 μm (Geballe et al., 1996). See Figure 1.2. Therefore, they could not have been produced in the photosphere of even the coolest low-mass star.

At about the same time, two candidate brown dwarfs were found in the Pleiades

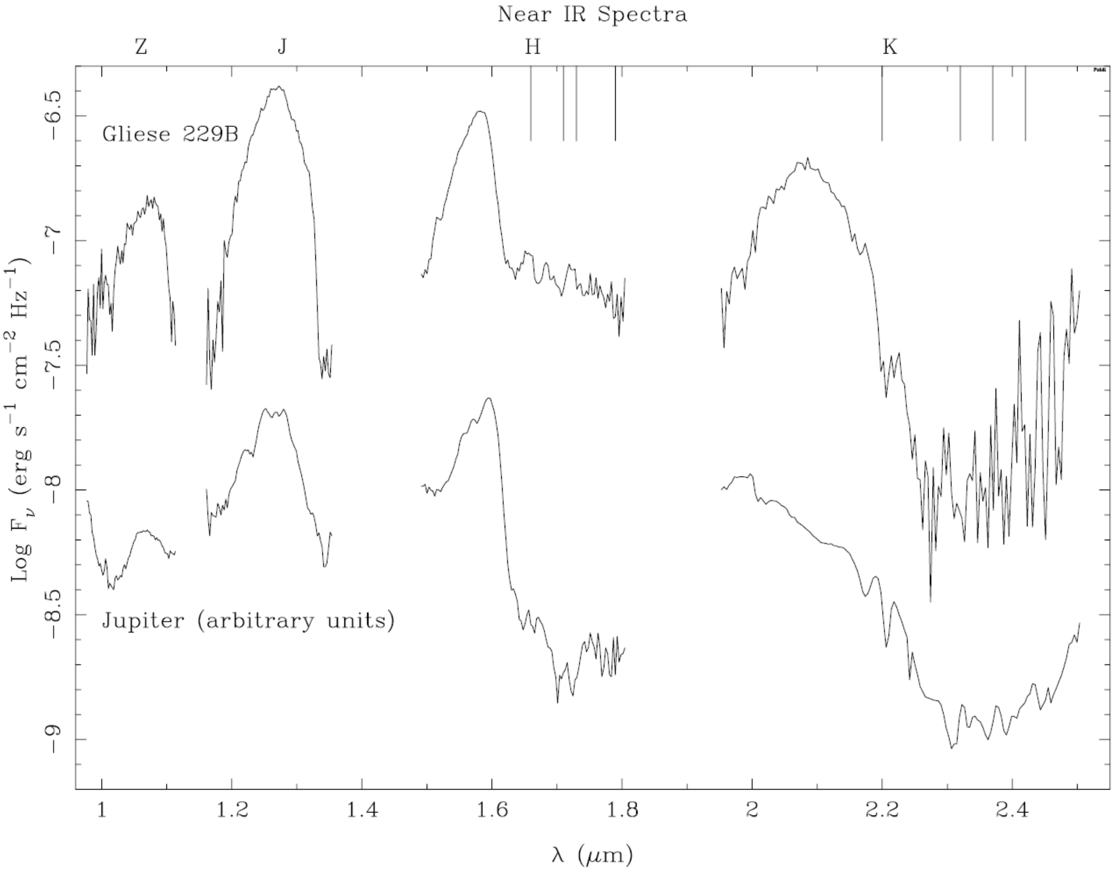

Fig. 1.2: Similarities in the near-infrared spectra of Jupiter and Gl 229B. Vertical lines indicate the locations of methane absorption bandheads in the *H* and *K* bandpasses. Plot from Oppenheimer (2014).

cluster (Stauffer, Hamilton & Probst 1994; Rebolo, Zapatero Osorio & Martín 1995). These were subsequently confirmed as brown dwarfs by the detection of lithium absorption in their optical spectra (Basri, Marcy & Graham 1996; Rebolo et al. 1996).[1] Neither of these objects were bound to a stellar companion. Thus, they are the first free-floating substellar objects.

1.1 The substellar initial mass function

A major aim of current research in Galactic astronomy is to determine the formation rate of brown dwarfs, the birthrate, and the number of brown dwarfs formed as a function of mass, known as the substellar initial mass function (IMF). The stellar mass distribution determines the evolution, surface brightness, chemical enrichment, and baryonic content of galaxies (Chabrier, 2003). While brown dwarfs may not be as numerous as previously thought, at least in the solar neighbourhood (Kirkpatrick et al., 2012), understanding the substellar IMF will still provide a major test of star formation theory, with implications for the evolution of the Galaxy.

The stellar IMF in the solar neighbourhood was originally described as a power law distribution (Salpeter, 1955), $NdM \propto N^{-\alpha}dM$, with α=2.35, and was derived for stars in the mass range 0.4 $\mathrm{M}_{\odot}$ $\lesssim$M$\lesssim$10 $\mathrm{M}_{\odot}$. Subsequent analyses have found the stellar IMF is consistent with Salpeter's value for stars with masses $\geq$ 1 $\mathrm{M}_{\odot}$ (Kroupa, 2001). Of course, there was no theoretical framework for the existence of substellar objects at the time of Salpeter's pioneering work. Regardless, since the mass function of objects cannot be observed directly, and must be inferred from the objects' integrated light, their luminosity function, by means of a mass-luminosity relation, the instrumentation of the time would not have been sufficiently sensitive to detect such faint objects. The introduction of charge-coupled devices (CCDs), in which the energy of photons is converted into electric charge, made the detection of these sources possible. At first, observers concentrated on young clusters and associations, where the higher luminosities of young brown dwarfs allows the mass function to be determined at lower masses.

---

[1] I have used the K band spectrum of one of these objects (Teide 1) in my analysis in Chapter 2.

Table 1.1: The substellar IMF in young clusters and star-forming regions

Cluster	Age (Myr)	α	Reference
Pleiades	125	0.6±0.11	Moraux et al. 2003; Casewell et al. 2007; Lodieu et al. 2007
Blanco 1	100	0.69±0.15	Moraux et al. 2007
α Per	80	0.59±0.05	Barrado y Navascués et al. 2002; Lodieu et al. 2005; Lodieu et al. 2012
IC 4665	30	∼0.6	de Wit et al. 2006; Lodieu et al. 2011
IC 348	2	0.7±0.4	Alves de Oliveira et al. 2013 Muench et al. 2007; Luhman et al. 2003b
NGC 1333	1	0.6±0.1	Scholz et al. 2012; Winston et al. 2009
σ Ori	3-7	0.6±0.2	Peña Ramírez et al. 2012; Caballero et al. 2012
λ Ori	2	∼0.3	Bayo et al. 2011
ONC	1	0.3-0.6	Weights et al. 2009
ρ Oph	1	0.7±0.3	Alves de Oliveira et al. 2012; Mužić et al. 2012

These studies found that the slope of the IMF in young clusters flattens, with α <1. Recently, large populations of brown dwarfs have been found in very young clusters where the mass function appears to extend below the deuterium-burning threshold of 0.012-0.013 $M_{\odot}$. Table 1.1 shows the substellar IMFs in a sample of young clusters and star-forming regions. Figure 1.3 shows the IMFs of several young clusters with ages from $\sim$2$-$125 Myr.

Figure 1.1 also demonstrates how the degeneracy of T_{eff}, age, and mass presents a major problem in deriving the substellar IMF. As brown dwarfs cool over time, the flux from these objects also reduces. At any given distance, the measured flux from old, massive brown dwarfs may be equivalent to that from younger, less massive objects. Therefore, model isochrones would assign similar masses to these objects.

The first part of this thesis is an attempt to address the issue of parameter degeneracy among the youngest, least massive brown dwarfs, those in the Orion Nebula Cluster (ONC), an intense star-forming region. Figure 1.4 show the Hertzsprung-Russell (HR) diagrams for a number of young sources (< 10 Myr) in the ONC. When model isochrones are fitted to these objects, the models converge at spectral types M9/L0. As a result, it is not possible to distinguish young, low-mass objects, from older, more massive objects, at these spectral types.

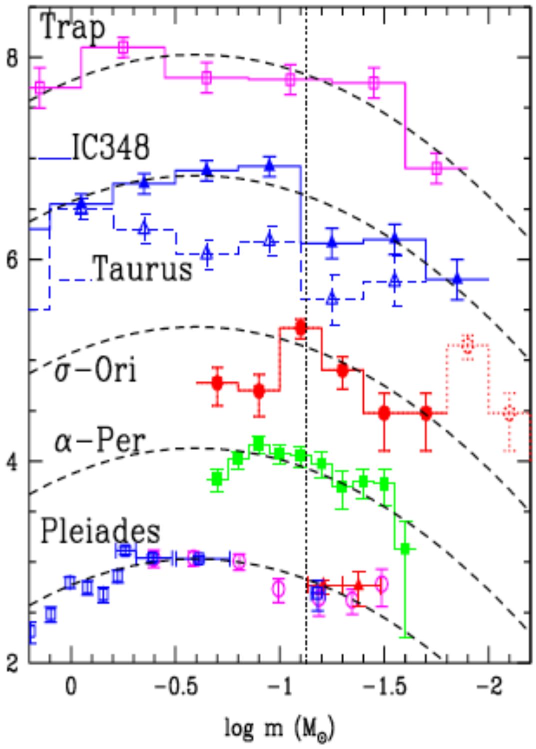

Fig. 1.3: The IMF in young clusters. The dashed line is the IMF in the Galactic field. The vertical dotted line is the minimum mass for Hydrogen burning. Plot from Chabrier (2005).

Interestingly, the substellar nature of brown dwarfs provides one solution to parameter degeneracy in these objects. Once a brown dwarf forms, it contracts to an equilibrium radius, where the gravitational force is balanced by degeneracy pressure. During this time, the brown dwarf's surface gravity is increasing. Thus, gravity-sensitive spectral features can be used as a proxy for age, so that the strongest features will be found in the most contracted, and hence the oldest objects. Previous studies have examined gravity-sensitive alkali metal absorption lines in the optical or near-infrared (Martin, Rebolo & Zapatero-Osorio 1996; Steele & Jameson 1995; Gorlova et al. 2003; Allers et al. 2007; Riddick, Roche & Lucas 2007; Luhman et al. 2007; Close et al. 2007; Cruz, Kirkpatrick & Burgasser 2009; Allers & Liu 2013). Such observations are technically challenging, however, and not possible at all for faint planetary mass targets.

In Chapter 2, I use high quality K band spectra of a sample of late M/early L brown dwarfs from clusters and associations with well-constrained ages, as well as a number of field brown dwarfs, to further constrain the ages and masses of these objects. In the course of this investigation I derive a new gravity-sensitive spectral index, the

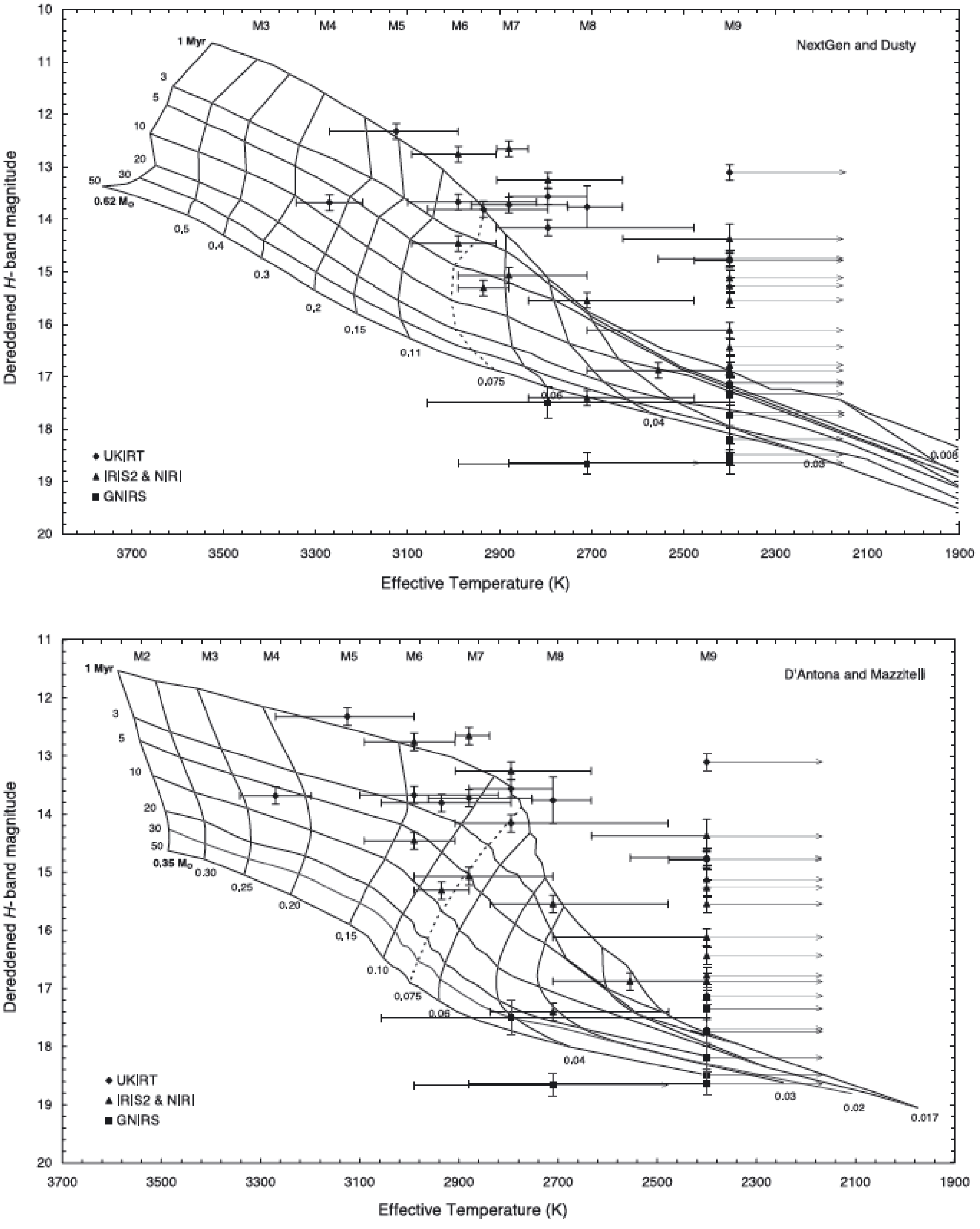

Fig. 1.4: In the HR diagrams for the ONC, the isochrones converge at M9/L0 dwarf temperatures, certainly within the observational errorbars. As a result, at late spectral types HR diagrams cannot be used to differentiate young, planetary mass objects (PMOs) from older, more massive brown dwarfs. Plots from Weights et al. (2009).

$H_2(K)$ index, which I believe will be of benefit in resolving the age-mass degeneracy associated with these objects. My investigation suggests that the $H_2(K)$ index will be of particular use in the analysis of noisy or low quality data where narrow spectral features are not resolved. The results of my investigation have been published (Canty et al., 2013b).

Since my results were published, the $H_2(K)$ index has been used by other researchers to support the young ages of objects they have found (Currie et al. 2014; Schneider et al. 2014; Currie, Burrows & Daemgen 2014; Pinfield et al. 2014). In addition, some researchers have extended the $H_2(K)$ index to objects with later spectral types than those I examine in Chapter 2. These researchers have found that the $H_2(K)$ index is capable of differentiating young objects even at these later spectral types. I examine the application by other researchers of the $H_2(K)$ index in Chapter 2 of this thesis.

1.2 The atmospheres of late T dwarfs

The second part of my thesis is an investigation into the appearance of CH_4 and NH_3 absorption features in the near-infrared spectra of two late T dwarfs, of consecutive spectral types. In addition to identifying new spectral features and correcting the identities of some features which had previously been wrongly identified, I examine how the strengths of these opacity sources vary in the spectra of the two T dwarfs.

1.2.1 Brown dwarf atmospheres

The relatively low effective temperatures of brown dwarfs allow molecules and condensates to form in their atmospheres. Indeed, the spectral types of brown dwarfs are classified according to the presence of certain chemical species in their atmospheres.

1.2.2 M dwarfs

At first, M dwarfs were characterised by the onset of TiO absorption at visible wavelengths (Morgan, Keenan & Kellman, 1943). Given that M dwarfs are cool and red, it was desirable to shift the spectral typing of these objects to longer wavelengths. However, this was prevented by the limited sensitivity of detectors at the time and only became possible after the invention of CCDs. M dwarfs were classified as early or late M dwarfs based on the relative strengths of the TiO and VO bands in their spectra (Bessell, 1991). Kirkpatrick, Henry & McCarthy (1991), hereafter K91, used two methods to define M dwarf spectral types. In the first method, a least-squares minimisation program was used to sort a sample of 39 spectral standards in order of increasing redness. A second method applied the same least-squares minimisation program to the relative strengths of atomic (Na I, Na II, K I) and molecular (TiO, VO, CaH) features in the standards' flattened spectra. Both methods yielded almost identical results but due to the low resolution of their data, K91 chose to assign spectral types to their sample using the first method.[2] The spectra used in K91's analysis are shown in Figure 1.5. It is clear from these spectra that TiO absorption is the defining characteristic of M dwarfs. TiO features are prominent in the wavelength ranges ∼6570-6850 Å, ∼7050-7270 Å, ∼7670-7860 Å, and ∼8210-8570 Å. VO absorption becomes apparent around spectral type M7 and increases in strength in later types. Metallic lines of Fe I and Ca II remain strong until approximately mid-M spectral types, then weaken as TiO and VO absorption increases. Figure 1.6 shows the evolution of these features in K9-M9 dwarfs.

---

[2] Coincidentally, the derivation of the $H_2(K)$ index in Chapter 2 was to some extent motivated by the limitations of low resolution data.

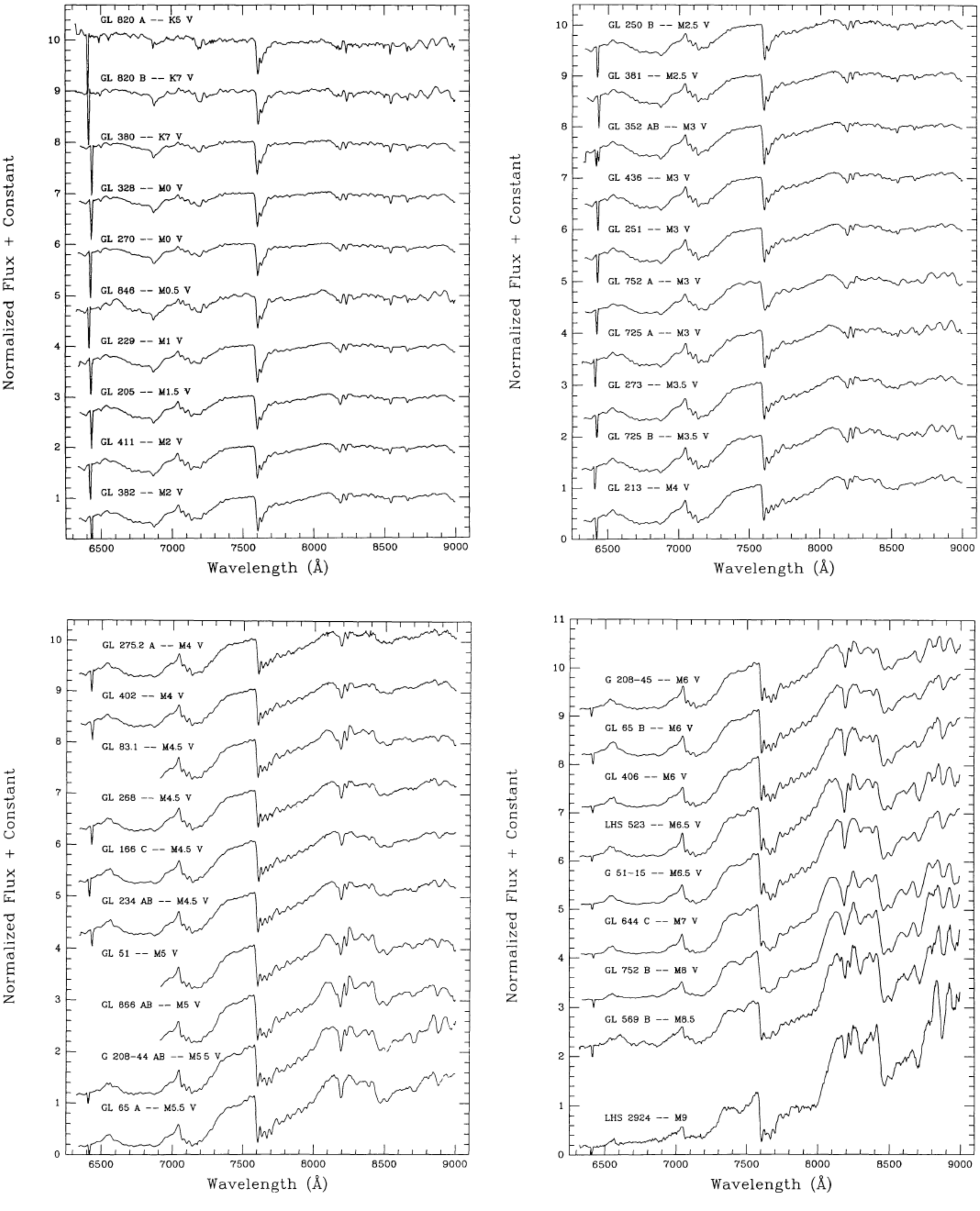

Fig. 1.5: The 39 primary spectral standards used by K91 to derive M dwarf spectral types. Plots from Kirkpatrick, Henry & McCarthy (1991).

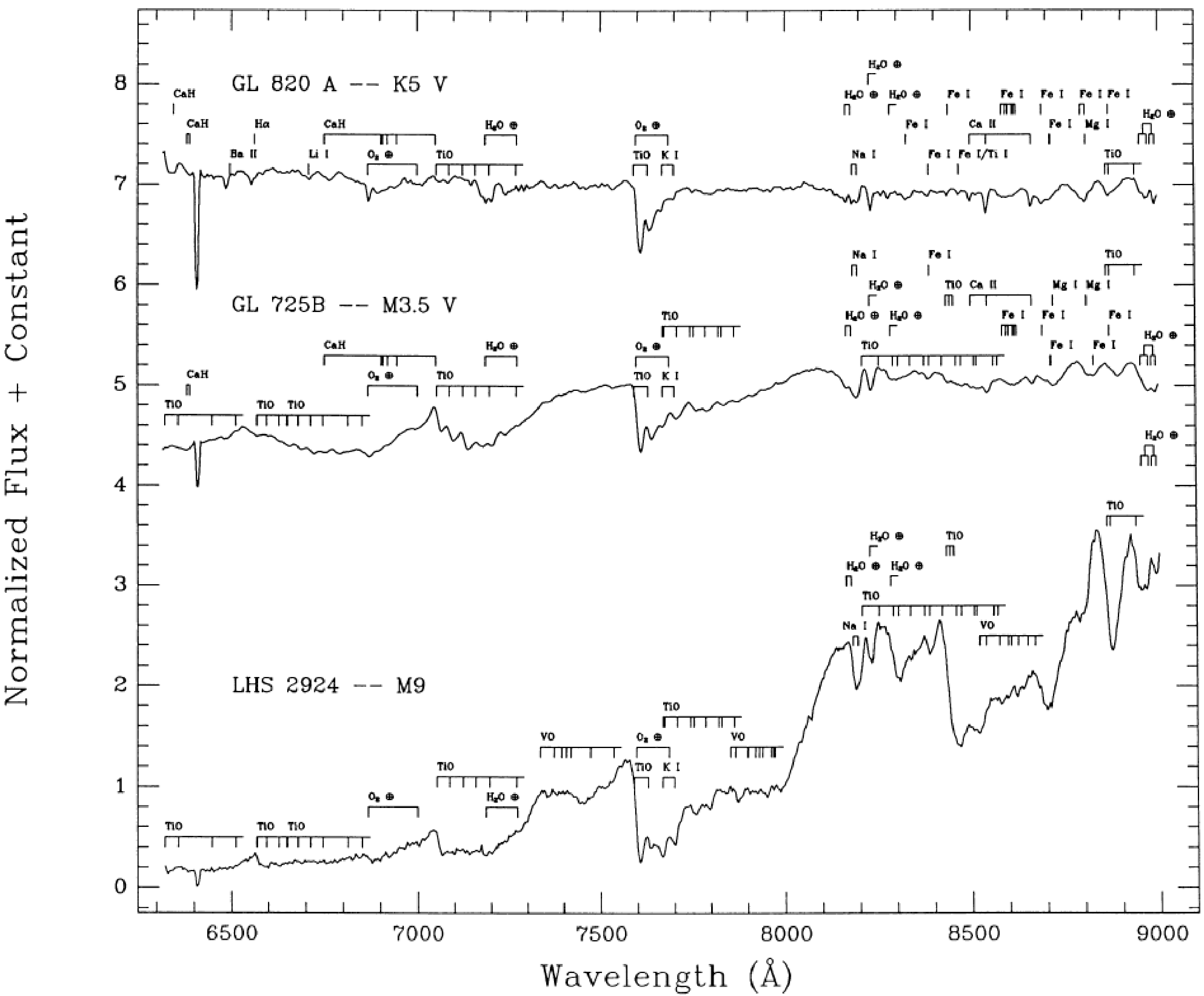

Fig. 1.6: The development of TiO and VO absorption in M dwarfs. Plots from Kirkpatrick, Henry & McCarthy (1991).

The least squares minimisation technique described in K91 was extended when Henry, Kirkpatrick & Simons (1994) used the same technique to assign spectral types to a sample of 92 objects within 8 pc. Ultra-cool brown dwarfs are defined as objects with spectral type ≥M7 corresponding to $T_{eff} \leq \sim 2500$ K (Kirkpatrick, Henry & Simons 1995; Kirkpatrick 1998).

1.2.3 L dwarfs

An optical spectrum of a cool companion ($T_{eff} \sim 2100$ K) to the white dwarf GD 165 showed no evidence of TiO absorption (Becklin & Zuckerman, 1988), nor did the shape of the absorption bands match those due to CH_4 and NH_3 found in the spectra of Jupiter and Saturn (Kirkpatrick, Henry & Liebert, 1993). GD 165B's spectrum suggested that this object may be the first member of a new spectral class.

Kirkpatrick et al. (1999), hereafter K99, identified 20 objects from the 2MASS (Skrutskie et al., 2006) survey whose spectra were similar to those of GD 165B and four other objects with spectral types later than M9.5. K99 defined these 25 objects as L dwarfs. In these objects' optical spectra, the TiO and VO absorption bands start to weaken and have largely disappeared by L6. As the oxide bands weaken, alkali metal (Rb I, Cs I) lines strengthen. The K I doublet at 7665/7699 Å broadens with increasing spectral type, while the cores weaken, disappearing entirely by L4. The metal hydride bands (FeH and CrH) increase in strength until approximately mid-L spectral types, then weaken as H_2O absorption increases. These changes can be seen in Figure 1.7. Figure 1.8 shows a detail of the wavelength regions where these structural changes occur.

To classify L dwarfs, K99 defined a set of spectral ratios to measure the strengths of the metal alkali lines, the metal hydride and metal oxide molecules. They also measured the broadening of the K I doublet. In addition, they constructed four colour ratios to measure increasing redness.

These spectral changes are thought to be due to the formation of dust particles as the dwarf's atmosphere cools below ∼2600 K. There is ample evidence that condensates

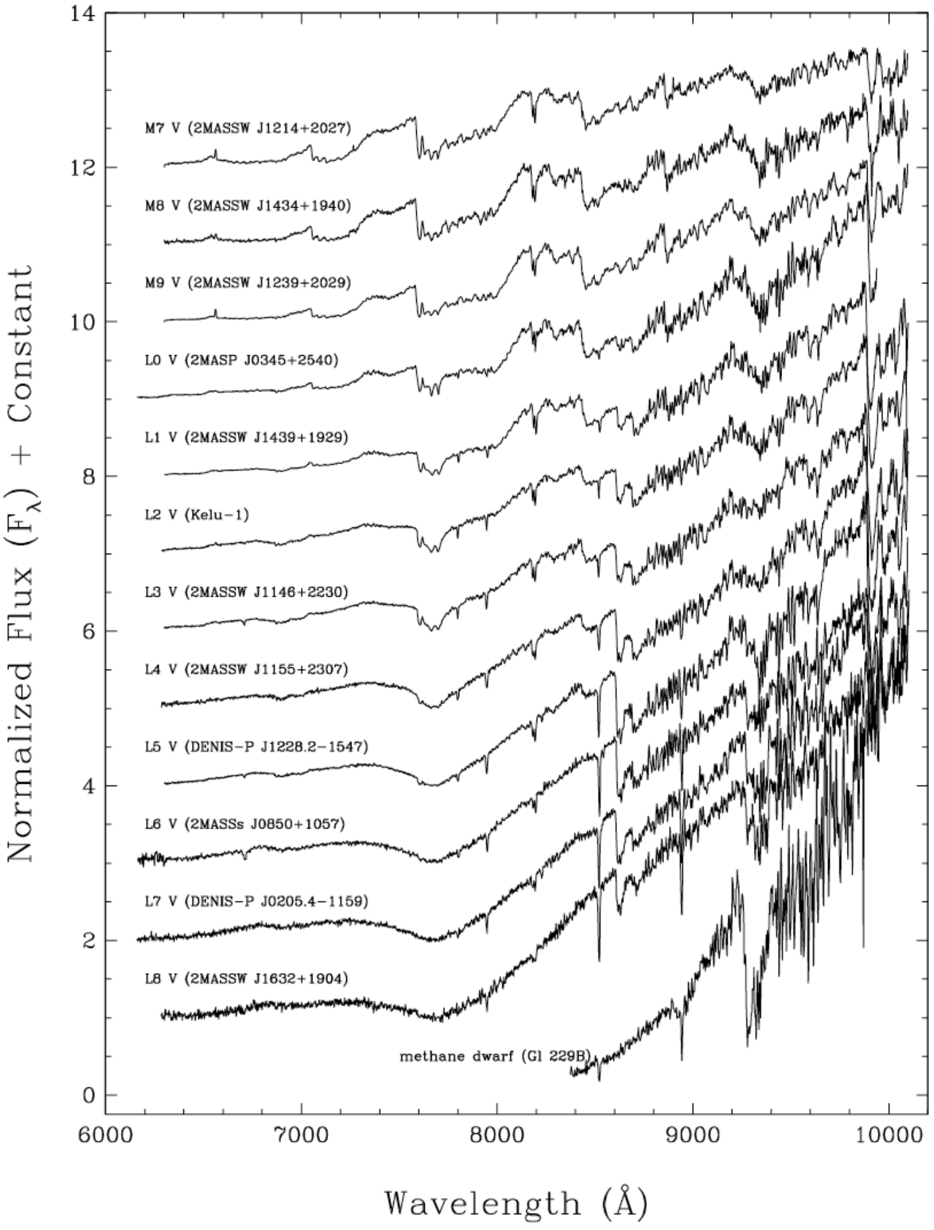

Fig. 1.7: A subset of the data in K99, showing how the optical spectra of L dwarfs change with increasing spectral type. Plots from Kirkpatrick et al. (1999).

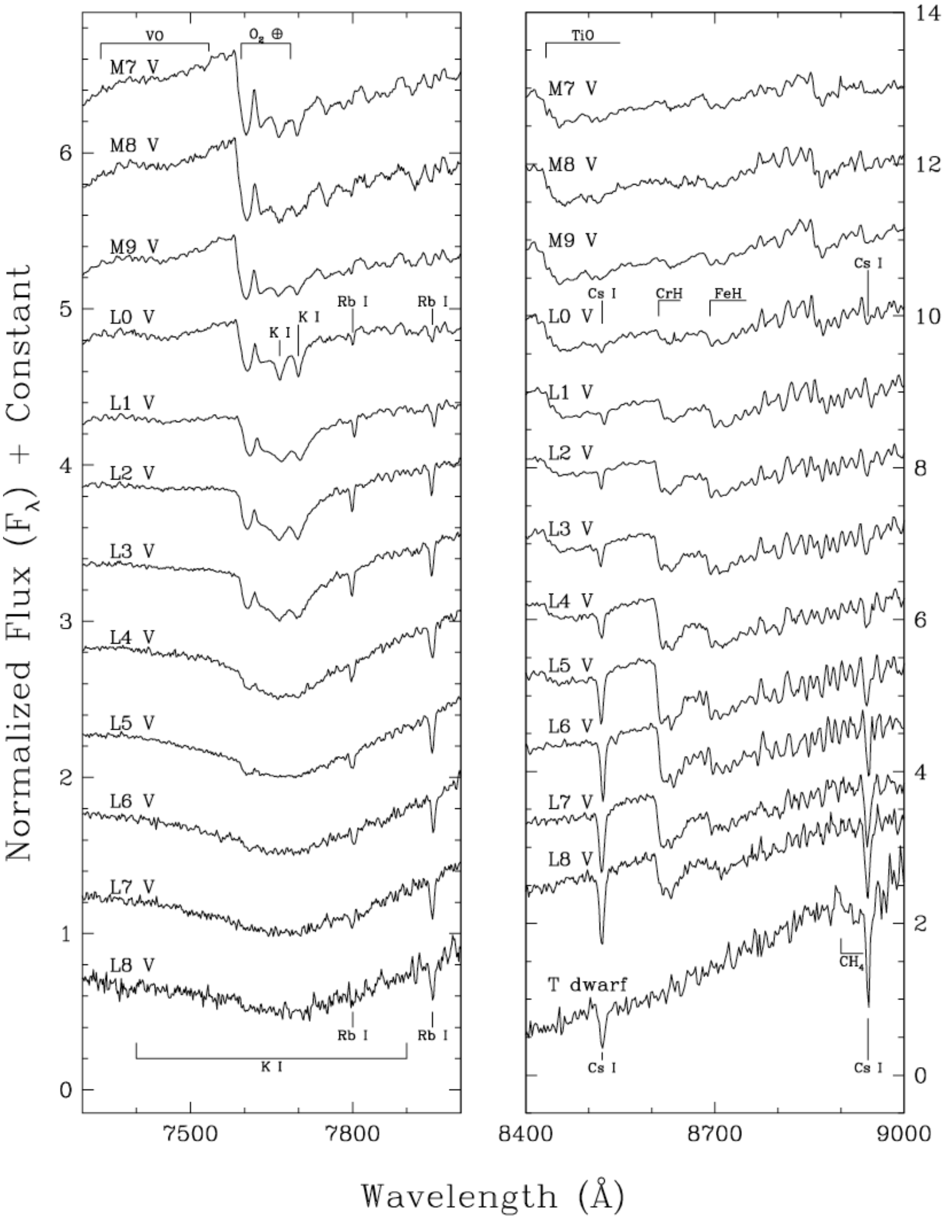

Fig. 1.8: A detail of the wavelength regions from Figure 1.7 containing diagnostic features for assigning spectral type. Plots from Kirkpatrick et al. (1999).

form at these temperatures. For example, the red near-infrared colours of late M and L dwarfs (Tsuji, Ohnaka & Aoki 1996; Marley et al. 2002), and the disappearance of spectral features as atoms or molecules condense into dust grains (Kirkpatrick et al. 1999; Lodders 2002). As the gas phase is depleted, the photosphere moves to greater depths in the atmosphere, and the growing prominence of alkali lines with increasing spectral type is thought to be due to the resulting increased column density of these species (Lodders 1999; Burrows & Sharp 1999). Emission from dust grains would also explain the unexpectedly shallow near-infrared H_2O absorption bands (Tsuji, Ohnaka & Aoki 1996; Jones & Tsuji 1997), while the flattening of the spectra of mid-L dwarfs from $\sim$9-11 μm is thought to be due to silicate grains (Cushing et al., 2006). Model spectra incorporating dust opacity are good fits to the data across the L dwarf regime (Cushing et al. 2008; Stephens et al. 2009). The recent discovery of peculiarly red L dwarfs can also be explained by dust opacity (Gizis et al. 2012; Liu et al. 2013; Marocco et al. 2014). It is thought that the red SEDs of some young L dwarfs are caused by enhanced photospheric dust scattering flux to longer wavelengths (Faherty et al., 2013).

As L dwarfs are cooler than M dwarfs and therefore brighter at near-infrared wavelengths, it makes even more sense to derive a technique to define spectral types at these longer wavelengths. The near-infrared spectra of L dwarfs tend to be characterised by deep H_2O absorption bands and by CO overtone bands which are first seen in the K band of late M dwarfs (see Figure 1.9).

Previous attempts to establish a set of near-infrared standard spectra for M and L dwarfs did so by comparing an object's near-infrared spectral ratios with the same ratios for an object whose spectral type was derived at optical wavelengths (Reid et al. 2001; Geballe et al. 2002; McLean et al. 2003). A set of J band spectral standards has been found to match spectral types derived at optical wavelengths for the same objects (Kirkpatrick et al., 2010).

Since objects aged <10 Myr have much lower surface gravities than old field dwarfs with the same T_{eff}, it is important that techniques for determining spectral types based on near-infrared wavelengths should be gravity-insensitive. Such a method has recently been derived for spectral typing M5-L7 dwarfs at near-infrared wavelengths

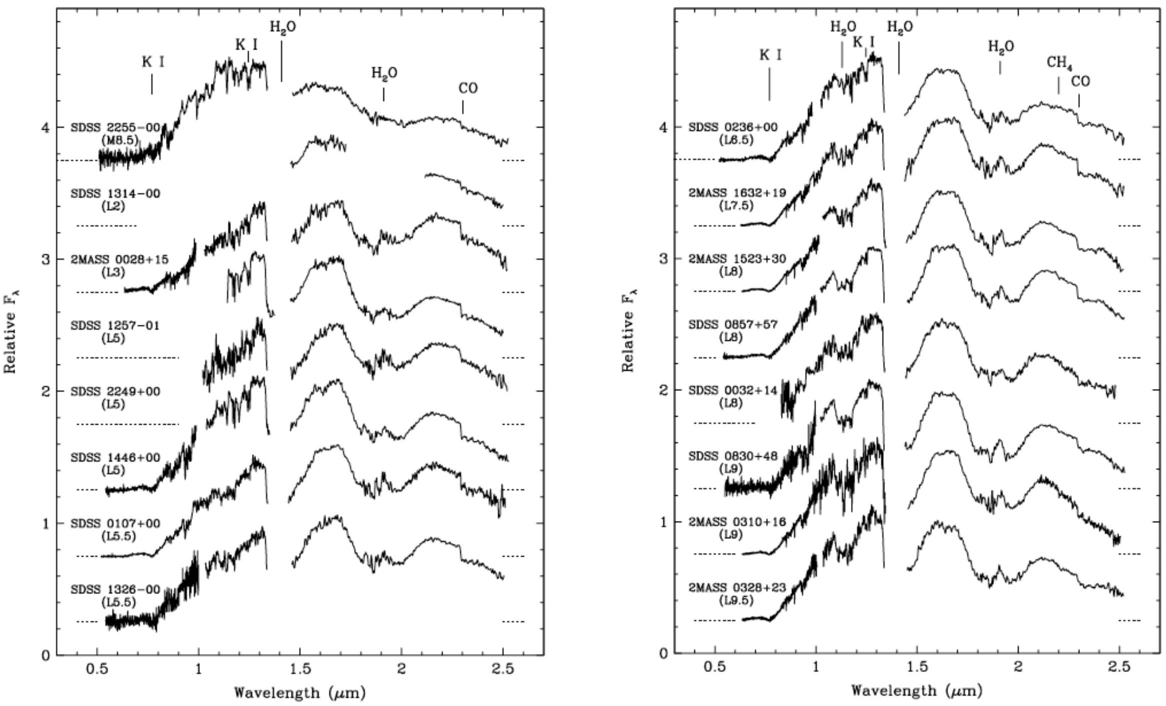

Fig. 1.9: L dwarf near-infrared spectra showing persistent H_2O and CO absorption bands. In later spectral types, the CO bandhead at ~2.3 μm weakens as CH_4 absorption increases. Gaps in the spectra between ~1.3-1.5 μm are caused by telluric water absorption. Plots from Geballe et al. (2002).

using spectral indices and visual comparison (Allers & Liu, 2013), and I used gravity-insensitive spectral indices developed in Lucas et al. (2006) and Weights et al. (2009) to assign spectral types to a set of very young PMOs in the ONC (see Chapter 2).

1.2.4 The L/T transition

The sedimentary layers which are so characteristic of L dwarf atmospheres have largely disappeared in T dwarfs. This decrease in condensate opacity occurs at approximately constant T_{eff} over a narrow range of spectral types (L7-T4) (Golimowski et al. 2004; Stephens et al. 2009). As brown dwarfs cool through L spectral types, CH_4 rather than CO becomes the main carbon-bearing compound. The first L/T transition objects were discovered by Leggett et al. (2000). Their near-infrared spectra are shown in Figure 1.10. The characteristics of the spectra are deepening H_2O absorption bands at 1.15, 1.4, and 1.9 μm, increasing CH_4 absorption in the range 1.6-1.7 μm and redward of 2.2 μm, and weakening CO absorption. Note also how the absorption features at 1.63, 1.67, and 2.20 μm deepen across the L/T transition objects. Leggett et al. (2000) identified these features as belonging to the methane $2\nu_2+\nu_3$, $2\nu_3$, and

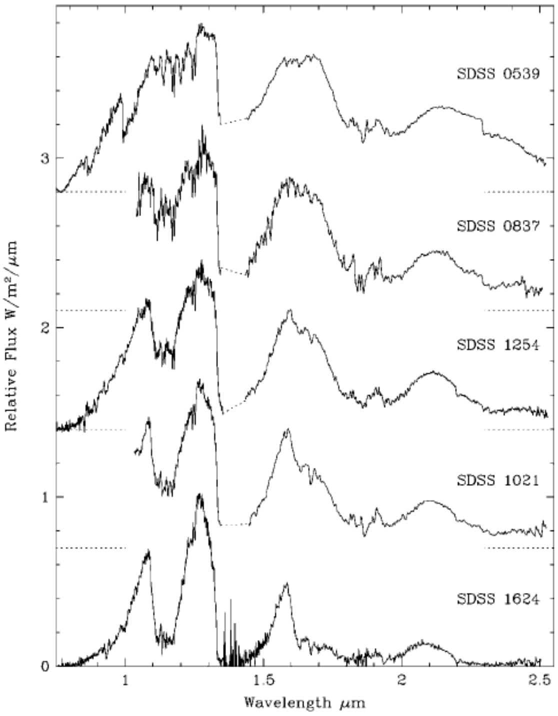

Fig. 1.10: The first L/T transition objects. The spectra of SDSS 0837, SDSS 1254, and SDSS 1021 are ordered by increasing CH_4 absorption. The L5 dwarf SDSS 0539 and the T6 dwarf SDSS 1624 are shown for comparison. Plot from Leggett et al. (2000).

ν_2+ν_3 vibrational bands respectively. Compare this analysis with my analysis of the CH_4 vibrational bands in the near-infrared spectra of a T8 and T9 dwarf in Chapter 3.

Models of brown dwarf atmospheres either side of the L/T transition are good fits to the data (Chabrier et al. 2000; Allard et al. 2001; Tsuji 2002; Allard et al. 2003; Burrows, Sudarsky & Hubeny 2006; Saumon & Marley 2008). However, the physical processes occurring within the L/T transition region, in particular the abrupt reversal in reddening in J-K_s colour, with blueward shifts of up to ∼2 magnitudes, together with a brightening in the J band (Vrba et al. 2004; Faherty et al. 2012), are not well understood. While atmospheric models incorporating dust formation and sedimentation show a reversal in J-K_s colour (Ackerman & Marley 2001; Tsuji 2002; Allard et al. 2003; Tsuji, Nakajima & Yanagisawa 2004; Tsuji 2005; Burrows, Sudarsky & Hubeny 2006; Helling et al. 2008; Saumon & Marley 2008; Allard, Homeier & Freytag 2011), the change is not as sudden as seen in the data. Suggestions to explain the dramatic change in J-K_s colour have included a rain-out of condensates or a sudden increase in efficiency in sedimentation (Knapp et al., 2004), or a fragmentation of the cloud

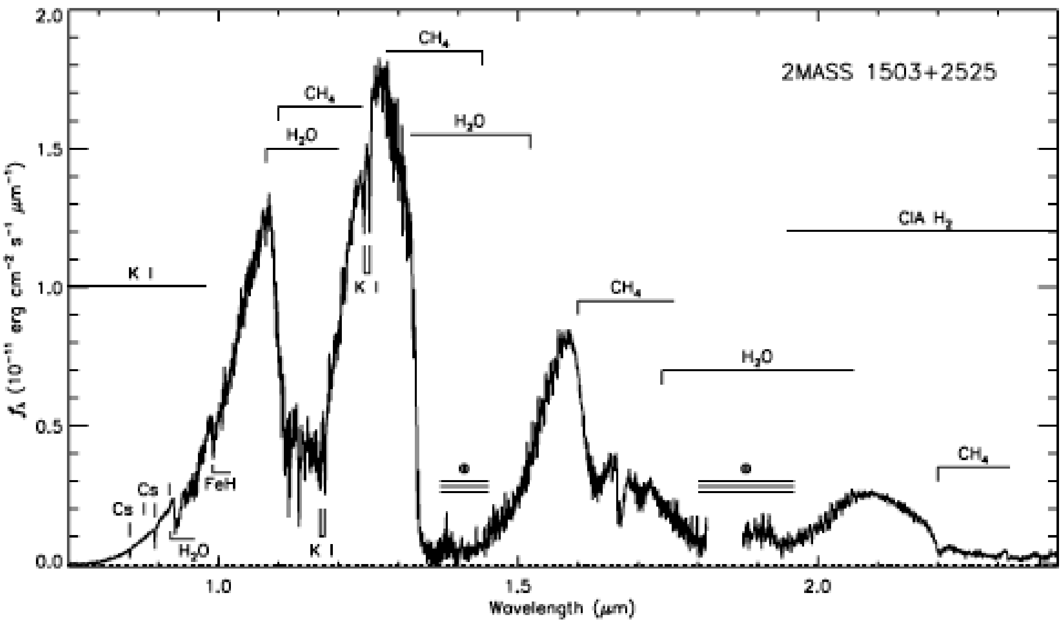

Fig. 1.11: The near-infrared spectrum of the T5 dwarf 2MASS 1503+2525 showing characteristic features of the T spectral class. Plot from Burgasser et al. (2006).

layer (Ackerman & Marley 2001; Burgasser et al. 2002a).

1.2.5 T dwarfs

T dwarfs are characterised by CH_4 absorption in the near-infrared (Geballe et al., 1996), pressure-broadened alkali lines, deep H_2O absorption bands, and collision-induced absorption by hydrogen molecules suppressing flux longward of 2 μm (Saumon et al. 1994; Borysow, Jorgensen & Zheng 1997). See Figure 1.11.

The first identified brown dwarf was a T dwarf (Nakajima et al. 1995; Oppenheimer et al. 1995). Since then, a large number of T dwarfs have been discovered in the local field using surveys such as 2MASS, SDSS (York et al., 2000), UKIDSS (Lawrence et al., 2007), and now WISE (Wright et al., 2010). T dwarfs provide a new arena for studying atmospheric physics at T_{eff} cooler than stars but warmer than gas giant planets such as Jupiter. WISE has recently discovered the first Y dwarfs, objects with T_{eff} ~275-400 K and a strong near-infrared ammonia feature (Cushing et al., 2011). However, as Y dwarfs are too faint for medium resolution spectroscopy of individual narrow molecular absorption features with instruments such as Gemini/Near-infrared Integral Field Spectrometer (NIFS) (McGregor et al., 2003), I do not consider them in this thesis. Figure 1.12 is an HR diagram of M_{K_S} versus spectral type for a sample of low-mass stars and brown dwarfs of spectral type M6-T2.

The range of T_{eff} of late T dwarfs are uncertain, owing to the complicated atmospheric microphysics of these very cool objects and, until recently, the absence of good methane and ammonia line lists. Distance and temperature estimates based on model fits to near-infrared spectra are often found to be incorrect, in some instances by a factor of 2 in distance (Liu et al., 2011). Improved model atmospheres are essential in order to derive reliable temperatures, luminosities, and gravities for cold brown dwarfs, without recourse to time-consuming parallax measurements (Dupuy & Kraus 2013; Beichman et al. 2014). This is a basic requirement in order to determine the substellar mass function in the local field, and to enable brown dwarfs to inform our understanding of the many warm gas giant exoplanets, which are hard to study in any detail.

In low resolution ($R\lesssim2000$) late T dwarf spectra, only broad and overlapping absorption bands of water and methane are typically observed at 1.0-2.4 μm. Medium resolution spectroscopy ($R\geq5000$) with instruments such as NIFS resolves the bands into narrow features produced by blends of individual transition lines and detects other features such as blends of numerous weak ammonia lines across the near-infrared, as well as the temperature sensitive K I doublet at 1.18 μm and 1.24 μm. Bochanski et al. (2011), hereafter B11, have demonstrated this with the first medium resolution spectrum of a single object, the T9 standard, UGPS J072227.51-054031.2 (Lucas et al. 2010) (hereafter UGPS 0722), obtained with Magellan/FIRE (Simcoe et al., 2010) during a commissioning run. Such data offer the opportunity to directly test the details of the previously inadequate near-infrared model spectra.

New experimental hot ammonia (Hargreaves, Li & Bernath, 2011) and hot methane (Hargreaves et al., 2012) line lists are available, although the wavelength ranges of these line lists, 740-2100 cm^{-1} (4.8-13.5 μm) and 960-5000 cm^{-1} (2.0-10.4 μm) respectively, limit their value in the analysis of near-infrared spectra. Saumon et al. (2012), hereafter S12, have recently published improved model atmospheres that incorporate a new high-temperature, synthetic ammonia line list (BYTe) (Yurchenko, Barber &

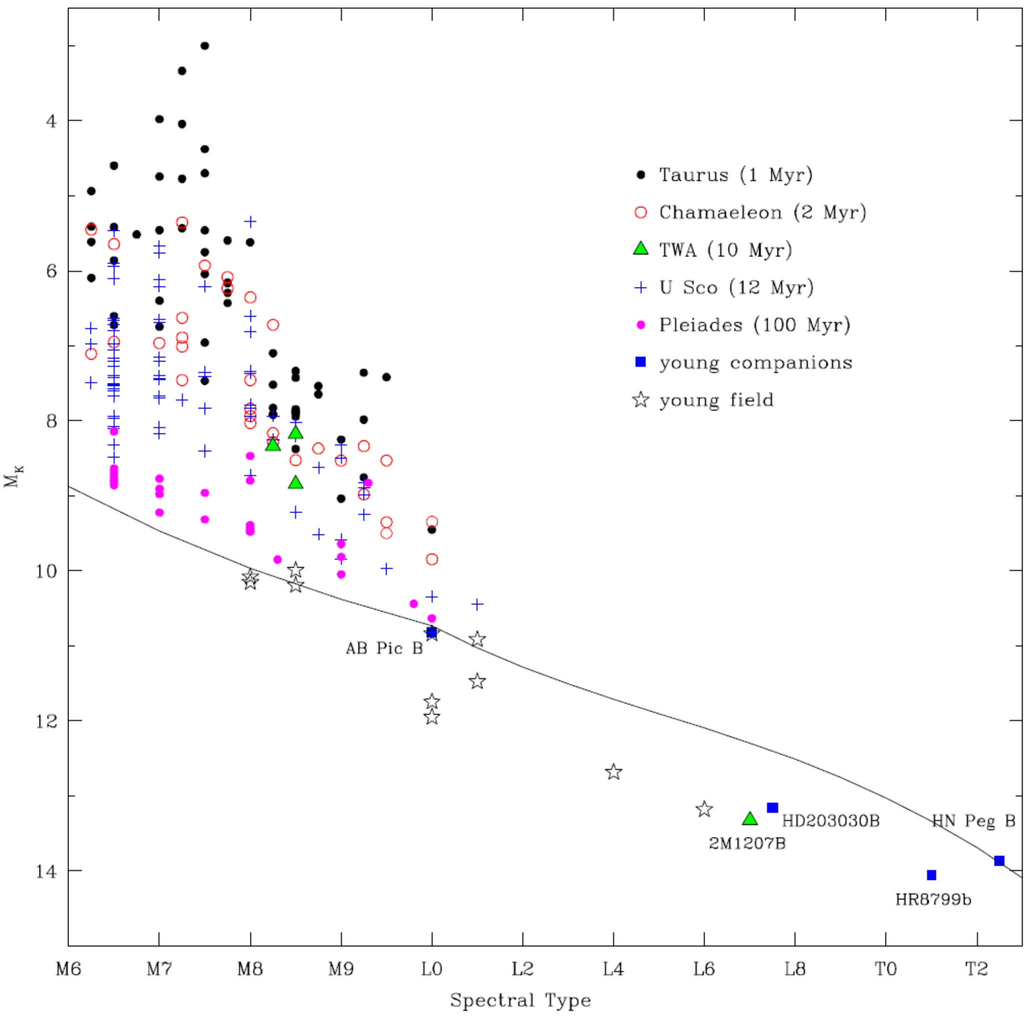

Fig. 1.12: M_K as a function of spectral type in nearby young clusters and associations. The solid line is a fit to young field dwarfs from Faherty et al. (2012). Plot from Luhman (2012).

Tennyson, 2011), and new calculations of collision-induced absorption of molecular hydrogen (H_2 CIA) (Richard et al., 2012). S12 also had access to an improved, though still incomplete, treatment of methane opacity (Freedman, Marley & Lodders, 2008). A new synthetic methane line list is also now available (Yurchenko & Tennyson, 2014). It is therefore timely to provide a high quality set of medium resolution spectra to compare with the new generation of models.

In Chapter 3 of this thesis, I examine the atmospheres of two late T dwarf standards by comparing absorption features in the near-infrared spectra of these objects with the synthetic spectra of important molecules such as H_2O, CH_4, and NH_3. I conduct an analysis of the quantum numbers of the rotational-vibrational (ro-vibrational) transition lines responsible for the methane and ammonia absorption features in these objects' near-infrared spectra. I also look at the *L* band spectrum of the T9 and use the new CH_4 line list to offer an explanation for the spectrum's structure in this waveband.

In Chapter 4 I conclude my thesis and address some remaining outstanding questions related to my analysis.

Chapter 2

Paper: Towards precise ages and masses of free floating planetary mass brown dwarfs

This chapter consists largely of the unedited journal paper published by Canty et al. 2013b, which was submitted and accepted for publication in Monthly Notices of the Royal Astronomical Society. The co-authors of this paper were Phil Lucas, my Supervisor, Pat Roche[1], and David Pinfield[2]. Some of the results in this paper were used by other researchers. These researchers' results are also discussed in this chapter.

Measurement of the substellar IMF in very young clusters is hampered by the possibility of the age spread of cluster members. This is particularly serious for candidate PMOs, which have a very similar location to older and more massive brown dwarfs on the Hertzsprung-Russell Diagram (HRD). This degeneracy can be lifted by the measurement of gravity sensitive spectral features. To this end I have obtained medium resolution (R≈5000) NIFS *K* band spectra of a sample of late M/early L-type dwarfs. The sample comprises old field dwarfs and very young brown dwarfs in the Taurus as-

---

[1] Astrophysics Department, University of Oxford, 1 Keble Road, Oxford OX1 3RH, UK

[2] Centre for Astrophysics Research, University of Hertfordshire, College Lane, Hatfield AL10 9AB, UK

sociation and in the σ Orionis cluster. I demonstrate a positive correlation between the strengths of the 2.21 μm Na I doublet and the objects' ages. I demonstrate a further correlation between these objects' ages and the shape of their K band spectra. I have quantified this correlation in the form of a new index, the $H_2(K)$ index. This index appears to be more gravity-sensitive than the Na I doublet and has the advantage that it can be computed for spectra where gravity-sensitive spectral lines are unresolved, while it is also more sensitive to surface gravity at very young ages (<10 Myr) than the triangular H band peak. Both correlations differentiate young objects from field dwarfs, while the $H_2(K)$ index can distinguish, at least statistically, populations of ∼1 Myr objects from populations of ∼10 Myr objects. I applied the $H_2(K)$ index to NIFS data for one ONC PMO and to previously published low resolution spectra for several other ONC PMOs where the 2.21 μm Na I doublet was unresolved and concluded that the average age of the PMOs is ∼1 Myr.

2.1 Introduction

Deriving the substellar IMF requires a representative sample of objects whose ages are well-constrained. Evolutionary models can then be used to assign masses and radii to these objects. However, because cooling is more rapid for less massive bodies, brown dwarfs of any given effective temperature have a well known degeneracy between age and mass. In very young (1-10 Myr) brown dwarfs this problem is most serious for the coolest and least massive objects with spectral types >M8 and masses <25 M_{Jup} (see, for example, Figure 5 of Weights et al. 2009, hereafter W09), where objects with planetary masses and ages of ∼1 Myr are not well separated in the HRD from brown dwarfs with ages of ∼10 Myr and masses 3 times higher. The Lyon DUSTY isochrones (Allard et al., 2001) and those of D'Antona & Mazzitelli (1997) agree in this. In order to derive the substellar IMF, this age-mass degeneracy must be lifted.

It has been shown that source ages can be measured using gravity-sensitive alkali metal absorption lines in the optical or near-infrared (Martin, Rebolo & Zapatero-Osorio 1996; Steele & Jameson 1995; Gorlova et al. 2003; Allers et al. 2007, hereafter

A07; Riddick, Roche & Lucas 2007; Luhman et al. 2007; Close et al. 2007; Cruz, Kirkpatrick & Burgasser 2009). This technique can differentiate 1 Myr objects from 5 Myr objects, and 5-10 Myr objects from field dwarfs with ages >5 Gyr, since very young substellar objects rapidly contract to smaller radii. The radii of evolved field brown dwarfs have little dependence on age or mass (Burrows & Liebert, 1993), while the radii of very young brown dwarfs can be up to six times the size of their final equilibrium radii (Stassun, Mathieu & Valenti, 2006). In consequence, their surface gravities ($g = GM/R^2$) can be substantially lower than those of older, more massive dwarfs of the same spectral type.

Theoretical models show that the luminosities of brown dwarfs decrease rapidly over time as they radiate away the internal energy supplied by gravity during the formation process (e.g. Burrows et al. 2001, hereafter B01). Therefore, many analyses have focussed on young clusters, where the higher luminosities of brown dwarfs at young ages allows the mass function to be derived for masses as low as 5-15 $\mathrm{M_{Jup}}$.

Among the uncertainties in these models are those dealing with the ages of the objects and the accuracy of the models themselves. These uncertainties are most significant in the cases of very young brown dwarfs in pre-main sequence clusters.

One uncertainty concerns a brown dwarf's initial energy. A 'hot start' brown dwarf forms from the collapse of a molecular cloud. A brown dwarf formed in a 'cold start' via core accretion has less gravitational potential energy stored as internal energy so that, mass for mass, the brown dwarf is cooler and less luminous than a 'hot start' brown dwarf. After ∼2 Myr, runaway gas accretion produces a peak in the luminosity of 'cold start' brown dwarfs (Marley et al., 2007). For the next ∼1 Myr and regardless of their mass, 'cold start' brown dwarfs outshine their 'hot start' counterparts, after which they cool quickly and become less luminous than 'hot start' brown dwarfs of a similar mass. This implies that 'cold start' brown dwarfs older than a few Myr would need to have higher masses in order to account for their observed luminosities. I note that since 'cold start' brown dwarfs form from a protoplanetary disk, this formation model is unlikely to apply to isolated brown dwarfs.

The constant mass accretion rate described in the standard model of star formation

(Shu 1977; Terebey, Shu & Cassen 1984) may give rise to the "luminosity problem", exemplified in the case of young nearby T Tauri stars with solar luminosities. These stars are under-powered in the sense that they should have several solar luminosities if they are descending approximately vertical Hayashi tracks on the HRD (Kenyon et al., 1990), depending on how young they are when they are observed. Time-variable accretion may resolve the "luminosity problem". It has been shown that episodic bouts of accretion rather than a spread of ages can also explain the luminosity spread in young clusters (Baraffe, Vorobyov & Chabrier 2012, hereafter B12).

These various uncertainties become less of a problem after only a few Myr, but they must be considered when dealing with the youngest brown dwarfs.

In this paper I investigate spectral signatures of age for substellar objects in pre-main sequence clusters. Previous work by this group and others has established the existence of a population of PMOs in the ONC (Lucas et al. 2006, hereafter L06; Riddick, Roche & Lucas 2007). A statistical analysis of the luminosity function by W09 indicates that most substellar objects in the cluster have ages of order 1 Myr, and it is unlikely that the PMO candidates represent a tail of older and more massive objects. However, the size of the planetary mass population cannot be tightly constrained until their ages are known with better precision.

The observations described in this paper were intended to produce the highest resolution spectra yet obtained (R≈5000) of three PMOs in the ONC and a sample of brighter calibrator brown dwarfs with known ages and/or gravities, including three objects on the deuterium-burning threshold in the σ Orionis cluster. In the event, I was unable to obtain useful data for two of the three ONC targets. However, the high quality of the data obtained for all of the calibrators has enabled a useful investigation of the effects of surface gravity on the K band spectra of very young brown dwarfs.

My aim was to use medium resolution spectroscopy to investigate the sensitivity of the Na I doublet at 2.21 μm to surface gravity, and hence age, while using the Ca I line at 2.26 μm and the CO absorption bands at 2.29 μm and 2.32 μm to correct for any metallicity variations or veiling by hot dust. It was also intended to use these spectra to provide more precise spectral types than had been possible previously, and also to confirm that the IMF extends below 10 M_{Jup}. An unexpected by-product of the investigation was the discovery that the slope of the K band also has strong sensitivity to gravity, which appears to provide a useful age indicator. While the effect of surface gravity on the K band spectra of pre-main sequence brown dwarfs has previously been noted (Luhman, Peterson & Megeath 2004; A07), it has not been studied in detail.

2.2 Selection of Targets

In the last few years, large populations of brown dwarfs have been discovered in several very young clusters where the mass function appears to extend below the deuterium-burning threshold of 0.012-0.013 $M_\odot$. Among these clusters are NGC 1333 (Scholz et al. 2012; Winston et al. 2009), IC 348 (Alves de Oliveira et al. 2013; Muench et al. 2007; Luhman et al. 2003b), ρ Oph (Alves de Oliveira et al. 2012; Mužić et al. 2012), and the ONC (Lucas & Roche 2000; W09). The ONC contains the largest known sample of very young brown dwarfs, and therefore is an ideal site to obtain good statistics on the IMF at planetary masses and to gain insights into low-mass brown dwarf formation processes. The formation mechanism responsible for the low masses of substellar objects is currently unknown. The theoretical minimum mass for gravitational fragmentation of gas is thought to be ~1-5 M_{Jup} (Whitworth & Stamatellos, 2006), while in the dynamic interaction of pre-stellar cores, the ejected objects may have planetary masses if they are ejected very early in the process (Reipurth & Clarke 2001; Bate, Bonnell & Bromm 2002; Goodwin, Whitworth & Ward-Thompson 2004). Turbulent fragmentation of molecular clouds can also produce PMOs. For example, the brown dwarf binary FU Tau A, B is thought to have been formed by turbulent fragmentation. The components of this binary have masses ~5 M_{Jup} and ~15 M_{Jup} (Luhman et al., 2009).

The three ONC PMOs are 183−729 (18), 152−717 (27) and 137−532 (172) (Lucas & Roche 2000; Lucas, Roche & Tamura 2005, hereafter LRT05) (the numbers in brackets are the source catalogue numbers quoted in LRT05). They were selected because each has a bright star I_{MAG}=15−16 and R_{MAG}=17−18 within ~25″ that could potentially be used as a tip/tilt guide star for laser-guided adaptive optics (AO) and they are bright enough for medium resolution ground based spectroscopy. I note that there is only a modest range of apparent K magnitudes amongst the spectroscopically confirmed PMOs in L06. Their PMO status is based on their spectral types of ∼M9−L0, their low surface gravities [L06; W09], and their low luminosities. Low gravity was determined by comparing these objects' H and K band pseudo-continuum profiles with those of other low gravity brown dwarfs and high gravity field dwarfs in low resolution spectra. These features confirmed that these objects were cluster members, and therefore that their ages are unlikely to be more than ∼10 Myr. The PMOs are within a few arcminutes of the centre of the ONC, so they are likely to be very young (∼1 Myr) objects, rather than members of the more dispersed and slightly older population that extends over a few degrees on the sky.

In the event, useful observations were obtained for only one ONC PMO, 152−717. This source has apparent magnitude K=17.6, which is typical of the sample in L06. It was not possible to obtain a guide star lock for the other two PMOs, owing to the bright background of the nebulosity. I note that this observing method could be more successfully employed in future when the patrol radius of the Gemini Altair AO system has been increased, allowing the use of brighter guide stars.

The calibrators consisted of two field dwarfs, 2MASS 0345+25, hereafter 2MASS 0345 (Kirkpatrick, Beichman & Skrutskie, 1997), BRI 0021−0214, hereafter BRI 0021 (Irwin, McMahon & Reid, 1991), three 3-7 Myr objects, σ Orionis 51 (Zapatero Osorio et al., 2000), σ Orionis 71 (Barrado y Navascués et al., 2002), σ Orionis J053849.5−024934, hereafter σ Orionis J053−024, and five 1-2 Myr objects, KPNO-Tau 1 (Briceño et al., 2002), KPNO-Tau 4 (Briceño et al., 2002), KPNO-Tau 12 (Luhman et al., 2003a), 0457+3015, and 2MASS 0535−0546 (Stassun, Mathieu & Valenti, 2006).

The calibrators were all chosen because they have similar spectral types to the ONC PMOs, with the exception of the eclipsing binary 2MASS 0535−0546 (spectral type M7) which was felt to be worthy of observation owing to the precisely known surface gravities of the components.

The three 3-7 Myr σ Orionis objects were selected because there was fairly good prior evidence that they were bona fide cluster members, as opposed to contaminating field dwarfs in front of this rather diffuse cluster. This evidence was either from previous spectroscopy of alkali metal lines (σ Orionis 51, (McGovern et al., 2004)) or from detection of mid-infrared excess and/or spectroscopic evidence (σ Orionis 71, σ Orionis J053−024, (Caballero et al., 2007)). Being older, they can be used to compare objects of slightly greater mass and gravity.

Further selection criteria for the 1-2 Myr calibrators in the Taurus-Auriga molecular cloud complex and the field dwarf calibrators were that they are bright objects with little or no extinction and that previous studies have found them to be fairly typical objects with no obvious veiling by a circumstellar accretion disc (see above references). While the 1-2 Myr calibrators are more massive than the ONC PMOs, the Lyon DUSTY isochrones predict that they also have larger radii, such that their surface gravities are very similar.

2.3 Observations & Data Reduction

Observations of the ten calibrators were made over eight nights between 23 August 2008 - 29 October 2009. Observations of the PMOs were made on 16 October 2009. Observations were made using the 8m Gemini Telescope at Gemini North with NIFS. The latter was fitted with the K band grating, centred at 2.2 μm. Observations were made in an ABBA pattern to facilitate the removal of the sky background and dark current. Some characteristics of the brown dwarf calibrators and of the observed PMO, together with some observational notes including the S/N range of the Na I absorption feature for each object are shown in Table 2.1. These ranges were chosen as they are typical of the S/N for each observation.

Table 2.1: Brown Dwarf Calibrator Sources and the PMO 152−717

	K band Magnitude	Integration Time (s)	S/N	Aperture Size (″)
2MASS 0345+25	12.7	480	80−116	0.5
BRI 0021−0214	10.6	480	158−184	0.6
σ Orionis 51	16.1	3600	29−59	0.23[1]
σ Orionis 71	16.1	3600	34−73	0.26[1]
σ Orionis J053−024	16.2	3600	22−44	0.26[1]
KPNO-Tau 1	13.7	1000	96−123	0.5
KPNO-Tau 4	13.3	1000	102−133	0.5
KPNO-Tau 12	14.9	1800	52−119	0.5
2MASS 0535−0546	13.8	500	84−131	0.45
0457+3015	14.5	1800	63−129	0.44
152−717	17.6	6300	4−8	0.2[1]

[1] Observed using Adaptive Optics

Raw data were reduced using the GEMINI NIFS package within IRAF. The reduction was made in three steps: a baseline calibration to produce a shift reference file, a flat field file, a flat bad pixel mask file, a wavelength referenced arc file, and a spatially referenced ronchi file; a telluric calibration reduction to produce a 1D spectrum of the standard star to be used for telluric calibration of the science data; and a science data reduction to produce a 3D data cube which has been sky subtracted, flat fielded, cleaned of bad pixels, and telluric corrected.

The first two steps in the reduction process were completed by editing processing scripts supplied by the Gemini Observatory. The science reduction also largely followed a Gemini script. However, several additional steps were required to complete the reduction. In particular, the hydrogen Brγ absorption line at 2.1661 μm in the spectrum of the standard star chosen for the telluric calibration of each science object had to be removed, the modified spectrum then being divided by the star's blackbody spectrum and normalised before being divided into the extracted 1D science object spectrum to correct the latter for telluric absorption features.

The spectra were extracted using an aperture size of 1.5 times the full width at half maximum (FWHM) of each object, as determined from the dispersed images, see Table 2.1.

Observations in the K band are susceptible to contamination by telluric OH sky lines. For the fainter objects observed here, the flux in the sky lines often varied sufficiently during the exposures that the lines were poorly subtracted in the reduction. To remove these lines as well as cosmic ray strikes and the general background, the data were processed using my own scripts to subtract the residual background along each column and interpolate across isolated pixels with highly anomalous counts. Care was taken to ensure that the scripts removed only noise features, using a comparison of the many image slices within each dispersed image to distinguish real features from noise.

I used the IRAF task CONTINUUM to normalise each science spectrum and remove the slope. I then fitted a second order chebyshev function to define a local pseudo-continuum. This pseudo-continuum set the flux level for measuring the equivalent widths of spectral features. While I experimented with higher-order fits, none differed significantly from the second-order fit. For this reason, the flux level of the pseudo-continuum was excluded as a source of error when I came to determine the uncertainties in my measurements. To obtain a representative pseudo-continuum, the fit excluded the Na I lines and the CO absorption bands starting at 2.29 μm. The wavelength range for the fit was from 2.10 μm → 2.20 μm, and 2.21 μm → 2.29 μm. As a pseudo-continuum was used to measure these equivalent widths, they are more accurately referred to as pseudo-equivalent widths (pEWs). Spectral features were deblended using the IRAF task SPLOT and the pEWs derived by fitting Voigt functions to the deblended lines.

2.4 Results

2.4.1 *K* band Spectra

The extracted 1D spectra of nine brown dwarf calibrators are shown in Figures 2.1 and 2.2. All spectra were smoothed using three pixel boxcars.

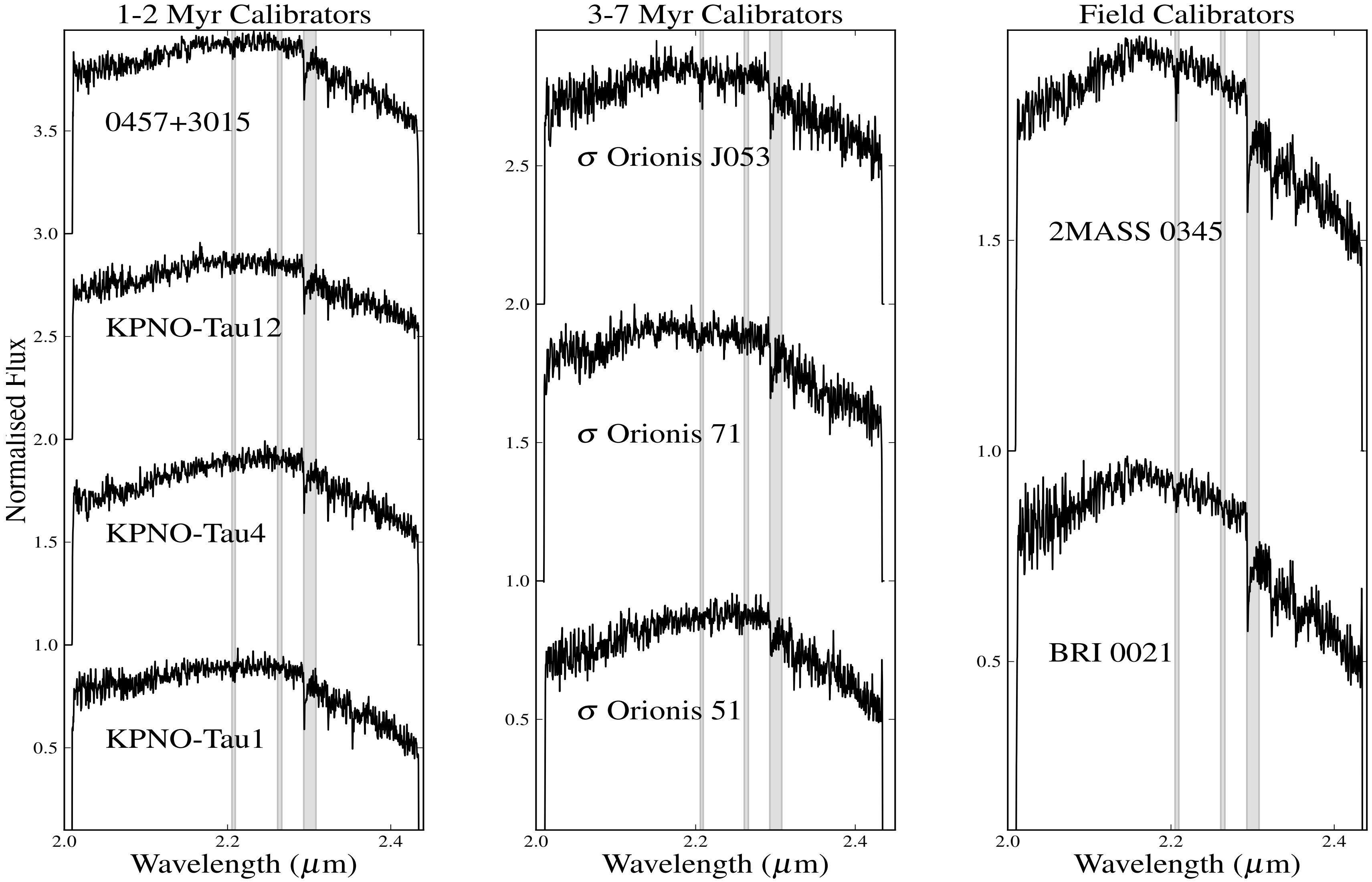

Fig. 2.1: Extracted spectra of the three types of calibrator. The normalised spectra are plotted with a constant integer offset. pEWs were calculated in the shaded regions. From left to right, these regions span the Na I doublet, the Ca I triplet, and the first CO bandhead.

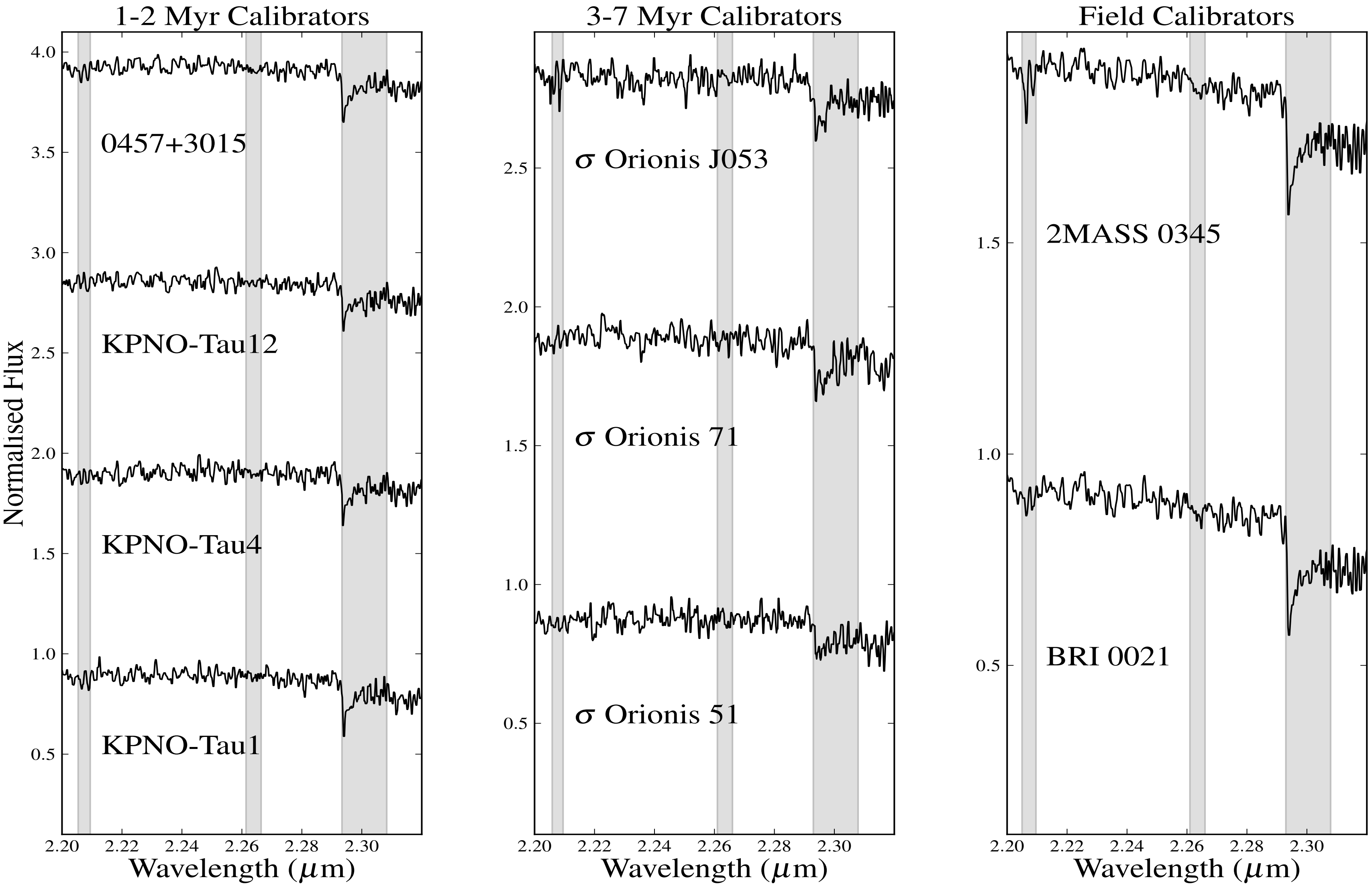

Fig. 2.2: Expanded views of the shaded regions in Figure 2.1.

2.4.2 Equivalent Widths

pEWs of the Na I doublet (2.206 μm and 2.209 μm) and of the CO band head starting at 2.294 μm were obtained for all brown dwarf calibrators. pEWs of the Ca I triplet (2.261 μm, 2.263 μm and 2.265 μm) were obtained for both field dwarfs, one 3-7 Myr old object, and four 1-2 Myr old objects. These results are shown in Table 2.2. Table 2.3 shows, where known, the rotational velocities of the calibrators (obtained from the literature). Figure 2.3 shows the pEWs and their associated uncertainties. For comparison, Figure 2.3 also shows the Na I EWs of a sample of field dwarfs, M8→M9.5, from the IRTF Spectral Library, contained in Cushing, Rayner & Vacca (2005) (hereafter C05) and Rayner, Cushing & Vacca (2009) (hereafter R09).

The pEW uncertainties in my sample of calibrator brown dwarfs were determined from the objects' dispersed 2D images. The image (before sky subtraction) was used to compute the total number of photons over the region containing the absorption feature. The width of this region was determined from the NIFS instrument profile and was found to be ~2.2040 μm-2.2095 μm for all my objects. The sky-subtracted 2D image of this region was used to determine the signal. The photon noise was then calculated using Poisson statistics.[3]

My sample consists of objects in two known age groups, ~1-2 Myr, ~3-7 Myr, and those in the field. The age of the field objects is unknown, but they are significantly older than the objects in the known age groups. It would be interesting to examine the pEWs of gravity-sensitive features in objects with ages of a few 100 Myr. For example, the Pleiades cluster (~120 Myr) is known to contain a number of late M/early L dwarfs (Moraux et al. 2003; Bihain et al. 2010, hereafter B10). (Note that later in this paper I examine an extended data set, in which I derive the $H_2(K)$ indices of several Pleiades objects.) I examined whether the Ca I triplet and the CO trough at 2.29 μm are also affected by surface gravity. For both these features, the pEWs of the two field dwarfs are larger than those of the other objects in my sample, particularly in the case

---

[3] I note that the VAR (variance) FITS extensions in the science data cannot be used for this purpose, owing to a problem with the GEMINI NIFS software package in IRAF. The Gemini IRAF team intends to fix this in a later release of the software.

Table 2.2: Brown Dwarf pseudo-Equivalent Widths (pEW)

	Age (Myr)	pEW NaI (Å)	pEW CaI (Å)	pEW CO (Å)
2MASS 0345+25	$\geq$1000	4.1± 0.2	1.1± 0.1	15.1± 0.2
BRI 0021−0214	$\geq$1000	2.2± 0.1	1.3± 0.1	18.8± 0.1
σ Orionis 51	3-7	1.0± 0.5	0.5± 0.3	9.3± 0.6
σ Orionis 71	3-7	1.8± 0.5	–	8.4± 0.5
σ Orionis J053−024	3-7	2.1± 0.6	–	9.4± 0.5
KPNO-Tau 1	1-2	1.8± 0.2	0.3± 0.1	12.4± 0.2
KPNO-Tau 4	1-2	1.0± 0.1	0.6± 0.1	10.3± 0.1
KPNO-Tau 12	1-2	1.2± 0.3	–	9.8± 0.2
2MASS 0535−0546	1-2	1.1± 0.1	0.9± 0.1	10.4± 0.1
0457+3015	1-2	1.7 ± 0.3	0.9 ± 0.1	10.5 ± 0.2

of the CO trough, while the pEWs for these features among the two sets of younger calibrators are broadly similar.

Age Spreads

Does the spread of values of pEW in each age category represent a real spread in ages? The spectrum either side of the Na I feature contains molecular absorption features which deepen with decreasing T_{eff} (see Section 2.7.3). These features depress the local pseudo-continuum, leading to lower values of pEW. If my sample contained a wide range of spectral types, this is a possible cause of the spread of values of pEW. However, with one exception, my sample are spectral types M8.5−L0. An $(I, I-J)$ colour-magnitude study of 35 σ Orionis cluster members found evidence of a spread in ages from 1-7 Myr (Kenyon, Jeffries & Naylor, 2001). A later survey of the σ Orionis cluster found a large spread in measured values of Li pEW (Kenyon et al., 2005), indicating a spread of ages. The authors did not reach any conclusions as to the cause of this spread in Li pEW, but noted that similar spreads in Li pEW have been observed among low mass objects in the Chamaeleon I cluster (Joergens & Guenther 2001; Natta et al. 2004). A study of the luminosity spread in the HRD of the ONC argued that there was little evidence to support age spreads greater than a few Myr (Jeffries et al., 2011).

There is some debate whether star formation is a slow process, taking place over

Table 2.3: Brown Dwarf Rotational Velocities

	Rotational Velocity (v sin i) kms^{-1}
2MASS 0345+25	25[1]
BRI 0021−0214	40[2]
σ Orionis 51	–
σ Orionis 71	–
σ Orionis J053−024	–
KPNO-Tau 1	5.5[3]
KPNO-Tau 4	10[3]
KPNO-Tau 12	5[3]
2MASS 0535−0546	10[4]
0457+3015	–

[1] Antonova et al. (2008)

[2] Reid et al. (1999)

[3] Mohanty, Jayawardhana & Basri (2005)

[4] Reiners et al. (2007)

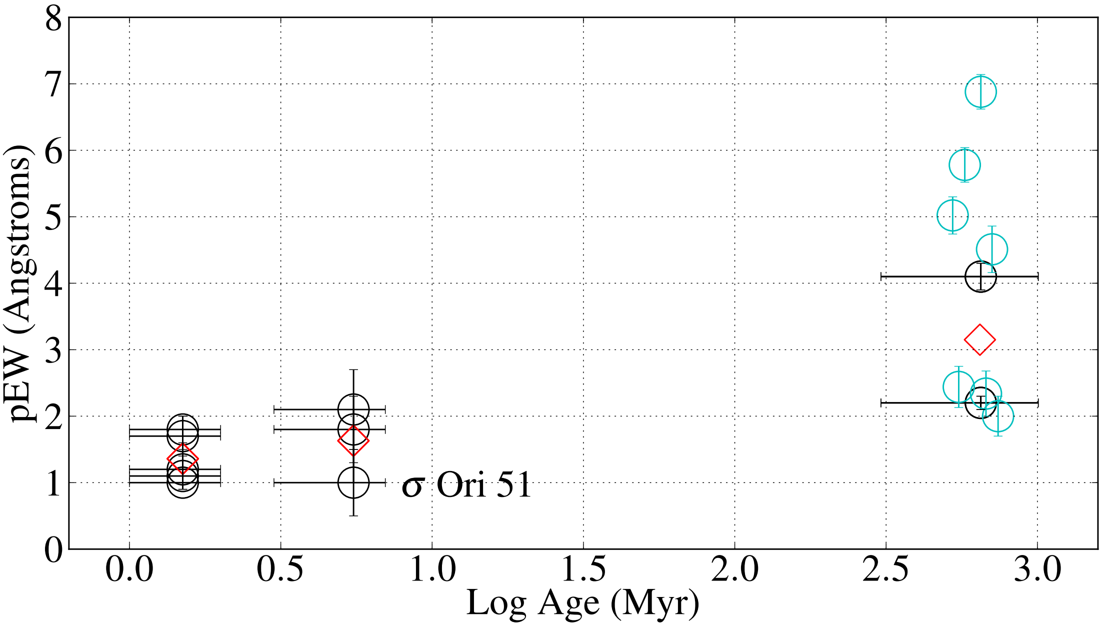

Fig. 2.3: Na I pEW as a function of age for my brown dwarf calibrators. The red diamonds are the mean pEWs of the brown dwarf calibrators at each age bin. The ages of the youngest objects are based on estimates in McGovern et al. (2004). The ages of the field dwarfs are speculative, but they are known to be much older than the other objects in this sample. σ Orionis 51's pEW is more typical of a younger object. The cyan circles are the EWs of field dwarfs described in C05 and R09.

several Myr, or whether it takes only as much time as is required for a sound wave to cross a molecular cloud. The sound crossing time depends on the radius of the cloud and on the sound speed, but Elmegreen (2000) has suggested that star formation could take as little as 1 Myr or less.

In the case of the σ Orionis objects, σ Orionis 51's pEW is 1.5σ from the mean pEW of its siblings which might indicate an age spread. The scatter in the pEWs of the 1-2 Myr objects is also slightly greater than would be expected from the 1σ uncertainties. However, the scatter in the data could have other causes. For example, magnetic activity can produce surface spots, so that in order to maintain its luminosity, an object has to increase in size. This results in the object having a lower surface gravity than it would have without any magnetic activity. An investigation of magnetic activity in field M dwarfs has suggested that activity peaks around M7, with significant activity continuing into later spectral types (Hawley, Reid & Gizis, 2000). Magnetic activity could be even greater among younger objects. A recent paper has suggested that the temperature reversal observed in 2MASS 0535−0546 could be due to magnetic fields inhibiting convection (Mohanty & Stassun, 2012).

While age spreads could explain the scatter in pEW values, my small sample size and the magnitude of the uncertainties on my data do not allow me to infer age spreads in young clusters. For example, the spread in data values could be due to observational scatter or may arise from differing formation mechanisms and accretion histories [B12]. To settle the question of age spreads, I would need a sufficiently large sample of objects in order to undertake a rigorous statistical analysis.

2.4.3 Spectral Typing

I took this opportunity to use my higher resolution spectra to re-examine the spectral typing of the younger objects in my sample, including the PMO. I used the WK and QK spectral indices previously defined by my group [L06]. The WK and QK spectral indices measure the strength of H_2O absorption in the K band. W09 used polynomial fits to these spectral indices to characterise the GNIRS and NIRI data in

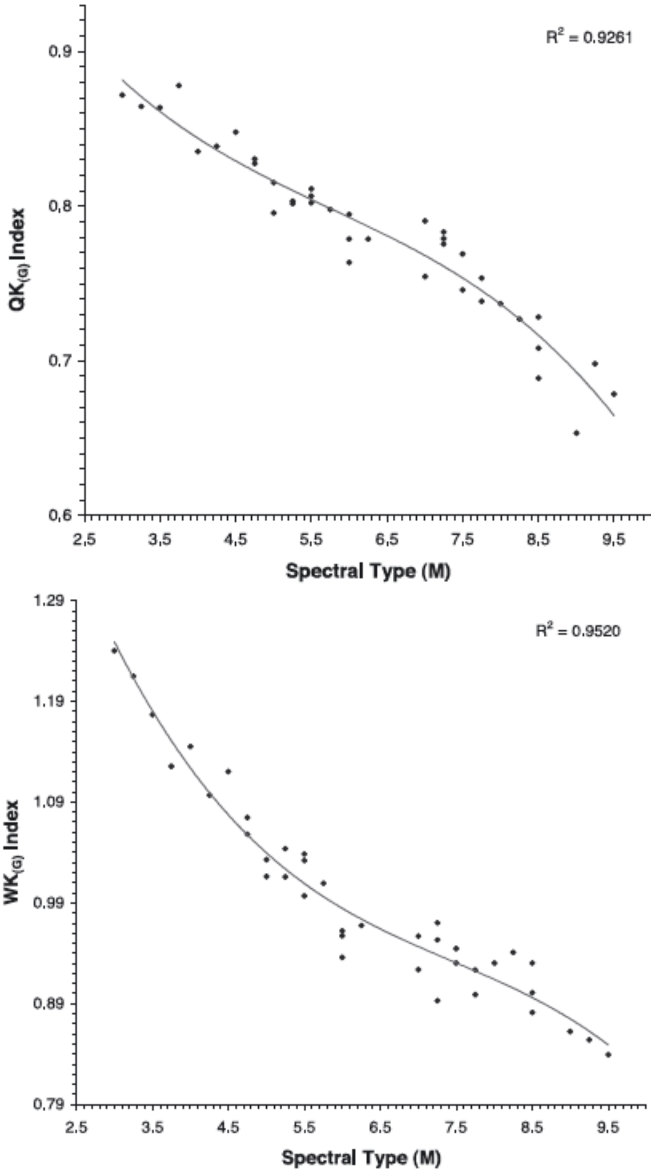

Fig. 2.4: Polynomial fits to the QK (top) and WK (bottom) indices of a sample of 39 young (1-2 Myr) objects with spectral types between M3 and M9.5. (Plots from W09).

LO6. The fits are shown in Figure 2.4. These indices provide spectral types consistent with the Luhman system of optical classification of spectra (Luhman, 1999). QK is a reddening independent index, whereas WK requires knowledge of the extinction toward the source.

For the PMO 152−717, the extinction $A_V = 3.7$ [L06]. Thus, I was able to use the dereddened spectrum in determining its spectral type. For the σ Orionis objects it is known that $A_V \leq 1$ mag, and, in most cases, changing A_V by ± 2 mag alters the derived spectral type by <0.5 types (Béjar et al., 2001). Thus, I do not expect these spectra to be significantly affected by reddening. The same conclusion was made in the case of the Taurus association objects. While the WK index is sensitive to reddening, and therefore should be dereddened where possible, I have used it as a check on the spectral type derived from the more accurate QK index. I did not re-examine the spectral types of the field dwarfs in my data set, as my spectral indices are only applicable to young objects. My results are shown in Table 2.4.

Spectral types were rounded to the nearest 0.25 subtype (which is the practice in the Luhman system). To assign a spectral type, I took the mean of the spectral types derived using the WK and QK indices. To determine the uncertainties in spectral types, I first measured the scatter in the fits to the WK and QK indices in the M8 to M9.5 interval in W09. This was added in quadrature to the mean average difference (0.3 sub-types) derived from the difference between the WK-based and QK-based spectral types, averaged over the 5 objects in this spectral type interval. Uncertainties were rounded up to the nearest 0.25 subtype. As the fits derived by W09 are uncalibrated beyond M9.5, when both WK and QK indices indicated a spectral type later than M9.5, I compared my spectra with the spectra of early L brown dwarfs in the Upper Sco association described in Lodieu et al. (2008), hereafter L08. As a result, I assigned a spectral type of L0 to these objects with an uncertainty of 0.5 spectral types.

I should qualify this re-examination of previously published spectra by saying that my classifications are based solely on my *K* band spectra. Spectral classifications using other near-infrared or optical wavebands may produce slight differences for different objects. To examine this, I recalculated the spectral types of the Upper Sco objects in L08 using my indices and found that my indices tended to produce spectral types ~0.5 spectral types earlier than those in L08. L08 determined spectral types by selecting spectral templates from their sample of Upper Sco objects. These templates were then used to classify the remaining Upper Sco objects. In addition, L08 compared their spectra with two Upper Sco objects outside their sample, whose spectral types had been determined optically. These objects comprised SCH 1625 (M8; (Slesnick, Carpenter & Hillenbrand, 2006)), and DENIS 1611 (M9; (Martín, Delfosse & Guieu, 2004)). Allers & Liu 2013 investigated the gravity dependence of visual spectral typing and found that the *K* band spectral types for low-gravity objects are typically 0.1

Table 2.4: Spectral Types

Object	Previous Spectral Type	Spectral Type WK	Spectral Type QK	Revised Spectral Type
2MASS 0345+25[1]	L0	–	–	–
BRI 0021−0214[1]	M9.5	–	–	–
σ Orionis 51	M9	>M9.5	>M9.5	L0±0.5
σ Orionis 71	L0	M7.8	M8.3	M8±0.5
σ Orionis J053−024	M9.5	M8.1	M9.3	M8.75±0.5
KPNO-Tau 1	M8.5	M8.3	M9.1	M8.75±0.5
KPNO-Tau 4	M9.5	>M9.5	>M9.5	L0±0.5
KPNO-Tau 12	M9	M9.1	M9.3	M9.25±0.5
0457+3015	M9.25	M9.1	M9.4	M9.25±0.5
152−717	M9	>M9.5	M9.3	M9.5±1.0

[1] Old field objects.

subtypes earlier than their corresponding optical spectral types. I have found a larger variation between optical and near-infrared spectral types. Nevertheless, the variations are close to my estimated uncertainties, however, and I feel justified in this exercise based on the high quality of my data.

2.5 H_2 Collision Induced Absorption in the *K* band

It has previously been observed that the F_λ spectra of young, late M brown dwarfs have a flat maximum between 2.18 μm and 2.28 μm (Luhman, Peterson & Megeath, 2004), while mature field dwarfs of the same spectral type have a peak between 2.14 μm and 2.18 μm then decline between 2.18 μm and 2.29 μm [L06]. In other words, the *K* band spectra of younger objects appear redder than the *K* band spectra of older objects (see Figure 2.5). This change in the *K* band spectrum is believed to be caused by increased collision-induced absorption (CIA) by H_2 in the atmosphere, owing to the increase in surface gravity with age (Saumon et al. 2012, hereafter S12). I wanted to see whether this behaviour was evident in my sample, and, if it was, to quantify it.

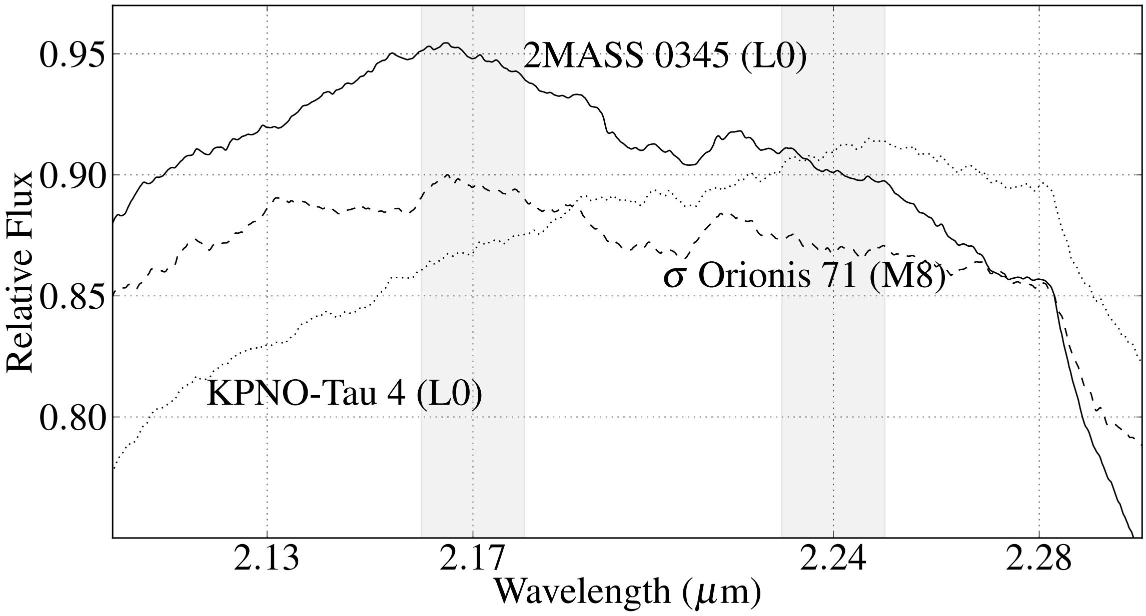

Fig. 2.5: Variations of the K band slope with surface gravity are easily discernible in low resolution spectra. Here I plot smoothed versions of the NIFS spectra of 2MASS 0345 (field dwarf, solid line), σ Orionis 71 (3-7 Myr, dashed line), and KPNO-Tau 4 (1-2 Myr, dotted line). The revised spectral types of these objects are indicated on the figure. The shaded areas are the wavelength regions over which the $H_2(K)$ index is calculated.

2.5.1 Measuring H_2 CIA

I used the smoothed NIFS spectra of my brown dwarf calibrators to identify the locations of the peaks in their continua. Figure 2.5 demonstrates how smoothed spectra can be used to trace the shape of the K band slope.

The 1-2 Myr object has a positive slope in the region of interest (2.17 ± 0.01 μm$\rightarrow$ 2.24 ± 0.01 μm), while the older objects have negative slopes. Note also that while σ Orionis 71 is only a few Myr older than KPNO-Tau 4, its slope is already negative. I expect that as σ Orionis 71 ages, its peak emission will not move far from its present wavelength value, but its K band slope will become more negative, similar to the field dwarf calibrators. Thus, the slope of the K band should be useful in differentiating very young pre-main sequence objects from older objects.

I found that the location of the peak in the continuum varies, depending on the surface gravity of the object. For objects with the largest surface gravity (the field dwarfs), the mean peak was at 2.17 μm, while for objects with the smallest surface gravity (the 1-2 Myr objects), the mean peak was at 2.24 μm. Using the unsmoothed

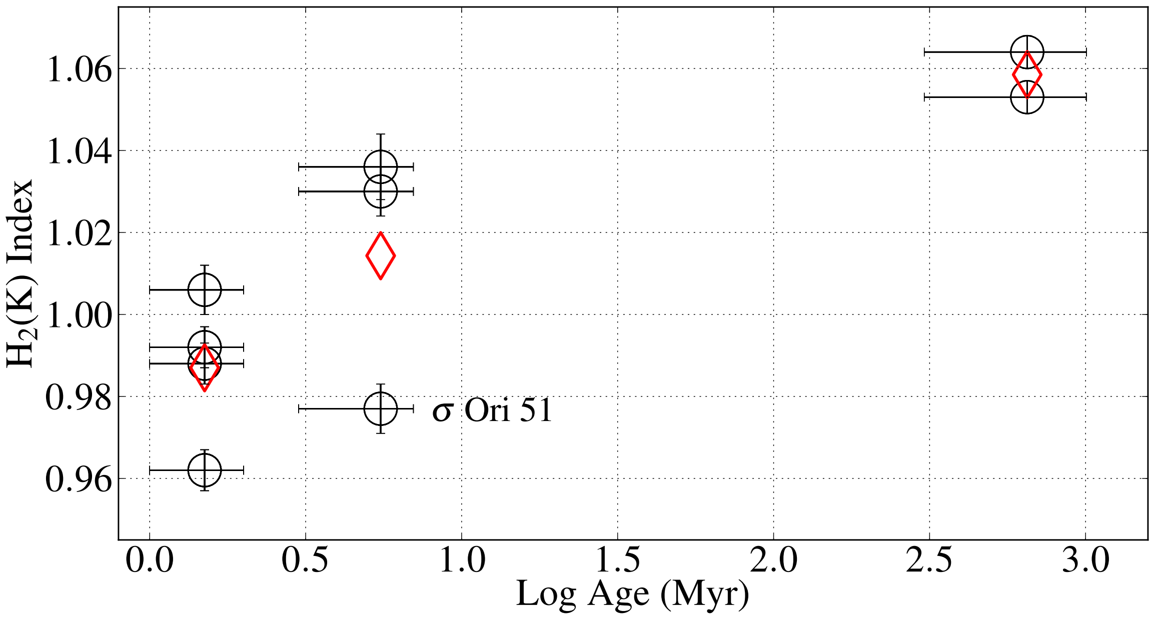

Fig. 2.6: $H_2(K)$ index as a function of age for my brown dwarf calibrators. The red diamonds are the mean $H_2(K)$ indices at each age bin. The ages of the objects are as described in Figure 2.3. Again, notice the position of σ Orionis 51.

spectrum, the ratio of the median flux over a range of 0.02 μm, centred at these wavelengths, defined an index, $H_2(K)$,

$$H_2(K) = \frac{F_\lambda(2.17\ \mu\mathrm{m})}{F_\lambda(2.24\ \mu\mathrm{m})}$$

For young objects, with a positive, or at least flat slope, between these limits, the index returns a value $\leq$1. For older objects, whose slope is negative, the index is >1.

The $H_2(K)$ indices for my sample of brown dwarf calibrators are shown in Figure 2.6 and in Table 2.5. They are consistent with the results for the correlation of age with pEW shown in Figure 2.3. The uncertainties on the indices were determined using the standard error on the mean in the 0.02 μm intervals over which the indices were calculated.

Among the calibrators, one 1-2 Myr object (KPNO-Tau 12) has a $H_2(K)$ value >1, implying a negative slope (if only slightly). Also, σ Orionis 51 has an unusually low $H_2(K)$ value. This is consistent with this object's Na I pEW. One should not use a single age/gravity indicator to infer the values of either of these quantities in one object. However, σ Orionis 51's Na I pEW and $H_2(K)$ index suggest that it has low gravity.

Table 2.5: H_2(K) Indices, Means and Standard Deviations

	$H_2(K)$ Index	$\lambda_{F_{MAX}}$ (μm)	$\bar{x}_{\mathrm{H_2(K)}}$	σ
2MASS 0345+25	1.053±0.004	2.16	1.059	0.008
BRI 0021−0214	1.064±0.004	2.16		
σ Orionis 51	0.977±0.006	2.26[1]	1.014	0.032
σ Orionis 71	1.030±0.006	2.16		
σ Orionis J053−024	1.036±0.008	2.19		
KPNO-Tau 1	0.992±0.005	2.23	0.987	0.018
KPNO-Tau 4	0.962±0.005	2.25		
KPNO-Tau 12	1.006±0.006	2.17		
0457+3015	0.988±0.005	2.25		

[1] Note that the peak flux occurs at a wavelength more typical of a younger object.

While this spread in data values may be due to differing formation mechanisms and/or accretion histories, it can also result from an age spread in the σ Orionis cluster.

Although the ONC PMO 152−717 is not one of my brown dwarf calibrators, the object's data were obtained in this observation and I think it is appropriate to discuss the results here. While the S/N of the extracted spectrum was too low to allow me to measure the Na I pEW, I was able to calculate its $H_2(K)$ index. With a value of 0.914±0.013, 152−717's $H_2(K)$ index is consistent with 152−717 being a low gravity object. Its value is also consistent with the values of the $H_2(K)$ indices for the other ONC PMOs in the extended data set (see Section 2.6 and Table 2.6). This highlights an important benefit of this method of constraining the surface gravity, and hence age, of these objects. Since the $H_2(K)$ index is obtained by sampling the slope of the K band, this technique allows me to obtain indications of surface gravity using spectra which are too noisy or where $\lambda/\Delta\lambda$ is too low to resolve narrow spectral features.

2.5.2 The Model H_2(K) Indices

Modelling H_2 CIA in the K band

The objects in my sample of brown dwarf calibrators are of a similar spectral type. They differ most significantly in age, and therefore in surface gravity. Molecular hydrogen is the most abundant constituent of brown dwarf atmospheres and H_2 CIA is positively correlated to density. At any given metallicity, objects with greater surface gravity will show enhanced H_2 CIA.

H_2 absorption in the K band has been examined before (Tokunaga & Kobayashi 1999, hereafter T99). T99 defined two parameters. The first parameter, K1, measures the slope of the spectrum between 2.00 μm and 2.14 μm. The second parameter, K2, measures the strength of H_2 absorption between 2.14 μm and 2.24 μm. T99 suggested that the K2 parameter could be used to estimate an object's T_{eff}. They did not apply this index to constrain an object's age, other than to say that the K2 parameter was negative for field dwarfs. In a subsequent survey of young cluster members, the K2 parameter was typically positive [L08].

To further examine the effect of H_2 CIA on the shape of the K band, I used newly computed models of H_2 CIA in the atmospheres of late brown dwarfs to generate synthetic spectra at T_{eff}=2200 K (the typical T_{eff} of an M9.5−L0 dwarf), over a range of surface gravities from log g=3.5→5.5 [S12]. The results are shown in Figure 2.7. These Saumon & Marley models assume that the dwarfs' atmospheres are cloudy (F_{sed}=2) and of solar metallicity.

The models show a change of slope in the region 2.16 μm-2.28 μm, with the slope decreasing with increasing gravity. They predict that the rate of change of the slope increases with increasing gravity. They also predict that the spectra should show greatest sensitivity to the increasing contribution of CIA H_2 to the opacity of the atmosphere in the K band at log g >4.5, rather than at the lower gravities expected in pre-main sequence clusters. The data imply a stronger dependence of CIA H_2 opacity on gravity than the models predict, particularly at log g <4.5.

In Figure 2.8, I used Lyon DUSTY isochrones (Chabrier et al. 2000; Baraffe et al. 2002) to estimate the surface gravities of my brown dwarf calibrators (see Section 2.7.1). I took the mean surface gravity for each age group of brown dwarf calibrators, and assigned to that gravity the mean $H_2(K)$ index for that age group. I then plotted the Saumon & Marley 2200 K model $H_2(K)$ indices as a function of surface gravity, fitted a simple polynomial to the data points and interpolated between the points to determine the values of the model $H_2(K)$ indices at the surface gravities of the brown

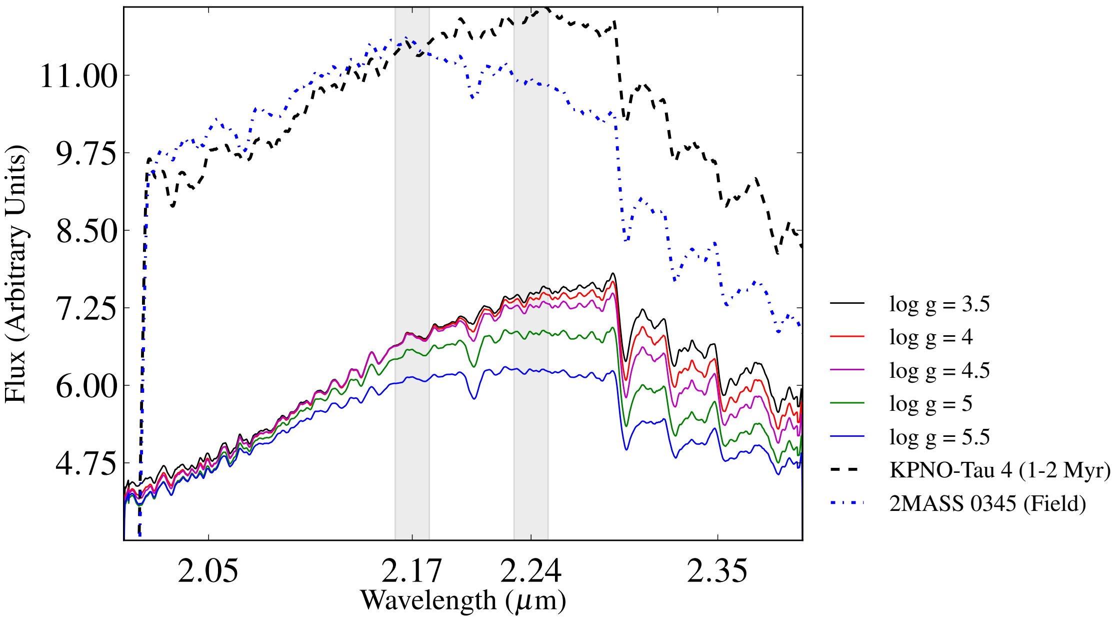

Fig. 2.7: Theoretical models made using new calculations of H_2 CIA show the K band slope decreasing with increasing surface gravity. The temperature for these models was set at 2200 K (the typical T_{eff} of an M9.5−L0 dwarf). Overplotted are two spectra from my data set of brown dwarf calibrators, a young Taurus object, and an older field dwarf. The shaded regions are as those described in the caption to Figure 2.5. All spectra have been smoothed to aid separation. (Models supplied by D. Saumon and M. Marley).

dwarf calibrators. I repeated the procedure using an extended data set (see Section 2.6), and found a similar relationship between data and models.

The disparity between models and data at lower gravities is clear. The changes in the $H_2(K)$ index at lower gravities are much larger for the data than for the models. It may be that the models overestimate the significance of dust opacity at these lower gravities. It is possible that young objects can have higher T_{eff} than field dwarfs of the same spectral type (Luhman et al., 2003c). This higher T_{eff} may prevent dust condensation, allowing H_2 CIA opacity to play a greater role.

The degeneracy in the data at log g ∼5 may be due to the very low resolution (R≈50) of the data point at log g=4.90 (Teide 1, a Pleiades object from the extended data set (see Section 2.6)). It is also possible that the $H_2(K)$ index becomes saturated at log g ≥5. While this behaviour is not shown by the model spectra, I note that the other Pleiades objects in the extended data set, H ɪɪ 1248B and BPL 62, have $H_2(K)$ indices of 1.068 and 1.138 respectively. I assume that these objects have similar surface gravities. If the $H_2(K)$ index does saturate at these values of log g, this would imply

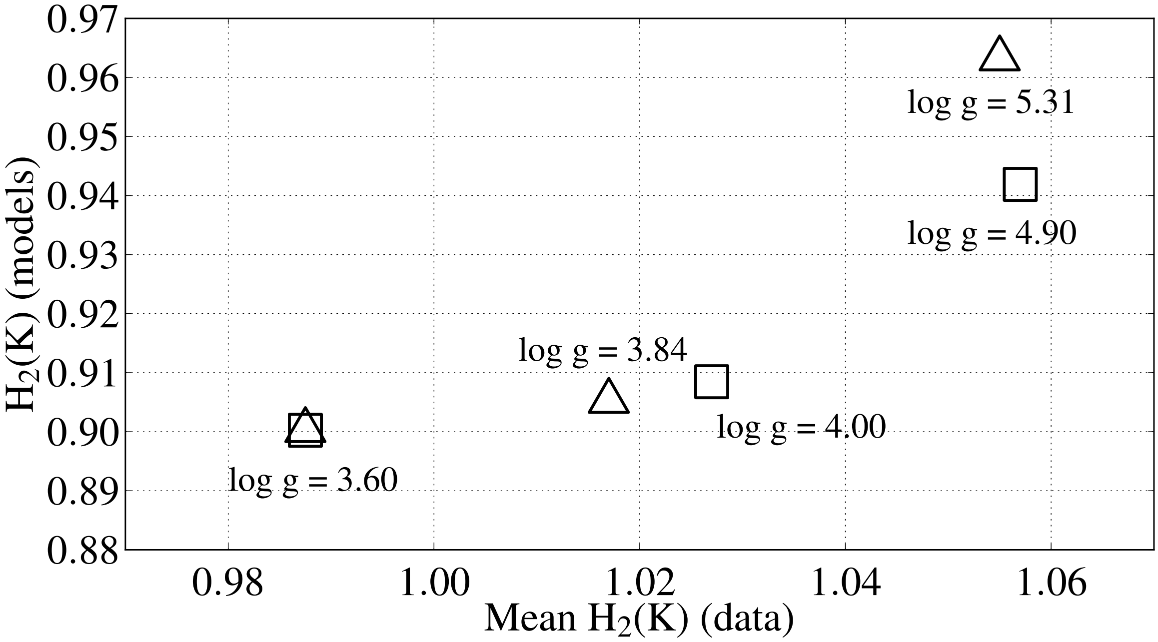

Fig. 2.8: The relationship between the mean H_2(K) indices of my original data set (triangles), the extended data set (squares) and the model $H_2(K)$ indices. The observed dependence of the $H_2(K)$ index as a function of gravity appears to be substantially steeper than predicted by the models at low surface gravities.

an upper limit on the age sensitivity of the index.

Figure 2.9 shows a strong correlation between the Na I pEWs and the $H_2(K)$ indices calculated from my data set of brown dwarf calibrators and from the Saumon & Marley 2200 K models. The strength of gravity-sensitive neutral alkali metal lines is a well-proven method in establishing the ages of late M dwarfs. This correlation suggests that the H_2(K) index is at least as good an age indicator. (See Section 2.8 for a more detailed comparison of the two age indicators.)

2.5.3 Testing the $H_2(K)$ Index

The Effect of Dust and Extinction

In cases of unresolved binarity, emission from a disc, non-sphericity, etc, the K band may exhibit a flux excess, affecting the $H_2(K)$ index. A common cause of K band flux excess in young objects is emission from a dusty accretion disc. To examine the effect of dust emission on the K band of a typical 1-2 Myr calibrator (KPNO-Tau 4), it was assumed that half the calibrator's flux was produced by dust, simulated by a blackbody function. This is the level of contamination I would expect to find in the

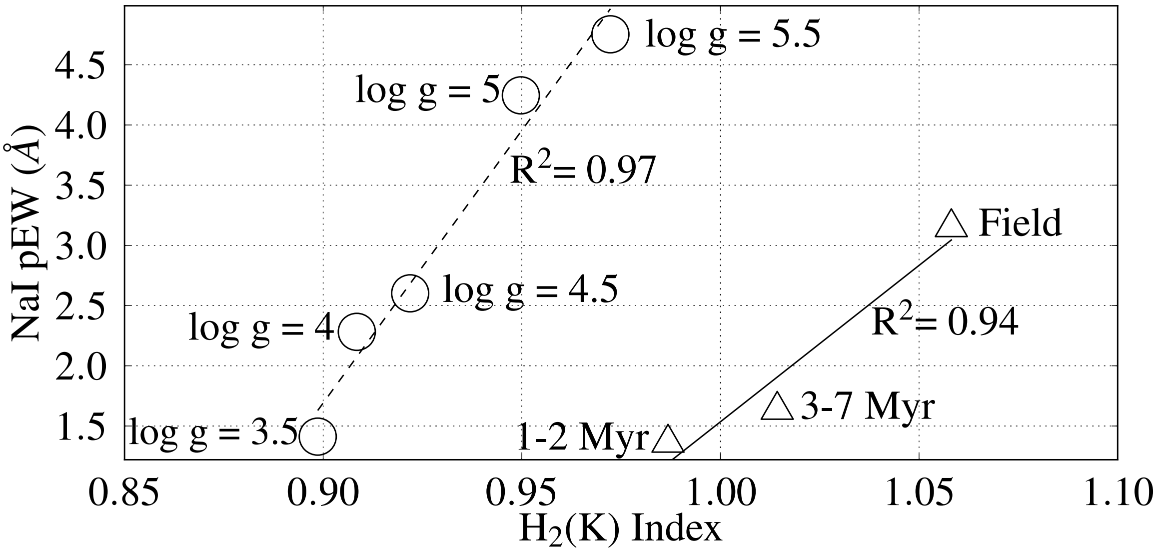

Fig. 2.9: The correlation between Na I pEWs and $H_2(K)$ indices for my original data set (triangles, solid line) and the Saumon & Marley model spectra (circles, dashed line). Note that I have used the means of these values for the original data set.

K band spectra of very dusty objects. I performed two simulations of the blackbody function, at 900 K and 1200 K respectively, see Figure 2.10. The 1200 K blackbody spectrum peaks at ~2.4 μm. The combined 1200 K blackbody and science object spectrum (dotted line) peaks at ~2.25 μm, relatively close to KPNO-Tau 4's peak flux (solid line). The blackbody spectrum is flatter near its peak so adding a large component of this flux to the spectrum of KPNO-Tau 4 causes the latter to similarly flatten, increasing its $H_2(K)$ index. The 900 K blackbody spectrum peaks at ~3.2 μm. The combined 900 K blackbody and science object spectrum (dashed line) peaks at ~2.28 μm. This has the opposite effect, steepening KPNO-Tau 4's spectrum and decreasing its $H_2(K)$ index.

The $H_2(K)$ index samples the K band flux, the region of the near-infrared most susceptible to contamination by dust emission. While the effect of contamination by dust emission is somewhat mitigated by the narrow baseline (0.07 μm) over which the index is calculated, the emission from the dusty objects simulated in Figure 2.10 does alter the $H_2(K)$ index of KPNO-Tau 4 by $\sim \pm 0.02$. While this is significant, I note that the presence of such large amounts of emission from a dusty disc becomes obvious in the spectrum (see Figure 2.10), so that such objects can be excluded when calculating

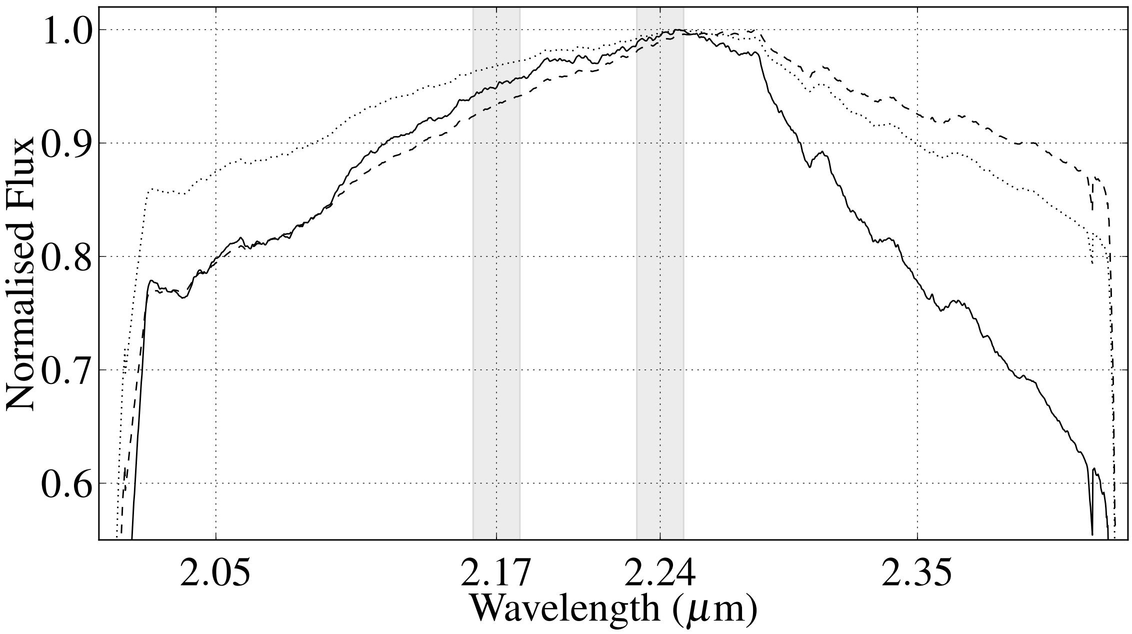

Fig. 2.10: The effect of dust emission on K band spectra. Emission from blackbodies at 900 K and at 1200 K are added to the smoothed spectrum of KPNO-Tau 4 (dashed line and dotted line, respectively) and contrasted with the original spectrum (solid line). The shaded areas are as described in Figures 2.5 and 2.7.

an average $H_2(K)$ index for a population.

The $H_2(K)$ index will be affected by extinction. For example, assuming A_V=5 magnitudes, the $H_2(K)$ index of a noiseless model spectrum decreases from 0.97 to 0.95. However, in most cases it will be possible to deredden a spectrum accurately, thereby minimising the effect.

The Effect of Noise

I carried out a Monte Carlo analysis to examine the effect of noise on the $H_2(K)$ index. I chose a noiseless model spectrum and added successively larger fractions of noise. The noise was added randomly to each pixel of the model spectrum, at the spectral resolution of my NIFS spectra. After 10^4 iterations of each stage I measured the mean absolute change in the $H_2(K)$ index. The results are shown in Figure 2.11. The change in the $H_2(K)$ index exceeds ±0.02 when noise comprises >20% of the flux.

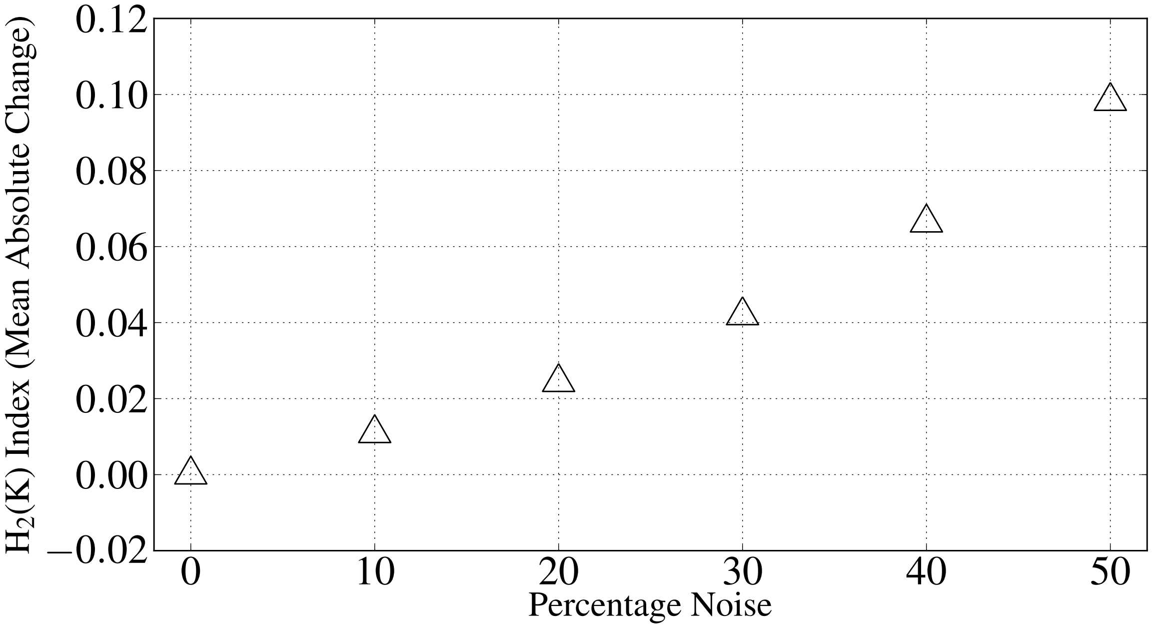

Fig. 2.11: The effect of noise on the $H_2(K)$ index. Randomly generated noise was added to a model spectrum (T_{eff} 2200 K, log g = 5.5).

The Effect of Metallicity

My discussion on 2MASS 0535−0546 (see Section 2.7.1) concludes that alkali metal absorption features in mid to late M dwarfs are almost pure measures of surface gravity, with very little dependence on temperature. While surface gravity is probably the largest factor in determining the shape of the K band slope, metallicity is likely to have some effect. Reducing the metallicity removes H_2O and CO opacity from the K band while other transmission windows (YJH) become more transparent since they don't have as much H_2 CIA absorption. Thus, the K band flux decreases relative to YJH (D. Saumon, private comm.). Increasing the metallicity has the opposite effect. In summary, K band flux is reduced in the case of low metallicity or high gravity, and enhanced where there is low gravity or high metallicity (Leggett et al., 2007).

While variations in metallicity may affect the K band slope, the objects I have examined in this paper reside in regions of solar metallicity where variations in metallicity are negligible (Santos et al., 2008).

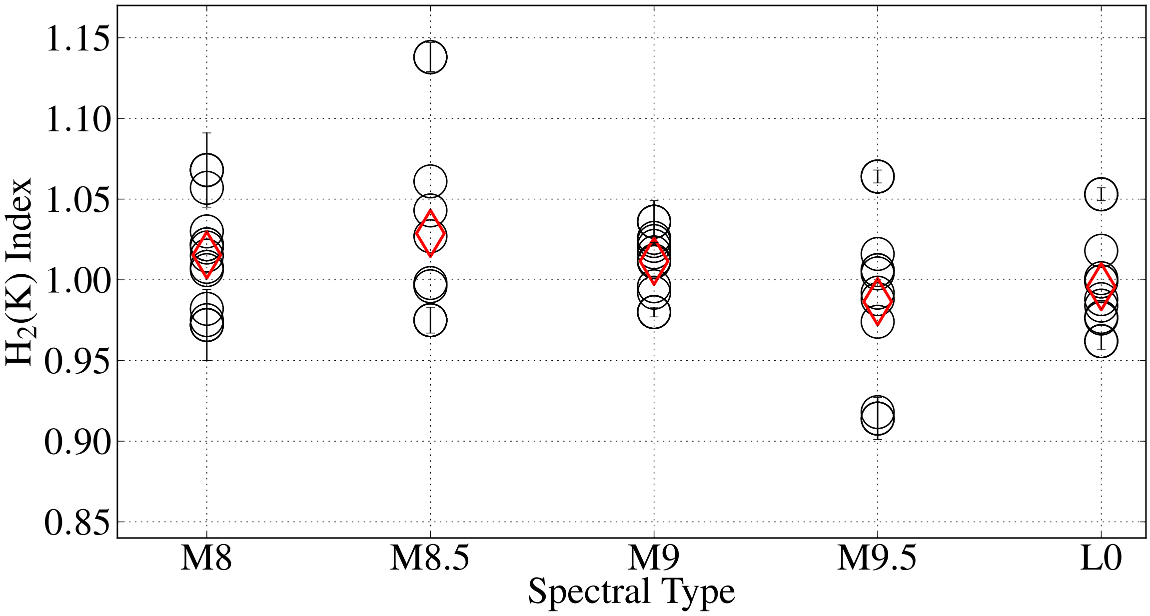

Fig. 2.12: The $H_2(K)$ indices of the complete data set, plotted as a function of spectral type. Red diamonds are the mean $H_2(K)$ index values. Error bars are shown for the outlying objects at each spectral type.

The H_2(K) index as a Function of Spectral Type

I looked at variations in the $H_2(K)$ index due to the spectral type of the objects in my complete data set. In Figure 2.12 I plot these objects' $H_2(K)$ indices as a function of their spectral types. The plot shows no clear trend and a simple linear fit to the data has a correlation coefficient of <0.1.

2.6 Extending the Data set

To further test the correlation of the $H_2(K)$ index with surface gravity, and hence age, I examined an extended data set from the literature, containing field dwarfs and objects in clusters with constrained ages. Although I have not found the $H_2(K)$ index to be sensitive to spectral type over the range M8 to L0 in my data set of calibrator brown dwarfs, objects in the extended data set were selected to cover the same range of spectral types to keep the analyses comparable. I should also point out that despite constraints, the ages of these clusters are not certain and my analysis should be interpreted in the light of this fact. For example, Pecaut, Mamajek & Bubar (2012) have argued that Upper Sco is 11 Myr old, compared to previous estimates of ~5 Myr.

Pecaut et al's argument is compelling and I have used their revised age for Upper Sco in my extended data set.

I was particularly keen to obtain spectra from clusters with ages ≥100 Myr since the older objects among my brown dwarf calibrators are field dwarfs of indeterminate age. I searched the literature for good quality *K* band spectra of members of clusters such as the Pleiades, Hyades and Praesepe, but found spectra of only three objects in the Pleiades and none at all in the Hyades or Praesepe. My attempt to constrain the $H_2(K)$ index has been hindered by this lack of high quality *K* band spectra of objects in older clusters.

The extended data set comprises

- an M8.5 field dwarf described in Geballe et al. (2002) [G02];
- an M8.5 field dwarf described in Leggett et al. (2001) [L01];
- seven field dwarfs, M8→M9.5, obtained from the IRTF Spectral Library, described in C05 and R09;
- Teide 1, an M8 dwarf in the ∼120 Myr Pleiades cluster, described in B10;
- H II 1348B, an M8±1 substellar companion to the Pleiad H II 1348 A, described in Geißler et al. (2012) [G12];
- BPL 62, an M8.3 dwarf in the Pleiades cluster. This is an unpublished spectrum taken by D. J. Pinfield. The object is described in Pinfield et al. (2000) [P00] and Pinfield et al. (2003) [P03];
- GSC08047 B, an M9.5 dwarf in the ∼30 Myr Tuc-Hor association, described in Patience et al. (2012) [P12];
- 13 M8→L0 brown dwarfs in the ∼11 Myr old Upper Sco association, described in L08;
- TWA 5B, an M8/M8.5 dwarf in the ∼8 Myr TW Hya association (TWA), described in Neuhäuser et al. (2009) [N09];

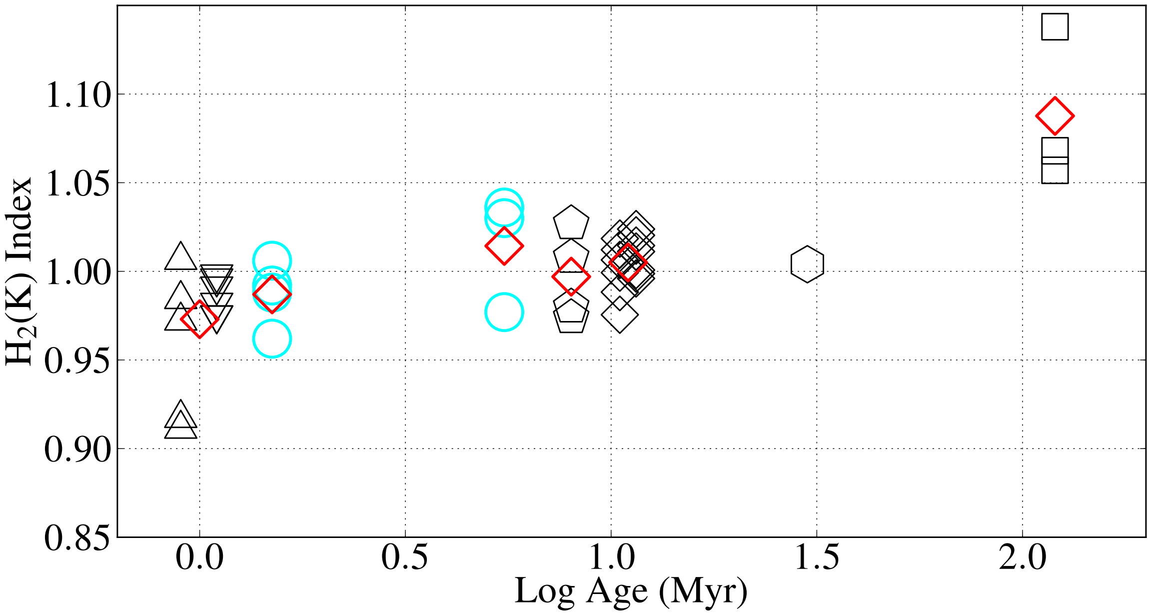

Fig. 2.13: The $H_2(K)$ indices of the extended data set, plotted as a function of age. Triangles are the GNIRS PMOs and 152−717, inverted triangles are the Taurus objects from L04b, diamonds are the Upper Sco objects described in L08, the pentagons are the TW Hya objects, the hexagon is GSC08047 B and the squares are the Pleiades substellar objects. The field dwarfs' $H_2(K)$ indices have not been plotted as the ages of these objects are uncertain. Red diamonds are the mean values at each age bin. Note that the rate of increase in the index is greatest for the youngest objects, as would be expected for rapidly contracting objects. The Taurus and ONC objects probably have similar ages so are shown offset slightly either side of 1 Myr, and share a common mean. For clarity, the Upper Sco objects are offset 0.5 Myr either side of 11 Myr. The cyan circles are the $H_2(K)$ indices of my brown dwarf calibrators.

- ◦ DENIS J124514.1-442907 and 2MASSW J1139511-31592 (2MASS 1139-3159), M8→M9.5 objects in TWA, described in Looper et al. (2007) [L07];
- ◦ 2MASS J12073346-3932539 (2M1207A), a TWA object, described in P12;
- ◦ CT Cha B, an M8 ∼2 Myr object described in Schmidt et al. (2008) [S08];
- ◦ four brown dwarfs in the Taurus association, M8.25→M9.25, described in Luhman (2004) [L04b];
- ◦ LRL 405, an M8 ∼1-2 Myr object in the IC 348 nebula, described in Muench et al. (2007) [M07];
- ◦ four ONC PMOs, M8→M9.5, described in W09;

The results are shown in Figure 2.13 and Table 2.6.

Table 2.6: Extended Dataset $H_2(K)$ Indices, Peak Flux Wavelength, Means, and Standard Deviations. (All USco and GNIRS objects have been dereddened.)

	Ref	Sp Type	~ Age (Myr)	$H_2(K)$ Index	$\lambda_{\max}$ (μm)	$\bar{x}_{H_2(K)}$	σ
SDSS 2255	G02	M8.5	Field	1.061±0.012	2.17	1.030	0.016
T 513	L01	M8.5	Field	1.043±0.003	2.15		
2MASS J07464256+2000321AB	C05	L0.5	Field	1.046±0.004	2.17		
DENIS-P J104814.7-395606.1	R09	M9	Field	1.026±0.004	2.17		
LP 944-20	C05, R09	M9	Field	1.017±0.003	2.15		
LHS 2065	R09	M9	Field	1.021±0.003	2.14		
LHS 2924	C05, R09	M9.5	Field	1.016±0.004	2.23		
Gl 752B	C05, R09	M8	Field	1.022±0.004	2.14		
LP 412-31	R09	M8	Field	1.022±0.003	2.14		
Teide 1	B10	M8	120	1.057±0.015	2.17	1.088	0.044
H II 1348B	G12	M8±1	120	1.068±0.023	2.19		
BPL 62	P00, P03	M8.3	120	1.138±0.009	2.15		
GSC08047 B	P12	M9.5	30	1.004±0.006	2.18	1.004	
USco J161047−223949	L08	M9	11	1.012±0.007	2.16	1.005	0.014
USco J160648−223040	L08	M8	11	1.006±0.006	2.18		
USco J160606−233513	L08	L0	11	1.018±0.006	2.17		
USco J160714−232101	L08	L0	11	0.976±0.011	2.24		
USco J160737−224247	L08	L0	11	0.988±0.007	2.22		
USco J160818−223225	L08	L0	11	0.999±0.006	2.25		
USco J160830−233511	L08	M9	11	1.024±0.004	2.17		
USco J160847−223547	L08	M9	11	1.011±0.005	2.17		
USco J161227−215640	L08	L0	11	0.999±0.019	2.22		
USco J161302−212428	L08	L0	11	1.001±0.009	2.20		
USco J155419−213543	L08	M8	11	1.015±0.005	2.17		
DENIS 161103−242642	L08	M9	11	0.996±0.006	2.19		
SCH 162528−165850	L08	M8	11	1.020±0.006	2.17		
TWA 5B	N09	M8/M8.5	8	1.027±0.004	2.17	0.997	0.025
DENIS J124514.1-442907	L07	M9.5	8	0.974±0.008	2.25		
2MASS 1139-3159	L07	M9	8	0.980±0.003	2.23		
2M1207A	P12	M8	8	1.008±0.003	2.23		
CT Cha B	S08	≥M8	2	0.982±0.007	2.29	0.986	0.010
04574903	L04b	M9.25	1-2	0.992±0.004	2.23		
KPNO-Tau 6[1]	L04b	M8.5	1-2	0.996±0.004	2.24		
KPNO-Tau 7[1]	L04b	M8.25	1-2	0.998±0.004	2.20		
KPNO-Tau 9	L04b	M8.5	1-2	0.975±0.008	2.25		
LRL 405	M07	M8	1-2	0.975±0.005	2.25		
152−717	This work	M9.5±0.5	1	0.914±0.013	2.27	0.959	0.041
057-247	L06	≥M9.5	1	0.918±0.038	2.22		
107-453	L06	M8.0±2.0	1	0.972±0.022	2.22		
137-532	L06	>M9.5	1	0.984±0.024	2.22		
183-729	L06	≥M9.5	1	1.006±0.036	2.22		

[1] Possible IR excess

Among the Pleiades objects described in B10, Calar 3 has an exceptionally low $H_2(K)$ index (0.978±0.020). This result may be associated with unresolved questions of Calar 3's binarity and variability (P03, Bailer-Jones & Mundt 2001). Therefore, I have excluded Calar 3 from the extended data set.

Among the Upper Sco objects, USco J154722−213914 has a relatively high $H_2(K)$ index (1.041), typical of an older object. This object has a flux excess from 1.9→2.1 μm which L08 were unable to explain. This flux excess may have affected the object's $H_2(K)$ index. Therefore, I have excluded USco J154722−213914 from the extended data set. Otherwise, the Upper Sco objects' $H_2(K)$ indices are scattered about 1.00, reflected in a mean $H_2(K)$ index of 1.005.

Two TWA objects (2MASS 1139-3159 and DENIS J124514.1-442907) have particularly low $H_2(K)$ indices see Table 2.6. The $H_2(K)$ index is sensitive to surface gravity and it was surprising to find that of the four objects in this co-eval association, two should have such different surface gravities. A recent paper by Stelzer et al. 2013, hereafter S13, used ROTFIT (Frasca et al., 2006) to determine stellar parameters, including surface gravity, from X-Shooter (Vernet et al., 2011) spectroscopy for a sample of young stellar objects from several star forming regions (SFRs), including TWA. Low mass young stars are expected to have similar gravities to brown dwarfs of the same age. Among the TWA stars, S13 observed the brown dwarfs, 2MASS 1139-3159 and DENIS J124514.1-442907, referred to in S13 as TWA 26 and TWA 29 respectively. The stellar parameters S13 derived using ROTFIT are shown in Table 2.7

S13 found that the T_{eff} values for the TWA objects derived using ROTFIT were in very good agreement with the values which had previously been obtained from spectral types (Manara et al., 2013). While the gravities which S13 derived for the M stars in TWA are consistent with TWA being the oldest of the SFRs in their analysis, they are higher than those predicted by evolutionary models for objects aged 10-15 Myr. Considering the uncertainties in the data, the differences may be marginal. See Figure 2.14.

S13 also found that the surface gravities of the two brown dwarfs were significantly lower than the M stars. Mohanty et al. (2004) had found a similar discrepancy in the

Table 2.7: ROTFIT derived stellar parameters of TWA sample. (Table from Stelzer et al. 2013.)

Source	SpT	$log\frac{L_{bol}}{L_{\odot}}$	d [pc]	T$_{eff}$ [K]	log g [cm s^{-2}]
TWA 9A	K5	-0.61	68	4333±47	4.9±4.9
TWA 6	K7	-0.96	51	4020±173	4.8±0.5
TWA 25	M0	-0.61	54	3749±60	4.7±0.5
TWA 14	M0.5	-0.83	96	3756±99	4.7±0.6
TWA 13B	M1	-0.70	59	3661±103	4.6±0.6
TWA 13A	M1	-0.61	59	3616±87	4.8±0.5
TWA 2A	M2	-0.48	47	3533±133	4.4±0.4
TWA 9B	M3	-1.17	68	3357±67	4.5±0.6
TWA 15B	M3	-0.96	111	3463±129	4.6±0.6
TWA 7	M3	-1.14	28	3408±85	4.4±0.4
TWA 15A	M3.5	-0.95	111	3347±125	4.5±0.3
TWA 26	M9	-2.70	42	2476±109	3.6±0.5
TWA 29	M9.5	-2.81	79	2390±109	3.6±0.3

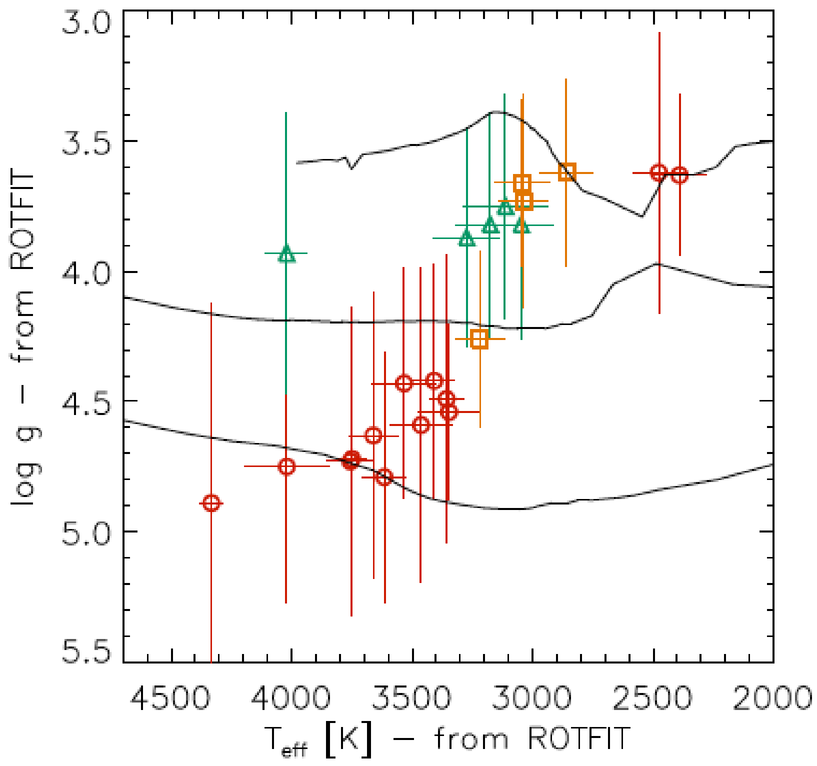

Fig. 2.14: Surface gravity as a function of T_{eff} compared with evolutionary pre-main sequence models by Baraffe et al. (1998) and Chabrier et al. (2000), shown for 1, 10, and 100 Myr isochrones (black lines, top to bottom). Objects are from σ Orionis (green triangles), Lupus (orange squares), and TW Hya (red circles). The two brown dwarfs in the TWA sample have significantly lower surface gravities than the stars in TWA. (See the two red circles in the top right-hand corner of the plot.) Plot and rubric from Stelzer et al. (2013).

surface gravities of low mass stars and substellar objects in their analysis of Upper Sco and suggested that the resulting apparent age difference could be due to uncertainties in evolutionary models related to accretion, deuterium burning and/or convection effects. Baraffe et al. (2002) found that uncertainties on evolutionary models at ages <10 Myr due to the initial radius of an object, the efficiency of convection in the object's outermost layers, and the object's initial deuterium abundance, can have dramatic effects on the object's luminosity and T_{eff}. Such uncertainties make the determination of the mass and age of such young objects problematic.

While the $H_2(K)$ indices of these TWA brown dwarfs support the discrepancies in their surface gravities, the TWA objects are one of the smaller subsets in my extended data set, and I would need more objects to obtain a more rigorous mean value of $H_2(K)$ for this association. I note that a number of Upper Sco objects have similarly low indices. Note also that 2M1207A is known to have a circumstellar disc (Gizis 2002; Sterzik et al. 2004; Scholz, Jayawardhana & Brandeker 2005).

Among the 1-2 Myr old objects, KPNO-Tau 6 and KPNO-Tau 7 have the largest $H_2(K)$ indices. These objects (as well as KPNO-Tau 12) have strong Hα emission, indicating the presence of an accretion disc (Muzerolle et al., 2005). In addition, KPNO-Tau 6 and KPNO-Tau 7 have significant mid-IR excesses in the *Spitzer*/IRAC passbands (Guieu et al., 2007). The youth of these objects is unquestioned. It is possible that their IR flux excesses slightly modify the shape of their K band spectra, producing larger than expected $H_2(K)$ indices, even though these objects form part of a sample with low extinction and no obviously unusual infrared spectroscopic features (K. Luhman, private comm.) That being so, the scatter in the $H_2(K)$ index for the Taurus objects is very small.

There is significant research to show that the ONC is very young, with an average age of $\leq$1 Myr (Prosser et al. 1994; Hillenbrand 1997; Palla & Stahler 1999; Riddick, Roche & Lucas 2007). In general, the $H_2(K)$ indices of the ONC PMOs in the extended data set are as low, or lower, than those of the 1-2 Myr objects in the same data set, indicating that they have similar surface gravities. I noted earlier that the Lyon models predict similar gravities for brown dwarfs and PMOs of a given age, with little dependence on mass. This therefore indicates that the age of the ONC PMOs is ∼1 Myr, on average.

2.7 Discussion

2.7.1 The Brown Dwarf Calibrators

The Field Dwarfs

BRI 0021's Na I pEW is substantially weaker than the same feature in the spectrum of the other field dwarf, 2MASS 0345. BRI 0021's rotational velocity (v sin i) is ∼ twice that of 2MASS 0345 (Antonova et al. 2008; Reid et al. 1999), and the strengths of stellar absorption lines are known to vary according to a star's rotational velocity and angle of inclination (Guthrie, 1965), but the variation is unlikely to be sufficient to explain this discrepancy (Stoeckley, 1968). Rapid rotation may alter the cloud structure, and thus may affect the observed spectrum. However, BRI 0021's $H_2(K)$ index is similar to that of 2MASS 0345. I therefore conclude that both field dwarfs have similar surface gravities.

The ages of these objects are unknown but assuming an age of 1 Gyr for both field dwarfs, at a distance of ∼27 pc (Faherty et al., 2009) and m_K=12.7 for 2MASS 0345, and at a distance of ∼11.8 pc (Faherty et al., 2009) and m_K=10.6 for BRI 0021, the Lyon group DUSTY model isochrone predicts $0.08\ M_\odot < M < 0.09\ M_\odot$ and $5.28 < \log g < 5.32$ for both objects. If these objects are as old as 10 Gyr, the mass range for both objects is unchanged, while their surface gravities now range from $5.29 < \log g < 5.34$.

σ Orionis Objects

σ Orionis 71 and σ Orionis J053−024 have flux excesses between 3.6 μm and 8 μm (Caballero et al., 2007). These are strong indicators of the presence of a disc. Emission from a disc could weaken an object's Na I EW, thereby reducing its apparent surface gravity. If the strength of the EWs are due to gravity plus veiling, this effect should correlate inversely with age. However, the effect could introduce more scatter both through geometric (viewing angle) effects, and if disc dispersal timescales vary from cluster to cluster. (For the effect of dust emission on the H_2(K) index, see Section 2.5.3). Since discs may persist for 10 Myr after birth (Jayawardhana et al. 1999; Sterzik et al. 2004), their detection is not inconsistent with these objects being categorised as the “older” of the young objects in this sample.

σ Orionis 51's Na I pEW and $H_2(K)$ index are markedly different from the corresponding values for σ Orionis 71 and σ Orionis J053−024. If σ Orionis 51 is younger than its siblings, it is more likely to be a member of the σ Orionis cluster, while admitting the likelihood that σ Orionis 71 and σ Orionis J053−024 are also cluster members. The age of the σ Orionis cluster is believed to be ≤10 Myr (Barrado y Navascués et al., 2001). If star formation occurred episodically over several Myr, it is not unreasonable to find objects with ages less than the maximum age of the cluster. Thus age spreads of a few Myr are plausible.

At a distance of ∼385 pc (Béjar et al., 2011), assuming an age of 3 Myr, and with m_K=16.1 for σ Orionis 51 and σ Orionis 71, and 16.2 for σ Orionis J053−024, the Lyon group DUSTY model isochrones predict $0.017\ M_\odot < M < 0.018\ M_\odot$. Assuming an age of 7 Myr, the model masses are $0.022\ M_\odot < M < 0.024\ M_\odot$. Over this age range, the model gravities are $3.75 < \log g < 3.93$.

The 1-2 Myr Objects

2MASS 0535−0546, a member of the ONC, is an eclipsing binary in which the masses and radii of the components have been determined (Stassun, Mathieu & Valenti, 2006). Thus the surface gravity of each component can be precisely known. For both primary (A1) and secondary (A2), the surface gravity is consistent with youthful objects, log g (A1)=3.52±0.03, log g (A2)=3.54±0.03 (Gómez Maqueo Chew et al. 2009, hereafter G09). Also, the large radii of the primary and secondary components ($R1=0.675\pm0.023\ R_\odot$, $R2=0.486\pm0.018\ R_\odot$ [G09]), are consistent with model predictions for 1 Myr old objects.

The Na I pEW determined here also supports the case for 2MASS 0535−0546 being among the youngest objects in my sample. 2MASS 0535−0546 has an earlier spectral type than the rest of the sample (M7), implying that the binary has a higher T_{eff}. The K band Na I doublet is temperature sensitive in that it usually becomes much weaker in early L dwarfs [C05] and somewhat weaker in early M dwarfs but there does not appear to be a strong temperature dependence between M7 and M9 in that work. Therefore, it is reasonable to include the Na I pEW of this object with those of the other 1-2 Myr objects. I note that the doublet remains strong in my spectrum of the L0 dwarf 2MASS 0345 (see Figure 2.2 and Table 2.2).

KPNO-Tau 4 and KPNO-Tau 12, have Na I pEWs consistent with low surface gravity. Although KPNO-Tau 1 has a Na I pEW suggesting it has a higher surface gravity, its $H_2(K)$ index is consistent with it being a low surface gravity object. This disagreement shows the danger of using single indicators to infer an age or even a surface gravity for individual objects.

The Taurus objects I chose for my sample, as well as those in the extended data set, have a K band magnitude distribution that is typical for the objects in this cluster (Jayawardhana et al. 2003; L04b). Therefore I am confident I have not introduced a bias in favour of younger objects in selecting my sample.

At a distance of 140 pc (Guieu et al., 2006), with m_K between 13.7 and 14.9, for 1 Myr old objects the Lyon DUSTY model isochrones predict $0.02\ M_\odot < M < 0.03\ M_\odot$ and $3.72 < \log g < 3.79$ for KPNO-Tau 1 and KPNO-Tau 4, and $0.006\ M_\odot < M < 0.007\ M_\odot$ and $3.50 < \log g < 3.51$ for KPNO-Tau 12. At a distance of 435 pc (Stassun, Mathieu & Valenti, 2006), with $m_K = 13.8$, the Lyon DUSTY model isochrones predict a total mass $M = 0.07\ M_\odot$ and $\log g = 3.54$ for 2MASS 0535−0546. Note that the surface gravities have been calculated for both components of this binary and are in close agreement with the model values.

2.7.2 152−717

Owing to the difficulty in maintaining a guide star lock even in the fainter parts of the Orion nebula, the integration time for 152−717 was shorter than requested. As a result, the extracted spectrum is not of sufficient quality to detect weak features such as the Na I doublet. Nonetheless, the spectrum shows the characteristic H_2O absorption of a young, late M-type object and the CO (v=2−0) absorption trough and the bandheads at 2.29 μm, 2.32 μm, 2.35 μm and 2.38 μm are clearly measured for the first time. See Figure 2.15.

152−717's $H_2(K)$ index is at the lower end of the range of $H_2(K)$ indices for the ONC PMOs in the extended data set (Table 2.6.). This is consistent with 152−717 being among the youngest of the ONC PMOs. However, as I only have a single surface gravity/age indicator, I caution against interpreting this object's $H_2(K)$ index as proof of its youth.

I was also able to derive a revised spectral type. I calculate that 152−717 has a spectral type M9.5±1.0. At a distance of ∼450 pc (Luhman et al., 2000), assuming an age of 1 Myr and m_K=17.6, the Lyon group DUSTY model isochrone predicts $0.005\ M_\odot < M < 0.006\ M_\odot$ and $3.47 < \log g < 3.50$ for this object (Chabrier et al. 2000; Baraffe et al. 2002).

2.7.3 Water Absorption in the *K* band

It was noted that a number of M dwarf spectra exhibit similar spectral structure in the vicinity of the 2.206 μm Na I absorption feature. The pattern is a feature of late-type dwarfs. (Synthetic spectra produced for objects with T_{eff} from 2500→3300 K show this pattern weakening with increasing T_{eff} (Lyubchik et al., 2012)). It is reproduced in the synthetic spectra used to model CIA opacity in this paper [S12] and arises from water absorption (D. Saumon, private comm.). See Figure 2.16.

2.8 Comparing the Age Indicators

I used my data set of calibrator brown dwarfs to study the merits of each age indicator. I computed the mean value of Na I pEW and $H_2(K)$ index for the Taurus and σ Orionis objects and found that the means agreed to within 0.75σ. This increased to 1.31σ for the $H_2(K)$ index. While the $H_2(K)$ index performs significantly better, neither method categorically differentiates the populations.

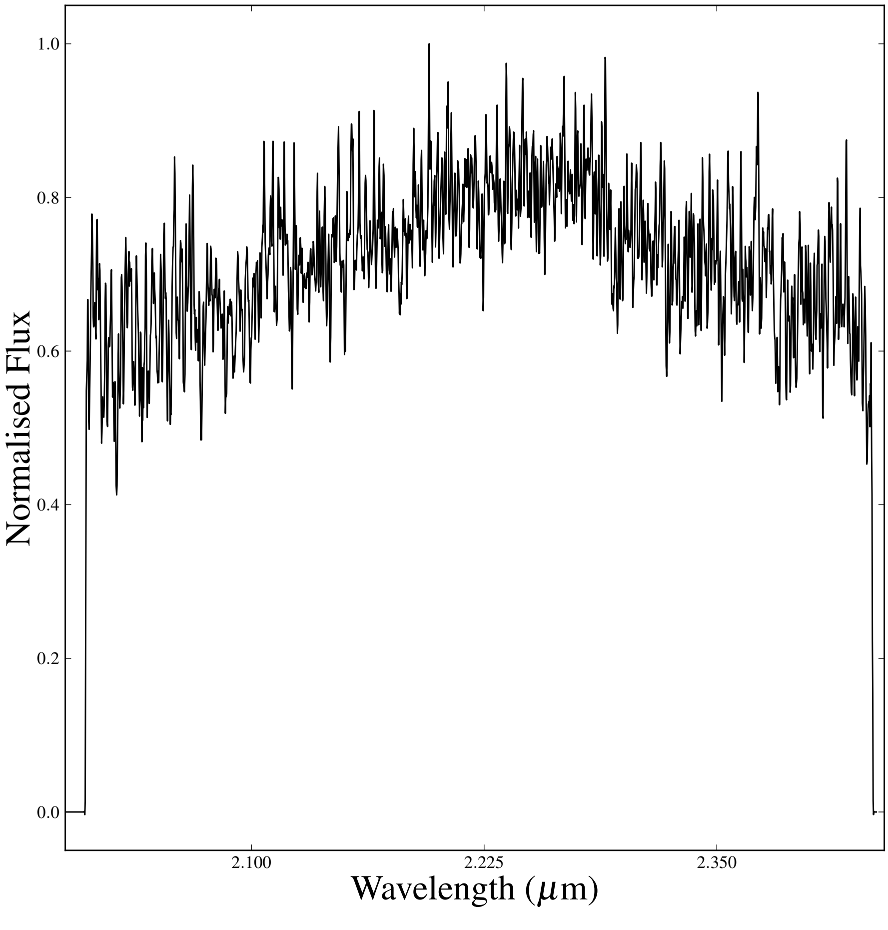

Fig. 2.15: The spectrum of 152−717 after 3 pixel boxcar smoothing. With a S/N of 5, narrow, gravity-sensitive spectral features are not discernible.

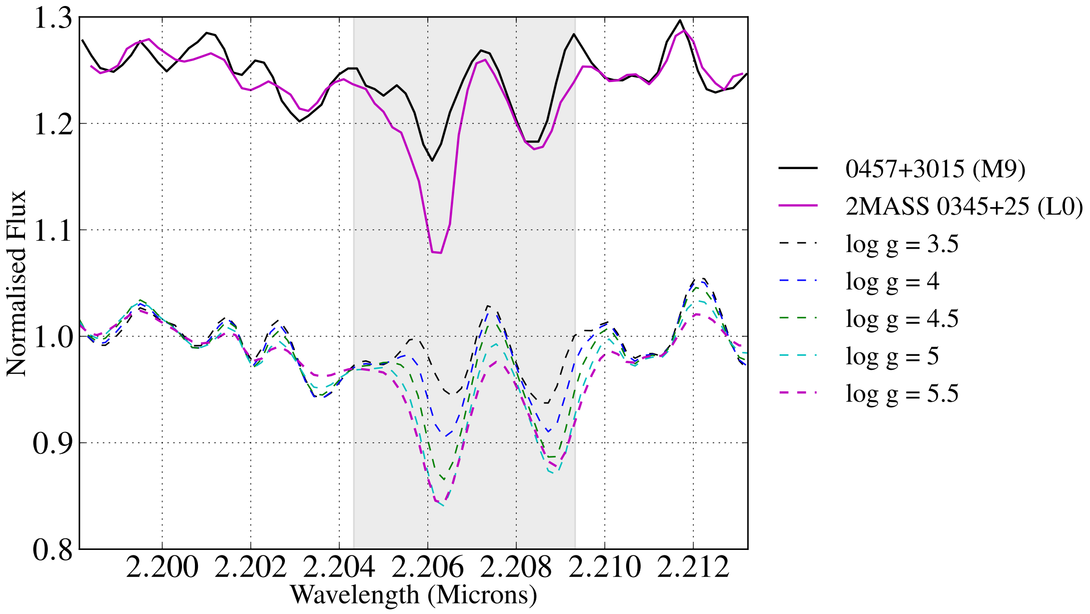

Fig. 2.16: Model spectra from S12 of the H_2O absorption lines adjacent to the Na I doublet (shaded region) compared to observations of a 1-2 Myr object (0457+3015) and field dwarf (2MASS 0345). My object spectra have been offset from the model spectra to aid comparison.

When I carried out the same exercise for the Taurus objects and my field dwarfs, the confidence level rose to 1.86σ (Na I pEW) and 6.76σ ($H_2(K)$ index).

The data set of brown dwarf calibrators contains only a few objects in each age group. To minimise the uncertainty in the $H_2(K)$ index, I examined the larger population of objects contained in my extended data set. I compared the mean $H_2(K)$ index for the 1-2 Myr objects in the extended data set with that of the Upper Sco objects and derived a 3.37σ confidence that these objects are from separate populations. The confidence level increased to 3.96σ when I compared the means of the 1-2 Myr objects with those of the Pleiades objects in my sample. The Pleiades has a wide scatter due to one object. Since the Pleiades has a more robust age determination than the younger clusters I have examined in this chapter, it is likely that this scatter will be reduced with the addition of more high quality K band spectra.

These results suggest that the $H_2(K)$ index is more gravity-sensitive than the Na I pEW. I have shown that the mean $H_2(K)$ index can change significantly between 1-2 Myr clusters and clusters $\geq$10 Myr. It therefore appears to be more gravity-sensitive at very young ages than the triangular H band continuum which is found in cluster objects with ages $\leq$5 Myr and in young field dwarfs, but which can persist for several tens of Myr [A07] and is found in some L dwarfs in the ∼120 Myr Pleiades cluster [B10]. The $H_2(K)$ index is applicable to lower resolution spectra. This has allowed me to suggest that the PMO in my original data set has low surface gravity. Since narrow spectral features were not resolved in the spectrum of this PMO, this would not have been possible had I depended only on the Na I pEW of the object.

I conclude that the $H_2(K)$ index is a more sensitive age indicator.

2.9 Applying and extending the $H_2(K)$ index

The $H_2(K)$ index has been used by others to support the young age of newly discovered brown dwarfs.

2.9.1 A substellar companion to ROXs 42B

In Currie et al. (2014), the authors report the direct imaging and spectroscopy of a candidate 6-15 M_{Jup} companion to ROXs 42B, a binary M star and probable member of the 1-3 Myr Ophiuchus star-forming region. The authors determined that the angular separation of ROXs 42Bb from the primaries corresponded to a projected physical separation of ∼150 AU. The authors concluded that the space motions of ROXs 42Bb are inconsistent with those of a background star, while it is statistically unlikely to be a free-floating PMO.

The authors compared their SINFONI (Eisenhauer et al. 2003; Bonnet et al. 2004) *K* band spectrum of ROXs 42Bb with spectra for M and L-type dwarfs in the Bonnefoy et al. (2014) SINFONI library and concluded that ROXs 42Bb's spectrum was most similar to the spectra of young objects near the M/L dwarf transition, at or below the deuterium-burning limit.

The authors calculated ROXs 42Bb's $H_2(K)$ index and found that it was smaller than the $H_2(K)$ indices of all but one of the objects in the Bonnefoy et al. (2014) SINFONI library, and is clearly distinguishable from the $H_2(K)$ indices of objects more massive than M ∼15 M_{Jup}. See Figure 2.17. The authors conclude that ROXs 42Bb's *K* band spectrum is further evidence that the object is young and has low

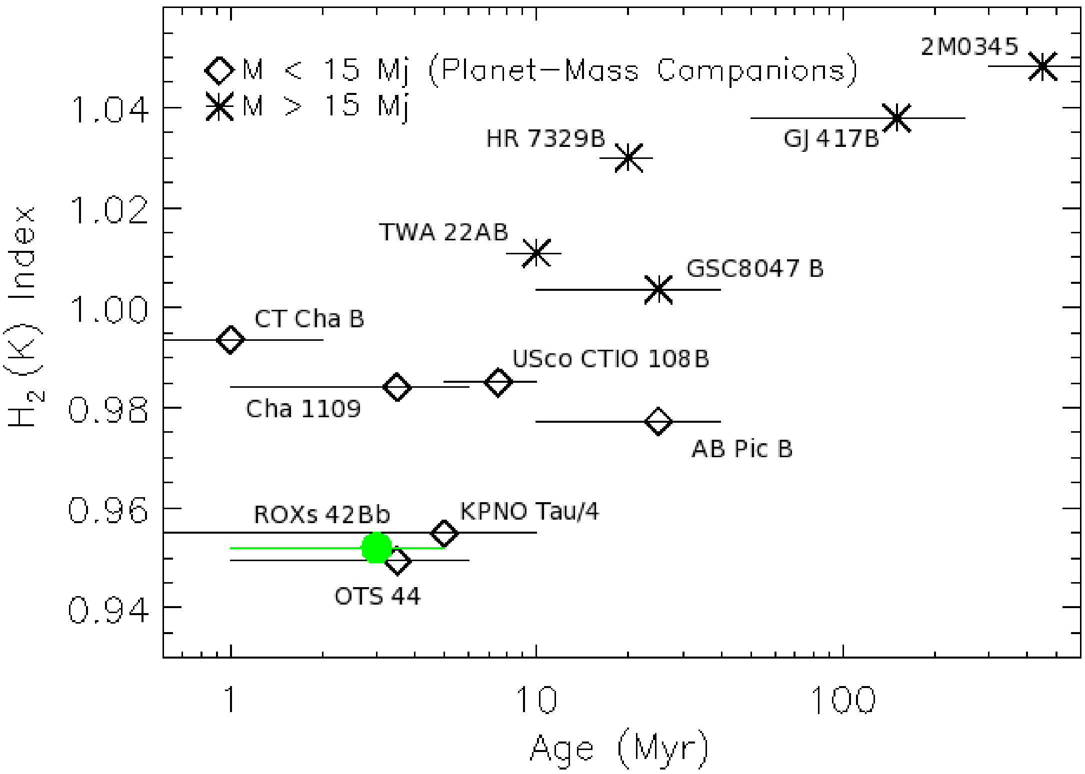

Fig. 2.17: The $H_2(K)$ index as a function of age for ROXs 42Bb compared to other objects in the Bonnefoy et al. (2014) library. For ROXs 42Bb to be as young and low mass as the authors suspect, it should appear in the lower left-hand corner of the plot. Plot and rubric from Currie et al. (2014).

mass/surface gravity.

The authors used the properties of the best-fitting comparison spectra to estimate that ROXs 42Bb has spectral type M8-L0, log g=3.5-4.5, and T_{eff}=1800-2600 K.

Given ROXs 42Bb's projected separation and mass with respect to the primaries, the authors suggest it may represent the lowest mass objects formed like binary stars or a class of PMOs formed by protostellar disc fragmentation/disc instability.

In their original analysis, the authors had estimated the spectral type and surface gravity of ROXs 42Bb from comparisons with the near-infrared spectra of known planetary-mass, substellar objects. In Currie, Burrows & Daemgen (2014), the spectrum of ROXs 42Bb was further analysed in order to determine its spectral type from gravity-independent (or weakly dependent) indices (Allers & Liu 2013; Bonnefoy et al. 2014), to identify chemical species, and to corroborate the evidence for low surface gravity discussed in my paper.

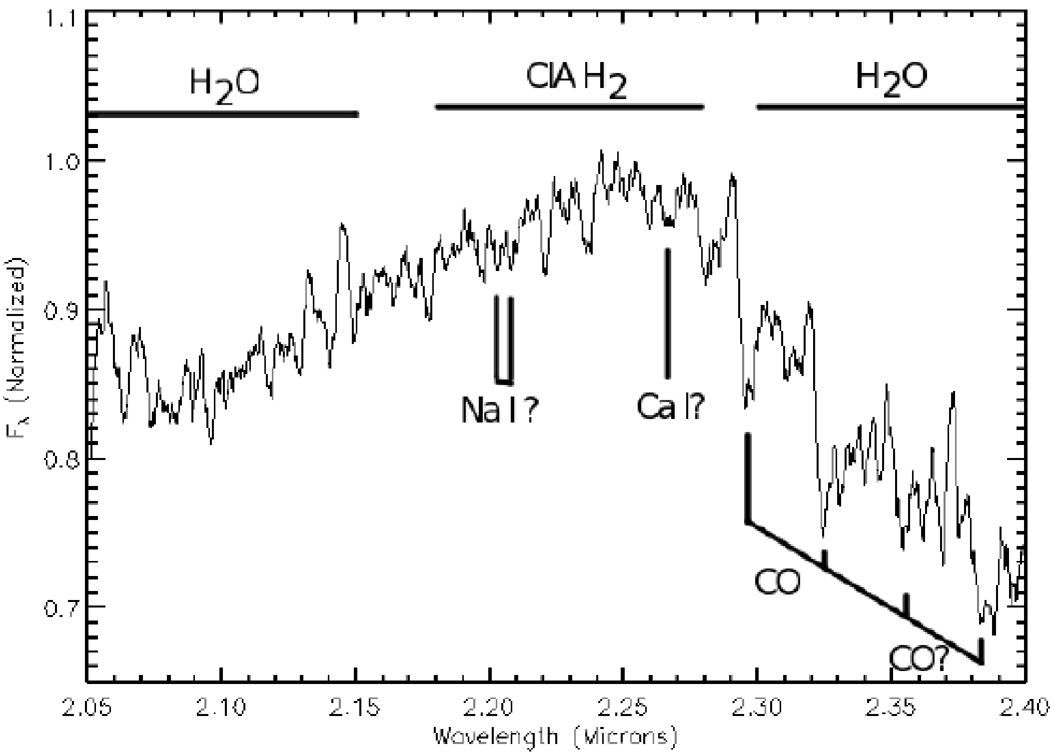

Fig. 2.18: The *K* band spectrum of ROXs 42Bb showing molecular absorption bands and the atomic lines used by Currie, Burrows & Daemgen (2014) as secondary gravity indicators. Plot and annotations from Currie, Burrows & Daemgen (2014).

In their discussion of the chemical composition and gravity-sensitive features of ROXs 42Bb, Currie, Burrows & Daemgen (2014) observe that the Na I and Ca I lines in the *K* band are weaker in field objects with late M/early L spectral types than in spectral types $\leq$M7 (see Cushing, Rayner & Vacca 2005), and cite my paper to suggest that these features may continue to weaken in young, lower surface gravity objects at the M/L boundary. See Figure 2.18.

Currie et al. (2014) had used ROXs 42Bb's $H_2(K)$ index as a measure of H_2 CIA to support their conclusion that ROXs 42Bb was a planetary mass companion to ROXs 42B. To augment this analysis, Currie, Burrows & Daemgen 2014 looked for evidence of other gravity-sensitive features in the *K* band spectrum of ROXs 42Bb. In particular they looked at the strengths of the CO bandhead at 2.29 μm and the Na I doublet and Ca I triplet and cite the analysis of these features which I had undertaken in my paper. They determine that the equivalent width of the CO bandhead is comparable to or smaller than any of the young objects I had studied, and much smaller than the equivalent widths of the late M/early L field dwarfs I had examined.

Currie, Burrows & Daemgen (2014) detect local minima in the K band continuum whose locations are consistent with the positions of the Na I doublet and Ca I triplet. However, they could not differentiate these minima from the noise in the spectrum so were unable to use these features in their analysis. This supports my observation that the $H_2(K)$ index can be used as an indicator of surface gravity in spectra in which narrow spectral features are too poorly resolved to be used. Currie, Burrows & Daemgen (2014) conclude that the surface gravity of ROXs 42Bb inferred from the line strengths of the secondary gravity diagnostics they examined was consistent with their previous value based on the $H_2(K)$ index of ROXs 42Bb.

Currie, Burrows & Daemgen (2014) also carried out model fits to new J, K_S, and L' photometry and to their previously published H band photometry and K band spectroscopy. They observed that the models had difficulty reproducing some gravity-sensitive features in the spectrum of ROXs 42Bb and noted that I had a similar experience when I attempted to fit Saumon & Marley models to the data in my paper. In particular, the $H_2(K)$ index appeared to be a much stronger function of gravity at low surface gravities than predicted by the models.

2.9.2 The $H_2(K)$ index in L dwarfs

In their paper, Schneider et al. (2014) report the discovery of the L dwarf WISE J174102.78-464225.5, hereafter WISE 1741-4642. This object was found during a search for local L dwarfs using WISE. The authors noted that the near-infrared spectrum of WISE 1741-4642 contained features which were characteristic of a young age, in particular the triangular shape of the peak of the H band flux, and red near-infrared colours ($J-K_S$=2.35±0.08). By comparing WISE 1741-4642's spectrum with spectral standards and other red L dwarfs, Schneider et al. (2014) inferred the object to be spectral type L7±2 (pec). The authors used spectral and low-mass evolutionary models to determine WISE 1741-4642's T_{eff}, log g, age and mass to be 1450±100 K, 4.0±0.25 cm s^{-2}, 10-100 Myr, and 4-21 M_{Jup} respectively. The authors observed that the distance and kinematics of WISE 1741-4642 suggested membership of a young nearby moving group, and offered the β Pictorus or AB Doradus associations as candidates.

The authors noted that I had shown that the shape of the *K* band continuum can distinguish young ($\leq$10 Myr) brown dwarfs from an older field population, and can be used with low resolution spectra. They noted that the sample of brown dwarfs I had used in my analysis of the *K* band continuum was lacking in objects with ages >10 Myr and less than the age of field dwarfs. As a result, the $H_2(K)$ index was not well constrained in this age range. I had made the same observation in my analysis.

The authors calculated the $H_2(K)$ index of WISE 1741-4642 and determined a value of 1.029. Compared with my analysis, this result appears high for a young object $\leq$10 Myr. However, Schneider et al. (2014) noted that my analysis had been done on a sample of brown dwarfs with spectral types $\leq$L0. They therefore decided to extend my analysis into the L dwarf regime.

To do this, the authors searched the Spex Prism Spectral Library (Rayner et al., 2003) for L dwarf spectra with resolutions R$\geq$120. As the spectral types of many of these objects had not been determined homogeneously, the authors reclassified the spectral types of their sample according to the L dwarf classification scheme described in Kirkpatrick et al. (2010). The authors excluded particularly noisy spectra from their analysis and determined the $H_2(K)$ indices of the rest. I have combined my results with those of Schneider et al. (2014). A plot of the outcome is shown in Figure 2.19.

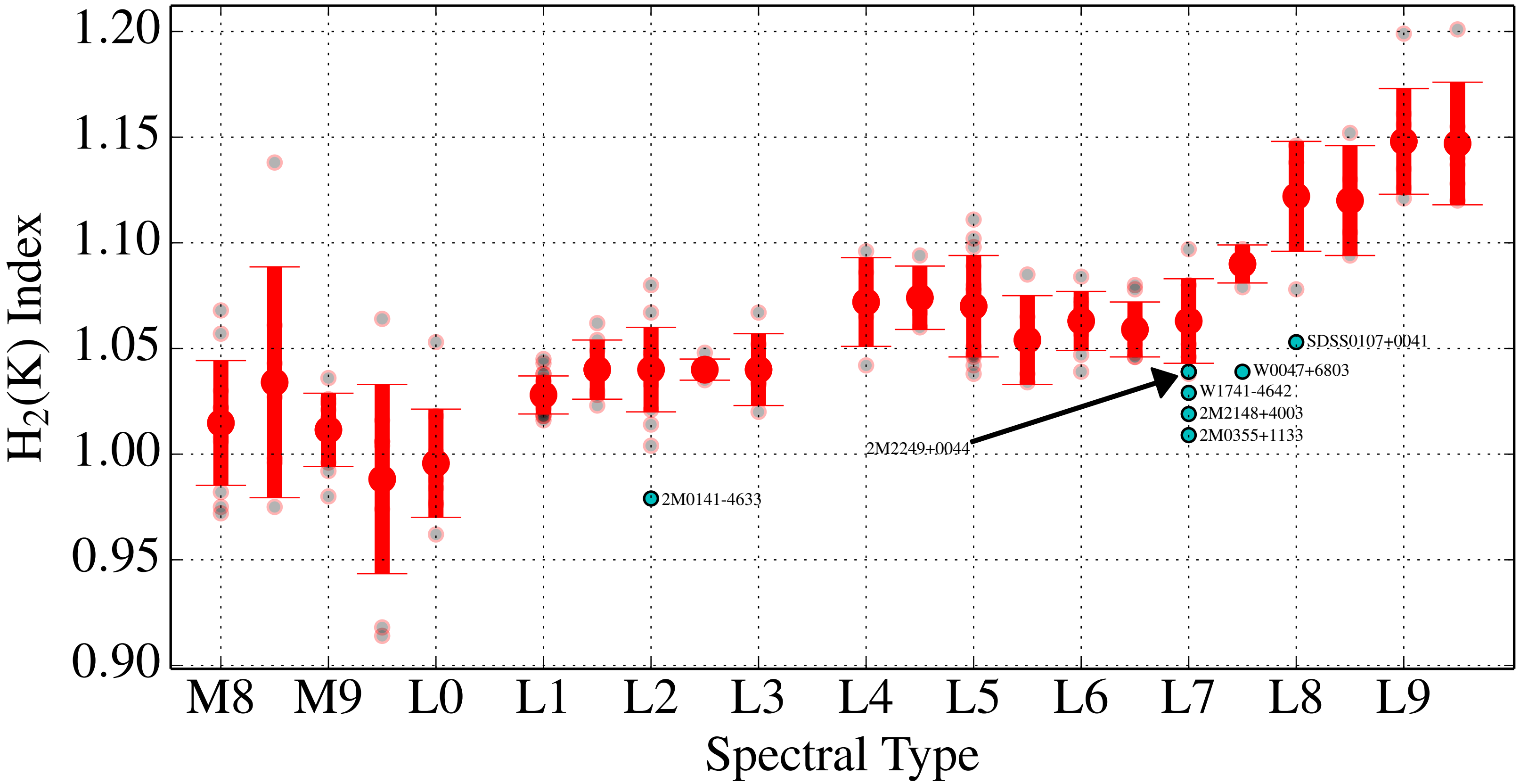

Fig. 2.19: $H_2(K)$ index as a function of spectral type for my brown dwarf calibrators and the objects in the extended data set and the L dwarfs from the SpeX Prism Spectral Library based on the new spectral typing system described in Schneider et al. (2014). Red points indicate the mean $H_2(K)$ index and standard deviation for L dwarfs binned by 0.5 subtype. The young and/or red L dwarfs 2M2148+4003, 2M0355+1133, 2M0141-4633, 2M2249+0044, W0047-6803, and SDSS 0107+0041, as well as WISE 1741-4642 are individually labelled. Plot and rubric developed from that in Schneider et al. (2014).

While the $H_2(K)$ index appears to be correlated with spectral type past L0 in that the $H_2(K)$ index increases with increasing spectral type, it is arguable that the index may be least affected by spectral type in the region M8-L3 (certainly within the errorbars). The $H_2(K)$ indices of WISE 1741-4642 and the red L dwarfs 2M0355+1133 and 2M0047+6803 are seen to deviate from the field population, while the young, red L6 dwarf 2MASS J214816.28+400359.3 (Looper et al., 2008), the young, red L2 dwarf 2MASS J014158.23-463357.4 (Kirkpatrick et al., 2006), the low gravity L dwarf 2MASS J224953.45+004404.6 ($\mathrm{SpT_{opt}}$=L4; Faherty et al. 2013), and the red L8 dwarf SDSSp J010752.33+004156.1 (Geballe et al., 2002) also show strong deviations below their near infrared spectral types.

Schneider et al. (2014) conclude that WISE 1741-4642's peaked H band continuum shape, its red near-infrared colours, and low $H_2(K)$ index are characteristic of a young age.

I should also note that while I was careful to insist that the $H_2(K)$ index should be applied statistically to populations of objects, in both cases where the index has been used by other researchers, it has been used to provide additional support for the young age of a *single* object.

2.10 Conclusions

The K band slope is a good indicator of an object's surface gravity, provided the object has solar metallicity. While most nearby star formation regions tend to have solar metallicity, individual objects' metallicities should be taken into account when considering the object's surface gravity.

I have defined a new spectral index, $H_2(K)$, which is a good indicator of surface gravity, particularly for the youngest sources (1-10 Myr), where it is more sensitive to surface gravity than the triangular H band peak. It is at least as good as the equivalent width of the 2.21 μm Na I doublet in differentiating the surface gravities of late-type objects, and does so with less scatter and without the need for high-resolution spectra. This has allowed me to examine other data sets, obtaining similar results to those obtained from my own brown dwarf calibrators. All data sets show some scattering of $H_2(K)$ indices within a cluster. Considering the uncertainties associated with the data, it is unclear whether or not this scatter reflects a genuine spread of ages.

I have shown that the $H_2(K)$ index and the EW of the 2.21 μm Na I doublet can find the difference, at least statistically, between a population of ~1 Myr objects and field dwarfs. In addition, the $H_2(K)$ index can statistically differentiate a population of ~1 Myr objects and a population of ~10 Myr objects. The $H_2(K)$ index can also be used to separate low-mass members from foreground and background objects in young clusters and associations.

By comparing the $H_2(K)$ indices of 152−717 and the ONC PMOs from L06 to the $H_2(K)$ indices of my 1-2 Myr calibrators, I infer that, on average, the ONC PMOs and my 1-2 Myr calibrators have a similar age.

The σ Orionis objects' $H_2(K)$ indices and Na I pEWs are consistent with one object being significantly younger than the others. If true, this would indicate a variation of ages within the cluster, rather than suggesting that the older objects are not cluster members. Indeed, if these objects were contaminants, they could only be much older field objects, and this is clearly not the case.

Given the differences in $H_2(K)$ index among the Pleiades objects and that some of their spectra have quite low S/N in the K band, it would be worthwhile obtaining higher S/N K band spectra of objects in clusters with well constrained ages so that these surface gravity indicators can be investigated.

I have shown that it is not necessary to have high-resolution spectra of these objects to be able to constrain the size of their population in young clusters and the low-mass end of the IMF.

I now have two gravity-sensitive methods of differentiating late-type dwarfs, the EW of neutral alkali metal lines and the $H_2(K)$ index, both of which show good correlations with age and which will allow researchers to ascribe statistical ages to samples of brown dwarfs in pre-main sequence clusters. These can then be used to distinguish between PMOs and somewhat older brown dwarfs with a similar luminosity and temperature.

An object of future research is to determine the extent to which scatter in these indicators of surface gravity is due to an age spread.

Chapter 3

CH_4 and NH_3 in the near-infrared spectra of late T dwarfs

In the following discussion, the terms CH_4 and methane, and NH_3 and ammonia, refer to the main isotopologues of methane and ammonia, $^{12}CH_4$ and $^{14}NH_3$ respectively.

In this chapter, I examine the atmospheres of two late T dwarfs, the T8 standard, 2MASS J04151954-09350662 (Burgasser et al. 2002b) (hereafter 2MASS 0415), and the T9 standard, UGPS 0722, by comparing absorption features in the near-infrared spectra of these objects with synthetic spectra and with absorption cross-sections of the most important gas-phase opacity sources at these wavelengths; H_2O, CH_4, and NH_3. I also conduct an analysis of the ro-vibrational transition lines responsible for the methane and ammonia absorption features in these objects' near-infrared spectra.

The synthetic line lists I have used in my analysis have been provided by the theoretical molecular physics group at University College London (UCL), creators of the ExoMol project (Tennyson & Yurchenko, 2012), a database (www.exomol.com) of high temperature line lists for astronomical use. The NH_3 line list BYTe (Yurchenko, Barber & Tennyson, 2011) has been available since 2011, but the CH_4 line list (10to10) (Yurchenko & Tennyson, 2014) has only been available since January, 2014. Yurchenko & Tennyson (2014) used the 10to10 line list to re-identify a number of methane absorption features first identified in the R≈1200 SpeX *H* band spectrum of the T4.5 brown dwarf 2MASS J0559-1404 (Cushing, Rayner & Vacca 2005). The 10to10 list has also been incorporated into the VSTAR model atmosphere code (Bailey & Kedziora-Chudczer, 2012) and used to model the *H* and *K* band spectrum of 2MASS J0559-1404 (Yurchenko et al., 2014). The model spectrum is a significantly better fit to the brown dwarf spectrum than an earlier VSTAR model using a methane line list computed with the STDS (Wenger & Champion, 1998) software. However, medium resolution spectra are needed to resolve individual features. It is therefore timely to provide a high quality set of medium resolution spectra to compare with the new generation of models. I believe that this is the first time the 10to10 line list has been used to analyse the complete near-infrared spectrum of a late T dwarf.

The 10to10 line list has been eagerly anticipated. It is the most complete high temperature line list yet produced and is suitable for characterising atmospheres with T_{eff} up to ∼1400 K. In addition to identifying CH_4 and NH_3 absorption features, I also identify the vibrational and rotational quantum numbers of the individual transitions producing the absorption features. The theoretical basis for these identifications is described in the next section.

3.1 The ro-vibrational spectroscopy of non-linear molecules

Much of the technical information in this section is derived from the NIST Chemistry WebBook[1], and from conversations with Sergei Yurchenko, Principal Research Associate, Dept of Physics & Astronomy, Faculty of Maths & Physical Sciences, UCL. Dr Yurchenko is a leading member of the theoretical molecular physics group at UCL, and the principal author of the 10to10 line list.

The near-infrared spectrum of a molecule can be analysed to obtain information about the rotation and vibration of the molecule. Unexcited molecules are in the lowest vibrational energy state, ν=0. The lowest energy transition is then ν=0→1. Since molecules are not harmonic oscillators, transitions other than $\Delta\nu$=±1 are allowed. These transitions are called overtones and may involve $\Delta\nu$=±2, ±4, ±6,...etc. I will

---

[1] Available at: http://webbook.nist.gov/chemistry/

show in this chapter that the strongest features in the *H* band absorption spectrum of CH_4 are produced by overtones. A manifold of rotational energy levels, J, is superimposed on each vibrational energy state so that molecular absorption features are produced by transitions between vibrational states and rotational states. Transitions between vibrational energy levels and between rotational energy levels (ro-vibrational transitions) can occur simultaneously. In such transitions, the values of ν and J both change. R-branch transitions are vibrational transitions from a lower rotational energy level to a higher rotational energy level, ΔJ=+1. P-branch transitions are transitions from a higher to a lower rotational energy level, ΔJ=-1. Or the transition may be between the same rotational energy level at different vibrational energy levels, ΔJ=0. These are called Q-branch transitions. There is a series of transitions corresponding to different changes in ΔJ associated with each vibrational transition.

The ro-vibrational spectrum for a particular vibrational transition is a series of peaks in the absorption cross-section. These peaks correspond to troughs in the observed spectrum. The peaks to the right and left of the Q-branch are produced by transitions between different rotational energy levels. R-branch transitions involve transitions to higher rotational energies, so peaks produced by these transitions are located at shorter wavelength values. P-branch transitions are produced by transitions to lower rotational energies and peaks produced by these transitions occur at longer wavelengths. In summary, each peak in a ro-vibrational spectrum corresponds to a different transition where ΔJ=0, ±1. The correspondence between a molecule's absorption cross-section and its ro-vibrational transitions is depicted in Figure 3.1.

There are also electric quadrupole transitions whose selection rules are ΔJ=±2, $\Delta\nu$=±1, ±2, ±3... O-branch transitions are transitions where ΔJ=-2, S-branch transitions are transitions where ΔJ=+2. However, these transitions are less likely than electric dipole transitions, and are therefore weaker (Irwin, 2003). I have not detected electric quadrupole transitions in my analysis of the T dwarf spectra. For ro-vibrational spectroscopy of non-linear molecules such as CH_4 and NH_3, the standard rotational angular momentum selection rule is ΔJ=0, ±1. Therefore, P-branch, R-branch, and Q-branch transitions are all allowed.

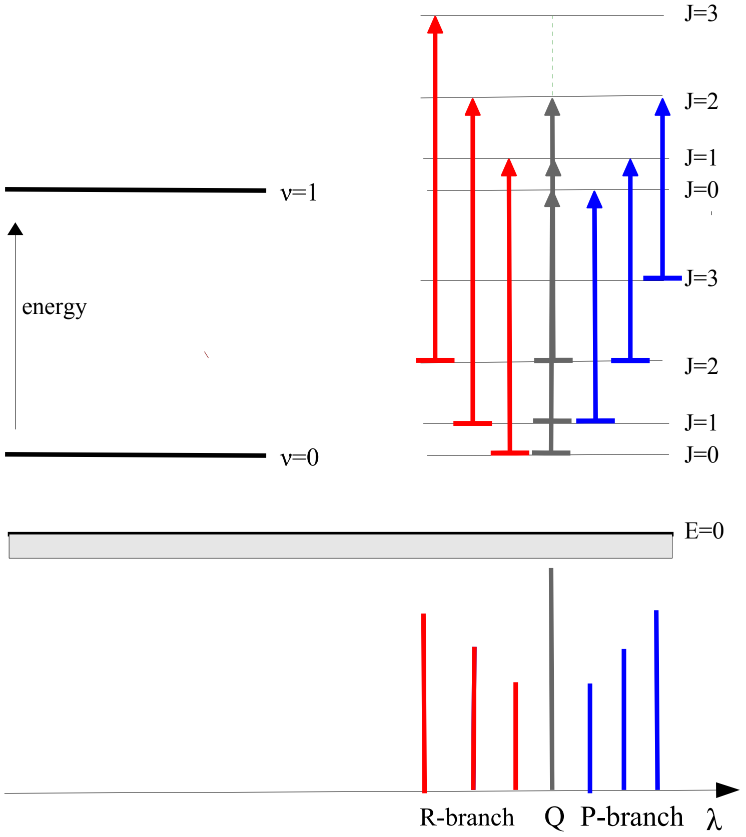

Fig. 3.1: The ro-vibrational energy level diagram and the corresponding absorption cross-section. The shape of the absorption cross-section is determined by the distribution of rotational transitions. (Plot based on http://home.strw.leidenuniv.nl/~michiel/ismclass_files/radproc07/chapter8.pdf.)

Table 3.1: The Fundamental Vibrational Modes of Methane and Ammonia

Molecule	Mode	Type	Wavenumber (cm^{-1})	Symmetry
Methane	ν_1	Symmetric Stretch	2917	A_1
	ν_2	Symmetric Bend	1534	E
	ν_3	Asymmetric Stretch	3019	F_1
	ν_4	Asymmetric Bend	1306	F_2
Ammonia	ν_1	Symmetric Stretch	3337	A_1
	ν_2	Symmetric Bend	950	A_1
	ν_3	Asymmetric Stretch	3444	E
	ν_4	Asymmetric Bend	1627	E

A molecule may be classified according to its symmetry, and assigned to a certain point group. CH_4 is a tetrahedral molecule and belongs to the T_d point group. NH_3 is a pyramidal molecule and belongs to the D_{3h} point group (Yurchenko, Barber & Tennyson, 2011). Each of these molecules has four fundamental vibrational modes or states, described by four quantum numbers. The modes and their properties are shown in Table 3.1.

In most cases, excited stretching states are stronger than excited bending states (S. Yurchenko, private comm.). In the *H* band, for example, the strongest features belong to the $2\nu_3$ vibrational band, which is a stretching band.

I will show that the absorption features in the near-infrared spectrum of CH_4 and NH_3 are produced by interactions between one or more vibrational modes.

3.2 Observations & Data Reduction

Observations were made with the 8m Gemini Telescope at Gemini North on Mauna Kea, Hawaii, using NIFS. Observations were made in the *Z*, *J*, *H*, and *K* passbands, (the *Z* passband includes the *Y* band flux peak in brown dwarfs), and followed an ABBA pattern to facilitate the removal of the sky background and dark current. The resolution in each passband was R≈5000. The T8 standard 2MASS 0415 was observed over four nights between 30 September 2010 and 12 October 2010. Observations of UGPS 0722 were made over seven nights between 17 October 2010 and 29 October 2012. Observations in the *H* and *K* passbands for UGPS 0722 were made using the

Table 3.2: T Dwarf Observations

Object	Observation period	Grating/Centred at	Range (λ)
2MASS 0415	2010 October 4	Z band/1.05 μm	0.95-1.15 μm
	2010 October 12	J band/1.25 μm	1.15-1.35 μm
	2010 October 1	H band/1.6 μm	1.45-1.75 μm
	2010 September 30	K band/2.14 μm	1.95-2.37 μm
UGPS 0722	2012 September 27 - 30	Z band/1.05 μm	0.95-1.15 μm
	2012 October 1 - 29	J band/1.25 μm	1.15-1.35 μm
	2011 December 11	H band/1.6 μm	1.45-1.75 μm
	2010 October 17	K band/2.14 μm	1.95-2.37 μm

Table 3.3: T Dwarf Physical Properties

	UGPS 0722	2MASS 0415
Spectral Type	T9$^{(1)}$	T8$^{(2)}$
T$_{eff}$	500 K$^{(3),(8)}$	750 K$^{(4)}$
v sin i	40$\pm$10 kms^{-1} $^{(5)}$	33.5 kms^{-1} $^{(6)}$
Age	1-5 Gyr $^{(5)}$	1-10 Gyr $^{(2)}$
log g	4.39-4.90$^{(7)}$	4.64-5.15$^{(7)}$
Mass	10.7-25.8 M$_{\rm Jup}$ $^{(7)}$	17.4-40.1 M$_{\rm Jup}$ $^{(7)}$
Distance	4.12$\pm$0.04 pc$^{(8)}$	5.71$\pm$0.05 pc$^{(9)}$

(1) Cushing et al. (2011)
(2) Burgasser et al. (2002a)
(3) Lucas et al. (2010)
(4) Saumon et al. (2007) (5) B11
(6) Zapatero Osorio et al. (2007)
(7) Dupuy & Kraus (2013)
(8) Leggett et al. (2012)
(9) Dupuy & Liu (2012)

Gemini ALTAIR adaptive optics system to improve the S/N ratio. Details of the observations and the physical properties of the two T dwarfs are shown in Tables 3.2 and 3.3 respectively.

Raw data were reduced using the GEMINI NIFS package within IRAF in the same manner as described in Section 2.3. The uncertainty in the wavelength calibration was 0.03-0.3 pixels, corresponding to $6(10^{-6})$-$6(10^{-5})$ μm. The science spectra were corrected for the T dwarfs' radial velocities using the IRAF task DOPCOR. The radial velocity for 2MASS 0415 was taken from Zapatero Osorio et al. (2007), that for UGPS 0722 from B11. Both T dwarf spectra were corrected for the heliocentric and barycentric velocity components of Earth using the IDL/AstroLib task BARYVEL. In the spectrum of UGPS 0722, I estimate the S/N ratio at the peaks of the Z, J, H, and K bands to be ∼250, 370, 300, and 80 respectively. B11's estimates for the corresponding values in their analysis of UGPS 0722 are ∼250, 350, 200, and 60. I note that Magellan/FIRE data split each passband into multiple orders which can cause more variation in the S/N ratio with wavelength. This is not the case with NIFS, where data are collected in separate observations in each passband. My T dwarf spectra are shown in Figure 3.2.

3.3 Methane and Ammonia

Carbon in the photospheres of early to mid L type brown dwarfs is predominantly found as carbon monoxide (CO) due to the molecule's high ionization energy (Geballe et al., 2009). By spectral type L5, the photosphere is cool enough to allow the hydrogenation of CO to CH_4 (Noll et al., 2000). As the photosphere continues to cool, CH_4 becomes the dominant carbon-bearing species (Fegley & Lodders, 1996). The conversion of N_2 into NH_3 occurs at T_{eff} ∼800 K [S12]. Bands of NH_3 opacity are first seen in the mid-infrared spectra of T2 dwarfs (Cushing et al., 2006), while the first unequivocal detection of NH_3 opacity in brown dwarfs was made in the mid-infrared spectra of the T dwarf binary ϵ Indi Bab (T1+T6) (Roellig et al. 2004; Mainzer et al. 2007). Features in low resolution near-infrared spectra of late T dwarfs and the recently discovered Y dwarfs have been attributed to weak bands of NH_3 opacity (Delorme et al. 2008; Cushing et al. 2011), but the first confirmed identification of ammonia features in the near-infrared spectrum of a late T dwarf was made by B11 using medium resolution spectra. This discovery has been significant in justifying the Y spectral class. Indeed, as I observe in Section 3.3.2, B11 may have underestimated the number of ammonia features in the J band of UGPS 0722.

I have used absorption cross-sections at 500 K and 750 K, derived from the 10to10 line list, to identify methane absorption features in the near-infrared spectra of the two T dwarfs. These cross-sections were compared with cross-sections at the same temper-

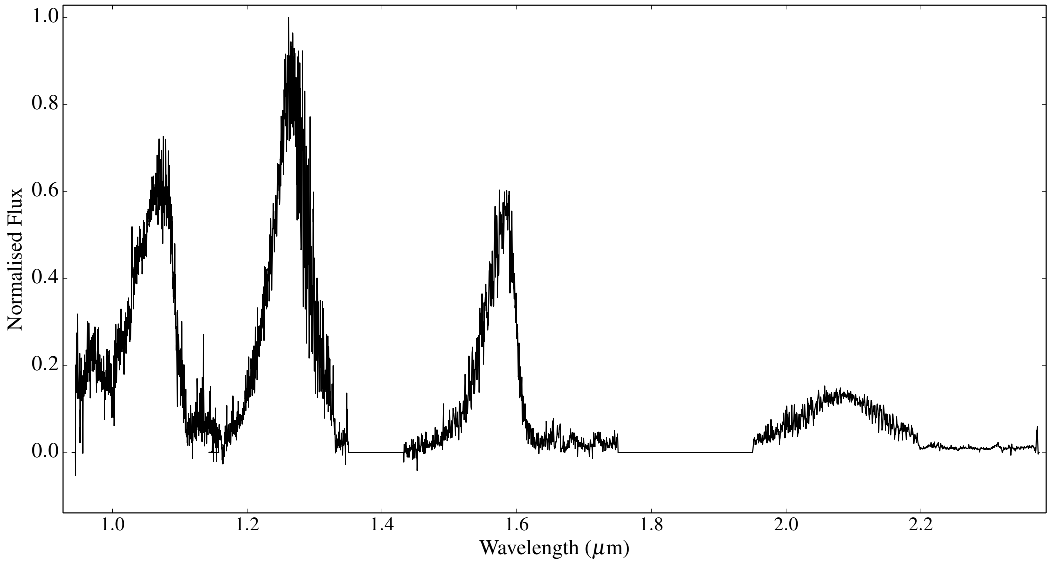

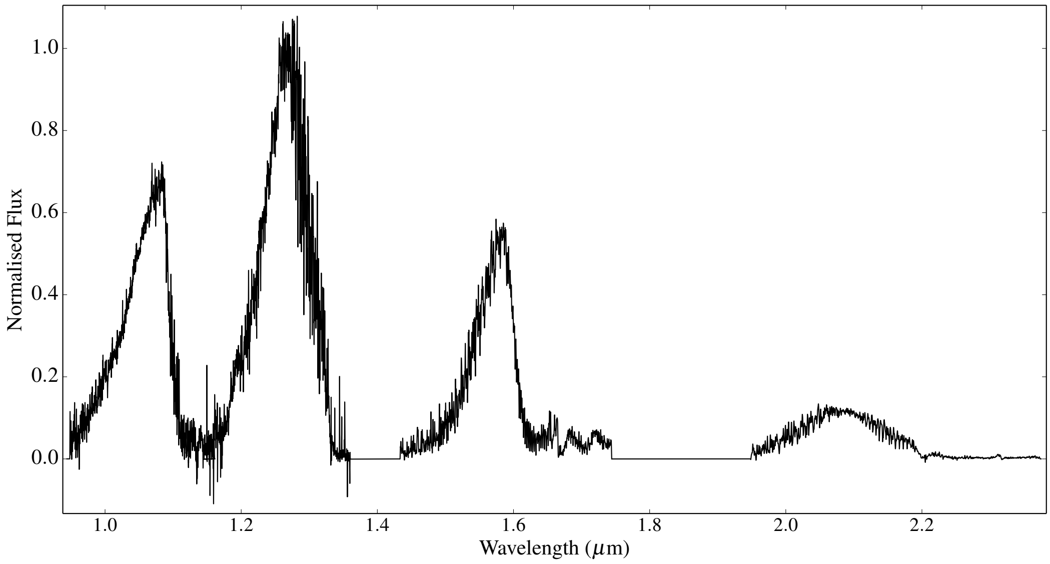

Fig. 3.2: **(Top)** The near-infrared spectrum of the T9 standard UGPS 0722. **(Bottom)** The near-infrared spectrum of the T8 standard 2MASS 0415.

atures for H_2O and NH_3, calculated from the latest computed line lists, BT2 (Barber et al., 2006), and BYTe (Yurchenko, Barber & Tennyson, 2011) respectively. Each cross-section was scaled by the relative abundances of these molecules according to Figure 3 in Saumon et al. (2006). (See Figure 3.3).

Figure 3.3 shows that the mole fractions of the equilibrium/non-equilibrium abundances of H_2O and CH_4, and the non-equilibrium abundances of NH_3 are constant over the range ∼1000-250 K. The reason for this in the equilibrium cases is that when the temperature is less than the bond energy ($T<T_{eff} \times k$, where k is Boltzmann's constant), chemical reactions stop, and the mole fraction of a molecule is fixed, even as the temperature continues to decrease. In the non-equilibrium case, vertical mixing determines the abundances of these species rather than chemical reactions. For these molecules, the mixing of hot and cold gas from different parts of the atmosphere occurs much faster than the chemical reactions through which these molecules form. The molecules have no time to transform toward their equilibrium mole fractions for the local temperature. As the temperature decreases, these molecules' mole fractions are fixed at abundances corresponding to a deeper, and therefore hotter level (D. Saumon, private comm). Therefore I am justified in using the abundances in Figure 3.3 to scale the opacity cross-sections. Saumon et al. (2006) found that prominent ammonia features in the near-infrared spectrum of the T7.5 dwarf Gliese 570D could only be fitted if the abundance of ammonia in their models was reduced by ∼1 order of magnitude from the value found at chemical equilibrium. Therefore, I have used non-equilibrium abundances for NH_3 when scaling the NH_3 cross-sections.

By comparing synthetic spectra derived from full model atmosphere calculations with and without NH_3 opacity with the Magellan/FIRE spectrum of UGPS 0722 in B11, S12 were able to identify a number of new NH_3 absorption features. I have applied the technique described in S12 to the Gemini/NIFS spectra of 2MASS 0415 and UGPS 0722. The synthetic spectra were produced with solar metallicity and $\log g = 4.25$. Non-equilibrium chemistry was assumed, with eddy diffusion constant $K_{zz}=10^4$ cm^2 s^{-1}. Separate models were produced at 750 K and 500 K, the respective effective temperatures of the T8 and T9 objects. The models included the most recent calculations of all major opacity sources, except the 10to10 line list. With that caveat in mind, with the possible exception of regions where methane is the dominant opacity source, the model spectra should appear similar to the T dwarf spectra. It is also useful to have spectra from two dwarfs of successive spectral types since absorption features missing in the spectrum of one T dwarf, may be present in the spectrum of the other.

By comparing the T dwarf spectra with the S12 model spectra and the scaled cross-sections for CH_4, H_2O, and NH_3, I have been able to identify a number of new ammonia features in the near-infrared spectra of the T dwarfs. In order to be confident in identifying an absorption feature, the shape of the continua of the S12 model spectra with and without NH_3 opacity should appear different, not simply in amplitude. In places, peaks in the NH_3 opacity do not coincide exactly with absorption troughs in the science spectrum. In these cases, I identify an ammonia feature at the wavelength of the peak in the NH_3 opacity when the science spectrum at this wavelength appears similar to the model spectrum with NH_3 opacity, e.g., the feature at 1.5240 μm (see Figure 3.18).

I examined a number of absorption features in the *H* band of UGPS 0722, which I suspected may have been produced by the $^{13}CH_4$ isotopologue of methane, but none of these features coincided with $^{13}CH_4$ lines in the HITRAN (Rothman et al., 2009) molecular spectroscopic database.

3.3.1 The *Z* Band

In the *Z* band, CH_4 is the dominant opacity source between ~0.95−1.03 μm. In this region, the cross-section appears as a continuum, with no obvious peaks. The S12 models predict NH_3 opacity only between 1.005 μm and 1.074 μm. Across most of this wavelength range the S12 model spectra differ only in amplitude. Only at 1.0256 μm do I find a slight variation in structure between the two models, corresponding to a peak in NH_3 opacity and weak absorption features in both T dwarfs. However, the detection is weak, and I cannot say with confidence that I have found any evidence of NH_3 absorption lines in the *Z* band.

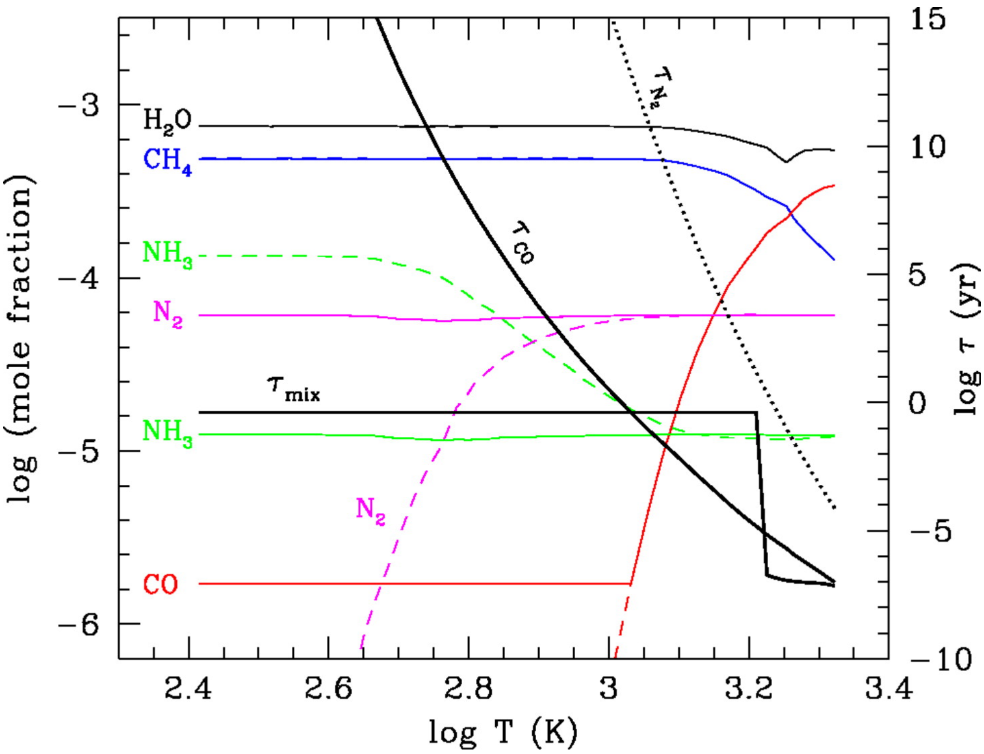

Fig. 3.3: Mole fractions of H_2O, CH_4 and NH_3 shown in equilibrium (dashed curves) and out of equilibrium (log K=2, solid curves) as a function of T_{eff} in a model atmosphere. Atmospheric pressure increases from left to right. Bold black lines show the mixing timescale (τ_{mix}) and the timescale for the destruction of CO (τ_{CO}, solid line) and N_2 (τ_{N_2}, dotted line). τ_{mix} is almost discontinuous where the atmosphere becomes convective (log $T \gtrsim 3.2$). Plot and rubric from Saumon et al. (2006).

3.3.2 The *J* Band

There has been very little work done on intermediate resolution spectroscopy of T dwarfs. Up till now, I am only aware of one paper that has been published in this area, that by B11. By comparing their spectrum of UGPS 0722 with molecular line lists, B11 were able to identify absorption features due to H_2O and CH_4. They have also made the first confirmed detections of NH_3 opacity in the near-infrared spectrum of a T dwarf. While B11 used the BT2 and BYTe line lists I have used in my analysis, they used an old CH_4 line list (Nassar & Bernath, 2003), supplemented by the HITRAN 2008 database (Rothman et al., 2009).

Methane

Figure 3.4 shows the *J* band spectra of UGPS 0722 and 2MASS 0415 and the corresponding CH_4 absorption cross-sections at 500 K and 750 K. The figure shows CH_4 opacity reducing with increasing wavelength over the width of the short side of the *J* band flux peak. This decrease in opacity is particularly smooth in the 750 K cross-section. On the long side of the *J* band flux peak, the opacity shown by both cross-sections increases, producing regular patterns of peaks, separated by ~0.002 μm, from ~1.30-1.33 μm. Figure 3.5 shows the region of the *J* band where CH_4 features have been identified.

B11 identified a number of blended CH_4 features on the short side of the *J* band flux peak in UGPS 0722's spectrum at 1.2390 μm, 1.2406 μm, 1.2439 μm, 1.2540 μm, 1.2578 μm, 1.2624 μm, 1.2635 μm, and 1.2661 μm. I have found absorption features at these wavelengths in the spectrum of UGPS 0722. (See Figure 3.6.[2]) However, none correspond to peaks in the CH_4 opacity. CH_4 opacity between ~1.235-1.270 μm is generally flat. While the mean CH_4 opacity is greater than the H_2O opacity in this region, in several places it is surpassed by peaks in the H_2O opacity. In fact, NH_3 is the main opacity source in this region and I find that the majority of these features can be attributed to ammonia opacity. In contrast, water is the major opacity source in the same region in the spectrum of 2MASS 0415.

---

[2] In Figure 3.6, note that "B11" indicates that B11 have identified a feature at this wavelength, while the opacity source associated with that feature is mine. This applies to all similar figures in this chapter.

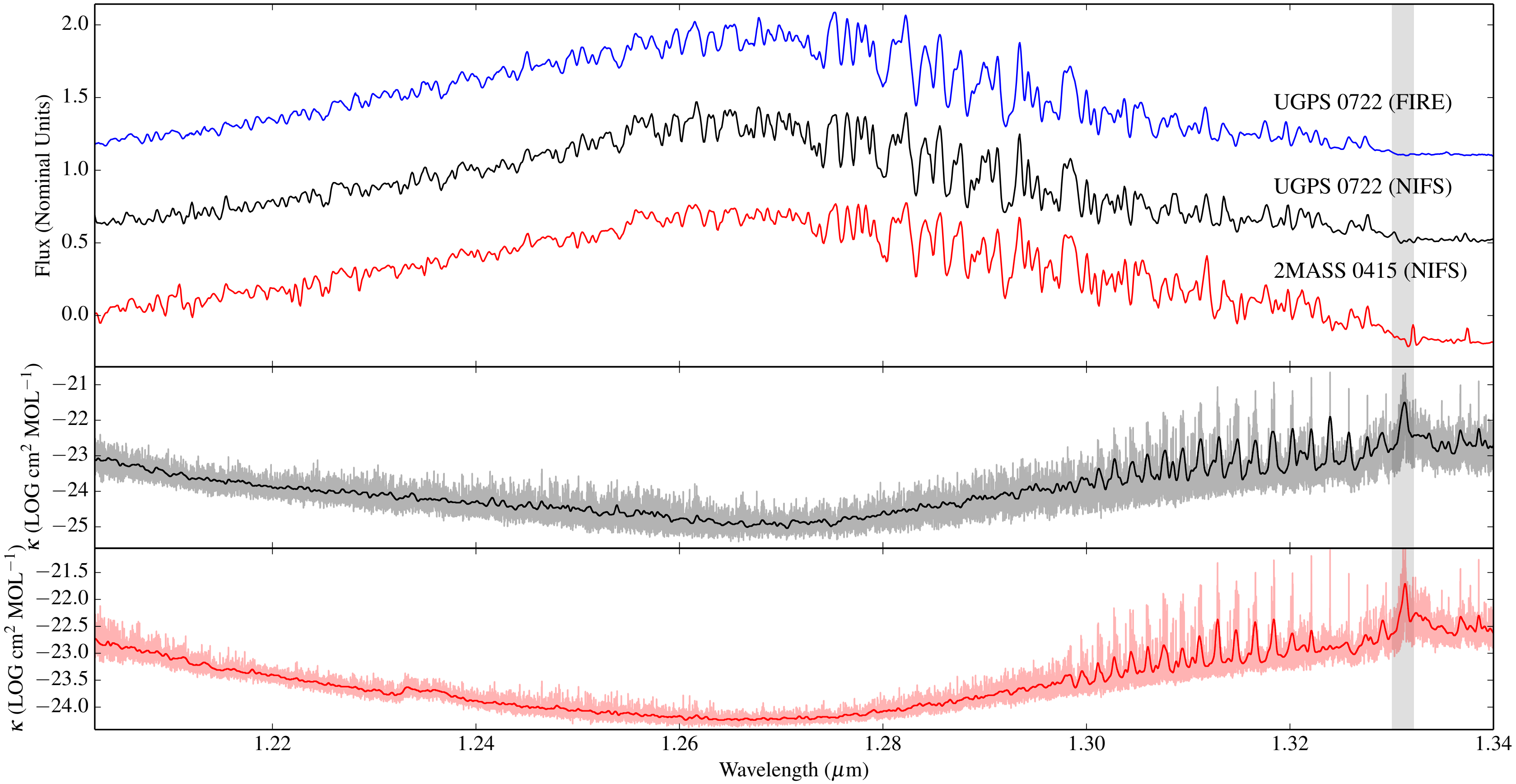

Fig. 3.4: CH$_4$ absorption in the J band spectra of 2MASS 0415 (red) and UGPS 0722 (black). The Magellan/FIRE spectrum of UGPS 0722 (blue) is shown for comparison. The middle and lower graphs show the unscaled absorption cross-sections at 500 K (black) and 750 K (red), smoothed to the same resolution as the T dwarf spectra, overplotted on the unsmoothed cross-sections. The shaded region indicates the Q-branch starting at $\sim$1.33 μm. (T dwarf spectra have been offset to aid identification of spectral features.)

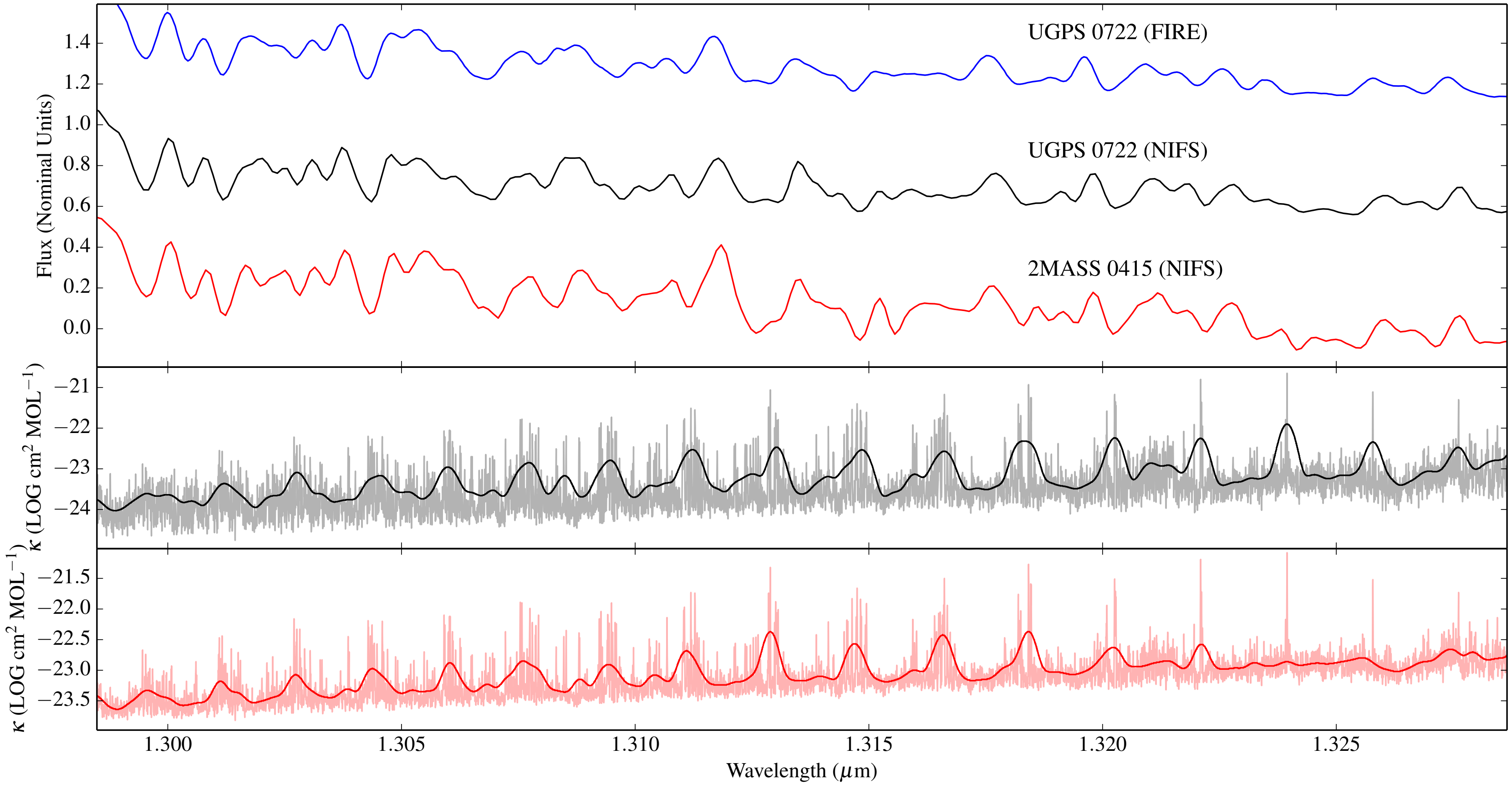

Fig. 3.5: The region of Figure 3.4 where CH_4 features have been identified.

B11 identified two possible CH_4/H_2O absorption features either side of the peak in the spectrum of UGPS 0722 at ~1.30 μm. Neither cross-section shows a peak in CH_4 opacity at these wavelengths. I have determined that the feature at 1.2994 μm is due to water opacity, and that at 1.3003 μm is produced by a combination of water and ammonia opacity. B11 were more confident in identifying two more CH_4/H_2O absorption features at 1.3043 μm and at 1.3067 μm. While there is a peak in the CH_4 opacity at 1.3043 μm, I find that water is again the major opacity source at this wavelength. There is no corresponding peak in the CH_4 opacity at 1.3067 μm and I conclude that this is another water feature. A blended CH_4/H_2O absorption feature at 1.3097 μm is consistent with a peak in the CH_4 opacity, and a much stronger peak in water opacity. A CH_4 feature identified by B11 at 1.3112 μm is consistent with methane as the main source of opacity. Opacities calculated using the 10to10 line list show that three CH_4 features at 1.3124 μm, 1.3148 μm, and 1.3202 μm are actually H_2O/CH_4 blends, while a CH_4/H_2O blend at 1.3183 μm is a "pure" methane feature. I can confirm the methane line at 1.3221 μm. A previously identified CH_4 feature at 1.3284 μm appears to be another blend.

While the 10to10 line list has enabled me to correct previous mis-identifications of spectral features, it has also allowed me to identify new CH_4 features at 1.3129 μm and 1.3166 μm. I have also identified a new H_2O/CH_4 blend at 1.3027 μm. See Figures 3.7, 3.8, and Table 3.4.

These are late T dwarfs, and I would expect CH_4 absorption features to be prominent in both objects' spectra. However, in places the methane absorption in the T9 is deeper and/or broader than in the T8. For example, the absorption features at ~1.3183 μm, 1.3202 μm and 1.3239 μm.

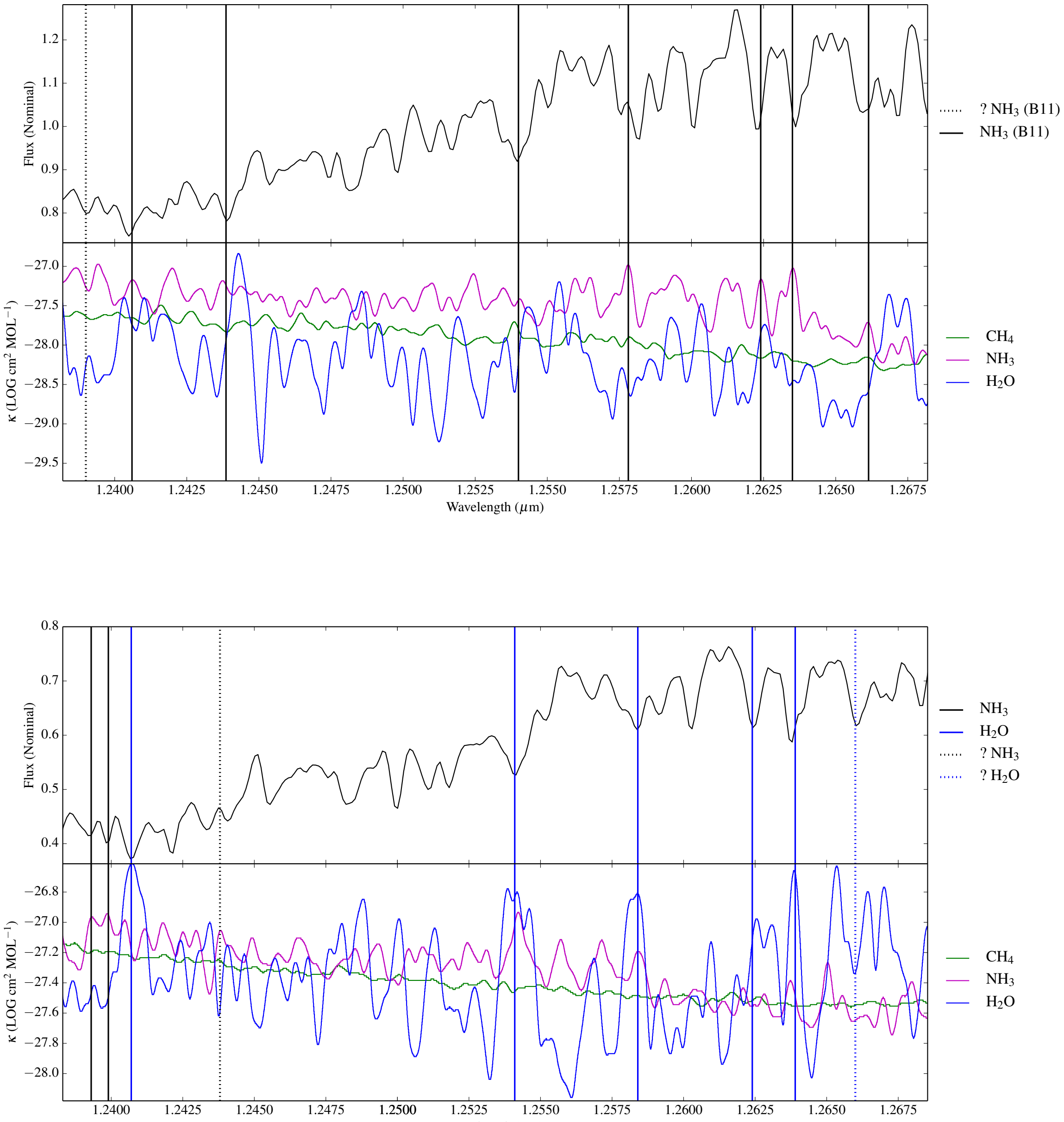

Fig. 3.6: **Top.** The black lines identify the features detected by B11 as CH_4 blends on the short side of the *J* band flux peak in the spectrum of UGPS 0722. Most of the features appear to be due to ammonia opacity. The lower graph shows the log of the scaled absorption cross-sections at 500 K for CH_4 (green), H_2O (blue) and NH_3 (mauve), smoothed to the same resolution as the T dwarf spectrum. By scaled, I mean that the cross-sections have been corrected for the relative molecular abundances expected for each molecule according to Figure 3 in Saumon et al. (2006). **Bottom.** The same region in the spectrum of 2MASS 0415. Scaled opacity cross-sections have been made at 750 K. While there appear to be NH_3 features at 1.2393 μm and 1.2439 μm, the dominant opacity source is H_2O. Note that the opacity sources associated with the absorption features identified by B11 have been made by me. This designation of opacity sources applies to all similar figures in this chapter.

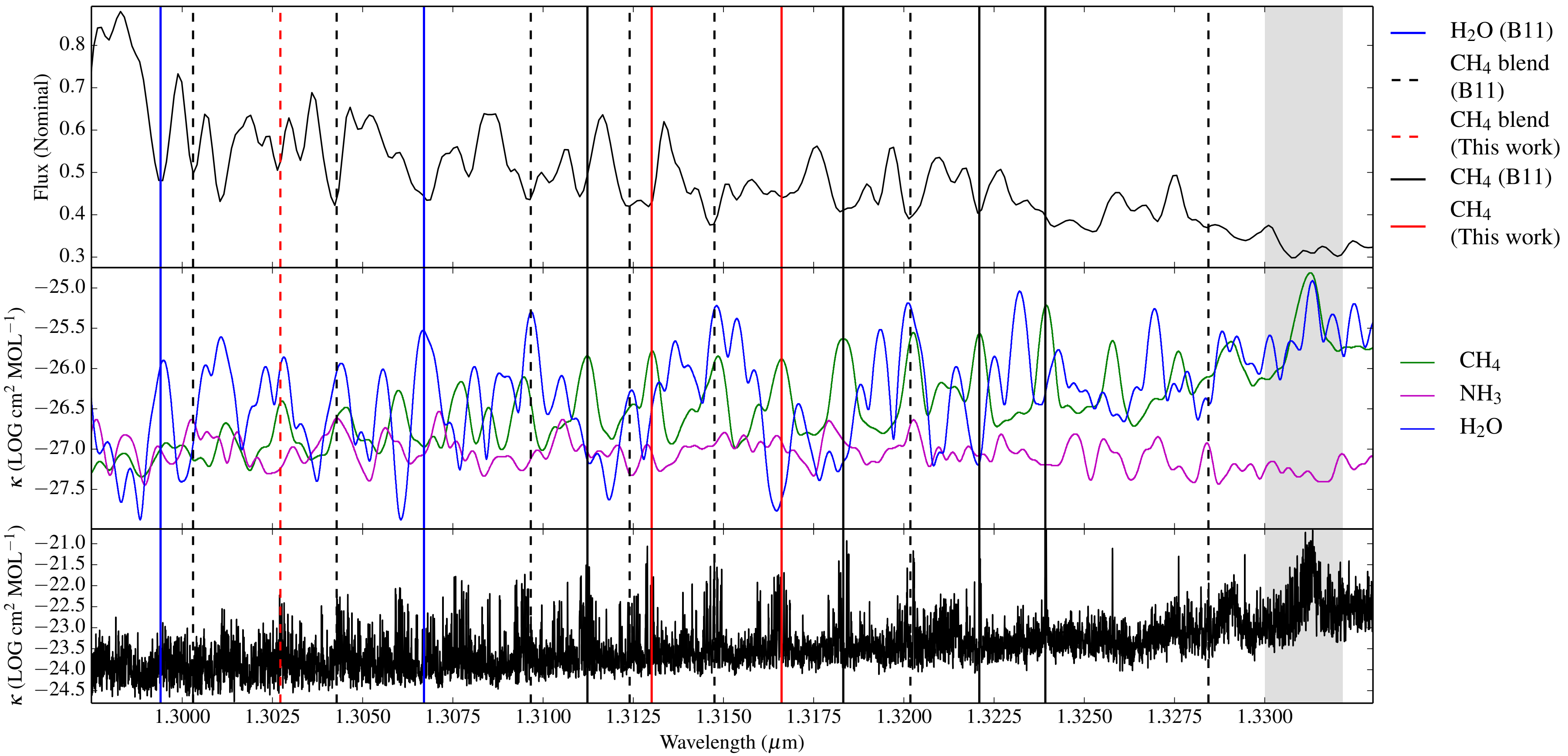

Fig. 3.7: CH$_4$ absorption features on the long side of the *J* band flux peak in the spectrum of UGPS 0722. Solid blue lines indicate H$_2$O features previously identified as mixed CH$_4$ features. Solid black lines are CH$_4$ features identified in B11. Solid red lines are CH$_4$ features identified in this work. Dashed black lines are mixed CH$_4$ features identified in B11. The dashed red line is a mixed CH$_4$ feature identified in this work. The middle graph shows the log of the absorption cross-sections at 500 K for CH$_4$ (green), H$_2$O (blue) and NH$_3$ (mauve), scaled by molecular abundances and smoothed to the same resolution as the T dwarf spectrum. The lower graph shows the log of the unscaled, unsmoothed CH$_4$ cross-sections at 500 K. The unsmoothed cross-sections make it clear that absorption features are produced by a blend of individual transition lines.

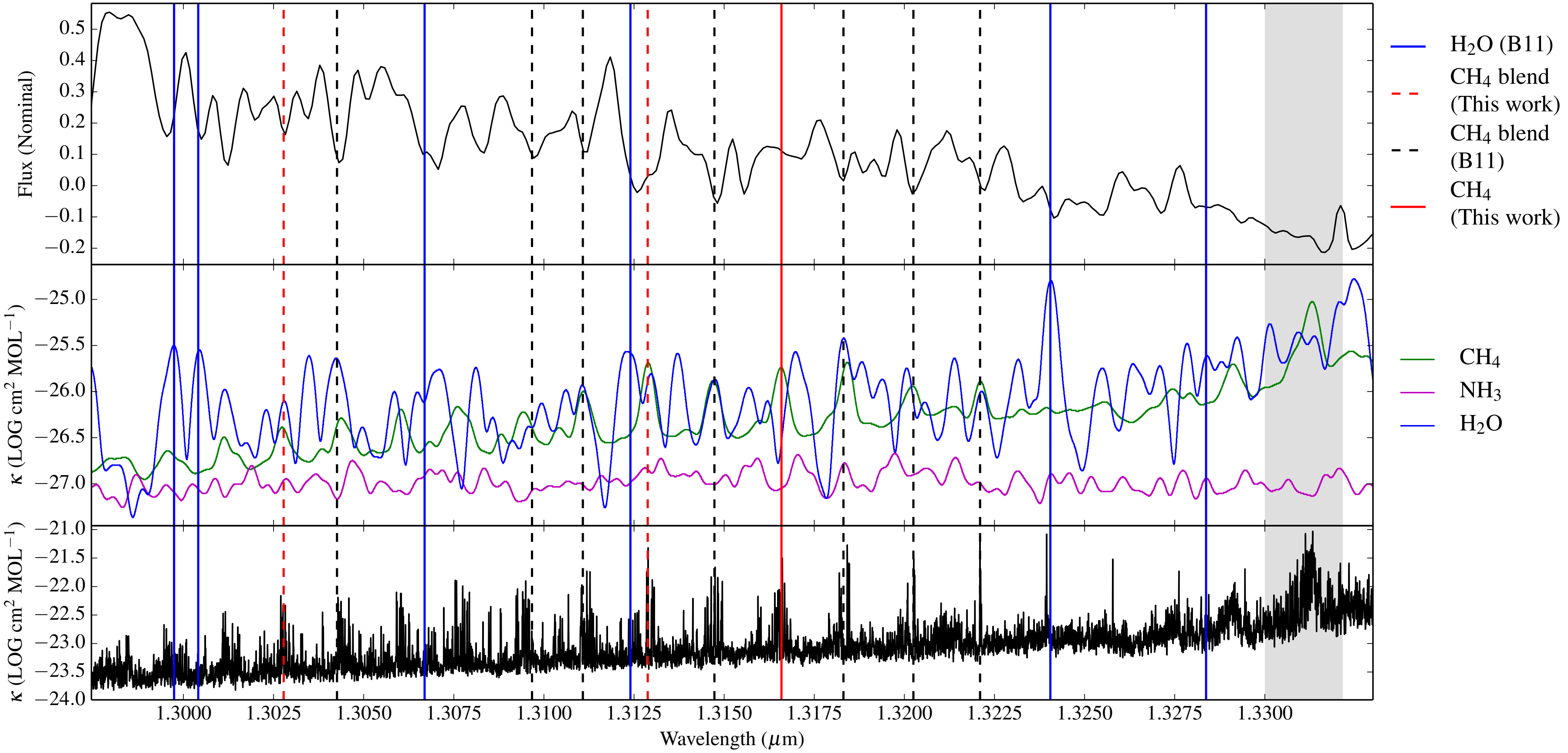

Fig. 3.8: CH_4 absorption features on the long side of the *J* band flux peak in the spectrum of 2MASS 0415. Scaled absorption cross-sections calculated at 750 K. Features are as those described in Figure 3.7.

Table 3.4: CH_4 Absorption Features in the *J* Band Spectra of Late T Dwarfs

Source	λ (μm)	Opacity Source (B11)	Opacity Source (500 K/750 K)	Absorption feature in UGPS 0722	Absorption feature in 2MASS 0415
B11	1.2994	CH_4(?)/H_2O	H_2O/H_2O	Yes	Yes
B11	1.3003	CH_4(?)/H_2O	(NH_3/H_2O)/H_2O	Yes	Yes
This work	1.3027	—	(H_2O/CH_4)/(H_2O/CH_4)	Yes	Yes
B11	1.3043	CH_4/H_2O	(H_2O/CH_4/NH_3)/(H_2O/CH_4)	Yes	Yes
B11	1.3067	CH_4/H_2O	H_2O/H_2O	Yes	Yes
B11	1.3097	CH_4/H_2O	(H_2O/CH_4)/(H_2O/CH_4)	Yes	Yes
B11	1.3112	CH_4	CH_4/(H_2O/CH_4)	Yes	Yes
B11	1.3124	CH_4	(H_2O/CH_4)/H_2O	Yes	Yes
This work	1.3129	—	CH_4/(CH_4/H_2O)	Yes	Yes
B11	1.3148	CH_4	(H_2O/CH_4)/(H_2O/CH_4)	Yes	Yes
This work	1.3166	—	CH_4/CH_4	Yes	Yes
B11	1.3183	CH_4/H_2O	CH_4/(H_2O/CH_4)	Yes	Yes
B11	1.3202	CH_4	(H_2O/CH_4/NH_3)/(H_2O/CH_4)	Yes	Yes
B11	1.3221	CH_4	CH_4/(CH_4/H_2O)	Yes	Yes
B11	1.3239	CH_4/H_2O	CH_4/H_2O	Yes	Yes
B11	1.3284	CH_4	(CH_4/H_2O/NH_3)/H_2O	Yes	Yes

In tables 3.4, 3.6, and 3.8, methane features produced by R-, Q-, and P-branch line transitions are highlighted in red, grey, and blue respectively. Non-shaded regions are features produced by other opacity sources, which had previously been identified as due to methane or methane blends.

Figures 3.9 shows the rotation-vibration *J* band spectrum of CH_4 made at 500 K. Table A.1 shows the final state quantum numbers of the ro-vibrational transitions responsible for the *J* band absorption features. While only the strongest transitions are shown, each absorption feature is produced by a number of individual transitions. Γ is the symmetry, J is the rotational (angular momentum) quantum number, ν_1, ν_2, ν_3, and ν_4, the normal mode vibrational quantum numbers, L2, L3, and L4, are the vibrational angular momenta and M_i (i=3,4, $M_i \leq L_i$) a multiplicity index which counts the states within a given vibrational mode. L and M are required to resolve the degeneracy of the ν_2, ν_3 and ν_4 states (Yurchenko & Tennyson, 2014).

It can be seen that the transitions are all R-branch transitions, and belong to the $\nu_2 + 2\nu_3$ vibrational bands.

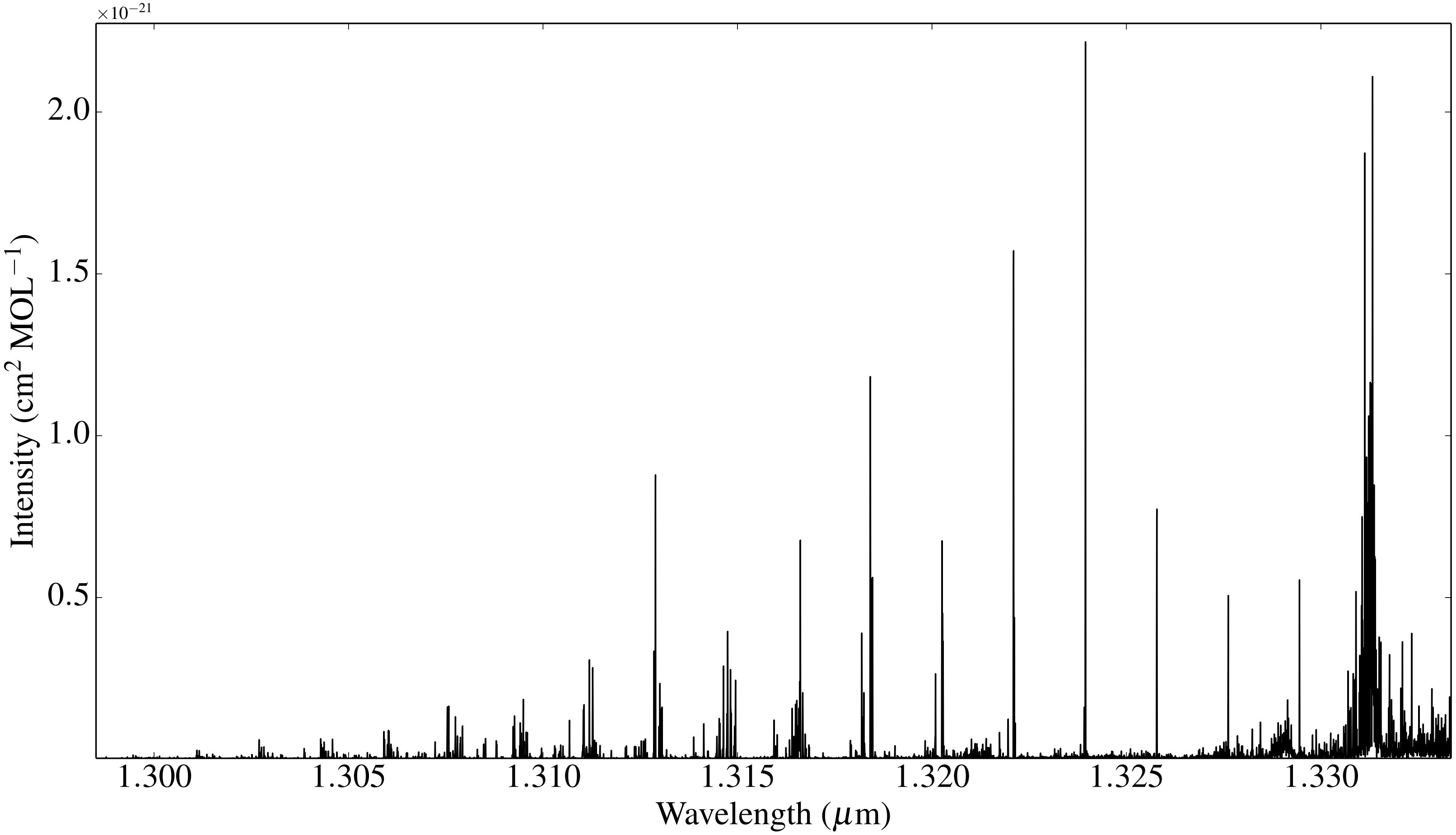

Fig. 3.9: The rotation-vibration J band spectrum of CH_4 made at 500 K.

Ammonia

The scaled opacity cross-sections at 500 K show peaks in the NH_3 opacity between ~1.210 μm and ~1.276 μm. I compared these cross-sections with the S12 synthetic spectra at 500 K and identified a number of features. These results and the results for 2MASS 0415 are summarised in Figures 3.10, 3.11, and Table 3.5.

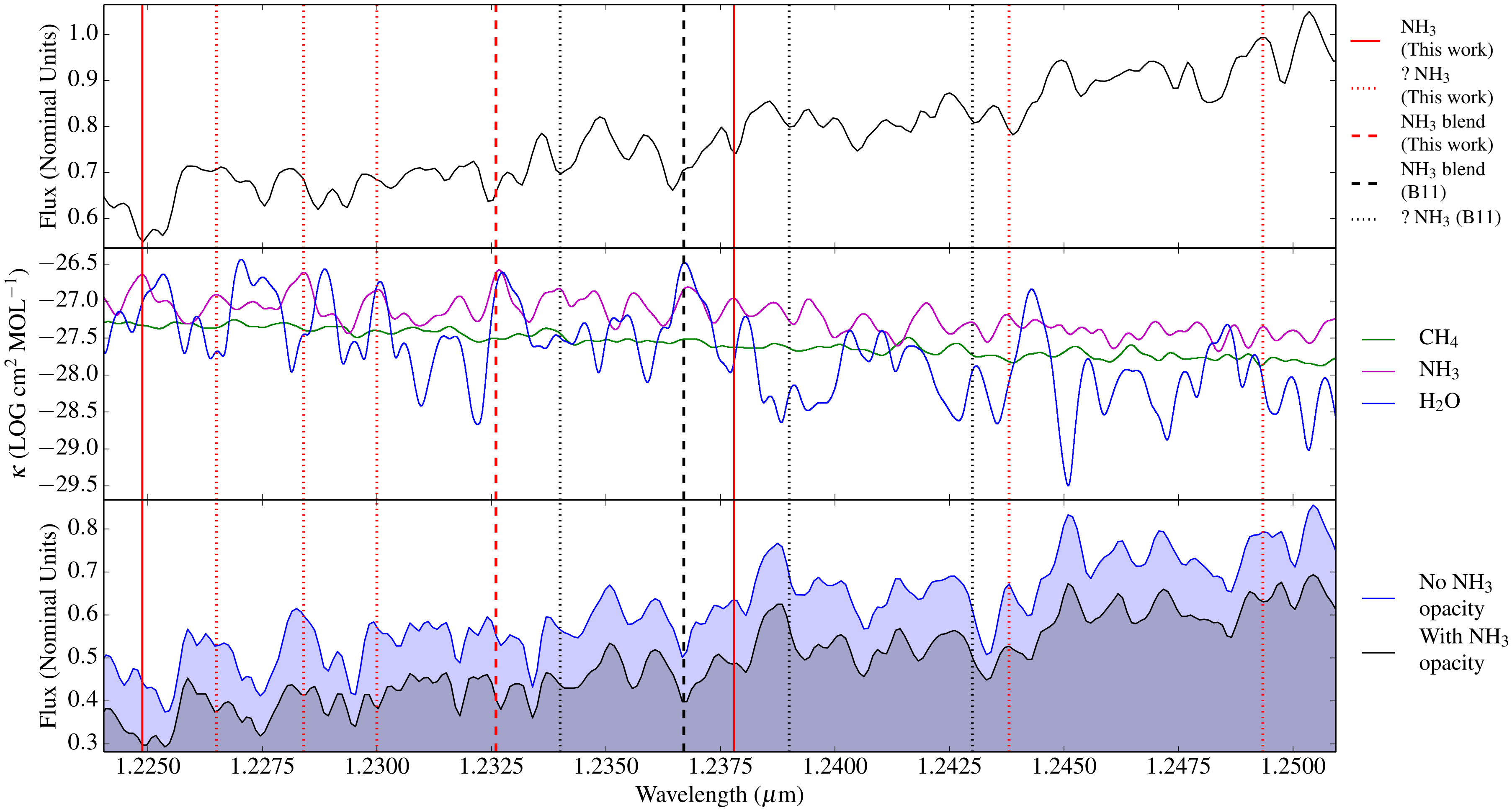

Fig. 3.10: NH$_3$ absorption in the *J* band spectrum of UGPS 0722. Absorption cross-sections, scaled for molecular abundances, are calculated at 500 K for CH$_4$ (green), H$_2$O (blue) and NH$_3$ (mauve). The lower graph contains S12 synthetic spectra with NH$_3$ opacity (dark shade) and without NH$_3$ opacity (light shade), also calculated at 500 K. Solid red lines are NH$_3$ features identified in this work. The dashed red line is an NH$_3$/H$_2$O feature identified in this work. Dotted red lines are features which are predicted by the scaled opacity cross-sections and the S12 models but which are either missing or ambiguous. The dotted black lines are features identified by B11, which coincide with peaks in the NH$_3$ opacity, but where the S12 models are ambiguous.

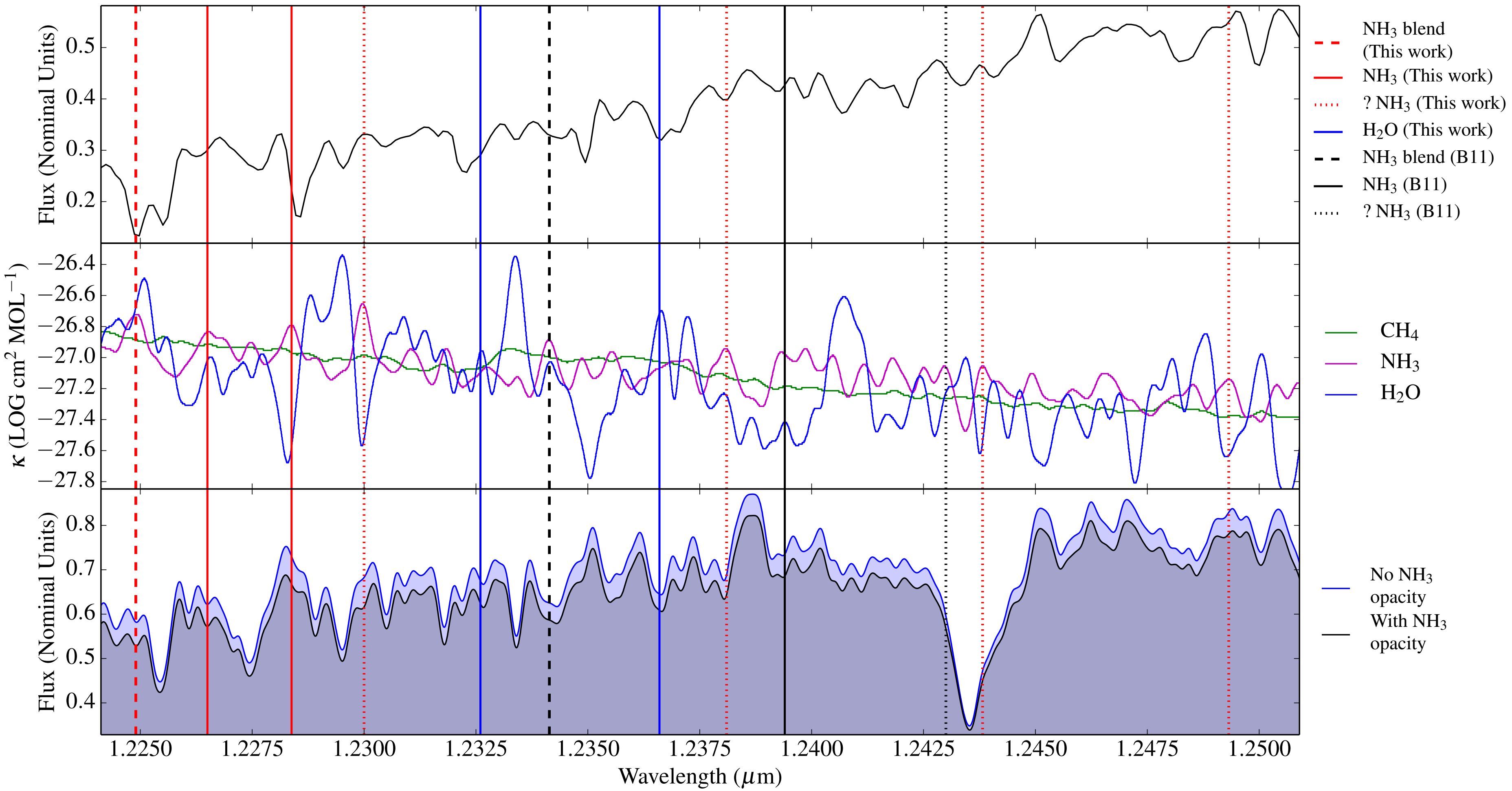

Fig. 3.11: NH_3 absorption features in the J band spectrum of 2MASS 0415. Features are as described in the J band spectrum of UGPS 0722. The solid blue lines are pure H_2O features which were NH_3/H_2O blends in the spectrum of UGPS 0722.

Table 3.5: NH_3 Absorption Features in the *J* Band Spectra of Late T Dwarfs

Source	λ (μm)	Opacity Source (500 K/750 K)	NH_3 feature in synthetic spectrum (500 K/750 K)	Absorption feature in UGPS 0722	Absorption feature in 2MASS 0415
This work	1.2249	NH_3/(H_2O/NH_3)	Yes/No	Yes	Yes
This work	1.2265	NH_3/NH_3	Yes/No	Yes(?)	Yes
This work	1.2284	NH_3/NH_3	Yes/Yes	Yes(?)	Yes
This work	1.2300	(H_2O/NH_3)/NH_3	Yes/Yes	Yes(?)	No
This work	1.2326	(NH_3/H_2O)/H_2O	No(?)/No	Yes	Yes
B11	1.2340	NH_3/(NH_3/H_2O)	No(?)/No	Yes	Yes
B11	1.2367	(H_2O/NH_3)/H_2O	No/No	Yes	Yes
This work	1.2378	NH_3/NH_3	Yes/No	Yes	Yes
B11	1.2390	NH_3/NH_3	No/No	Yes	Yes
B11	1.2430	NH_3/NH_3	No(?)/No	Yes	Yes(?)
This work	1.2438	NH_3/NH_3	Yes/No	Yes	No(?)
This work	1.2494	NH_3/NH_3	Yes/No	No	Yes(?)

In tables 3.5, 3.7, and 3.9, ammonia features produced by R-, Q-, and P-branch line transitions are highlighted in red, grey, and blue respectively.

B11 found isolated NH_3 features at 1.2340 μm and 1.2430 μm in the FIRE spectrum of UGPS 0722. There are peaks in the NH_3 absorption cross-sections at these wavelengths, corresponding to absorption features in my spectrum of UGPS 0722. There are no well-defined differences in the synthetic spectra with and without NH_3 opacity at these wavelengths. It may be that there are ammonia features at 1.2340 μm and 1.2430 μm which the model spectra are unable to identify. At the moment, these features are unconfirmed. B11 identified an NH_3/H_2O feature at 1.2367 μm. I find that this feature is an H_2O/NH_3 feature. B11 identified a feature at 1.2438 μm as an H_2O/CH_4 blend. There is a peak in the NH_3 opacity at this wavelength, corresponding to an absorption feature in the spectrum of UGPS 0722. However, the S12 model spectra show no absorption feature at this location. While I believe this feature is most likely an NH_3 feature, it remains unconfirmed.

The ro-vibrational transitions responsible for the NH_3 absorption features in the J band spectra of the two T dwarfs are P-branch transitions, with the exception of a relatively weak Q-branch transition line in the feature at 1.2284 μm, and a relatively strong R-branch transition line in the feature at 1.2494 μm. Contrast this with the ro-vibrational transition lines responsible for the CH_4 absorption features in the J band, which are all R-branch transition lines. Here, the shorter wavelength P-branch transitions arise from the $\nu_1+3\nu_4$ vibrational bands, while the longer wavelength P-branch transition lines, and the single Q-branch transition line, are from the $\nu_1+\nu_3+\nu_4$ vibrational bands. The single R-branch transition line is from the $\nu_2+2\nu_3$ vibrational bands. These results are shown in Figure 3.12 and Table B.1.

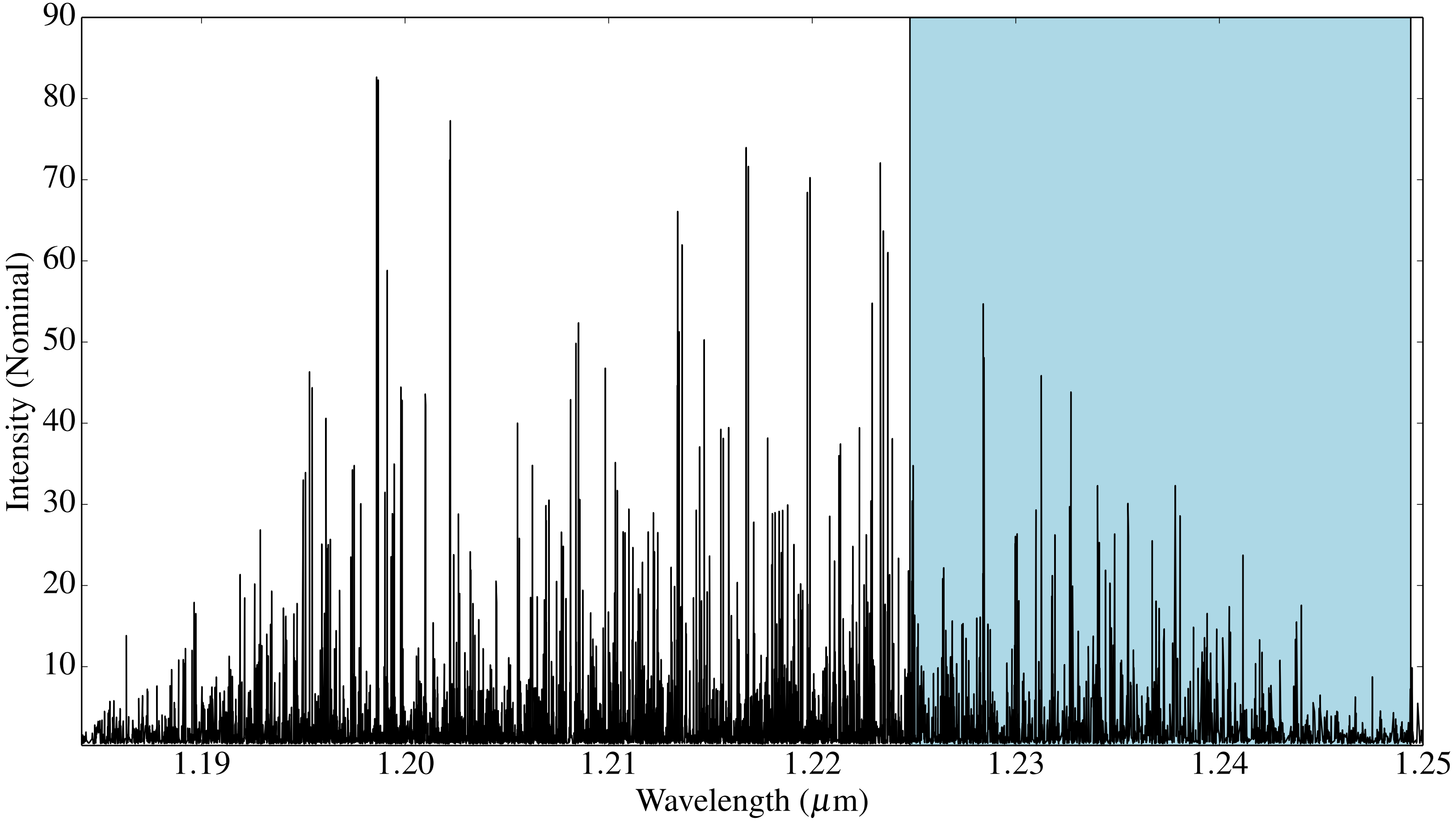

Fig. 3.12: The NH$_3$ J band ro-vibrational spectrum at 500 K. The blue shaded region defines the P-branch transition lines responsible for the J band absorption features.

3.3.3 The *H* Band

Methane

The CH_4 absorption cross-sections at 500 K and 750 K show CH_4 opacity reaching a maximum on the long side of the *H* band flux peak, producing regular patterns of peaks, separated by ∼0.002 μm, from ∼1.61-1.70 μm. The spectrum has a strong Q-branch composed of many transitions (see Figures 3.13 and 3.14). A comparison of the observed and modelled spectral energy distributions (SEDs) of three T7.5-8 dwarfs (Saumon et al. 2006; Saumon et al. 2007), ascribed a divergence in the model SEDs at 1.6-1.7 μm to an incomplete CH_4 line list. I expect that this discrepancy will be resolved with the inclusion of the 10to10 line list in model spectra.

B11 identified CH_4 absorption features at 1.6145 μm, 1.6170 μm, 1.6191 μm, 1.6214 μm, and 1.6259 μm. While CH_4 is the dominant opacity source in this wavelength range, the absorption cross-sections at 500 K show no peaks in the CH_4 opacity corresponding to these wavelengths. The same is true for the CH_4 absorption cross-sections made at 750 K, apart from the feature at 1.6259 μm. However, the absorption features in the T dwarfs' spectra in this wavelength region are a clear extension of the pattern in absorption features at longer wavelengths in the data, and are only very slightly off-set from peaks in the CH_4 opacity. I suspect that these are methane features, and the failure of the peaks in the CH_4 opacity to correspond with these features may be a deficiency in the 10to10 list. The authors of the 10to10 line list are aware of this discrepancy and are examining the line list for any artefacts which may be responsible (S. Yurchenko and J. Tennyson, private comm.).

B11 did not identify CH_4 absorption features longward of 1.6354 μm. I have identified numerous CH_4 absorption features either side of the CH_4 Q-branch starting at ∼1.6650 μm. (See Figures 3.15, 3.16, and Table 3.6). In this region of the *H* band, the CH_4 absorption cross-sections are ∼2 magnitudes stronger than other opacity sources, and all the features I have identified are "pure" CH_4 absorption features.

While all the *J* band absorption features I observed are from the R-branch, *H* band absorption features in both T dwarfs are produced by ro-vibrational transitions in the R-, P-, and Q-branches. I did not identify isolated Q-branch absorption features. Instead, I note that the cluster of transition lines forming the Q-branch corresponds to broad absorption troughs in the T dwarfs' spectra between ~1.6651-1.6682 μm. These and the identified absorption features in 2MASS 0415 and UGPS 0722 belong to the $2\nu_3$ vibrational band. While the features at 1.6976 μm and 1.7010 μm are largely due to P-branch transitions, each feature does contain an R-branch transition line. The R-branch lines have a similar intensity to the P-branch transition lines and belong to the $\nu_2+\nu_3+\nu_4$ vibrational bands (1.6976 μm) and $\nu_1+\nu_3$ vibrational bands (1.7010 μm). I consider it likely that these two lines are outlying members of the next set of R-branch transition lines.

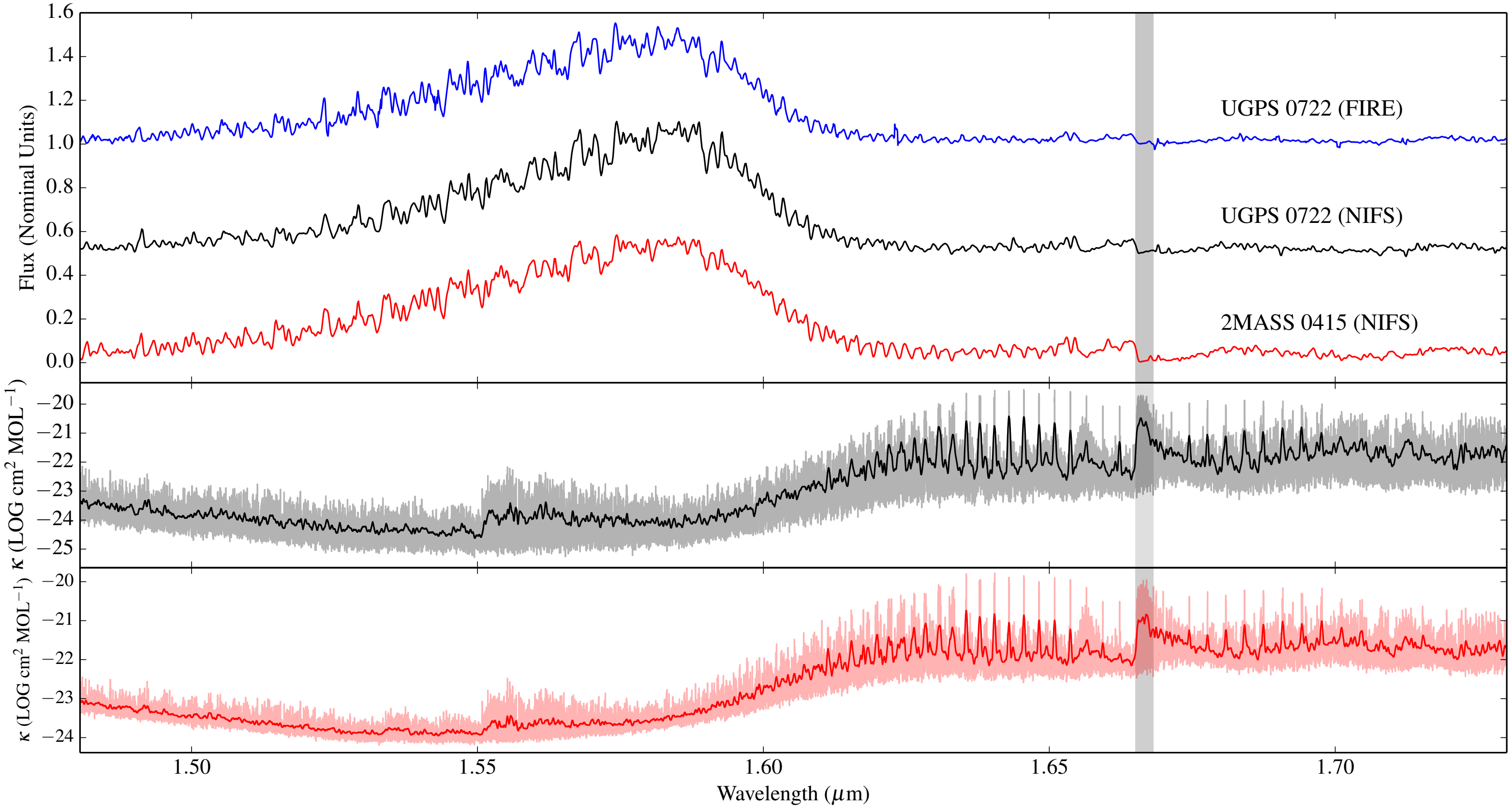

Fig. 3.13: CH_4 absorption in the *H* band spectra of 2MASS 0415 (red), UGPS 0722 (black), and the Magellan/FIRE spectrum of UGPS 0722 (blue). The shaded region indicates the Q-branch starting at $\sim$1.665 μm. The centre and lower graphs contains the cross-sections as described in Figure 3.4. (T dwarf spectra have been offset to aid identification of spectral features.)

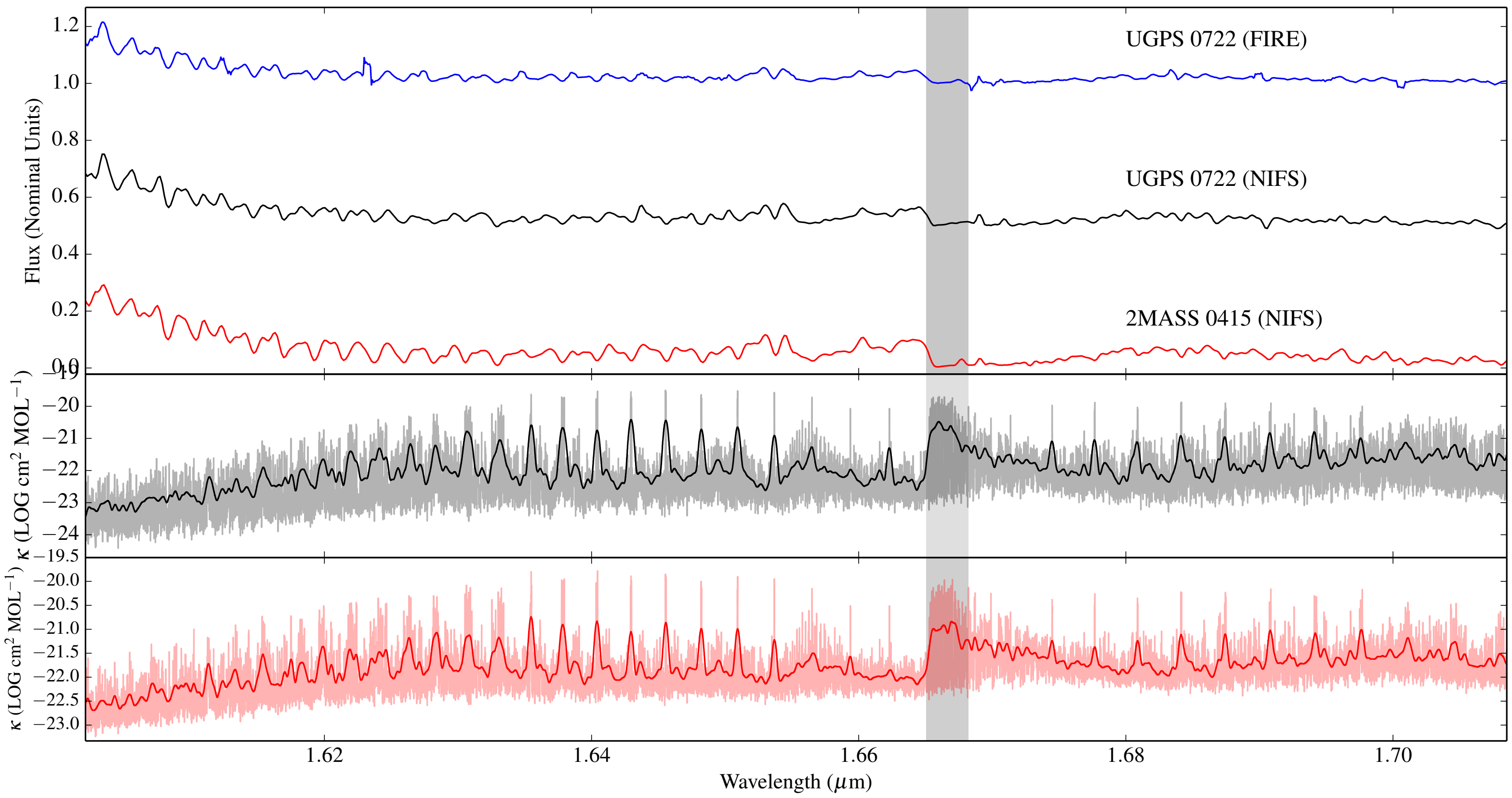

Fig. 3.14: The region of Figure 3.13 where CH$_4$ features have been identified.

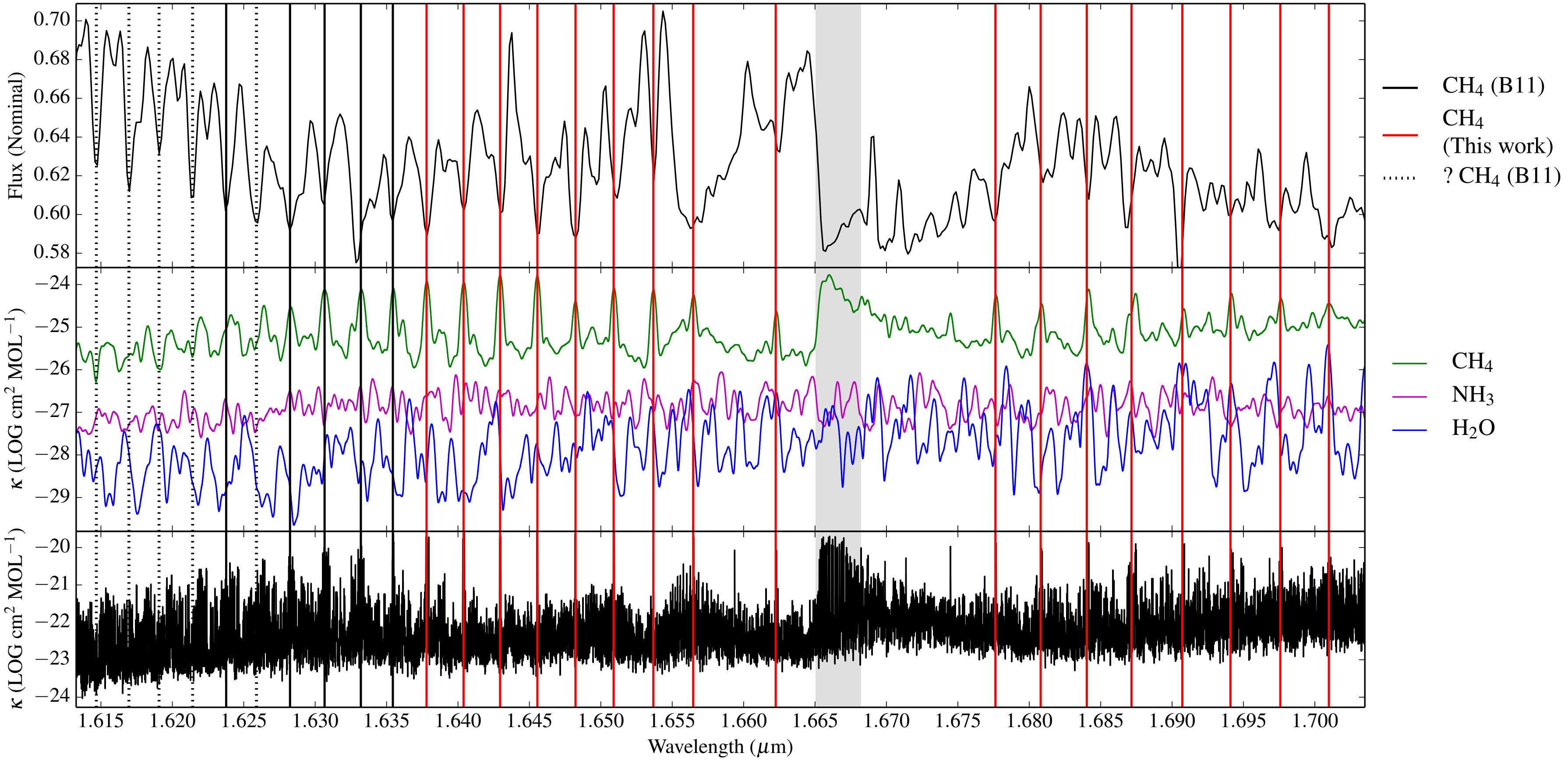

Fig. 3.15: CH_4 absorption features in the H band spectrum of UGPS 0722. A large number of new methane features are detected (red lines) and several previously identified features are recovered (solid black lines). The black dotted lines are the locations of features which B11 identified as CH_4 absorption features but which do not correspond to peaks in CH_4 opacity. Otherwise, features are as described in Figure 3.7.

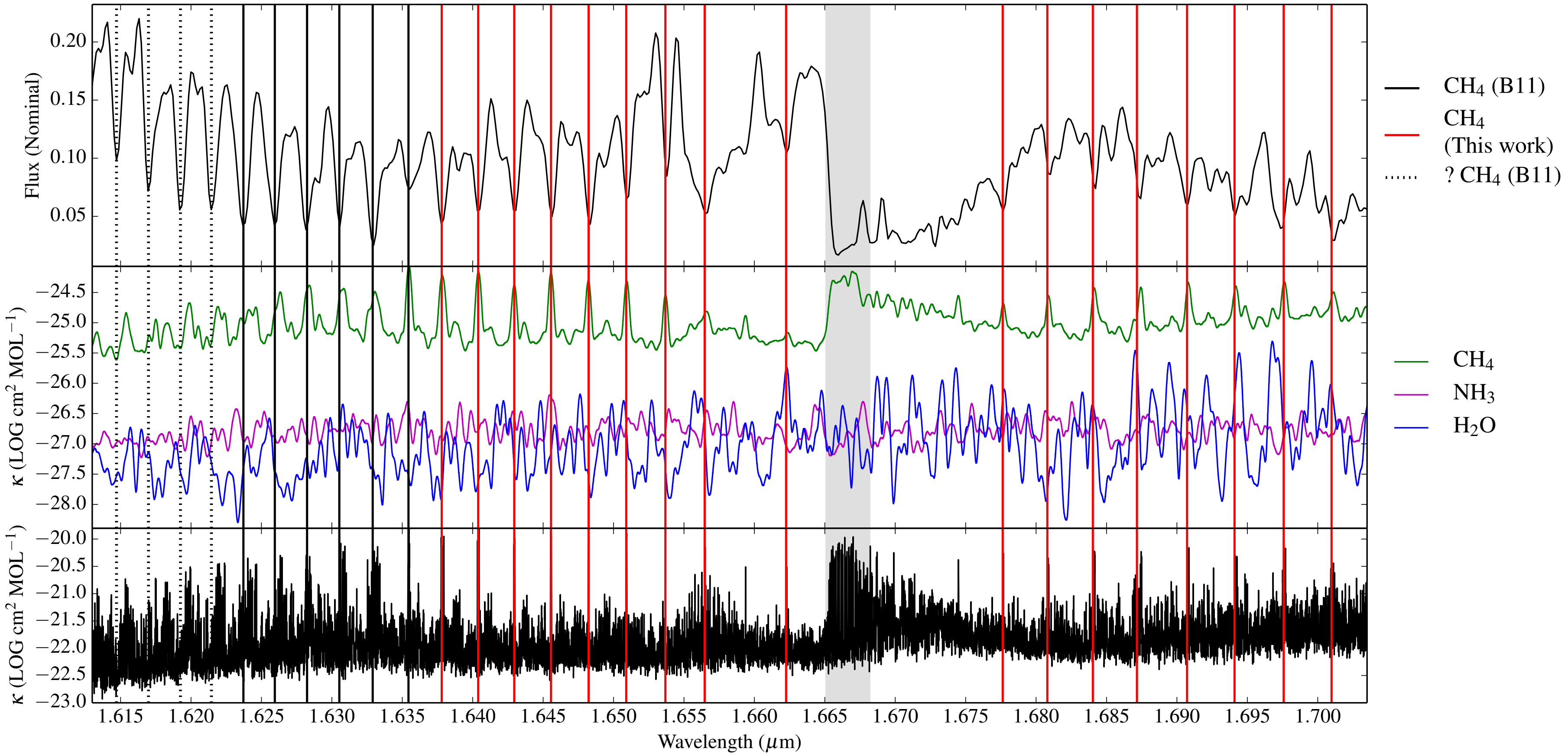

Fig. 3.16: CH$_4$ absorption features in the *H* band spectrum of 2MASS 0415.

Table 3.6: CH_4 Absorption Features in the *H* Band Spectra of Late T Dwarfs

Source	λ (μm)	Opacity Source (B11)	Opacity Source (500 K/750 K)	Absorption feature in UGPS 0722	Absorption feature in 2MASS 0415
B11	1.6145	CH_4	CH_4(?)/CH_4(?)	Yes	Yes
B11	1.6170	CH_4	CH_4(?)/CH_4(?)	Yes	Yes
B11	1.6191	CH_4	CH_4(?)/CH_4(?)	Yes	Yes
B11	1.6214	CH_4	CH_4(?)/CH_4(?)	Yes	Yes
B11	1.6236	CH_4	CH_4/CH_4	Yes	Yes
B11	1.6259	CH_4	CH_4(?)/CH_4	Yes	Yes
B11	1.6282	CH_4	CH_4/CH_4	Yes	Yes
B11	1.6307	CH_4	CH_4/CH_4	Yes	Yes
B11	1.6332	CH_4	CH_4/CH_4	Yes	Yes
B11	1.6354	CH_4	CH_4/CH_4	Yes	Yes
This work	1.6378	—	CH_4/CH_4	Yes	Yes
This work	1.6404	—	CH_4/CH_4	Yes	Yes
This work	1.6430	—	CH_4/CH_4	Yes	Yes
This work	1.6456	—	CH_4/CH_4	Yes	Yes
This work	1.6482	—	CH_4/CH_4	Yes	Yes
This work	1.6509	—	CH_4/CH_4	Yes	Yes
This work	1.6537	—	CH_4/CH_4	Yes	Yes
This work	1.6565	—	CH_4/CH_4	Yes	Yes
This work	1.6623	—	CH_4/CH_4	Yes	Yes
This work	$\sim$(1.6651$\rightarrow$1.6682)	—	CH_4/CH_4	Yes	Yes
This work	1.6776	—	CH_4/CH_4	Yes	Yes
This work	1.6808	—	CH_4/CH_4	Yes	Yes
This work	1.6840	—	CH_4/CH_4	Yes	Yes
This work	1.6874	—	CH_4/CH_4	Yes	Yes
This work	1.6907	—	CH_4/CH_4	Yes	Yes
This work	1.6941	—	CH_4/CH_4	Yes	Yes
This work	1.6976	—	CH_4/CH_4	Yes	Yes
This work	1.7010	—	CH_4/CH_4	Yes	Yes

Figure 3.17 is the absorption cross-section at 500 K.

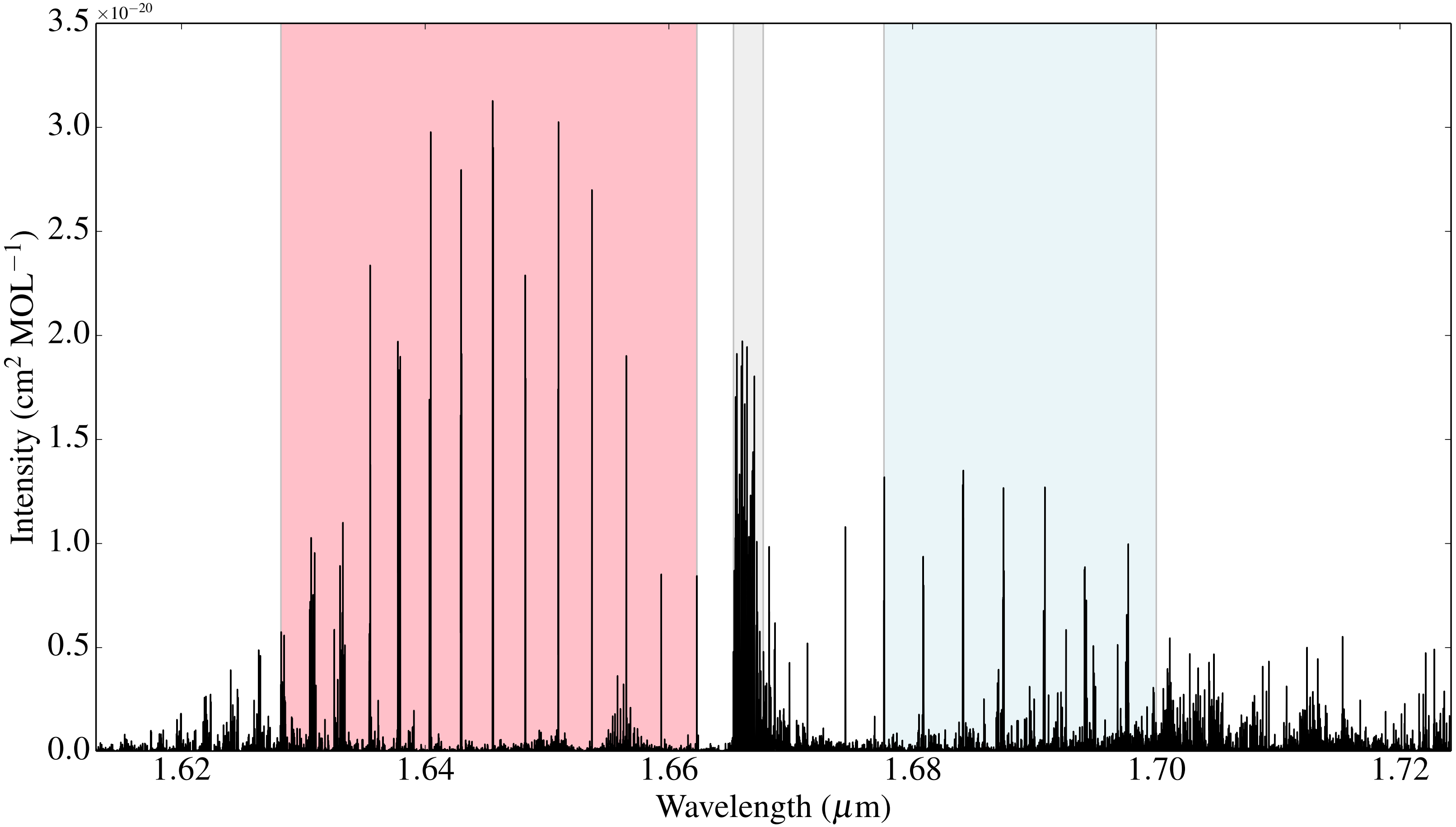

Fig. 3.17: The ro-vibrational *H* band spectrum of CH_4 made at 500 K. Shaded regions indicate R-branch (red), Q-branch (grey), and P-branch (blue) transitions.

Ammonia

Figure 5 in Cushing et al. (2011) shows that NH_3 is the dominant source of opacity across the blue wing of the *H* band (1.50-1.59 μm) in T dwarfs with $T_{eff} \leq 600$ K. I also find that this is the case. In contrast, CH_4 is by an order of two magnitudes the dominant opacity source on the red slope of the *H* band peak flux. At 750 K, the NH_3 and H_2O scaled absorption cross-sections from $\sim 1.5140-1.550 \mu$m are of the same order of magnitude ($\kappa \sim 10^{-26}$ cm^2 MOL^{-1}). Therefore, some features that were produced by NH_3 only in the spectrum of UGPS 0722 ($T_{eff} \sim 500$ K), are produced by a combination of ammonia and water opacities in the spectrum of 2MASS 0415 ($T_{eff} \sim 750$ K). These results are summarised in Figures 3.18, 3.19 and Table 3.7.

B11 observed a number of “pure” NH_3 absorption features in the *H* band spectrum of UGPS 0722. Of these, the feature at 1.5140 μm corresponds to a peak in both NH_3 and H_2O opacity. The strengths of the opacities are broadly similar. There is no significant difference in the model spectra computed with and without NH_3 opacity, other than a small change in amplitude. Therefore, I conclude that this feature is most likely an ammonia/water blend. The feature at 1.5152 μm corresponds to a peak in NH_3 opacity and absorption features in UGPS 0722 and 2MASS 0415. There appears to be a difference in opacity between the model spectrum computed at 500 K but not that computed at 750 K, other than in amplitude. I confirm that this NH_3 absorption feature is due entirely to NH_3 in the spectrum of UGPS 0722, but is an H_2O/NH_3 feature in 2MASS 0415. The features at 1.5260 μm and 1.5270 μm correspond to peaks in NH_3 opacity. However, there is no clear difference between the S12 model spectra with and without NH_3 opacity. I therefore cannot confirm the presence of these features. The feature at 1.5282 μm corresponds to a peak in NH_3 opacity and to a clear difference between the S12 model spectra computed at 500 K. The model spectra show that without NH_3 opacity a rather strong peak would be expected at 1.5282 μm while only a small one is present. Indeed, the spectrum of UGPS 0722 at this wavelength does look similar to the model spectrum with NH_3 opacity computed at 500 K. The spectrum of 2MASS 0415 at this wavelength looks similar to UGPS

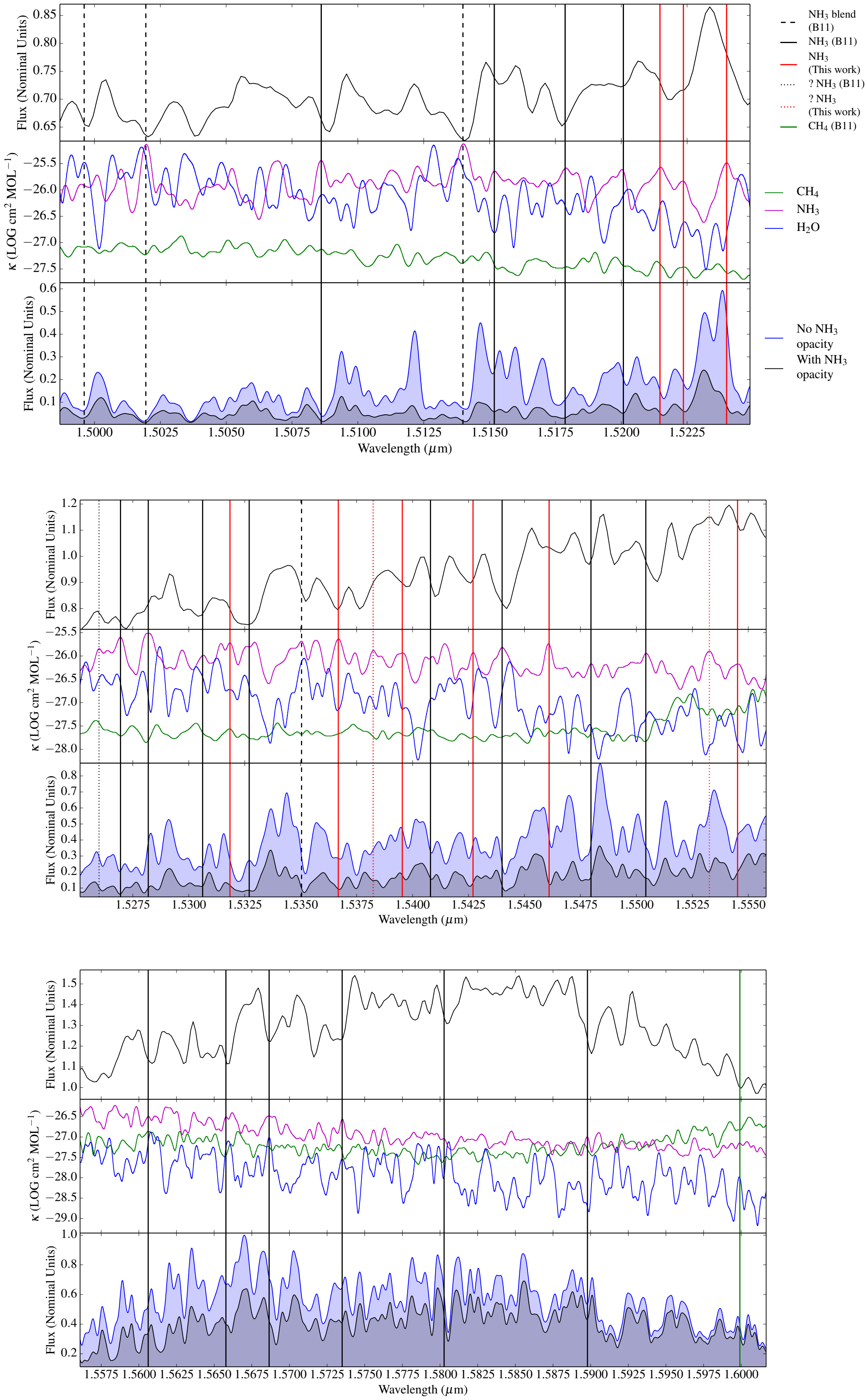

Fig. 3.18: NH_3 absorption features in the *H* band spectrum of UGPS 0722. Scaled absorption cross-sections are calculated at 500 K for CH_4 (green), H_2O (blue) and NH_3 (mauve). Features are as described in Figure 3.10. Dashed lines are features produced by a combination of molecular species. The dotted lines are NH_3 features predicted by the S12 models, but missing or ambiguous in the data.

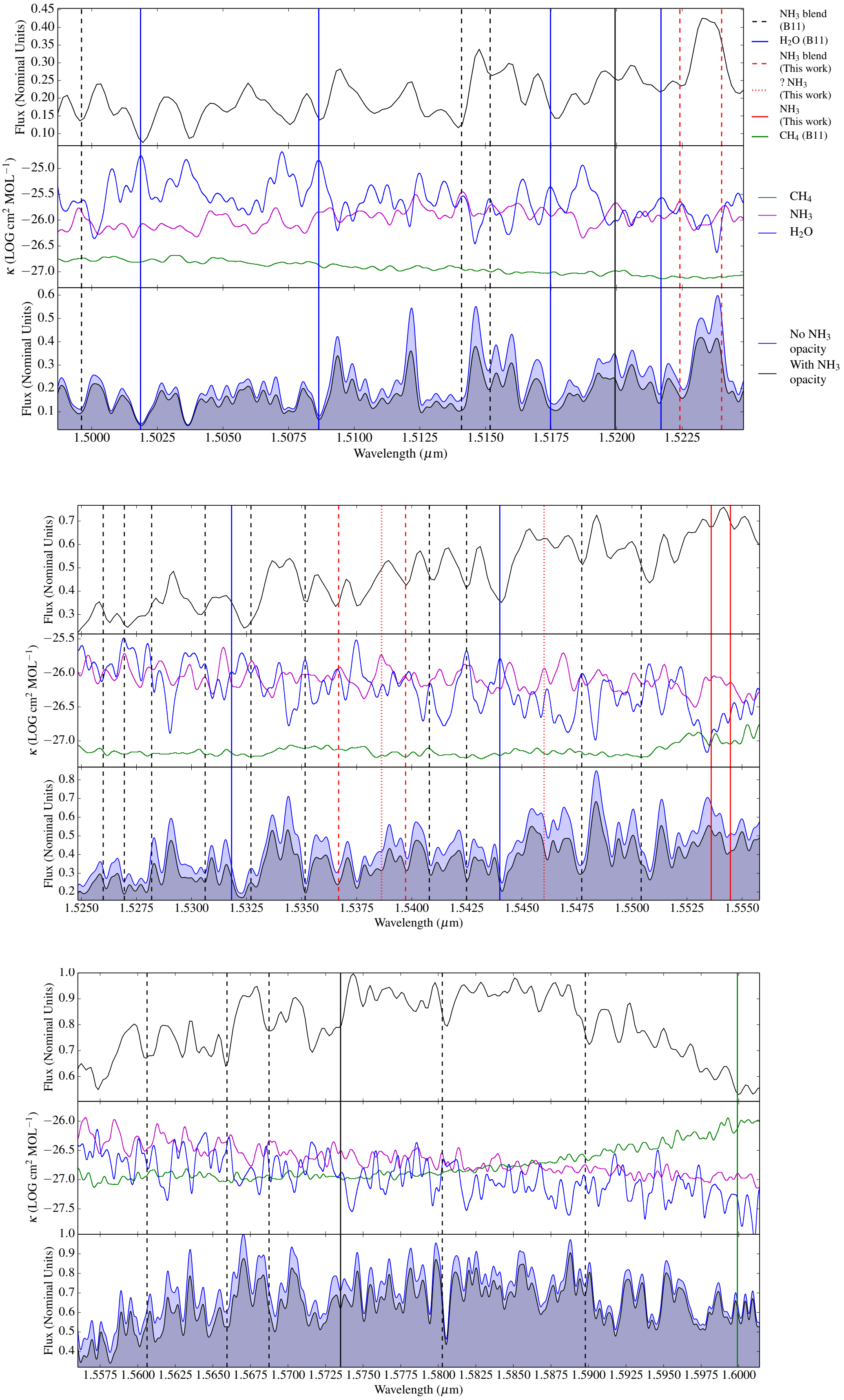

Fig. 3.19: NH$_3$ absorption features in the *H* band spectrum of 2MASS 0415. Features are as described in Figures 3.10 and 3.18. Scaled absorption cross-sections are calculated at 750 K for CH$_4$ (green), H$_2$O (blue) and NH$_3$ (mauve).

Table 3.7: NH_3 Absorption Features in the *H* Band Spectra of Late T Dwarfs.

Source	λ (μm)	Opacity Source (500 K/750 K)	NH_3 feature in synthetic spectrum (500 K/750 K)	Absorption feature in UGPS 0722	Absorption feature in 2MASS 0415
B11	1.4996	$(H_2O/NH_3)/(H_2O/NH_3)$	No/No	Yes	Yes
B11	1.5020	$(NH_3/H_2O)/H_2O$	No/No	Yes	Yes
B11	1.5086	NH_3/H_2O	No/No	Yes	Yes
B11	1.5140	$(NH_3/H_2O)/(NH_3/H_2O)$	No(?)/No(?)	Yes	Yes
B11	1.5152	$NH_3/(H_2O/NH_3)$	Yes/No	Yes	Yes
B11	1.5179	NH_3/H_2O	Yes/No	Yes	Yes
B11	1.5201	NH_3/NH_3	Yes/Yes	Yes	Yes
This work	1.5215	NH_3/H_2O	Yes/No	Yes	Yes
This work	1.5224	$NH_3/(NH_3/H_2O)$	Yes/No	Yes	Yes
This work	1.5240	$NH_3/(NH_3/H_2O)$	Yes/Yes(?)	Yes	Yes(?)
B11	1.5260	$NH_3/(NH_3/H_2O)$	Yes(?)/No	No(?)	Yes(?)
B11	1.5270	$NH_3/(H_2O/NH_3)$	No(?)/No	Yes	Yes
B11	1.5282	$NH_3/(H_2O/NH_3)$	Yes/Yes	Yes	Yes
B11	1.5306	$NH_3/(H_2O/NH_3)$	Yes(?)/No	Yes	Yes
This work	1.5318	NH_3/H_2O	Yes/No	Yes	Yes(?)
B11	1.5327	$NH_3/(NH_3/H_2O)$	Yes/No	Yes	Yes
B11	1.5350	$(NH_3/H_2O)/(H_2O/NH_3)$	Yes(?)/No	Yes	Yes
This work	1.5367	$NH_3/(NH_3/H_2O)$	Yes/No	Yes	Yes
This work	$1.5382^{\dagger}$	NH_3/NH_3	Yes/Yes	No(?)	No(?)
This work	1.5395	$NH_3/(H_2O/NH_3)$	Yes/No	Yes	Yes
B11	1.5408	$NH_3/(NH_3/H_2O)$	Yes(?)/No	Yes	Yes
This work	1.5427	$NH_3/(H_2O/NH_3)$	Yes/No	Yes	Yes
B11	1.5440	NH_3/H_2O	Yes(?)/No	Yes	Yes
This work	1.5461	NH_3/NH_3	Yes/Yes(?)	Yes	Yes(?)
B11	1.5480	$NH_3/(H_2O/NH_3)$	Yes(?)/No	Yes	Yes
B11	1.5504	$NH_3/(H_2O/NH_3)$	Yes/No	Yes	Yes
This work	1.5533	NH_3/NH_3	Yes/Yes	No	Yes
This work	1.5545	NH_3/NH_3	Yes/No	Yes	Yes
B11	1.5606	$NH_3/(NH_3/H_2O)$	No/No	Yes	Yes
B11	1.5658	$NH_3/(NH_3/H_2O)$	Yes/No	Yes	Yes
B11	1.5687	$NH_3/(NH_3/H_2O)$	Yes/No	Yes	Yes
B11	1.5735	NH_3/NH_3	Yes/No	Yes	Yes
B11	1.5803	$NH_3/(NH_3/H_2O)$	Yes(?)/No	Yes	Yes
B11	1.5898	$NH_3/(CH_4/NH_3/H_2O)$	No(?)/No	Yes	Yes
B11	1.5999	CH_4/CH_4	No/No	Yes	Yes

† In 2MASS 0415, the peak in NH_3 opacity is at 1.5386 μm.

0722, suggesting that NH_3 opacity is again the dominant opacity source. However, the synthetic spectra computed at 750 K show two relatively strong peaks, which differ only in amplitude between the two spectra. The scaled molecular opacities at 750 K suggest that the feature in 2MASS 0415's spectrum is produced by a blend of H_2O/NH_3 opacity and I have listed this as such in Table 3.7. While the remaining B11 detections in the *H* band coincide with peaks in NH_3 opacity, none correspond to significant differences between the S12 model spectra.

In addition, I believe I have identified nine new NH_3 absorption features that correspond both to peaks in the NH_3 opacity and differences between the model spectra with and without NH_3. Among these, the feature at 1.5240 μm corresponds to a peak in the NH_3 opacity at 500 K and there appears to be a corresponding absorption feature in the spectra of both T dwarfs. Indeed, the spectrum of UGPS 0722 is most similar to the synthetic spectrum with NH_3 opacity at 500 K. However, the spectrum of 2MASS 0415 at this wavelength looks most similar to the synthetic spectrum without NH_3 opacity at 750 K. The feature at 1.5318 μm corresponds to NH_3 opacity. While there appear to be absorption features at this wavelength in both T dwarf spectra, careful examination of the feature shows a "shoulder" in the feature in 2MASS 0415 which is absent in the spectrum of UGPS 0722. This shoulder is a feature of the synthetic spectrum without NH_3 opacity at 500 K, and is present in the synthetic spectra with and without NH_3 opacity calculated at 750 K. I conclude that this feature is probably a real NH_3 feature in the spectrum of UGPS 0722. This is also true of the feature at 1.5533 μm. Finally, the S12 models at 500 K predict a feature at 1.5382 μm. This feature appears to be missing in the spectra of both T dwarfs.

The ro-vibrational transition lines responsible for the NH_3 absorption features are shown in Figure 3.20 and Tables B.2, B.3, and B.4.

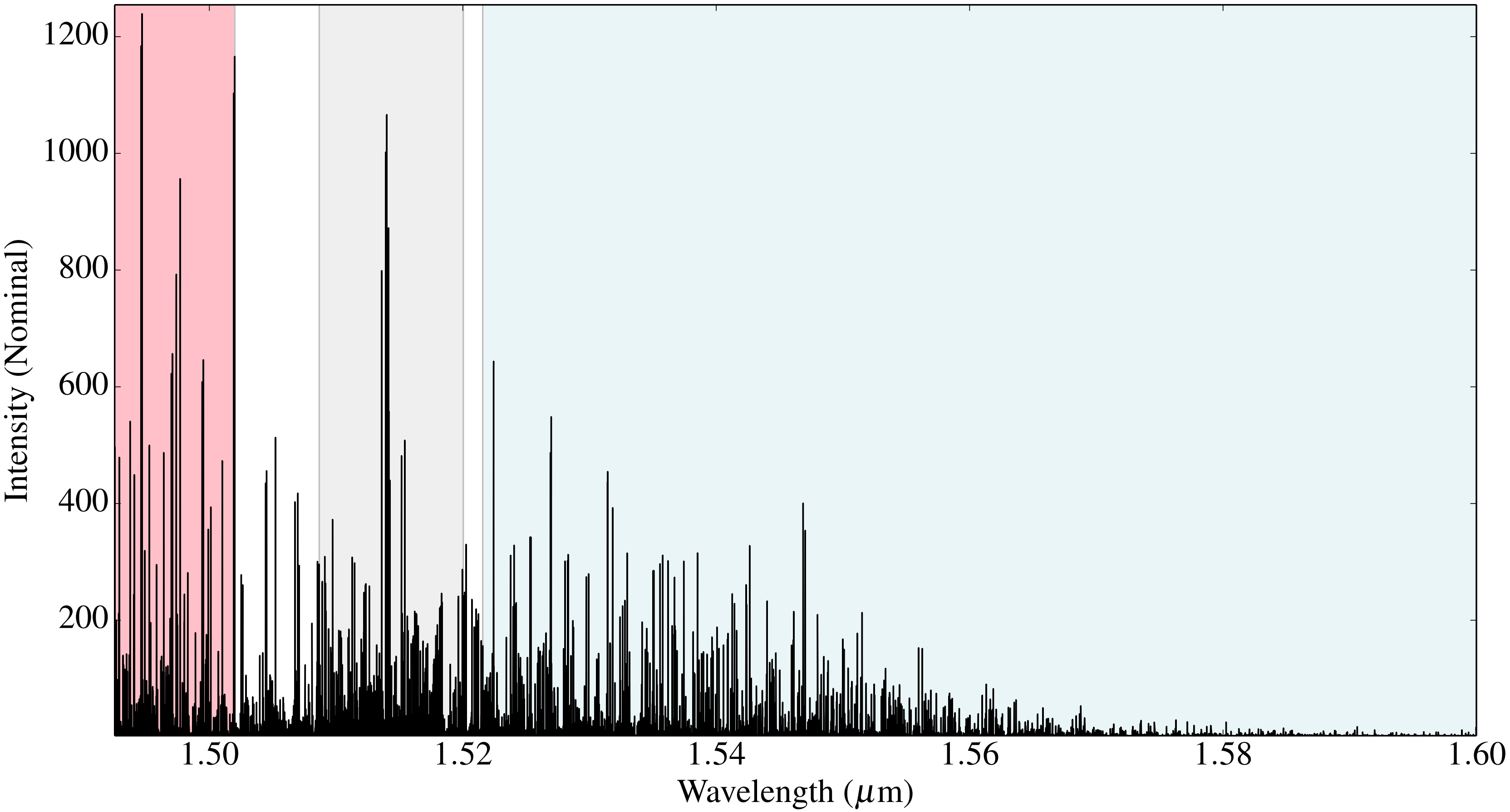

Fig. 3.20: The NH_3 H band ro-vibrational spectrum at 500 K.

I have found no significant differences in the identities of the ro-vibrational lines responsible for the absorption features in the two T dwarfs. The two blended NH_3 features at the shortest wavelengths, 1.4996 μm and 1.5020 μm, are produced by R-branch line transitions. A weak Q-branch transition line is found in the feature at 1.4996 μm. The R-branch transition lines belong to the $\nu_1+\nu_3$ vibrational bands, while the single Q-branch line arises from the the $\nu_1+2\nu_4$ bands.

NH_3 features in the *H* band are produced by ro-vibrational transitions from the P-, Q-, and R-branches. The CH_4 absorption features in the *H* band are also produced by ro-vibrational transitions from all three branches. However, most of the NH_3 absorption features in the *H* band are produced by P-branch transition lines, while the CH_4 absorption features in the *H* band are almost equally distributed across the P-, Q-, and R-branches. Q-branch transition lines are mostly from the $\nu_1+\nu_3$ vibrational bands. However, of the four strongest transition lines responsible for the absorption feature at 1.5152 μm, while three lines are Q-branch transition lines, two of these lines include overtones. These two lines have approximately half the intensity of the Q-branch line from the $\nu_1+\nu_3$ vibrational bands. Another line responsible for the feature at 1.5152 μm is a P-branch transition line from the $2\nu_2+3\nu_4$ vibrational bands. This line has approximately twice the intensity of the strongest Q-branch line. The absorption features at 1.5179 μm and 1.5201 μm also contain single P-branch transition lines with overtones. The feature at 1.5201 μm also contains a Q-branch transition line with an overtone. As expected, this line is approximately half the strength of the other Q-branch transition lines. In the absorption features produced by P-branch line transitions (1.5215-1.5999 μm), there are a few Q-branch transition lines in the absorption features at longer wavelengths. Otherwise, absorption features are entirely due to P-branch transition lines. However, these lines belong to a larger assortment of vibrational bands than is the case for absorption features due to R- or Q-branch transition lines. Approximately half the absorption features are produced by transition lines belonging to the $\nu_1+\nu_3$ vibrational bands, while somewhat less than half the features are from the $\nu_1+2\nu_4$ vibrational bands. It does appear that absorption features at shorter wavelengths belong predominantly to the $\nu_1+\nu_3$ vibrational bands, while those at longer wavelengths arise from the $\nu_1+2\nu_4$ vibrational bands. The two absorption features at the longest wavelengths, 1.5906 μm and 1.5999 μm, are due mostly to overtones ($4\nu_4$ and $3\nu_2$ respectively).

3.3.4 The K Band

Methane

The CH_4 absorption cross-sections show CH_4 opacity increasing with increasing wavelength over the long side of the K band flux peak, reaching a maximum at $\sim$2.20 μm (see Figures 3.21 and 3.22). The absorption cross-sections clearly show the Q-branch transitions centred at $\sim$2.20 μm.

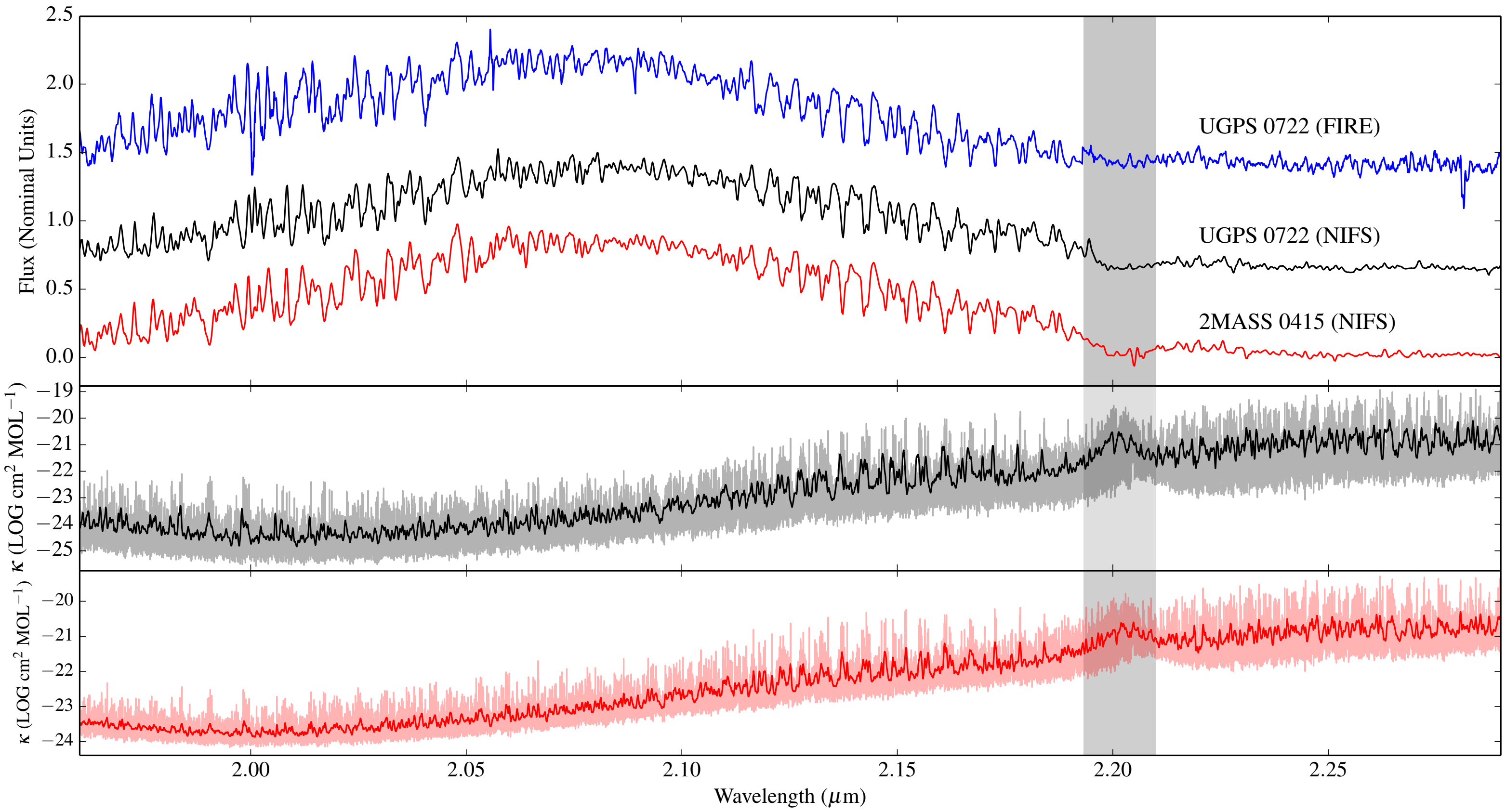

Fig. 3.21: CH$_4$ absorption in the K band spectra of 2MASS 0415 (red), UGPS 0722 (black), and the Magellan/FIRE spectrum of UGPS 0722 (blue). The shaded region indicates the Q-branch transitions centred at $\sim$2.20 μm. The lower graphs contains the cross-sections as described in Figure 3.4. (T dwarf spectra have been offset to aid identification of spectral features.)

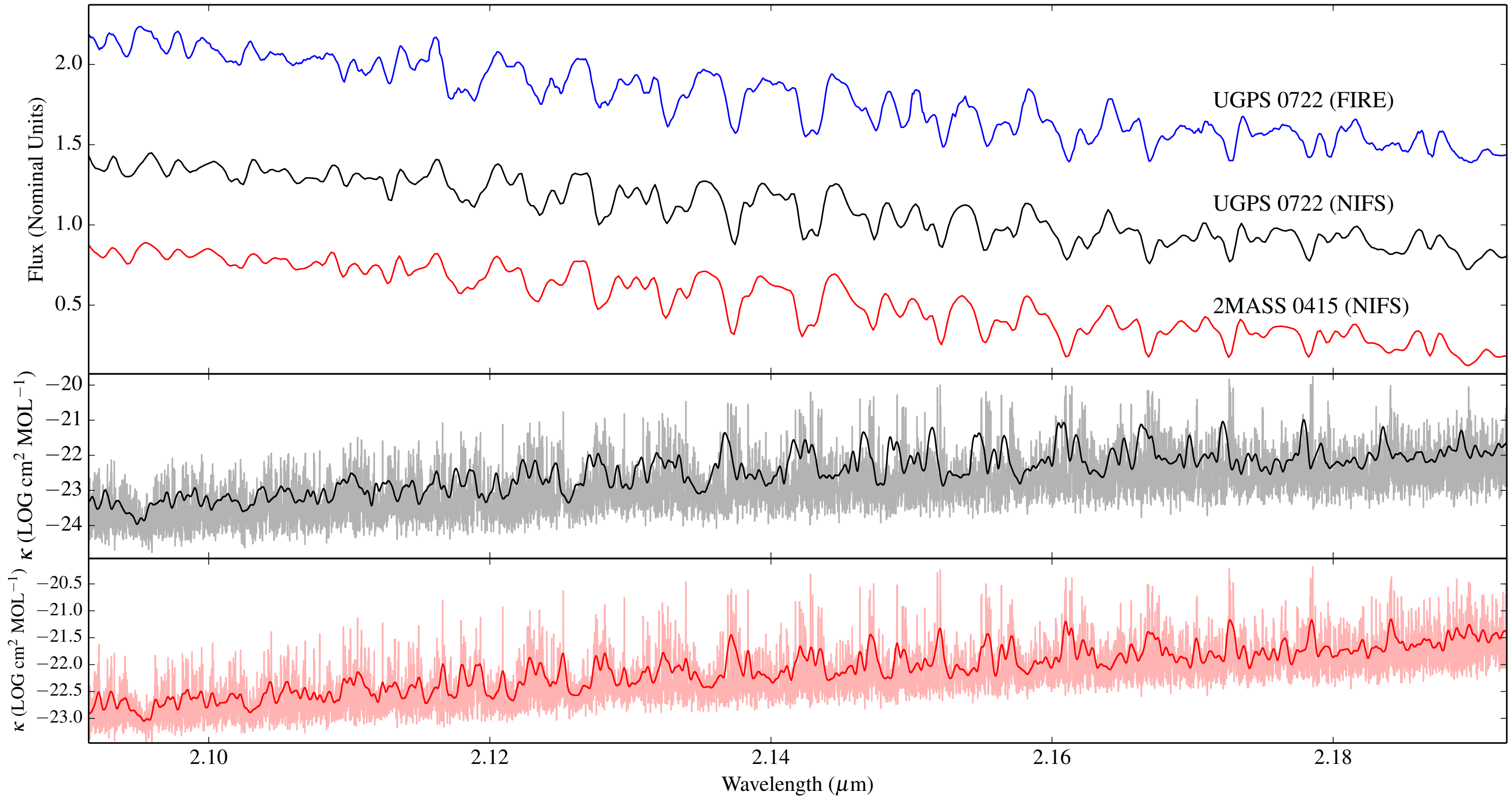

Fig. 3.22: The region of Figure 3.21 where CH_4 features have been identified.

B11 detected a number of absorption features between ∼2.14 μm and ∼2.18 μm. Using the high quality of the Gemini/NIFS spectra and the greater accuracy of the 10to10 line list I have identified a number of new absorption features within this range. See Figures 3.23, 3.24 and Table 3.8. Note that the features centred at ∼2.1233 μm, ∼2.1278 μm, and ∼2.1428 μm are actually due to multiple peaks in the methane opacity which at this resolution (R≈5000) are marginally resolved.

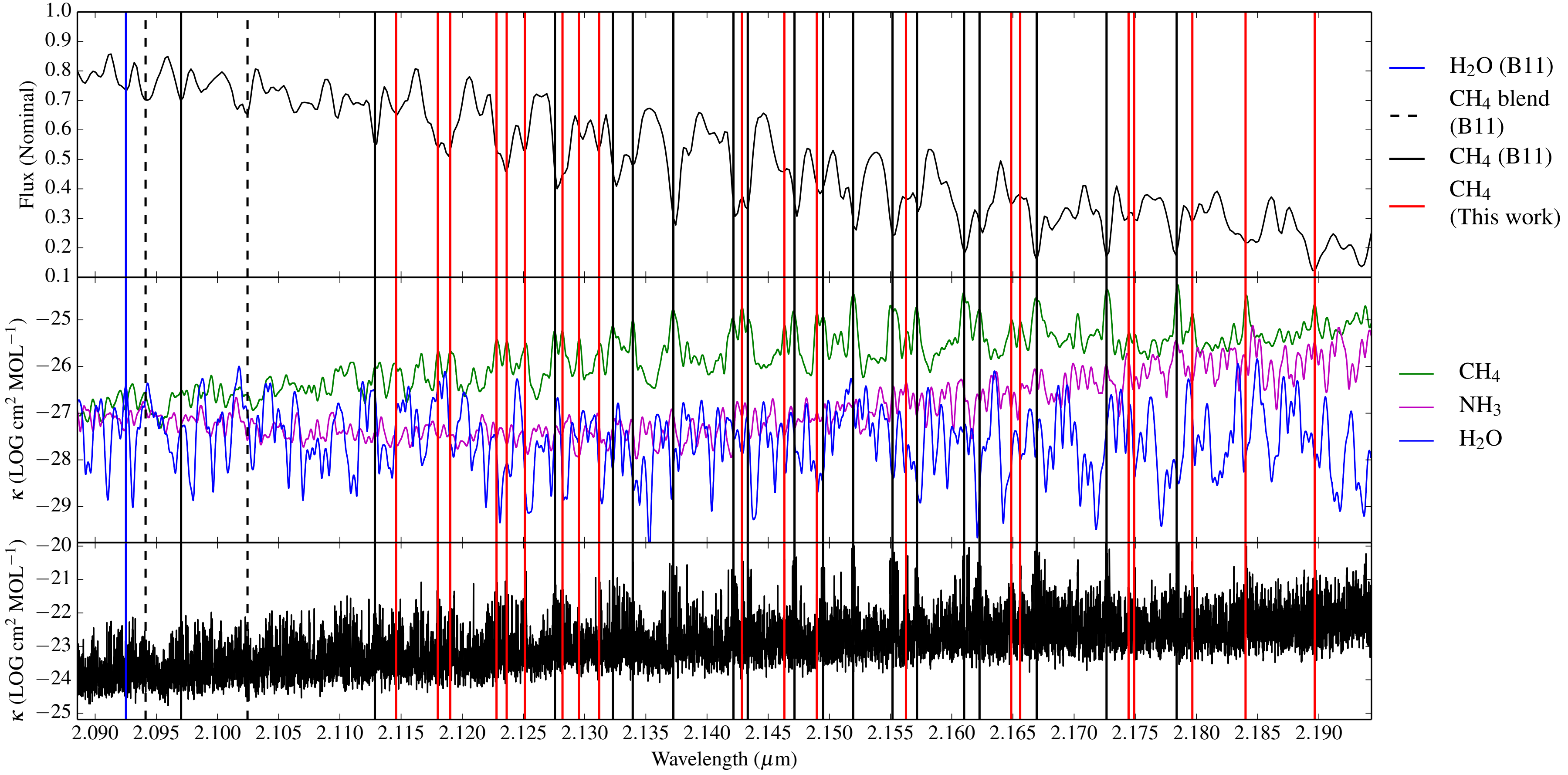

Fig. 3.23: CH_4 absorption features in the *K* band spectrum of UGPS 0722. Solid black lines are features previously detected by B11. Solid red lines are features identified in this work. Black dashed lines are features identified by B11 as CH_4 features which I find to be due to CH_4 and one or more other molecular species. The solid blue line is a water feature which B11 had identified as a methane feature.

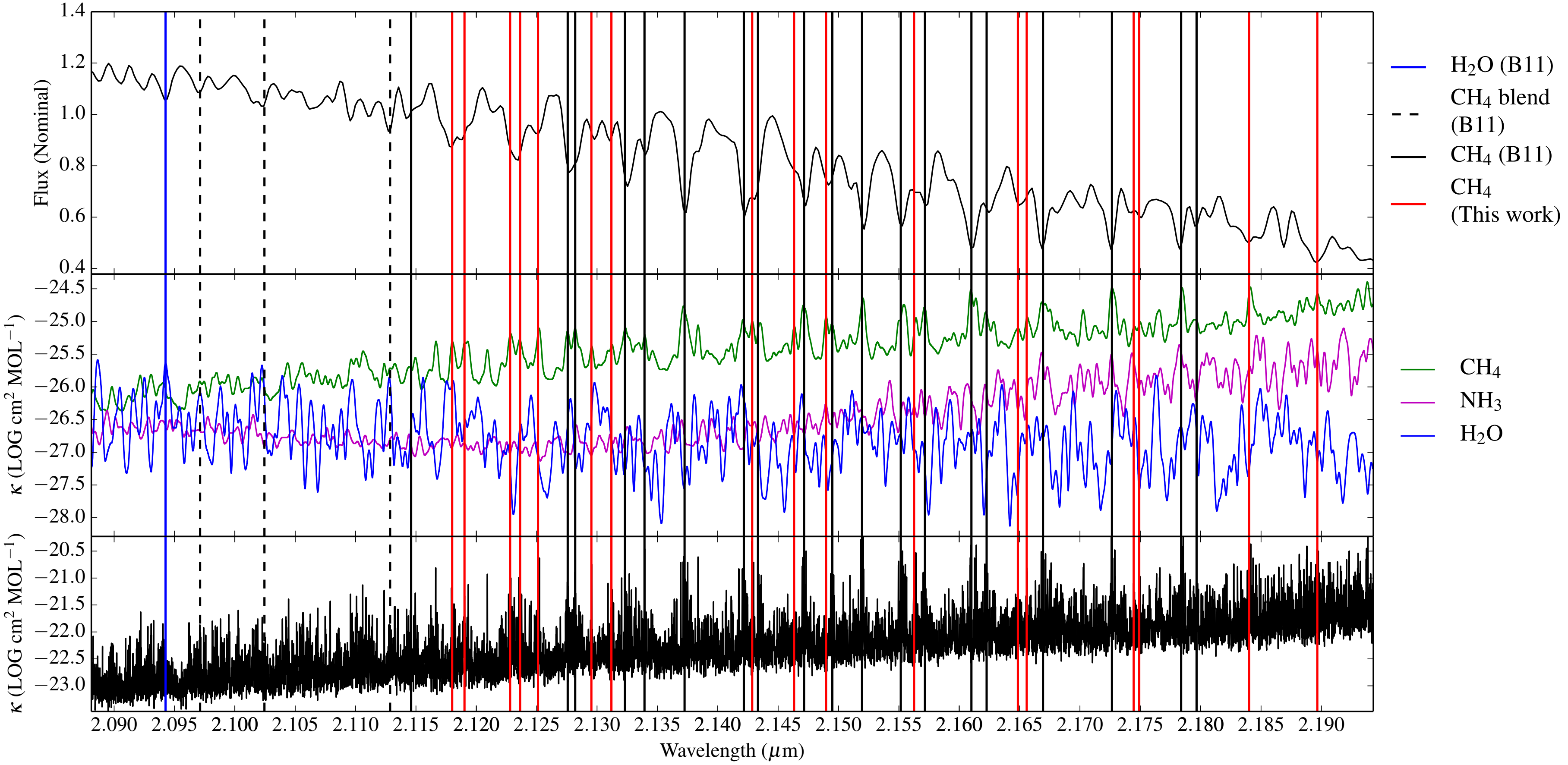

Fig. 3.24: CH_4 absorption features in the K band spectrum of 2MASS 0415.

The K band ro-vibrational spectrum at 500 K shows the intensity of transitions increasing in the range ~2.11-2.18 μm. The increase in intensity of the transition lines is visible in the spectra of the T dwarfs, particularly in the absorption features at 2.1520 μm and 2.1610 μm (see Figures 3.23, 3.25, and 3.26).

Table 3.8: CH_4 Absorption Features in the K Band Spectra of Late T Dwarfs

Source	λ (μm)	Opacity Source (B11)	Opacity Source (500 K/750 K)	Absorption feature in UGPS 0722	Absorption feature in 2MASS 0415
B11	2.0925	CH_4	H_2O/H_2O	Yes	Yes
B11	2.0943	CH_4	$(CH_4/H_2O/NH_3)/(H_2O/CH_4)$	Yes	Yes
B11	2.0971	CH_4	$CH_4/(CH_4/H_2O)$	Yes	Yes
B11	2.1025	CH_4	$(CH_4/H_2O)/(H_2O/CH_4)$	Yes	Yes
B11	2.1129	CH_4	$CH_4/(CH_4/H_2O)$	Yes	Yes
This work	2.1146	—	CH_4/CH_4	Yes	Yes
This work	2.1180	—	CH_4/CH_4	Yes	Yes
This work	2.1190	—	CH_4/CH_4	Yes	Yes
This work	2.1228	—	CH_4/CH_4	Yes	Yes
This work	2.1236	—	CH_4/CH_4	Yes	Yes
This work	2.1251	—	CH_4/CH_4	Yes	Yes
B11	2.1276	CH_4	CH_4/CH_4	Yes	Yes
This work	2.1282	—	CH_4/CH_4	Yes	Yes
This work	2.1295	—	CH_4/CH_4	Yes	Yes
This work	2.1312	—	CH_4/CH_4	Yes	Yes
B11	2.1323	CH_4	CH_4/CH_4	Yes	Yes
B11	2.1339	CH_4	CH_4/CH_4	Yes	Yes
B11	2.1373	CH_4	CH_4/CH_4	Yes	Yes
B11	2.1421	CH_4	CH_4/CH_4	Yes	Yes
This work	2.1429	—	CH_4/CH_4	Yes	Yes
B11	2.1433	CH_4	CH_4/CH_4	Yes	Yes
This work	2.1463	—	CH_4/CH_4	Yes	Yes
B11	2.1472	CH_4	CH_4/CH_4	Yes	Yes
This work	2.1490	—	CH_4/CH_4	Yes	Yes
B11	2.1495	CH_4	CH_4/CH_4	Yes	Yes
B11	2.1520	CH_4	CH_4/CH_4	Yes	Yes
B11	2.1552	CH_4	CH_4/CH_4	Yes	Yes
This work	2.1564	—	CH_4/CH_4	Yes	Yes
B11	2.1572	CH_4	CH_4/CH_4	Yes	Yes
B11	2.1610	CH_4	CH_4/CH_4	Yes	Yes
B11	2.1623	CH_4	CH_4/CH_4	Yes	Yes
This work	2.1649	—	CH_4/CH_4	Yes	Yes
This work	2.1656	—	CH_4/CH_4	Yes	Yes
B11	2.1669	CH_4	CH_4/CH_4	Yes	Yes
B11	2.1727	CH_4	CH_4/CH_4	Yes	Yes
This work	2.1745	—	CH_4/CH_4	Yes	Yes
This work	2.1749	—	CH_4/CH_4	Yes	Yes
B11	2.1784	CH_4	CH_4/CH_4	Yes	Yes
This work	2.1797	—	CH_4/CH_4	Yes	Yes
This work	2.1841	—	CH_4/CH_4	Yes	Yes
This work	2.1897	—	CH_4/CH_4	Yes	Yes

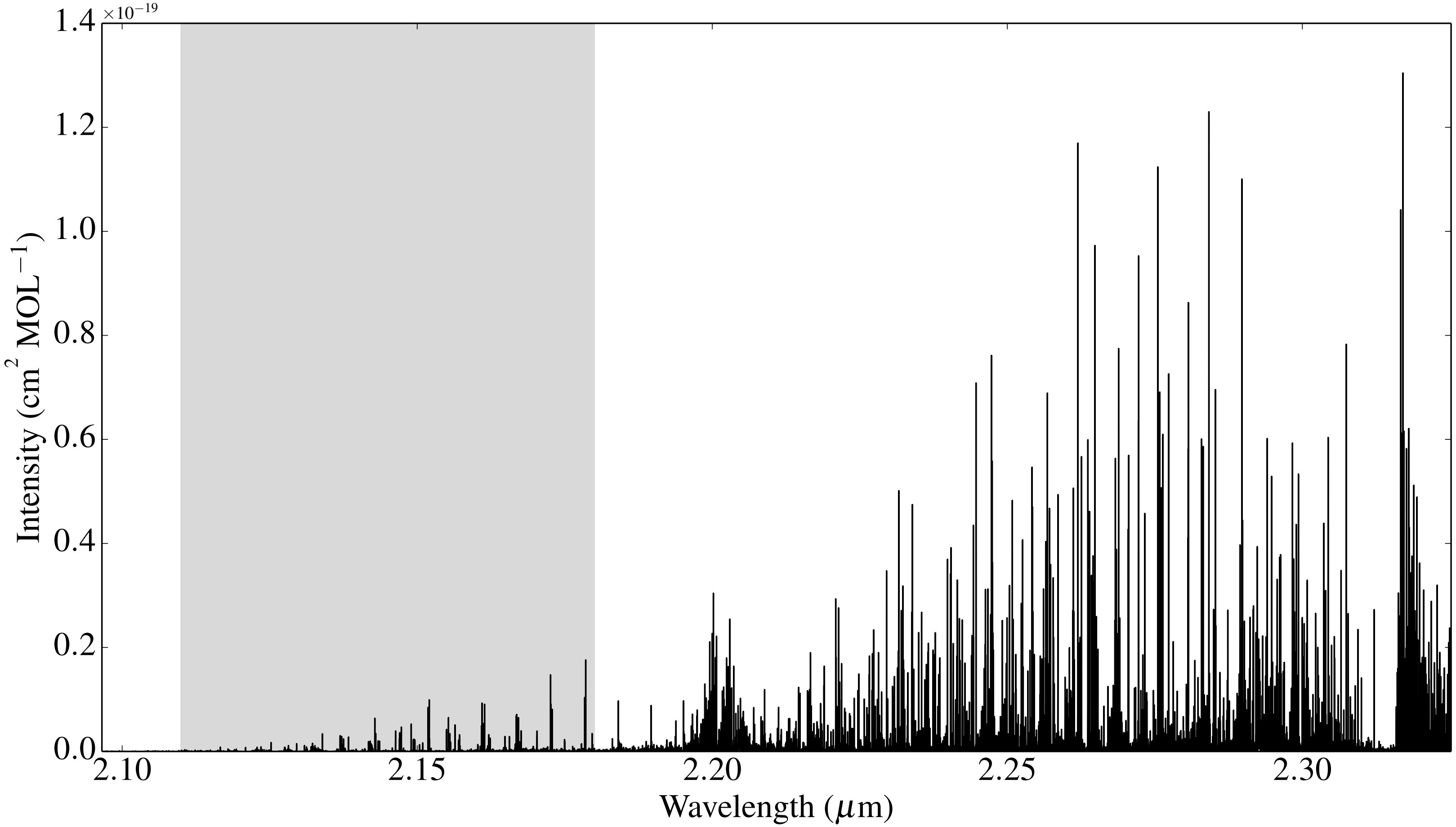

Fig. 3.25: The ro-vibrational *K* band spectrum of CH_4 made at 500 K. The shaded region corresponds to the region where CH_4 absorption features have been detected in the spectrum of UGPS 0722.

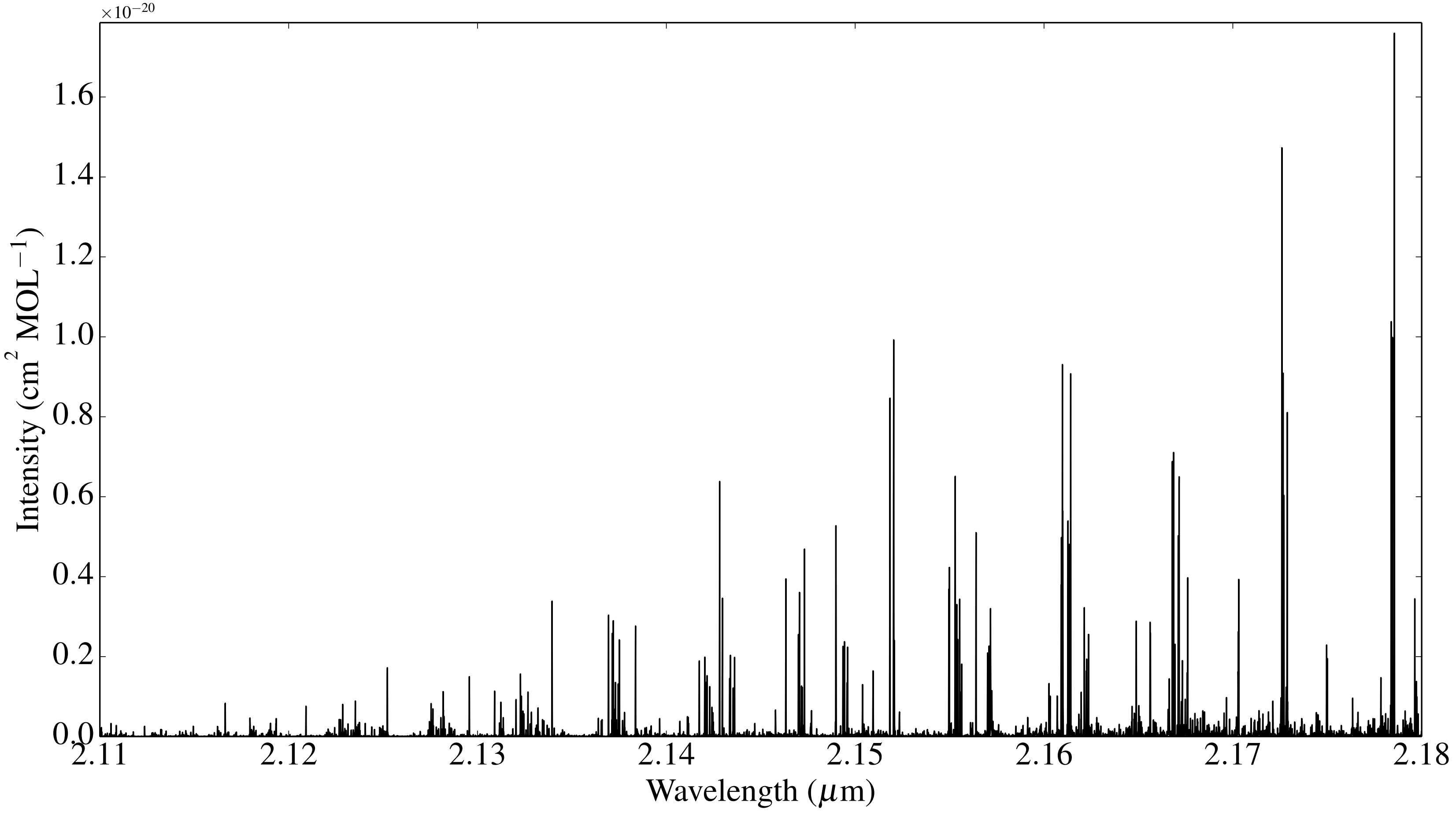

Fig. 3.26: The shaded region in Figure 3.25.

The peak in the *K* band flux at ~2.06 μm coincides with the start of increasing CH_4 opacity (see Figures 3.21−3.24). H_2 CIA is also a significant opacity source in the *K* band. H_2 CIA is produced by ro-vibrational transitions in H_2 molecules, forming a series of bands corresponding to $\Delta\nu$=0, 1, 2, 3, etc. [S12]. The $\Delta\nu$=1 band is centred at ~0.42 μm^{-1} (~2.4 μm). Figure 3.27 shows the strength of the H_2 CIA absorption coefficient at this wavelength. The roles played by these mechanisms in the *K* band spectra of late T dwarfs will be clearer once the 10to10 line list is included in model atmospheres. The shape of the *K* band continuum is also affected by metallicity, but model fits to the SED and spectrum of UGPS 0722, combined with its small space motion, indicate that it is a young object and therefore low metallicity is unlikely (Leggett et al. 2012; Morley et al. 2012, hereafter M12).

In T dwarfs, the *K* band flux weakens with increasing spectral type, i.e. decreasing temperature. In my analysis of H_2 CIA in Chapter 2, I found that H_2 CIA is dependent on pressure (surface gravity) rather than temperature. On the other hand, methane absorption becomes stronger as the temperature drops. It is possible that methane absorption is sufficiently strong on its own to completely suppress the *K* band in this region. For example, the Q-branch peak transition at 2.20 μm is an order of magnitude stronger than most of the transitions responsible for the absorption features detected by B11 and me. The Q-branch peak transition at 2.32 μm is an order of magnitude stronger still.

The quantum numbers of the ro-vibrational transitions responsible for the *K* band methane absorption features are shown in Table A.5. All the identified absorption features in UGPS 0722 and 2MASS 0415 arise from the $\nu_2 + \nu_3$ vibrational band. As with the *J* band, these are all R-branch transitions.

Ammonia

In the *K* band, S12 identified 19 absorption features corresponding to peaks in NH_3 opacity. Eight of these features matched absorption features in the Magellan/FIRE spectrum of UGPS 0722. A further six absorption features were tentatively identified. The remaining five features did not have any counterparts in the T dwarf spectrum.

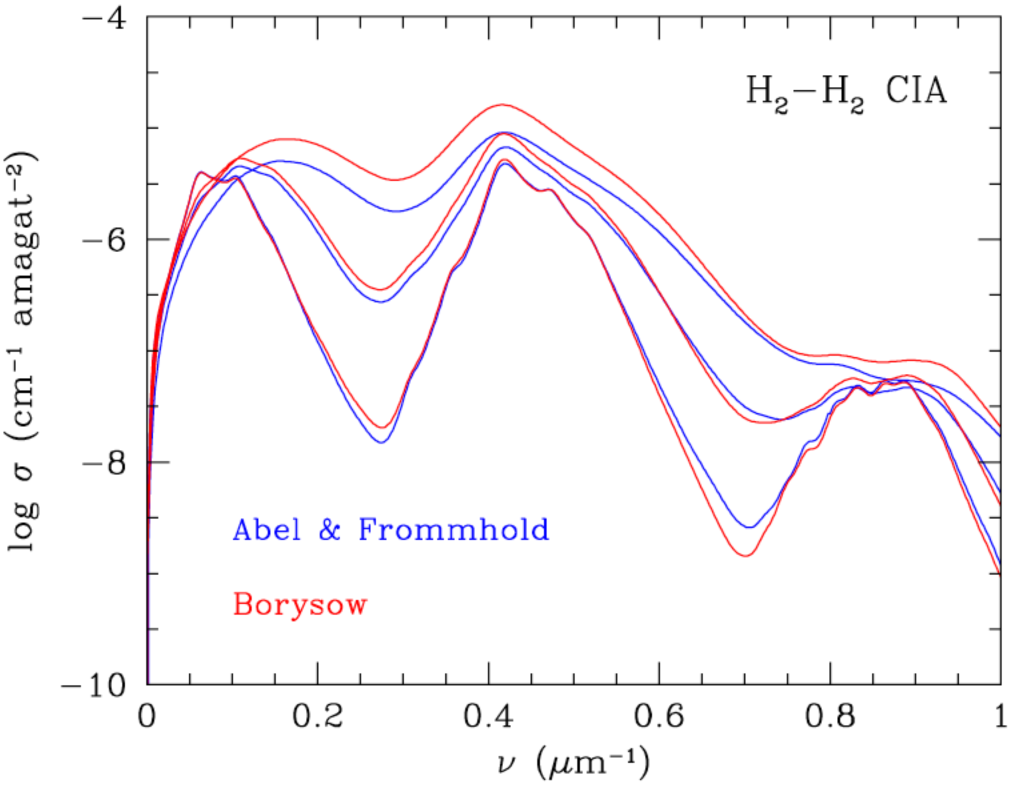

Fig. 3.27: Collision-induced absorption coefficient for H_2-H_2 collisions at T=500 K (bottom), 1000 K, and 2000 K (top). From left to right, peaks correspond to $\Delta\nu$=0, 1, 2. Calculations from Borysow (2002), Frommhold et al. (2010) and references in S12. Plot and rubric from S12.

I have been able to confirm the eight absorption features first identified by S12. I am also able to confirm seven of the uncertain/missing detections. In addition, I have identified five new absorption features. These results are summarised in Figures 3.28, 3.29, and Table 3.9.

The absorption feature identified by B11 at 1.9900 μm as due to a combination of ammonia and water opacity does not correspond to a change in ammonia opacity in the S12 models. However, Figure 3.28 suggests that water opacity rather than ammonia opacity is the stronger component in this feature. Indeed, in the spectrum of 2MASS 0415 the water opacity at this wavelength is an order of magnitude stronger.

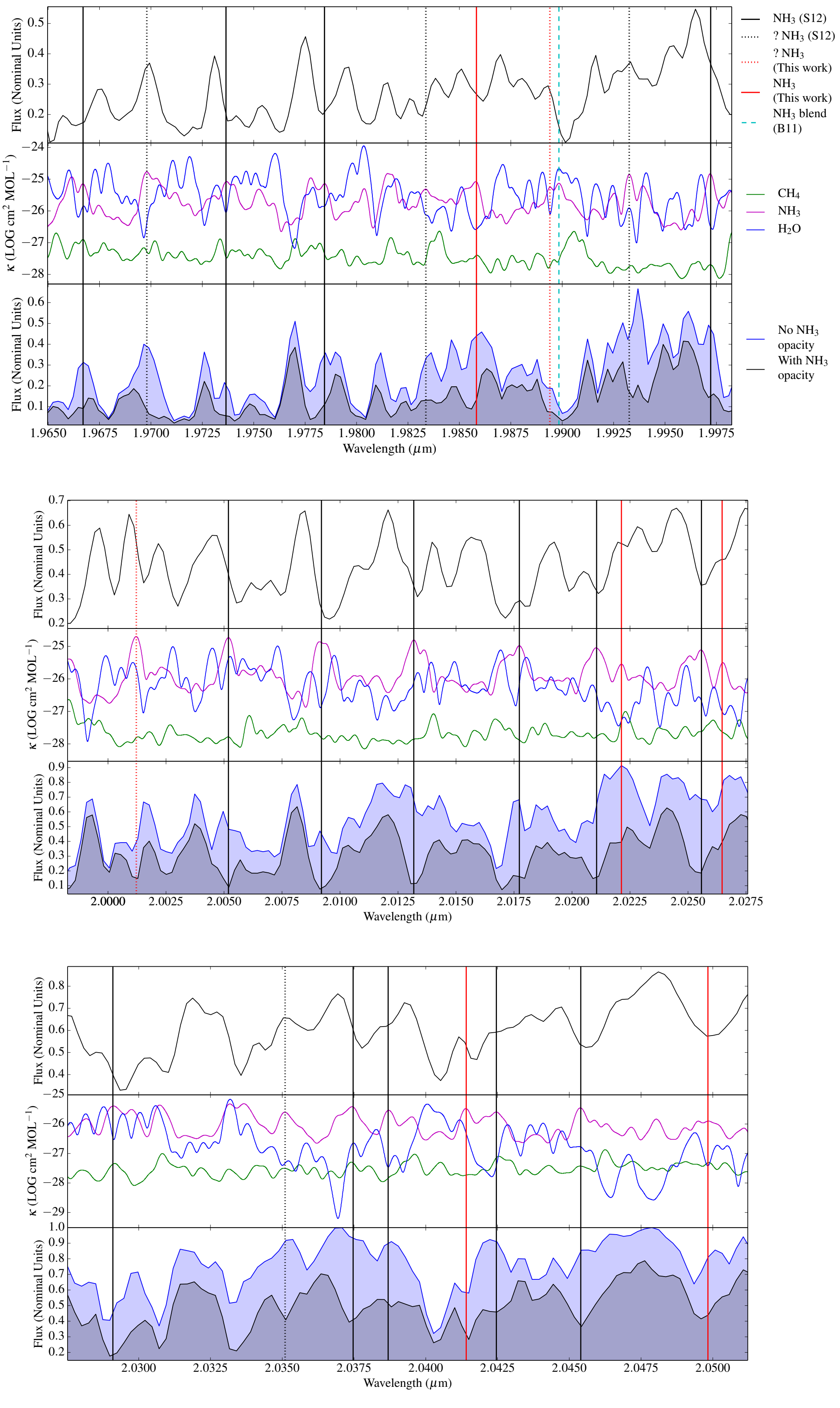

Fig. 3.28: NH_3 absorption features in the *K* band spectrum of UGPS 0722. Solid black lines are features in S12 which I can now confirm. These include seven features which were either missing or ambiguous in S12. The dotted lines are four S12 features which remain missing. The solid red lines are features detected in this work. The cyan line is an H_2O/NH_3 blend detected in B11. Scaled absorption cross-sections are calculated at 500 K for CH_4 (green), H_2O (blue) and NH_3 (mauve).

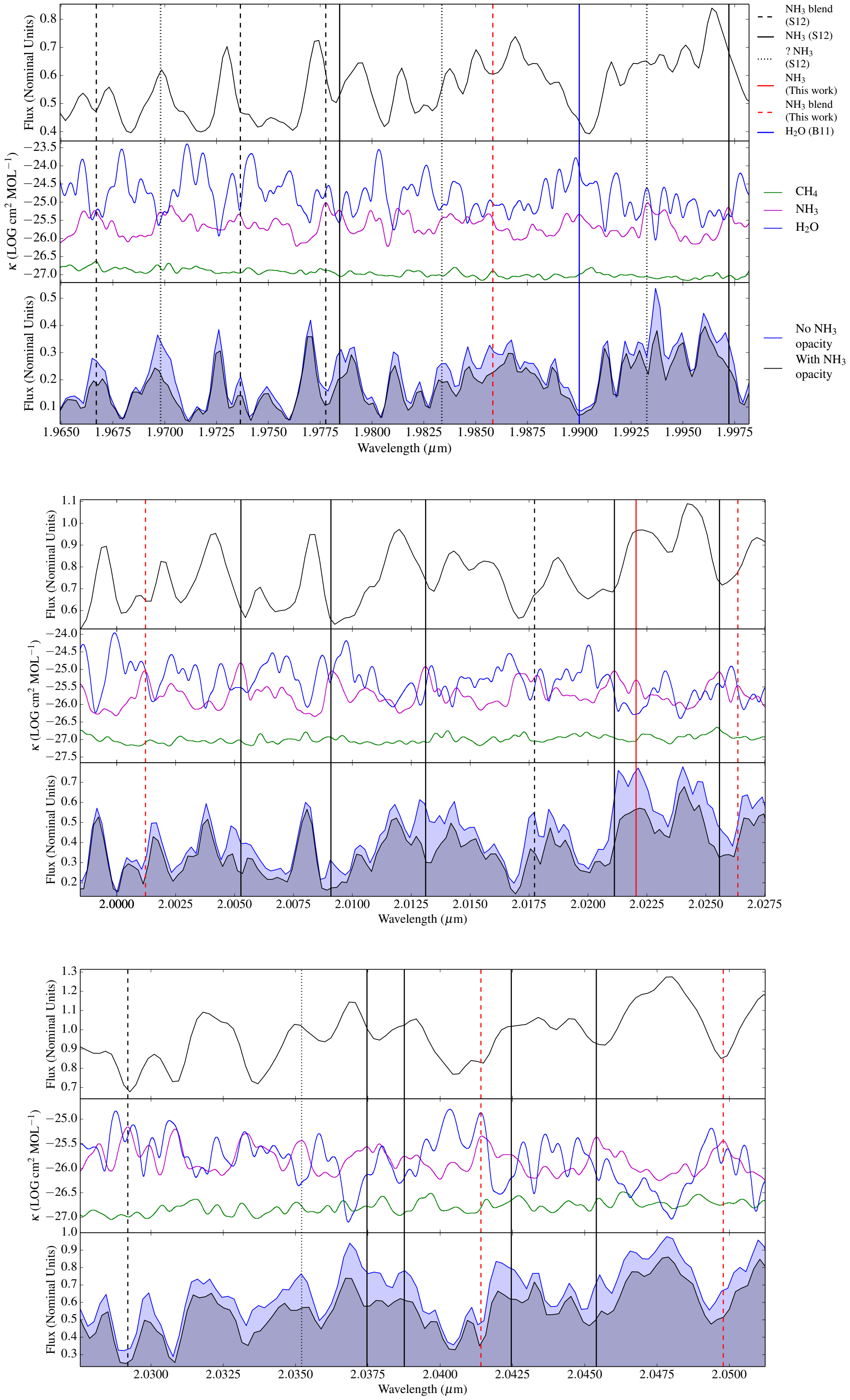

Fig. 3.29: NH$_3$ absorption features in the *K* band spectrum of 2MASS 0415. Scaled absorption cross-sections are calculated at 750 K for CH$_4$ (green), H$_2$O (blue) and NH$_3$ (mauve).

Table 3.9: NH_3 Absorption Features in the *K* Band Spectra of Late T Dwarfs

Source	λ (μm)	Opacity Source (500 K/750 K)	NH_3 feature in synthetic spectrum (500 K/750 K)	Absorption feature in UGPS 0722	Absorption feature in 2MASS 0415
S12	1.9667	NH_3/(H_2O/NH_3)	Yes/Yes	Yes	Yes
S12	1.9698	NH_3/(NH_3/H_2O)	Yes/Yes	No	No
S12	1.9737	NH_3/(H_2O/NH_3)	Yes/No	Yes	Yes
S12	1.9784	NH_3/NH_3	Yes/Yes	Yes	Yes
S12	1.9833	NH_3/(H_2O/NH_3)	Yes/Yes	Yes(?)	No
This work	1.9858	NH_3/(H_2O/NH_3)	Yes/Yes	Yes	Yes
This work	1.9894	NH_3/H_2O	Yes/Yes	No	Yes
B11	1.9900	(H_2O/NH_3)/H_2O	No/No	Yes	Yes
S12	1.9933	NH_3/(H_2O/NH_3)	Yes/No	No	No
S12	1.9972	NH_3/NH_3	Yes/Yes	Yes	Yes
This work	2.0012	NH_3/(H_2O/NH_3)	Yes/No	No(?)	Yes
S12	2.0052	NH_3/NH_3	Yes/Yes	Yes	Yes
S12	2.0092	NH_3/NH_3	Yes/Yes	Yes	Yes
S12	2.0132	NH_3/NH_3	Yes/Yes	Yes	Yes
S12	2.0177	NH_3/(NH_3/H_2O)	Yes/Yes	Yes	Yes
S12	2.0211	NH_3/NH_3	Yes/Yes	Yes	Yes
This work	2.0221	NH_3/NH_3	Yes/Yes	Yes	Yes
S12	2.0256	NH_3/NH_3	Yes/Yes	Yes	Yes
This work	2.0265	NH_3/(NH_3/H_2O)	Yes/No	Yes	Yes
S12	2.0291	NH_3/(H_2O/NH_3)	Yes/No	Yes	Yes
S12	2.0351	NH_3/NH_3	Yes/Yes	No	No
S12	2.0375	NH_3/NH_3	Yes/No(?)	Yes	Yes
S12	2.0387	NH_3/NH_3	Yes/No(?)	Yes	Yes
This work	2.0414	NH_3/(H_2O/NH_3)	Yes/No	Yes	Yes
S12	2.0425	NH_3/NH_3	Yes/Yes	Yes	Yes
S12	2.0454	NH_3/NH_3	Yes/Yes	Yes	Yes
This work	2.0498	NH_3/(NH_3/H_2O)	Yes/Yes	Yes	Yes

The ro-vibrational spectrum for this region of the K band is shown in Figure 3.30. The ro-vibrational transitions responsible for the detected NH_3 absorption features are listed in Tables B.5 and B.6. In the ro-vibrational spectrum for this region of the K band, there is a weak $4\nu_2$ overtone among the transition lines contributing to the absorption feature at 2.0132 μm. Otherwise all the NH_3 absorption features in the K band belong to the $\nu_1+\nu_4$ vibrational bands. Approximately 70% of the absorption features are produced by P-branch transition lines. There is a single feature at 1.9667 μm produced by R-branch transitions alone, and there is a very strong R-branch transition line among the Q-branch transition lines responsible for the absorption feature at 1.9737 μm. The remaining absorption features are generated by Q-branch transitions. Note that NH_3 absorption features in the K band spectra of these two T dwarfs are produced by transition lines from the P-, Q-, and R-branches, whereas I found only R-branch transition lines in the K band absorption features due to CH_4.

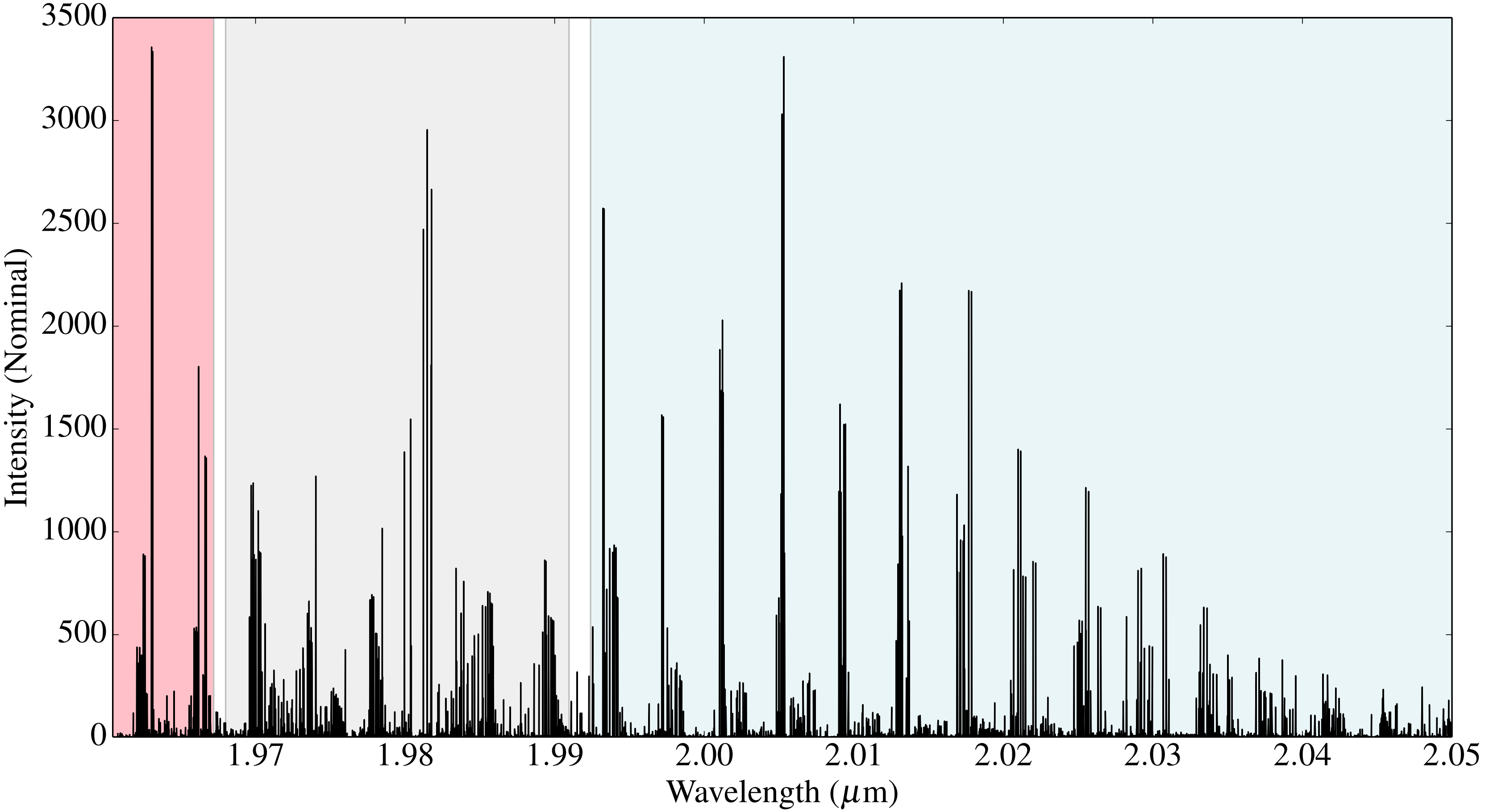

Fig. 3.30: NH_3 *K* band ro-vibrational spectrum. R-branch cross-sections (red), Q-branch cross-sections (gray), P-branch cross-sections (blue).

3.4 Discussion

In my analysis of CH_4 absorption features, I have assumed that the photospheres of these T dwarfs can be modelled using single values of T_{eff}. Of course, there is a range of temperatures in the photosphere. Absorption features tend to be produced in the higher, cooler parts of the photosphere. While it is possible that an absorption feature seen in the spectrum of 2MASS 0415 may be better modelled with a 500 K model than a 750 K model, I have not found any examples of this in my analysis. I have determined that the strongest absorption features on the long side of the *H* and *K* band flux peaks of both T dwarfs are due to CH_4 opacity (apart from mixed absorption features at 2.0943 μm and 2.1025 μm in the spectra of both T dwarfs, and mixed features at 2.0971 μm and 2.1129 μm in the spectrum of 2MASS 0415). The disagreement between the 10to10 line list and the science data between 1.6145 μm-1.6259 μm is puzzling. The differences are so slight that I am inclined to believe that the absorption features in the T dwarfs' spectra are due to methane. However, the mismatch requires an explanation. It cannot be due to faulty calibration of either the science spectra or the 10to10 line list, since elsewhere the correspondence between methane opacity and absorption feature is excellent. I suspect that there is some deficiency in the 10to10 line list in this wavelength region which should be investigated. There are significant differences between opacity sources in the spectra of the two T dwarfs on the long side of the *J* band flux peak, where I identified a single methane feature in the spectrum of 2MASS 0415, compared to six features in the spectrum of UGPS 0722. There are a large number of methane blends in the *J* band spectra of these objects compared to the methane features I have observed in these objects' *H* and *K* band spectra.

While several ammonia absorption features predicted by the S12 model spectra between ~1.223-1.235 μm remain undetected, I have found a number of others. Although the S12 model spectra with and without NH_3 opacity show no significant differences at the wavelengths corresponding to possible NH_3 absorption features between ~1.239-1.266 μm, I find that NH_3 opacity is the strongest opacity source in this region. The failure of the S12 model spectra to predict these features may be because without a comprehensive, high-temperature methane line list, the models overestimate the importance of methane opacity in this region.

It has recently been suggested that the relatively red $J-H$ and $J-K$ colours seen in T dwarfs of spectral types $\gtrsim$T8 in comparison with model predictions could be explained by the formation of sulphide clouds [M12]. The model spectra used in the analyses here and in S12 are cloudless. While the BYTe line list and the improved calculations of H_2 CIA have reddened the $J-K$ colours of model spectra for T dwarfs with T_{eff} $\gtrsim$600 K, the reddening is insufficient to match the observed colours of the coolest T dwarfs [M12]. It is also possible that the inclusion of sulphide cloud opacity in a new set of synthetic spectra may be a better match to the data.

In UGPS 0722, NH_3 ro-vibrational transition lines in the H band are an order of magnitude stronger than those in the J band and NH_3 is the dominant source of opacity across the blue wing of the H band (1.50-1.59 μm). This region of the H band shows clear differences in the species responsible for the absorption features in the two T dwarfs' spectra. At 750 K, the scaled absorption cross-sections are of the same order of magnitude for all three of the main molecular opacity sources (H_2O, CH_4, NH_3) (see particularly the middle panel of Figure 3.19) so that features due to NH_3 opacity alone in the spectrum of UGPS 0722, are produced by a combination of opacities in the spectrum of 2MASS 0415.

3.5 Conclusions

The BYTe (Yurchenko, Barber & Tennyson, 2011) and 10to10 (Yurchenko & Tennyson, 2014) line lists appear to be validated in that I have detected previously known features at the correct wavelengths. In addition, I have found new absorption features and corrected features which had previously been mis-identified. The reasons for this are the high quality science spectra used in this analysis, and the 10to10 line list, which is more complete at these temperatures than any previously available list. For example, the CH_4 laboratory line list used by B11 was made at 800 K and covered the spectral range 2000-5000 cm^{-1} (wavelengths $\geq$2.00 μm) at a resolution of 0.02 cm^{-1}, and the spectral range 5000-6400 cm^{-1} (wavelengths between 1.56-2.00 μm) at a resolution of 0.04 cm^{-1} (Nassar & Bernath, 2003). B11 used the HITRAN 2008 database (Rothman et al., 2009), calculated at 296 K, to supplement the experimental line list. These facts may explain B11's mis-identications, particularly in the *J* and *H* bands. The use of adaptive optics has allowed me to obtain data in the *H* and *K* bands with improved S/N ratios compared with the same passbands in B11. This has enabled me to add significantly to the number of detections of methane and ammonia absorption features in this region of the near-infrared. My near-infrared spectrum of UGPS 0722 and that of B11 appear very similar and I have not found any sign of variability of features between the two spectra. As both data sets are independent, I am confident that these features are real.

The BYTe and 10to10 line lists indicates that NH_3 is the dominant opacity source between ~1.233-1.266 μm in the spectrum of UGPS 0722, and I have tentatively identified several absorption features in this wavelength range which may be due entirely to ammonia opacity.

The 10to10 line list has allowed me to accurately identify the opacity sources responsible for many of the T dwarf absorption features. I have also found that absorption features common to both T dwarf standards may have different opacity sources, or the relative strengths of the opacity sources producing these features may vary between them. This is particularly noticeable in the *J* band, where the number of absorption features due solely to CH_4 opacity are fewer than previously thought.

Using the high quality spectra of these T dwarfs, I have been able to confirm the presence of 15 of the 19 NH_3 absorption features in the *K* band predicted by the S12 models. In addition, I have identified five previously unknown absorption features. The ro-vibrational transition lines responsible for these features have up to twice the intensity of those in the *H* band. The lines also appear to be more highly ordered than those in the *J* or *H* bands, making the identification of corresponding absorption features in the T dwarfs' spectra easier.

In this work I have looked at the most common isotopologues of methane and ammonia. In particular, the relative abundance of methane isotopologues is determined by the reaction rates of these isotopologues with methane sinks (Rigby, Manning & Prinn, 2012), and is therefore useful in understanding the structure and evolution of atmospheres. While the use of high-temperature line lists of other methane isotopologues in model spectra could be applied to the near-infrared spectra of T dwarfs and lead possibly to a greater understanding of the evolution of their atmospheres, most brown dwarfs will have burned their stock of deuterium early in their evolution. The ratio of $^{13}CH_4$ to $^{12}CH_4$ in these objects is ~0.01, so that $^{13}CH_4$ is probably undetectable in brown dwarf spectra (D. Saumon, private comm.).

3.6 The *L* Band Spectrum of UGPS 0722

This analysis of the *L* band spectrum of UGPS 0722 was published in Leggett et al. (2012), in which I am a co-author. I was one of the observers who obtained the *L* band data used in this paper. I extracted and optimised the *L* band spectrum.

A 2.8-4.2 μm spectrum for UGPS 0722 was obtained using the Infrared Camera and Spectrograph (IRCS) (Kobayashi et al., 2000) on the Sabaru telescope on Mauna Kea, Hawaii. UGPS 0722 was observed on the nights of 2011 January 23 and 24 with the *L* band grism, using a $0''.9$ slit, giving a spectral resolution of R≈180. The total integration time was 120 minutes, consisting of 48 minutes from January 23 and 72 minutes from January 24. Observations were made in an ABBA pattern with 60 s integrations and a $6''$ nod. The spectrum was extracted in IRAF using a $0''.75$ aperture. No suitable arc lamp is available for the *L* band. I therefore adopted a linear solution for calibrating the wavelength, based on two widely spaced telluric features, following the procedure described in the IRCS data reduction cookbook (http://www.subarutelescope.org/Observing/DataReduction/index.html). The estimated accuracy in the wavelength calibration is ~1 nm. On each night, two A- to F-type stars were observed as telluric standards before and after the observation of UGPS 0722. The extracted telluric-corrected spectra from January 23 and January 24 were similar, with just a slight disagreement in the slope of the continuum at the longest wavelengths (4.00-4.18 μm). The spectrum was flux calibrated using IRAC [3.6]

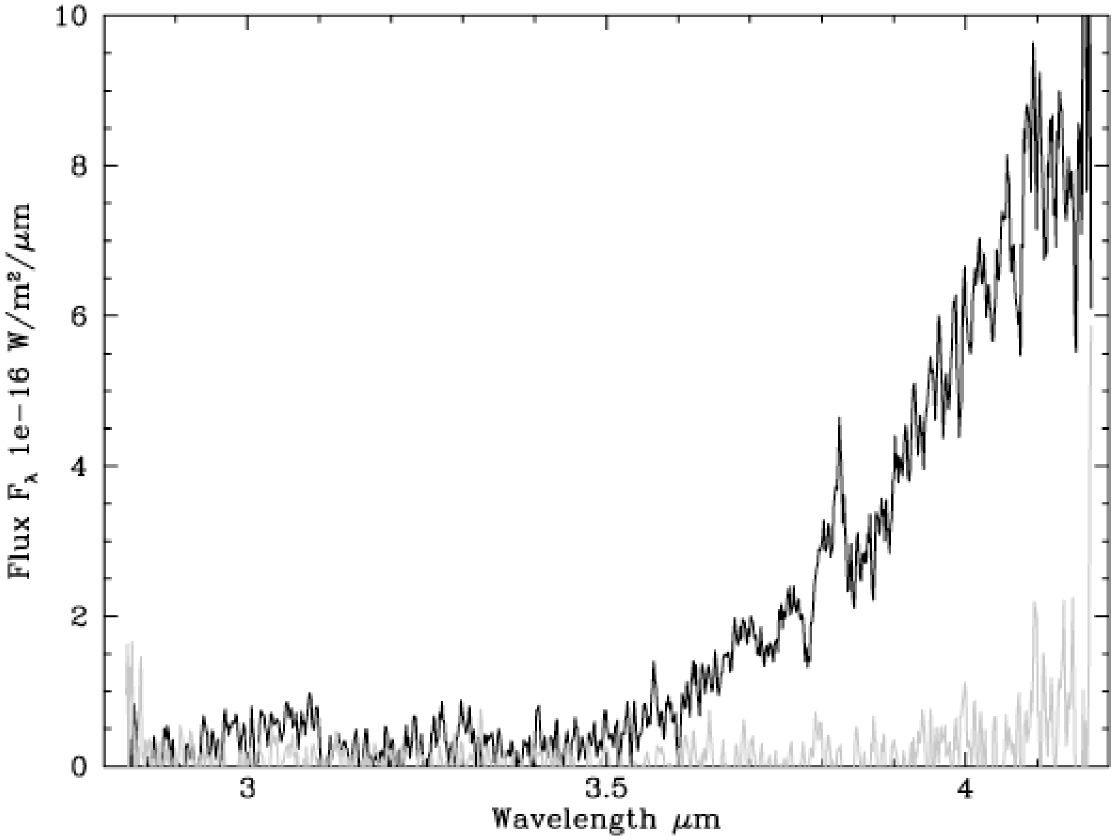

Fig. 3.31: The 2.8-4.2 μm spectrum of UGPS 0722 obtained using the Infrared Camera and Spectrograph on Subaru, median-smoothed by three pixels. The error spectrum is shown in grey. The spectrum is dominated by CH_4 absorption. Plot from Leggett et al. (2012).

photometry which has an uncertainty of 5% (Lucas et al., 2010). The final reduced spectrum is shown in Figure 3.31. The error spectrum is also shown, which is based on the difference between the two subsets of data.

The S/N ratio varies across the spectrum and is ∼5-15 from 3.7 μm to 4.1 μm, the region of the wavelength region which is less affected by strong CH_4 absorption. The spectrum has a noticeable peak in the flux at ∼3.8 μm, while there are absorption features at 3.71-3.74 μm, 3.77-3.79 μm, and 3.83-3.86 μm. Models provided by D. Saumon and M. Marley suggest that the structure in this region of the spectrum is due to CH_4 absorption. See Figure 3.32.

The peak in the flux at ∼3.8 μm is similar to a structure in the R≈600 spectrum of the 900-1000 K T6 dwarf ε Indi Bb (King et al., 2010). This feature is missing in the *L* band spectrum of the other binary component. See Figure 3.33.

The R≈100 AKARI *L* band spectrum of the 750 K dwarf 2MASS 0415 (Yamamura,

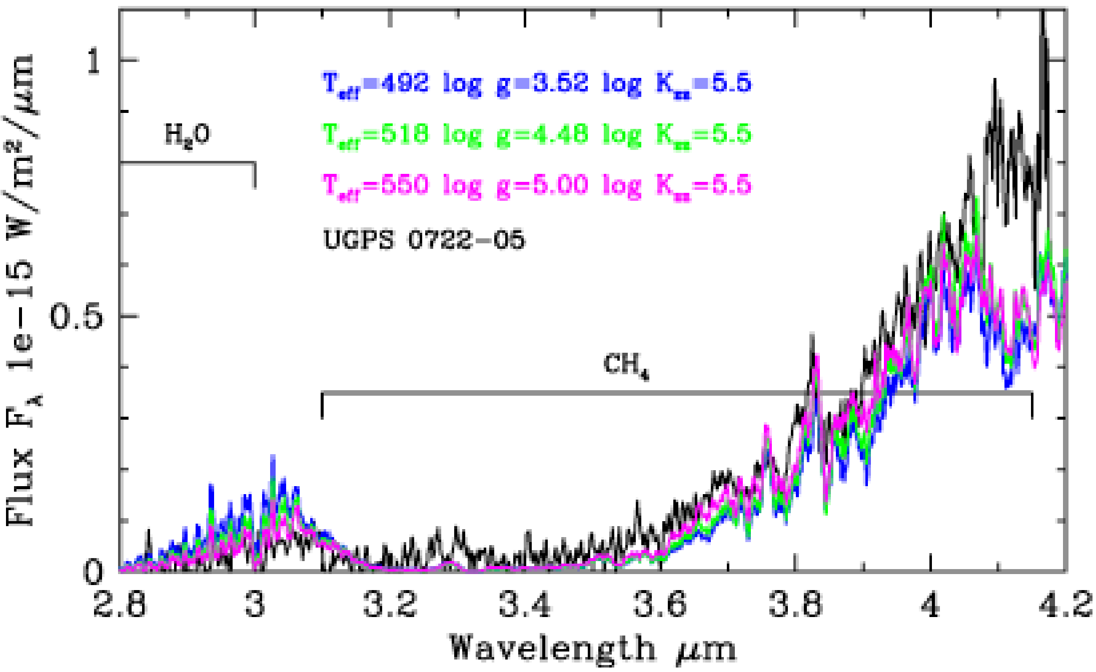

Fig. 3.32: Comparison of the observed and modeled spectra for UGPS 0722. Principal opacity sources are indicated. These Saumon and Marley models are cloudless, solar-metallicity models which include non-equilibrium chemistry. The legend shows the T_{eff}, log g, and log K_{zz} values for each model. The synthetic spectra are calibrated using the measured distance to the object and the radius implied by evolutionary models for each (T_{eff}, log g). There is an obvious discrepancy between the models and data at 4.1 μm. Plot and rubric from Leggett et al. (2012).

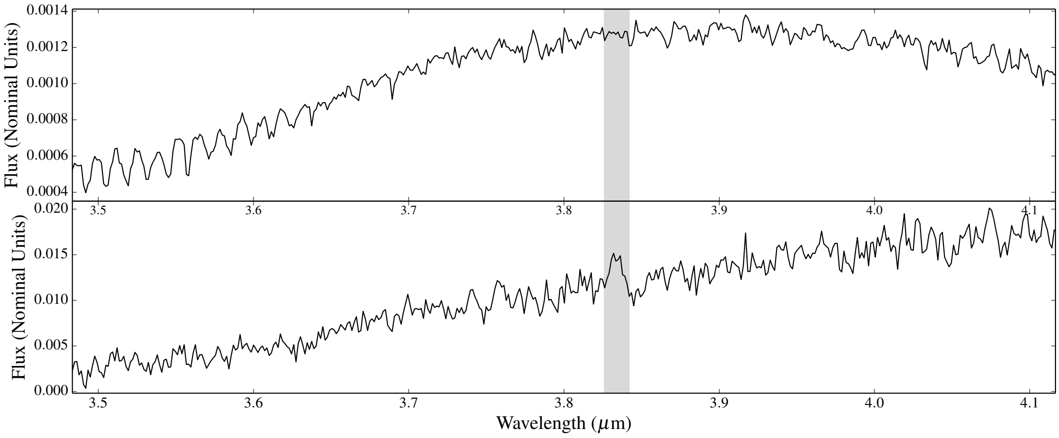

Fig. 3.33: The *L* band spectra of ε Indi Ba (top) and ε Indi Bb (bottom). The shaded region indicates the position of the feature which is also prominent in the *L* band spectrum of UGPS 0722. (Spectra from King et al. 2010.)

Tsuji & Tanabé, 2010) is too low resolution to show these features.

There is a clear discrepancy between the models and the data at ~4.1 μm. Leggett et al. (2012) suggest that this discrepancy may be due to the incomplete CH_4 line lists which were available to the modellers, while thin clouds in the T9 dwarf's atmosphere may also affect the relative peak fluxes in the near-infrared. More recently, the modellers have suggested that this discrepancy may be due to H_2O absorption. At T_{eff} ~500 K, the ~4 μm spectrum peak is shaped by CH_4 and H_2O absorption. Non-equilibrium models have less CH_4, hence H_2O absorption becomes more important redward of 4 μm, resulting in a dip in the flux at 4.1 μm. This reduction in flux is absent in models in chemical equilibrium where the spectrum is flatter. The dip in the flux at this wavelength is a generic feature of the Saumon & Marley cool, non-equilibrium models.

The L band spectrum derived from the 10to10 line list suggests that the discrepancy between models and data at ~4.1 μm may be due to incompleteness in previous line lists. Figure 3.34 shows the L band spectrum of UGPS 0722 and the corresponding scaled absorption cross-sections at 500 K for H_2O, NH_3 and CH_4. The latter was derived from the 10to10 line list. The intensities of the molecular opacities are generally falling over this wavelength range, suggesting that the disparity at ~4.1 μm may be resolved once the 10to10 line list is incorporated into new atmospheric models.

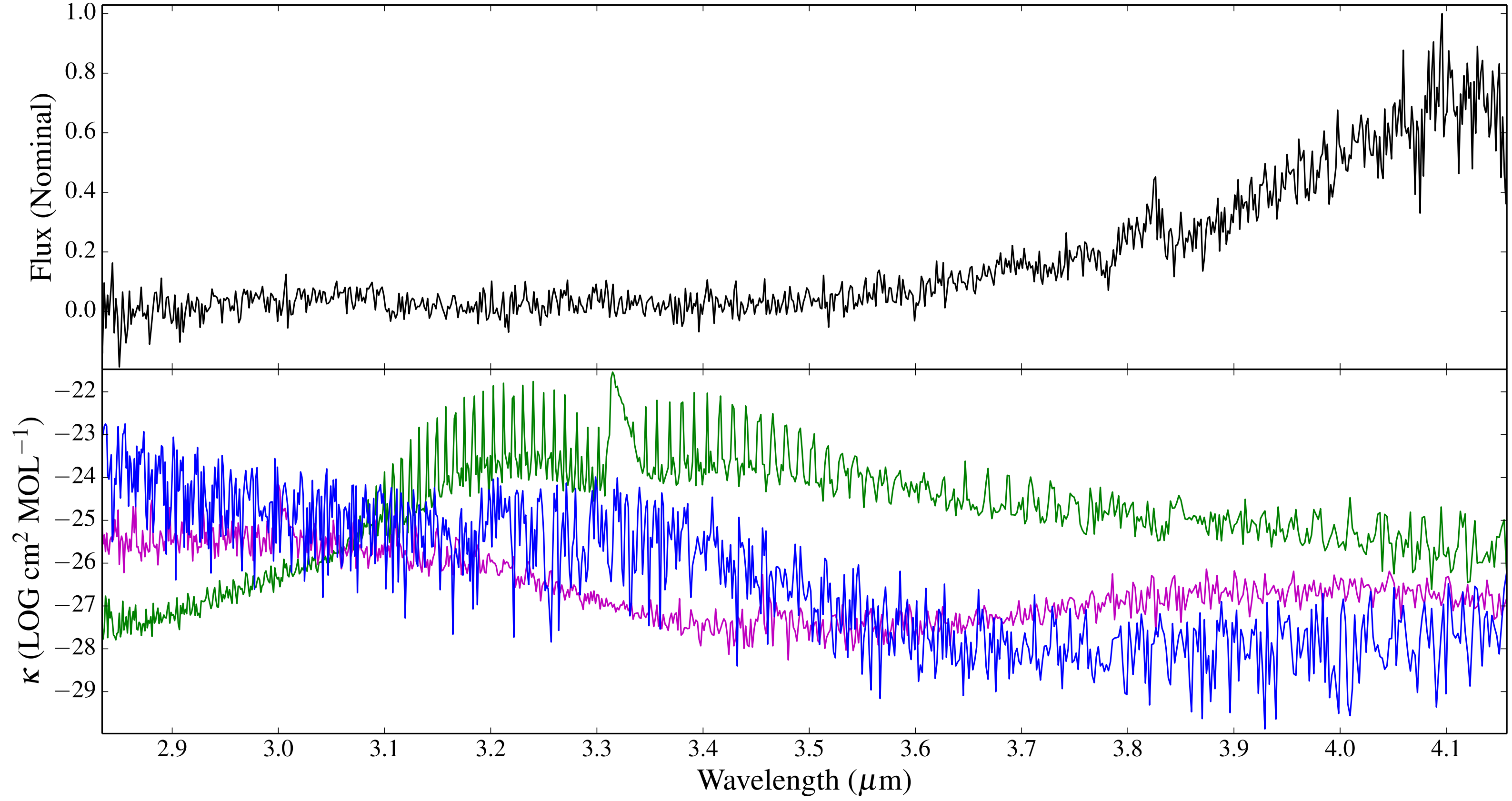

Fig. 3.34: Upper graph is the *L* band spectrum of UGPS 0722. Lower graph shows the scaled absorption cross-sections at 500 K of H_2O, NH_3 and CH_4 derived from the 10to10 line list. Peaking at ~3.3 μm, the CH_4 opacity gradually falls away. This reduction in opacity is matched by an increase in flux in the science spectrum. This suggests that the fall off in flux in the model spectra is indeed due to the shortcomings of an incomplete CH_4 opacity line list.

Chapter 4

Conclusions and further questions

4.1 The $H_2(K)$ index

In Chapter 2, I demonstrated that the K band continuum can be used to constrain the surface gravity in a sample of late M/early L brown dwarfs. I determined that this is most likely due to increased H_2 CIA. Since the K band slope may also be affected by changes in metallicity, I suggested that H_2 CIA will be the dominant factor in shaping the K band slope as long as the brown dwarf has solar metallicity. As the objects I examined in my analysis in Chapter 2 have solar metallicity, surface gravity rather than variations in metallicity will be responsible for the slope of the K band in these objects. I stated that this will be the case for similar objects in the solar neighbourhood, where most star-forming regions have solar metallicity.

I have quantified the change in the K band slope by defining a new spectral index, the $H_2(K)$ index. I found that the $H_2(K)$ index is a good indicator of surface gravity, and, by inference, of age, particularly for objects $\leq$10 Myr, and compares well with other age indicators. For example, the mean $H_2(K)$ index of the 1-2 Myr objects in the extended data set in Chapter 2 is significantly smaller than that of the $\sim$120 Myr Pleiades objects in the same data set (see Table 2.6). Compare this with another age indicator, the triangular H band peak, which is largely unchanged over the same age range. In addition, I found that the mean $H_2(K)$ index of the PMOs in the ONC is smaller than that of the 1-2 Myr objects. I suggest that this is an indicator of the extreme youth of these objects. I also found that the $H_2(K)$ index is at least as good a gravity indicator as the equivalent widths of alkali metal lines, in this case the 2.21 μm Na I doublet. Determining the strength of features such as alkali metal lines requires high quality spectra. This is not the case in calculating the $H_2(K)$ index. As a result, I was able to use the $H_2(K)$ index to corroborate the young age of a PMO in the ONC, whose spectrum was too noisy to resolve narrow spectral features. The $H_2(K)$ index's greater tolerance of low quality data also allowed me to apply my analysis to a sample of objects from other data sets in the literature. The objects had similar spectral types to those in my analysis, and I obtained similar results to those I obtained for the brown dwarfs in my analysis.

In my analysis, I demonstrated that the $H_2(K)$ index can statistically differentiate a population of ~1 Myr objects and a population of ~10 Myr objects. The $H_2(K)$ index can also be used to separate low-mass members from foreground and background objects in young clusters and associations.

My research has shown that the $H_2(K)$ index and the strength of the Na I doublet in σ Orionis 51 indicate that this object's surface gravity is significantly weaker than the other σ Orionis objects in my data set. I found a similar discrepancy in the $H_2(K)$ indices of two TWA objects in the extended data set, although their spectra were not of sufficient quality to allow me to measure the strengths of the corresponding Na I doublets. The surface gravities of these two TWA objects were determined by other researchers (Stelzer et al., 2013) and were found to be weaker than the surface gravities of the TWA M-type stars in their sample. I suggest that my analysis of the σ Orionis cluster is consistent with one object being significantly younger than the others. If true, this would indicate a variation of ages within the cluster. It is also possible that the variations in surface gravities may arise from variations in accretion/formation histories within these clusters and associations. All the data sets I have examined show some scattering of $H_2(K)$ indices within clusters and associations. Considering the uncertainties associated with the data, I cannot say whether this scatter reflects a genuine spread of ages.

While the $H_2(K)$ index is a significant step towards resolving age/mass degeneracy in late M/early L brown dwarfs, I am aware that my sample was lacking objects from clusters and associations with constrained ages >10 Myr. This was particularly noticeable in my analysis of Pleiades objects. While the $H_2(K)$ indices of these objects are consistent with objects having higher surface gravities, there is a large scatter in the values. While the $H_2(K)$ index is more resilient to noise in spectra than other gravity indicators, some of the Pleiades objects' spectra had quite low S/N. The effectiveness of the $H_2(K)$ index as a gravity-indicator would be better tested if it was calculated from better quality spectra from the Pleiades cluster and from other clusters and associations with a greater range of constrained ages.

The $H_2(K)$ index has been used by other researchers to confirm the young ages of newly discovered objects. In particular, Currie et al. (2014) used the $H_2(K)$ index as evidence of the youth of an M8-L0 companion to an M0 primary in the 1−3 Myr ρ Ophiuchus star-forming region.

I am also aware that I have only applied the $H_2(K)$ index to a relatively narrow range of spectral types. Since the near-infrared spectra of brown dwarfs with spectral types <M7 are due more to temperature than to chemical opacity, the K band continua of these objects appear more like those of blackbodies (see Figure 4.1). Therefore, the $H_2(K)$ indices of these objects would be meaningless.

However, it is still possible that the $H_2(K)$ index could be extended to cooler objects. I did not have time to investigate this as I was nearing the end of my PhD studentship. I did consider how the $H_2(K)$ index might be affected in these objects. For example, would the formation of dust particles scatter photons to longer wavelengths, making objects appear younger than their true age? Alternatively, would the increasing importance of CH_4 opacity have the opposite effect, suppressing flux on the long wavelength side of the K band peak, and increasing an object's $H_2(K)$ index? An inspection of the K band spectra of L dwarfs of increasing spectral type suggests that the latter is the case (see Figure 1.9). Fortunately, Schneider et al. (2014) have conducted an analysis of the $H_2(K)$ index in a sample of L dwarfs from the SpeX Prism Spectral Library. As I discussed in Chapter 2, the $H_2(K)$ index in L dwarfs tends to increase with increasing spectral type (see Figure 2.19). Nevertheless, Schneider et al.

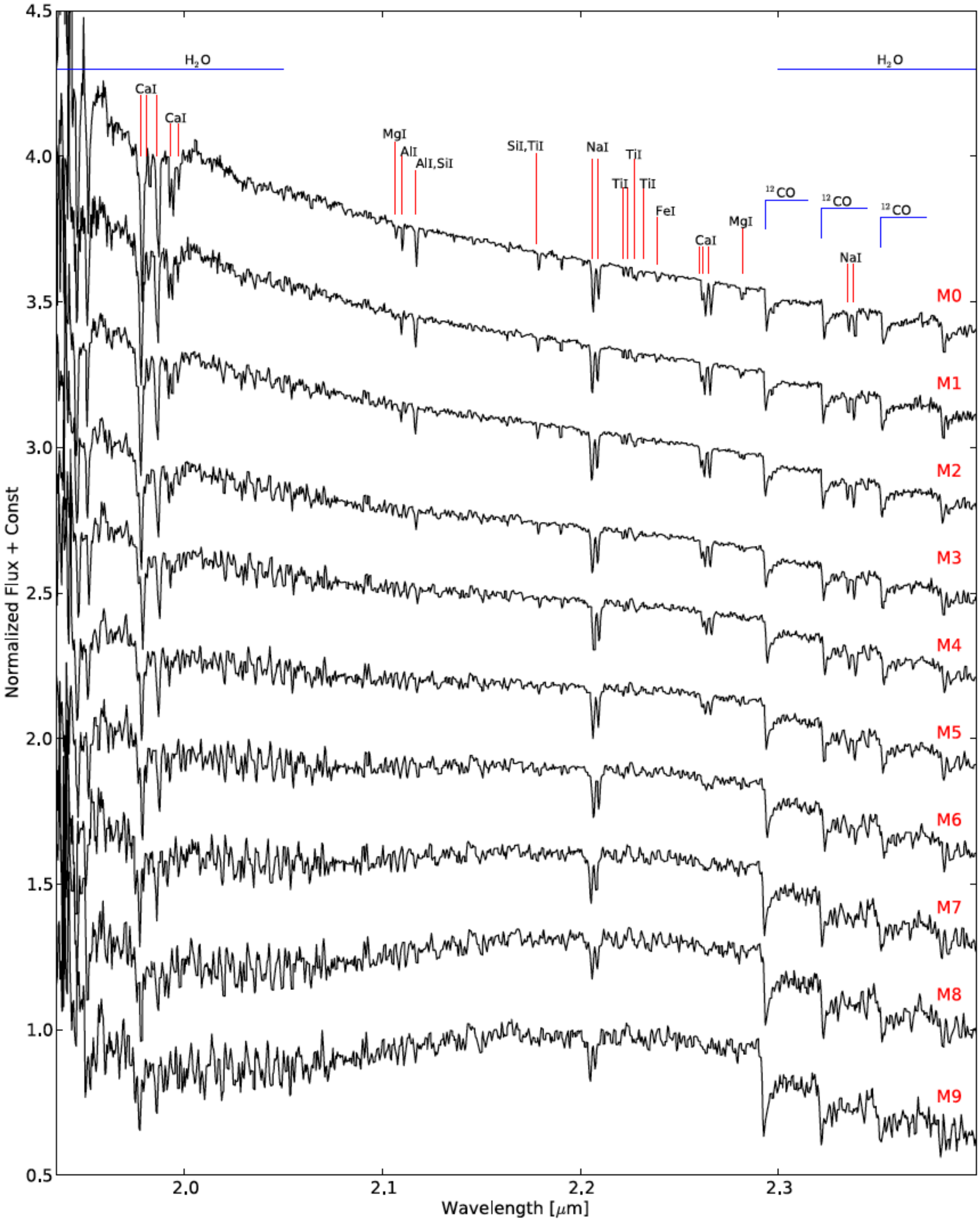

Fig. 4.1: The K band spectrum as a function of spectral type in M-type stars. While narrow spectral features are seen across the range of spectral types, the K band continuum is formed largely by temperature rather than chemical opacity. This is particularly noticeable in the region 2.17-2.24 μm, where the $H_2(K)$ index is calculated. Plot from Rojas-Ayala et al. (2012).

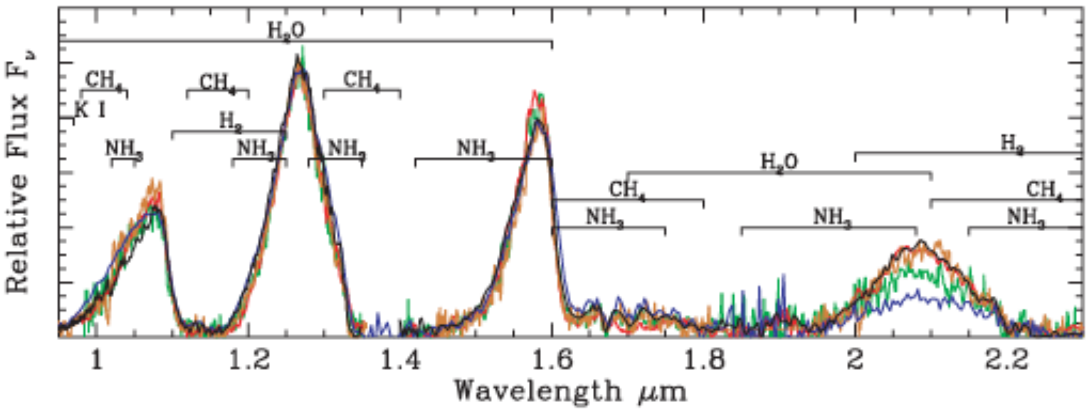

Fig. 4.2: The near-infrared spectra of 2MASS 0415 (T8) (black), ULAS J0034−00 (T9) (brown), ULAS J1335+11 (T9) (red), CFBD J0059−01 (T9) (green), and 2MASS J0939−24 (T8) (blue). CH_4 and NH_3 opacity has largely depleted flux in the region 2.17−2.24 μm. Plot from Leggett et al. (2009).

(2014) found that the $H_2(K)$ index still managed to differentiate young L dwarfs from field dwarfs of similar spectral types.

I have not had time to examine the viability of the $H_2(K)$ index in T dwarfs. However, I think it is unlikely that the index could be applied to these objects. As in the case of M dwarfs, the reason is temperature. At the very cool temperatures of these objects, while H_2 CIA is still an important source of opacity, the near-infrared atmospheres of T dwarfs are dominated by other molecular opacities. In particular, CH_4 opacity, by which T dwarfs are defined, is important, and, for late T dwarfs, NH_3 opacity. It can be seen from Figure 4.2 that in the case of late T dwarfs, CH_4 and NH_3 opacity has removed most of the flux in the wavelength region where the $H_2(K)$ index is calculated.

In both cases where the $H_2(K)$ index has been use by other researchers, it has been used to provide additional support for the young age of a *single* object. In Chapter 2, I observed that the $H_2(K)$ index is more likely to be meaningful when it is applied statistically to populations of objects. However, I think it is reasonable for researchers to use the $H_2(K)$ index for single objects as long as it is understood that the index is only an indicator. The $H_2(K)$ index is not reliable if it is used as a sole indicator, but it could be used for single objects if these objects have other, independent indicators of age.

In this thesis, I have shown that it is not necessary to have high-quality spectra of late M/early L dwarfs in order to constrain the number of these objects in young clusters and the low-mass end of the IMF. The $H_2(K)$ index is well-correlated with age and can be used to assign statistical ages to samples of brown dwarfs in pre-main sequence clusters, which can then be used to differentiate planetary mass brown dwarfs from older brown dwarfs with similar luminosities and temperatures. The $H_2(K)$ index will be of benefit in resolving parameter degeneracy in substellar objects and is already being used by members of the community.

An interesting outcome of my research is the apparent age spread in some young clusters. An object of future research is to determine the extent to which age spreads are responsible for the scatter in measures of surface gravity.

4.2 Opacity in T dwarf atmospheres

The 10to10 line list and the high quality of my data have allowed me to identify a number of new absorption features produced by CH_4 and NH_3 opacity in the near-infrared spectra of two late T dwarfs. I have also been able to correct features which had previously been wrongly identified. Interestingly, a number of features on the short side of the peak flux in the *J* band spectrum of UGPS 0722 which had previously been identified as blended features, appear to be due to NH_3 opacity. While the *J* band spectra of the two T dwarfs appear similar, some absorption features due to CH_4 alone in the spectrum of UGPS 0722 are caused by CH_4 in combination with other opacity sources, or by different opacity sources altogether, in the spectrum of 2MASS 0415. Otherwise, CH_4 opacity is similar in both T dwarfs.

There is a clear discrepancy between the model spectra at ~4.1 μm and the same region in the *L* band spectrum of UGPS 0722. Opacity cross-sections derived from the 10to10 line list suggest that CH_4 opacity decreases across the *L* band. The failings of the model spectra may be remedied when the 10to10 line list is incorporated into new model spectra.

Similarly, the inclusion of the 10to10 line list in model atmospheres will clarify to what extent CH_4 opacity or H_2 CIA is responsible for the steep fall in flux in UGPS 0722 at wavelengths >2.1 μm.

The discrepancies between the data and the Saumon & Marley model spectra which I discussed in Chapter 3 may also be resolved by the inclusion in these model spectra of the 10to10 line list.

References

Ackerman A. S., Marley M. S., 2001, ApJ, 556, 872

Allard F., Guillot T., Ludwig H.-G., Hauschildt P. H., Schweitzer A., Alexander D. R., Ferguson J. W., 2003, in IAU Symposium, Vol. 211, Brown Dwarfs, Martín E., ed., p. 325

Allard F., Hauschildt P. H., Alexander D. R., Tamanai A., Schweitzer A., 2001, ApJ, 556, 357

Allard F., Homeier D., Freytag B., 2011, in Astronomical Society of the Pacific Conference Series, Vol. 448, 16th Cambridge Workshop on Cool Stars, Stellar Systems, and the Sun, Johns-Krull C., Browning M. K., West A. A., eds., p. 91

Allers K. N. et al., 2007, ApJ, 657, 511

Allers K. N., Liu M. C., 2013, ApJ, 772, 79

Alves de Oliveira C., Moraux E., Bouvier J., Bouy H., 2012, A&A, 539, A151

Alves de Oliveira C., Moraux E., Bouvier J., Duchêne G., Bouy H., Maschberger T., Hudelot P., 2013, A&A, 549, A123

Antonova A., Doyle J. G., Hallinan G., Bourke S., Golden A., 2008, A&A, 487, 317

Bailer-Jones C. A. L., Mundt R., 2001, A&A, 367, 218

Bailey J., Kedziora-Chudczer L., 2012, MNRAS, 419, 1913

Baraffe I., Chabrier G., Allard F., Hauschildt P. H., 1998, A&A, 337, 403

Baraffe I., Chabrier G., Allard F., Hauschildt P. H., 2002, A&A, 382, 563

Baraffe I., Vorobyov E., Chabrier G., 2012, ApJ, 756, 118

Barber R. J., Tennyson J., Harris G. J., Tolchenov R. N., 2006, MNRAS, 368, 1087

Barrado y Navascués D., Bouvier J., Stauffer J. R., Lodieu N., McCaughrean M. J., 2002, A&A, 395, 813

Barrado y Navascués D., Stauffer J. R., Bouvier J., Martín E. L., 2001, ApJ, 546, 1006

Basri G., Marcy G. W., Graham J. R., 1996, ApJ, 458, 600

Bate M. R., Bonnell I. A., Bromm V., 2002, MNRAS, 332, L65

Bayo A. et al., 2011, A&A, 536, A63

Becklin E. E., Zuckerman B., 1988, Nature, 336, 656

Beichman C., Gelino C. R., Kirkpatrick J. D., Cushing M. C., Dodson-Robinson S., Marley M. S., Morley C. V., Wright E. L., 2014, ApJ, 783, 68

Béjar V. J. S. et al., 2001, ApJ, 556, 830

Béjar V. J. S., Zapatero Osorio M. R., Rebolo R., Caballero J. A., Barrado D., Martín E. L., Mundt R., Bailer-Jones C. A. L., 2011, ApJ, 743, 64

Bessell M. S., 1991, AJ, 101, 662

Bihain G., Rebolo R., Zapatero Osorio M. R., Béjar V. J. S., Caballero J. A., 2010, A&A, 519, A93

Bochanski J. J., Burgasser A. J., Simcoe R. A., West A. A., 2011, AJ, 142, 169

Bonnefoy M., Chauvin G., Lagrange A.-M., Rojo P., Allard F., Pinte C., Dumas C., Homeier D., 2014, A&A, 562, A127

Bonnet H. et al., 2004, The Messenger, 117, 17

Borysow A., 2002, A&A, 390, 779

Borysow A., Jorgensen U. G., Zheng C., 1997, A&A, 324, 185

Briceño C., Luhman K. L., Hartmann L., Stauffer J. R., Kirkpatrick J. D., 2002, ApJ, 580, 317

Burgasser A. J., Geballe T. R., Leggett S. K., Kirkpatrick J. D., Golimowski D. A., 2006, ApJ, 637, 1067

Burgasser A. J. et al., 2002a, ApJ, 564, 421

Burgasser A. J. et al., 2002b, ApJ, 564, 421

Burningham B. et al., 2013, MNRAS, 433, 457

Burrows A., Hubbard W. B., Lunine J. I., Liebert J., 2001, Reviews of Modern Physics, 73, 719

Burrows A., Liebert J., 1993, Reviews of Modern Physics, 65, 301

Burrows A., Sharp C. M., 1999, ApJ, 512, 843

Burrows A., Sudarsky D., Hubeny I., 2006, ApJ, 640, 1063

Caballero J. A. et al., 2007, A&A, 470, 903

Caballero J. A., Cabrera-Lavers A., García-Álvarez D., Pascual S., 2012, A&A, 546, A59

Canty J. I., Lucas P. W., Roche P. F., Pinfield D. J., 2013a, Mem. Soc. Astron. Italiana, 84, 1110

Canty J. I., Lucas P. W., Roche P. F., Pinfield D. J., 2013b, MNRAS, 435, 2650

Casewell S. L., Dobbie P. D., Hodgkin S. T., Moraux E., Jameson R. F., Hambly N. C., Irwin J., Lodieu N., 2007, MNRAS, 378, 1131

Chabrier G., 2003, PASP, 115, 763

Chabrier G., 2005, in Astrophysics and Space Science Library, Vol. 327, The Initial Mass Function 50 Years Later, Corbelli E., Palla F., Zinnecker H., eds., p. 41

Chabrier G., Baraffe I., 1997, A&A, 327, 1039

Chabrier G., Baraffe I., Allard F., Hauschildt P., 2000, ApJ, 542, L119

Close L. M. et al., 2007, ApJ, 660, 1492

Cruz K. L., Kirkpatrick J. D., Burgasser A. J., 2009, AJ, 137, 3345

Currie T., Burrows A., Daemgen S., 2014, ApJ, 787, 104

Currie T., Daemgen S., Debes J., Lafreniere D., Itoh Y., Jayawardhana R., Ratzka T., Correia S., 2014, ApJ, 780, L30

Cushing M. C. et al., 2011, ApJ, 743, 50

Cushing M. C. et al., 2008, ApJ, 678, 1372

Cushing M. C., Rayner J. T., Vacca W. D., 2005, ApJ, 623, 1115

Cushing M. C. et al., 2006, ApJ, 648, 614

D'Antona F., Mazzitelli I., 1997, Mem. Soc. Astron. Italiana, 68, 807

de Wit W. J. et al., 2006, A&A, 448, 189

Delorme P. et al., 2008, A&A, 482, 961

Dupuy T. J., Kraus A. L., 2013, Science, 341, 1492

Dupuy T. J., Liu M. C., 2012, ApJS, 201, 19

Eisenhauer F. et al., 2003, in Society of Photo-Optical Instrumentation Engineers (SPIE) Conference Series, Vol. 4841, Instrument Design and Performance for Optical/Infrared Ground-based Telescopes, Iye M., Moorwood A. F. M., eds., pp. 1548–1561

Elmegreen B. G., 2000, ApJ, 530, 277

Faherty J. K., Burgasser A. J., Cruz K. L., Shara M. M., Walter F. M., Gelino C. R., 2009, AJ, 137, 1

Faherty J. K. et al., 2012, ApJ, 752, 56

Faherty J. K., Rice E. L., Cruz K. L., Mamajek E. E., Núñez A., 2013, AJ, 145, 2

Fegley, Jr. B., Lodders K., 1996, ApJ, 472, L37

Frasca A., Guillout P., Marilli E., Freire Ferrero R., Biazzo K., Klutsch A., 2006, A&A, 454, 301

Freedman R. S., Marley M. S., Lodders K., 2008, ApJS, 174, 504

Frommhold L., Abel M., Wang F., Gustafsson M., Li X., Hunt K., 2010, Molecular Physics, 108, 2265

Geballe T. R. et al., 2002, ApJ, 564, 466

Geballe T. R., Kulkarni S. R., Woodward C. E., Sloan G. C., 1996, ApJ, 467, L101

Geballe T. R., Saumon D., Golimowski D. A., Leggett S. K., Marley M. S., Noll K. S., 2009, ApJ, 695, 844

Geißler K., Metchev S. A., Pham A., Larkin J. E., McElwain M., Hillenbrand L. A., 2012, ApJ, 746, 44

Gizis J. E., 2002, ApJ, 575, 484

Gizis J. E. et al., 2012, AJ, 144, 94

Golimowski D. A. et al., 2004, AJ, 127, 3516

Gómez Maqueo Chew Y., Stassun K. G., Prša A., Mathieu R. D., 2009, ApJ, 699, 1196

Goodwin S. P., Whitworth A. P., Ward-Thompson D., 2004, A&A, 414, 633

Gorlova N. I., Meyer M. R., Rieke G. H., Liebert J., 2003, ApJ, 593, 1074

Guieu S., Dougados C., Monin J.-L., Magnier E., Martín E. L., 2006, A&A, 446, 485

Guieu S. et al., 2007, A&A, 465, 855

Guthrie B. N. G., 1965, Publications of the Royal Observatory of Edinburgh, 3, 264

Hargreaves R. J., Beale C. A., Michaux L., Irfan M., Bernath P. F., 2012, ApJ, 757, 46

Hargreaves R. J., Li G., Bernath P. F., 2011, ApJ, 735, 111

Hawley S., Reid I. N., Gizis J., 2000, in Astronomical Society of the Pacific Conference Series, Vol. 212, From Giant Planets to Cool Stars, Griffith C. A., Marley M. S., eds., p. 252

Hayashi C., Nakano T., 1963, Progress of Theoretical Physics, 30, 460

Helling C. et al., 2008, MNRAS, 391, 1854

Henry T. J., Kirkpatrick J. D., Simons D. A., 1994, AJ, 108, 1437

Hillenbrand L. A., 1997, AJ, 113, 1733

Irwin M., McMahon R. G., Reid N., 1991, MNRAS, 252, 61P

Irwin P. G. J., 2003, Giant planets of our solar system : atmospheres compositions, and structure

Jayawardhana R., Ardila D. R., Stelzer B., Haisch, Jr. K. E., 2003, AJ, 126, 1515

Jayawardhana R., Hartmann L., Fazio G., Fisher R. S., Telesco C. M., Piña R. K., 1999, ApJ, 521, L129

Jeffries R. D., Littlefair S. P., Naylor T., Mayne N. J., 2011, MNRAS, 418, 1948

Joergens V., Guenther E., 2001, A&A, 379, L9

Jones H. R. A., Tsuji T., 1997, ApJ, 480, L39

Kenyon M. J., Jeffries R. D., Naylor T., 2001, ArXiv Astrophysics e-prints

Kenyon M. J., Jeffries R. D., Naylor T., Oliveira J. M., Maxted P. F. L., 2005, MNRAS, 356, 89

Kenyon S. J., Hartmann L. W., Strom K. M., Strom S. E., 1990, AJ, 99, 869

King R. R., McCaughrean M. J., Homeier D., Allard F., Scholz R.-D., Lodieu N., 2010, A&A, 510, A99

Kirkpatrick J. D., 1998, in Astronomical Society of the Pacific Conference Series, Vol. 134, Brown Dwarfs and Extrasolar Planets, Rebolo R., Martin E. L., Zapatero Osorio M. R., eds., p. 405

Kirkpatrick J. D., 2005, ARA&A, 43, 195

Kirkpatrick J. D., Barman T. S., Burgasser A. J., McGovern M. R., McLean I. S., Tinney C. G., Lowrance P. J., 2006, ApJ, 639, 1120

Kirkpatrick J. D., Beichman C. A., Skrutskie M. F., 1997, ApJ, 476, 311

Kirkpatrick J. D. et al., 2012, ApJ, 753, 156

Kirkpatrick J. D., Henry T. J., Liebert J., 1993, ApJ, 406, 701

Kirkpatrick J. D., Henry T. J., McCarthy, Jr. D. W., 1991, ApJS, 77, 417

Kirkpatrick J. D., Henry T. J., Simons D. A., 1995, AJ, 109, 797

Kirkpatrick J. D. et al., 2010, ApJS, 190, 100

Kirkpatrick J. D. et al., 1999, ApJ, 519, 802

Knapp G. R. et al., 2004, AJ, 127, 3553

Kobayashi N. et al., 2000, in Society of Photo-Optical Instrumentation Engineers (SPIE) Conference Series, Vol. 4008, Optical and IR Telescope Instrumentation and Detectors, Iye M., Moorwood A. F., eds., pp. 1056–1066

Kroupa P., 2001, MNRAS, 322, 231

Kumar S. S., 1962, AJ, 67, 579

Lawrence A. et al., 2007, MNRAS, 379, 1599

Leggett S. K., Allard F., Geballe T. R., Hauschildt P. H., Schweitzer A., 2001, ApJ, 548, 908

Leggett S. K. et al., 2009, ApJ, 695, 1517

Leggett S. K. et al., 2000, ApJ, 536, L35

Leggett S. K., Saumon D., Marley M. S., Geballe T. R., Golimowski D. A., Stephens D., Fan X., 2007, ApJ, 655, 1079

Leggett S. K. et al., 2012, ApJ, 748, 74

Liu M. C. et al., 2011, ApJ, 740, L32

Liu M. C. et al., 2013, ApJ, 777, L20

Lodders K., 1999, ApJ, 519, 793

Lodders K., 2002, ApJ, 577, 974

Lodieu N., de Wit W.-J., Carraro G., Moraux E., Bouvier J., Hambly N. C., 2011, A&A, 532, A103

Lodieu N., Deacon N. R., Hambly N. C., Boudreault S., 2012, MNRAS, 426, 3403

Lodieu N., Dobbie P. D., Deacon N. R., Hodgkin S. T., Hambly N. C., Jameson R. F., 2007, MNRAS, 380, 712

Lodieu N., Hambly N. C., Jameson R. F., Hodgkin S. T., 2008, MNRAS, 383, 1385

Lodieu N., McCaughrean M. J., Barrado Y Navascués D., Bouvier J., Stauffer J. R., 2005, A&A, 436, 853

Looper D. L., Burgasser A. J., Kirkpatrick J. D., Swift B. J., 2007, ApJ, 669, L97

Looper D. L. et al., 2008, ApJ, 686, 528

Lucas P. W., Roche P. F., 2000, MNRAS, 314, 858

Lucas P. W., Roche P. F., Tamura M., 2005, MNRAS, 361, 211

Lucas P. W. et al., 2010, MNRAS, 408, L56

Lucas P. W., Weights D. J., Roche P. F., Riddick F. C., 2006, MNRAS, 373, L60

Luhman K. L., 1999, ApJ, 525, 466

Luhman K. L., 2004, ApJ, 617, 1216

Luhman K. L., 2012, ARA&A, 50, 65

Luhman K. L., Allers K. N., Jaffe D. T., Cushing M. C., Williams K. A., Slesnick C. L., Vacca W. D., 2007, ApJ, 659, 1629

Luhman K. L., Briceño C., Stauffer J. R., Hartmann L., Barrado y Navascués D., Caldwell N., 2003a, ApJ, 590, 348

Luhman K. L., Mamajek E. E., Allen P. R., Muench A. A., Finkbeiner D. P., 2009, ApJ, 691, 1265

Luhman K. L., Peterson D. E., Megeath S. T., 2004, ApJ, 617, 565

Luhman K. L., Rieke G. H., Young E. T., Cotera A. S., Chen H., Rieke M. J., Schneider G., Thompson R. I., 2000, ApJ, 540, 1016

Luhman K. L., Stauffer J. R., Muench A. A., Rieke G. H., Lada E. A., Bouvier J., Lada C. J., 2003b, ApJ, 593, 1093

Luhman K. L., Stauffer J. R., Muench A. A., Rieke G. H., Lada E. A., Bouvier J., Lada C. J., 2003c, ApJ, 593, 1093

Lyubchik Y., Jones H. R. A., Pavlenko Y. V., Pinfield D. J., Covey K. R., 2012, MNRAS, 422, 2195

Mainzer A. K. et al., 2007, ApJ, 662, 1245

Manara C. F. et al., 2013, A&A, 551, A107

Marley M. S., Fortney J. J., Hubickyj O., Bodenheimer P., Lissauer J. J., 2007, ApJ, 655, 541

Marley M. S., Seager S., Saumon D., Lodders K., Ackerman A. S., Freedman R. S., Fan X., 2002, ApJ, 568, 335

Marocco F. et al., 2014, MNRAS, 439, 372

Martín E. L., Delfosse X., Guieu S., 2004, AJ, 127, 449

Martin E. L., Rebolo R., Zapatero-Osorio M. R., 1996, ApJ, 469, 706

McGovern M. R., Kirkpatrick J. D., McLean I. S., Burgasser A. J., Prato L., Lowrance P. J., 2004, ApJ, 600, 1020

McGregor P. J. et al., 2003, in Society of Photo-Optical Instrumentation Engineers (SPIE) Conference Series, Vol. 4841, Instrument Design and Performance for Optical/Infrared Ground-based Telescopes, Iye M., Moorwood A. F. M., eds., pp. 1581–1591

McLean I. S., McGovern M. R., Burgasser A. J., Kirkpatrick J. D., Prato L., Kim S. S., 2003, ApJ, 596, 561

Mohanty S., Basri G., Jayawardhana R., Allard F., Hauschildt P., Ardila D., 2004, ApJ, 609, 854

Mohanty S., Jayawardhana R., Basri G., 2005, ApJ, 626, 498

Mohanty S., Stassun K. G., 2012, ApJ, 758, 12

Moraux E., Bouvier J., Stauffer J. R., Barrado y Navascués D., Cuillandre J.-C., 2007, A&A, 471, 499

Moraux E., Bouvier J., Stauffer J. R., Cuillandre J.-C., 2003, A&A, 400, 891

Morgan W. W., Keenan P. C., Kellman E., 1943, An atlas of stellar spectra, with an outline of spectral classification

Morley C. V., Fortney J. J., Marley M. S., Visscher C., Saumon D., Leggett S. K., 2012, ApJ, 756, 172

Muench A. A., Lada C. J., Luhman K. L., Muzerolle J., Young E., 2007, AJ, 134, 411

Mužić K., Scholz A., Geers V., Jayawardhana R., Tamura M., 2012, ApJ, 744, 134

Muzerolle J., Luhman K. L., Briceño C., Hartmann L., Calvet N., 2005, ApJ, 625, 906

Nakajima T., Oppenheimer B. R., Kulkarni S. R., Golimowski D. A., Matthews K., Durrance S. T., 1995, Nature, 378, 463

Nassar R., Bernath P., 2003, J. Quant. Spec. Radiat. Transf., 82, 279

Natta A., Testi L., Muzerolle J., Randich S., Comerón F., Persi P., 2004, A&A, 424, 603

Neuhäuser R., Schmidt T. O. B., Seifahrt A., Bedalov A., Helling C., Witte S., Hauschildt P., 2009, in American Institute of Physics Conference Series, Vol. 1094, 15th Cambridge Workshop on Cool Stars, Stellar Systems, and the Sun, Stempels E., ed., pp. 844–847

Noll K. S., Geballe T. R., Leggett S. K., Marley M. S., 2000, ApJ, 541, L75

Oppenheimer B. R., 2014, in Astrophysics and Space Science Library, Vol. 401, Astrophysics and Space Science Library, Joergens V., ed., p. 81

Oppenheimer B. R., Kulkarni S. R., Matthews K., Nakajima T., 1995, Science, 270, 1478

Palla F., Stahler S. W., 1999, ApJ, 525, 772

Patience J., King R. R., De Rosa R. J., Vigan A., Witte S., Rice E., Helling C., Hauschildt P., 2012, A&A, 540, A85

Peña Ramírez K., Béjar V. J. S., Zapatero Osorio M. R., Petr-Gotzens M. G., Martín E. L., 2012, ApJ, 754, 30

Pecaut M. J., Mamajek E. E., Bubar E. J., 2012, ApJ, 746, 154

Pinfield D. J., Dobbie P. D., Jameson R. F., Steele I. A., Jones H. R. A., Katsiyannis A. C., 2003, MNRAS, 342, 1241

Pinfield D. J. et al., 2014, MNRAS, 444, 1931

Pinfield D. J., Hodgkin S. T., Jameson R. F., Cossburn M. R., Hambly N. C., Devereux N., 2000, MNRAS, 313, 347

Prosser C. F., Stauffer J. R., Hartmann L., Soderblom D. R., Jones B. F., Werner M. W., McCaughrean M. J., 1994, ApJ, 421, 517

Rayner J. T., Cushing M. C., Vacca W. D., 2009, ApJS, 185, 289

Rayner J. T., Toomey D. W., Onaka P. M., Denault A. J., Stahlberger W. E., Vacca W. D., Cushing M. C., Wang S., 2003, PASP, 115, 362

Rebolo R., Martin E. L., Basri G., Marcy G. W., Zapatero-Osorio M. R., 1996, ApJ, 469, L53

Rebolo R., Zapatero Osorio M. R., Martín E. L., 1995, Nature, 377, 129

Reid I. N., Burgasser A. J., Cruz K. L., Kirkpatrick J. D., Gizis J. E., 2001, AJ, 121, 1710

Reid I. N., Kirkpatrick J. D., Gizis J. E., Liebert J., 1999, ApJ, 527, L105

Reiners A., Seifahrt A., Stassun K. G., Melo C., Mathieu R. D., 2007, ApJ, 671, L149

Reipurth B., Clarke C., 2001, AJ, 122, 432

Richard C. et al., 2012, J. Quant. Spec. Radiat. Transf., 113, 1276

Riddick F. C., Roche P. F., Lucas P. W., 2007, MNRAS, 381, 1077

Rigby M., Manning A. J., Prinn R. G., 2012, Journal of Geophysical Research (Atmospheres), 117, 12312

Roellig T. L. et al., 2004, ApJS, 154, 418

Rojas-Ayala B., Covey K. R., Muirhead P. S., Lloyd J. P., 2012, ApJ, 748, 93

Rothman L. S. et al., 2009, J. Quant. Spec. Radiat. Transf., 110, 533

Salpeter E. E., 1955, ApJ, 121, 161

Santos N. C., Melo C., James D. J., Gameiro J. F., Bouvier J., Gomes J. I., 2008, A&A, 480, 889

Saumon D., Bergeron P., Lunine J. I., Hubbard W. B., Burrows A., 1994, ApJ, 424, 333

Saumon D., Marley M. S., 2008, ApJ, 689, 1327

Saumon D., Marley M. S., Abel M., Frommhold L., Freedman R. S., 2012, ApJ, 750, 74

Saumon D., Marley M. S., Cushing M. C., Leggett S. K., Roellig T. L., Lodders K., Freedman R. S., 2006, ApJ, 647, 552

Saumon D. et al., 2007, ApJ, 656, 1136

Schmidt T. O. B., Neuhäuser R., Seifahrt A., Vogt N., Bedalov A., Helling C., Witte S., Hauschildt P. H., 2008, A&A, 491, 311

Schneider A. C., Cushing M. C., Kirkpatrick J. D., Mace G. N., Gelino C. R., Faherty J. K., Fajardo-Acosta S., Sheppard S. S., 2014, AJ, 147, 34

Scholz A., Jayawardhana R., Brandeker A., 2005, ApJ, 629, L41

Scholz A., Jayawardhana R., Muzic K., Geers V., Tamura M., Tanaka I., 2012, ApJ, 756, 24

Shu F. H., 1977, ApJ, 214, 488

Simcoe R. A. et al., 2010, in Society of Photo-Optical Instrumentation Engineers (SPIE) Conference Series, Vol. 7735, Society of Photo-Optical Instrumentation Engineers (SPIE) Conference Series

Skrutskie M. F. et al., 2006, AJ, 131, 1163

Slesnick C. L., Carpenter J. M., Hillenbrand L. A., 2006, AJ, 131, 3016

Stamatellos D., 2014, in Advances in Solid State Physics, Vol. 36, Advances in Solid State Physics, Stamatellos D., Goodwin S., Ward-Thompson D., eds., p. 17

Stassun K. G., Mathieu R. D., Valenti J. A., 2006, Nature, 440, 311

Stauffer J. R., Hamilton D., Probst R. G., 1994, AJ, 108, 155

Steele I. A., Jameson R. F., 1995, MNRAS, 272, 630

Stelzer B. et al., 2013, A&A, 558, A141

Stephens D. C. et al., 2009, ApJ, 702, 154

Sterzik M. F., Pascucci I., Apai D., van der Bliek N., Dullemond C. P., 2004, A&A, 427, 245

Stoeckley T. R., 1968, MNRAS, 140, 149

Tennyson J., Yurchenko S. N., 2012, MNRAS, 425, 21

Terebey S., Shu F. H., Cassen P., 1984, ApJ, 286, 529

Tokunaga A. T., Kobayashi N., 1999, AJ, 117, 1010

Tsuji T., 2002, ApJ, 575, 264

Tsuji T., 2005, ApJ, 621, 1033

Tsuji T., Nakajima T., Yanagisawa K., 2004, ApJ, 607, 511

Tsuji T., Ohnaka K., Aoki W., 1996, A&A, 305, L1

Vernet J. et al., 2011, A&A, 536, A105

Vrba F. J. et al., 2004, AJ, 127, 2948

Weights D. J., Lucas P. W., Roche P. F., Pinfield D. J., Riddick F., 2009, MNRAS, 392, 817

Wenger C., Champion J. P., 1998, J. Quant. Spec. Radiat. Transf., 59, 471

Whitworth A. P., Stamatellos D., 2006, A&A, 458, 817

Winston E. et al., 2009, AJ, 137, 4777

Wright E. L. et al., 2010, AJ, 140, 1868

Yamamura I., Tsuji T., Tanabé T., 2010, ApJ, 722, 682

York D. G. et al., 2000, AJ, 120, 1579

Yurchenko S. N., Barber R. J., Tennyson J., 2011, MNRAS, 413, 1828

Yurchenko S. N., Tennyson J., 2014, MNRAS

Yurchenko S. N., Tennyson J., Bailey J., Hollis M. D. J., Tinetti G., 2014, Proc. Am. Acad. Sci., 111, 9379

Zapatero Osorio M. R., Béjar V. J. S., Martín E. L., Rebolo R., Barrado y Navascués D., Bailer-Jones C. A. L., Mundt R., 2000, Science, 290, 103

Zapatero Osorio M. R., Martín E. L., Béjar V. J. S., Bouy H., Deshpande R., Wainscoat R. J., 2007, ApJ, 666, 1205

Appendix A

CH_4 ro-vibrational transition lines

Table A.1: R-branch CH_4 ro-vibrational transition lines producing absorption features in the *J* band spectra of UGPS 0722 and 2MASS 0415 (shaded)

λ (μm)	Intensity (cm MOL^{-1})	$\Delta\Gamma$	ΔJ	$\Delta\nu_2$	ΔL2	$\Delta\nu_3$	ΔL3	ΔM3
1.3111927	1.94E-23	A1 → A2	10 → 11	0 → 1	0 → 1	0 → 2	0 → 2	0 → 1
	1.38E-23	A1 → A2	10 → 11	0 → 1	0 → 1	0 → 2	0 → 2	0 → 1
1.3128914	3.59E-23	A1 → A2	9 → 10	0 → 1	0 → 1	0 → 2	0 → 2	0 → 1
	2.32E-23	A1 → A2	9 → 10	0 → 1	0 → 1	0 → 2	0 → 2	0 → 1
1.3166163	6.50E-23	A2 → A1	7 → 8	0 → 1	0 → 1	0 → 2	0 → 2	0 → 1
	3.54E-23	A2 → A1	7 → 8	0 → 1	0 → 1	0 → 2	0 → 2	0 → 1
1.3184149	7.76E-23	F1 → F2	6 → 7	0 → 1	0 → 1	0 → 2	0 → 2	0 → 1
	3.94E-23	F1 → F2	6 → 7	0 → 1	0 → 1	0 → 2	0 → 2	0 → 1
1.3184160	7.66E-23	A1 → A2	6 → 7	0 → 1	0 → 1	0 → 2	0 → 2	0 → 1
	3.89E-23	A1 → A2	6 → 7	0 → 1	0 → 1	0 → 2	0 → 2	0 → 1
1.3184211	7.48E-23	F2 → F1	6 → 7	0 → 1	0 → 1	0 → 2	0 → 2	0 → 1
	3.80E-23	F2 → F1	6 → 7	0 → 1	0 → 1	0 → 2	0 → 2	0 → 1
1.3184622	7.26E-23	E → E	6 → 7	0 → 1	0 → 1	0 → 2	0 → 2	0 → 1
	3.69E-23	E → E	6 → 7	0 → 1	0 → 1	0 → 2	0 → 2	0 → 1
1.3184644	6.57E-23	F2 → F1	6 → 7	0 → 1	0 → 1	0 → 2	0 → 2	0 → 1
	3.33E-23	F2 → F1	6 → 7	0 → 1	0 → 1	0 → 2	0 → 2	0 → 1
1.3184738	6.14E-23	A2 → A1	6 → 7	0 → 1	0 → 1	0 → 2	0 → 2	0 → 1
	3.12E-23	A2 → A1	6 → 7	0 → 1	0 → 1	0 → 2	0 → 2	0 → 1
1.3220974	1.54E-22	A1 → A2	4 → 5	0 → 1	0 → 1	0 → 2	0 → 2	0 → 1

Continued on next page

Table A1 – Continued from previous page

λ (μm)	Intensity (cm MOL^{-1})	$\Delta\Gamma$	ΔJ	$\Delta\nu_2$	ΔL2	$\Delta\nu_3$	ΔL3	ΔM3
	7.00E-23	A1 → A2	4 → 5	0 → 1	0 → 1	0 → 2	0 → 2	0 → 1
1.3220991	1.17E-22	F1 → F2	4 → 5	0 → 1	0 → 1	0 → 2	0 → 2	0 → 1
	5.31E-23	F1 → F2	4 → 5	0 → 1	0 → 1	0 → 2	0 → 2	0 → 1
1.3221013	1.01E-22	F2 → F1	4 → 5	0 → 1	0 → 1	0 → 2	0 → 2	0 → 1
	4.59E-23	F2 → F1	4 → 5	0 → 1	0 → 1	0 → 2	0 → 2	0 → 1
1.3221177	1.32E-22	E → E	4 → 5	0 → 1	0 → 1	0 → 2	0 → 2	0 → 1
	6.00E-23	E → E	4 → 5	0 → 1	0 → 1	0 → 2	0 → 2	0 → 1
1.3239472	1.47E-22	F1 → F2	3 → 4	0 → 1	0 → 1	0 → 2	0 → 2	0 → 1
	6.40E-23	F1 → F2	3 → 4	0 → 1	0 → 1	0 → 2	0 → 2	0 → 1
1.3239478	1.88E-22	F2 → F1	3 → 4	0 → 1	0 → 1	0 → 2	0 → 2	0 → 1
	8.20E-23	F2 → F1	3 → 4	0 → 1	0 → 1	0 → 2	0 → 2	0 → 1
1.3239481	2.02E-22	A2 → A1	3 → 4	0 → 1	0 → 1	0 → 2	0 → 2	0 → 1
	8.80E-23	A2 → A1	3 → 4	0 → 1	0 → 1	0 → 2	0 → 2	0 → 1

Table A.2: R-branch CH_4 ro-vibrational transition lines producing absorption features in the *H* band spectra of UGPS 0722 and 2MASS 0415 (shaded)

λ (μm)	Intensity (cm MOL^{-1})	$\Delta\Gamma$	ΔJ	$\Delta\nu_3$	ΔL3	ΔM3
1.6240333	1.52E-22	A2 → A1	15 → 16	0 → 2	0 → 2	0 → 1
	2.08E-22	A2 → A1	15 → 16	0 → 2	0 → 2	0 → 1
1.6240517	1.48E-22	F2 → F1	15 → 16	0 → 2	0 → 2	0 → 1
	2E-22	F2 → F1	15 → 16	0 → 2	0 → 2	0 → 1
1.6281563	2.50E-22	F1 → F2	13 → 14	0 → 2	0 → 2	0 → 1
	2.56E-22	F1 → F2	13 → 14	0 → 2	0 → 2	0 → 1
1.6281768	2.38E-22	A1 → A2	13 → 14	0 → 2	0 → 2	0 → 1
	2.43E-22	A1 → A2	13 → 14	0 → 2	0 → 2	0 → 1
1.6282749	1.57E-22	F2 → F1	13 → 14	0 → 2	0 → 2	0 → 1
	1.61E-22	F2 → F1	13 → 14	0 → 2	0 → 2	0 → 1
1.6282869	1.01E-22	F2 → F1	13 → 14	0 → 2	0 → 2	0 → 1
	1.03E-22	F2 → F1	13 → 14	0 → 2	0 → 2	0 → 1
1.6282912	2.22E-22	E → E	13 → 14	0 → 2	0 → 2	0 → 1
	2.27E-22	E → E	13 → 14	0 → 2	0 → 2	0 → 1
1.6283965	1.17E-22	F1 → F2	13 → 14	0 → 2	0 → 2	0 → 1
	1.20E-22	F1 → F2	13 → 14	0 → 2	0 → 2	0 → 1
1.6284230	2.53E-22	A2 → A1	13 → 14	0 → 2	0 → 2	0 → 1
	2.59E-22	A2 → A1	13 → 14	0 → 2	0 → 2	0 → 1
1.6284413	1.81E-22	F1 → F2	13 → 14	0 → 2	0 → 2	0 → 1
	1.85E-22	F1 → F2	13 → 14	0 → 2	0 → 2	0 → 1
1.6284557	2.05E-22	F1 → F2	13 → 14	0 → 2	0 → 2	0 → 1
	2.10E-22	F1 → F2	13 → 14	0 → 2	0 → 2	0 → 1
1.6284920	1.82E-22	F2 → F1	13 → 14	0 → 2	0 → 2	0 → 1
	1.86E-22	F2 → F1	13 → 14	0 → 2	0 → 2	0 → 1
1.6285142	2.62E-22	E → E	13 → 14	0 → 2	0 → 2	0 → 1
	2.68E-22	E → E	13 → 14	0 → 2	0 → 2	0 → 1
1.6305299	4.19E-22	E → E	12 → 13	0 →2	0 → 2	0 → 1
	3.76E-22	E → E	12 → 13	0 →2	0 → 2	0 → 1
1.6305331	3.67E-22	F2 → F1	12 → 13	0 →2	0 → 2	0 → 1
	3.30E-22	F2 → F1	12 → 13	0 →2	0 → 2	0 → 1
1.6305519	3.59E-22	A2 → A1	12 → 13	0 →2	0 → 2	0 → 1

Continued on next page

Table A2 – Continued from previous page

λ (μm)	Intensity (cm MOL^{-1})	ΔΓ	ΔJ	$\Delta\nu_3$	ΔL3	ΔM3
	3.22E-22	A2 → A1	12 → 13	0 →2	0 → 2	0 → 1
1.6306226	4.69E-22	F2 → F1	12 → 13	0 →2	0 → 2	0 → 1
	4.21E-22	F2 → F1	12 → 13	0 →2	0 → 2	0 → 1
1.6306305	5.00E-22	F1 → F2	12 → 13	0 →2	0 → 2	0 → 1
	4.49E-22	F1 → F2	12 → 13	0 →2	0 → 2	0 → 1
1.6306371	4.98E-22	A1 → A2	12 → 13	0 →2	0 → 2	0 → 1
	4.47E-22	A1 → A2	12 → 13	0 →2	0 → 2	0 → 1
1.6307596	4.62E-22	F1 → F2	12 → 13	0 →2	0 → 2	0 → 1
	4.15E-22	F1 → F2	12 → 13	0 →2	0 → 2	0 → 1
1.6307951	4.76E-22	E → E	12 → 13	0 →2	0 → 2	0 → 1
	4.27E-22	E → E	12 → 13	0 →2	0 → 2	0 → 1
1.6307968	3.78E-22	F2 → F1	12 → 13	0 →2	0 → 2	0 → 1
	3.39E-22	F2 → F1	12 → 13	0 →2	0 → 2	0 → 1
1.6308561	4.61E-22	F1 → F2	12 → 13	0 →2	0 → 2	0 → 1
	4.14E-22	F1 → F2	12 → 13	0 →2	0 → 2	0 → 1
1.6309237	5.04E-22	A1 → A2	12 → 13	0 →2	0 → 2	0 → 1
	4.53E-22	A1 → A2	12 → 13	0 →2	0 → 2	0 → 1
1.6310294	1.58E-22	A2 → A1	12 → 13	0 →2	0 → 2	0 → 1
	1.42E-22	A2 → A1	12 → 13	0 →2	0 → 2	0 → 1
1.6330080	6.53E-22	F1 → F2	11 → 12	0 → 2	0 → 2	0 → 1
	5.21E-22	F1 → F2	11 → 12	0 → 2	0 → 2	0 → 1
1.6330100	1.82E-22	F1 → F2	11 → 12	0 → 2	0 → 2	0 → 1
	1.45E-22	F1 → F2	11 → 12	0 → 2	0 → 2	0 → 1
1.6330698	1.11E-22	E → E	11 → 12	0 → 2	0 → 2	0 → 1
	8.82E-23	E → E	11 → 12	0 → 2	0 → 2	0 → 1
1.6331019	4.12E-22	F1 → F2	11 → 12	0 → 2	0 → 2	0 → 1
	3.28E-22	F1 → F2	11 → 12	0 → 2	0 → 2	0 → 1
1.6331070	1.35E-22	F2 → F1	11 → 12	0 → 2	0 → 2	0 → 1
	1.07E-22	F2 → F1	11 → 12	0 → 2	0 → 2	0 → 1
1.6331108	4.36E-22	E → E	11 → 12	0 → 2	0 → 2	0 → 1
	3.47E-22	E → E	11 → 12	0 → 2	0 → 2	0 → 1
1.6331446	4.33E-22	F2 → F1	11 → 12	0 → 2	0 → 2	0 → 1

Continued on next page

Table A2 – Continued from previous page

λ (μm)	Intensity ($\mathrm{cm\ MOL^{-1}}$)	$\Delta\Gamma$	ΔJ	$\Delta\nu_3$	ΔL3	ΔM3
	3.45E-22	F2 → F1	11 → 12	0 → 2	0 → 2	0 → 1
1.6331960	6.24E-22	F2 → F1	11 → 12	0 → 2	0 → 2	0 → 1
	4.97E-22	F2 → F1	11 → 12	0 → 2	0 → 2	0 → 1
1.6332477	5.76E-22	A2 → A1	11 → 12	0 → 2	0 → 2	0 → 1
	4.59E-22	A2 → A1	11 → 12	0 → 2	0 → 2	0 → 1
1.6333335	4.09E-22	F2 → F1	11 → 12	0 → 2	0 → 2	0 → 1
	3.26E-22	F2 → F1	11 → 12	0 → 2	0 → 2	0 → 1
1.6333619	4.42E-22	E → E	11 → 12	0 → 2	0 → 2	0 → 1
	3.52E-22	E → E	11 → 12	0 → 2	0 → 2	0 → 1
1.6333711	1.10E-22	F2 → F1	11 → 12	0 → 2	0 → 2	0 → 1
	8.77E-23	F2 → F1	11 → 12	0 → 2	0 → 2	0 → 1
1.6334067	4.63E-22	F1 → F2	11 → 12	0 → 2	0 → 2	0 → 1
	3.69E-22	F1 → F2	11 → 12	0 → 2	0 → 2	0 → 1
1.6354053	3.70E-22	F1 → F2	10 → 11	0 → 2	0 → 2	0 → 1
	2.64E-22	F1 → F2	10 → 11	0 → 2	0 → 2	0 → 1
1.6354256	3.38E-22	F1 → F2	10 → 11	0 → 2	0 → 2	0 → 1
	3.84E-22	F1 → F2	10 → 11	0 → 2	0 → 2	0 → 1
1.6354368	5.33E-22	F2 → F1	10 → 11	0 → 2	0 → 2	0 → 1
	3.80E-22	F2 → F1	10 → 11	0 → 2	0 → 2	0 → 1
1.6354533	8.40E-22	E → E	10 → 11	0 → 2	0 → 2	0 → 1
	6.00E-22	E → E	10 → 11	0 → 2	0 → 2	0 → 1
1.6354603	4.28E-22	F2 → F1	10 → 11	0 → 2	0 → 2	0 → 1
	3.05E-22	F2 → F1	10 → 11	0 → 2	0 → 2	0 → 1
1.6354658	5.93E-22	F1 → F2	10 → 11	0 → 2	0 → 2	0 → 1
	4.23E-22	F1 → F2	10 → 11	0 → 2	0 → 2	0 → 1
1.6354677	3.53E-22	F2 → F1	10 → 11	0 → 2	0 → 2	0 → 1
	2.52E-22	F2 → F1	10 → 11	0 → 2	0 → 2	0 → 1
1.6354776	1.00E-21	A1 → A2	10 → 11	0 → 2	0 → 2	0 → 1
	7.14E-22	A1 → A2	10 → 11	0 → 2	0 → 2	0 → 1
1.6354826	9.02E-22	A2 → A1	10 → 11	0 → 2	0 → 2	0 → 1
	6.44E-22	A2 → A1	10 → 11	0 → 2	0 → 2	0 → 1
1.6354860	3.91E-22	F1 → F2	10 → 11	0 → 2	0 → 2	0 → 1

Continued on next page

Table A2 – Continued from previous page

λ (μm)	Intensity (cm MOL^{-1})	$\Delta\Gamma$	ΔJ	$\Delta\nu_3$	ΔL3	ΔM3
	2.79E-22	F1 → F2	10 → 11	0 → 2	0 → 2	0 → 1
1.6354912	4.45E-22	F2 → F1	10 → 11	0 → 2	0 → 2	0 → 1
	3.18E-22	F2 → F1	10 → 11	0 → 2	0 → 2	0 → 1
1.6355011	8.37E-22	E → E	10 → 11	0 → 2	0 → 2	0 → 1
	5.98E-22	E → E	10 → 11	0 → 2	0 → 2	0 → 1
1.6355022	7.82E-22	F2 → F1	10 → 11	0 → 2	0 → 2	0 → 1
	5.58E-22	F2 → F1	10 → 11	0 → 2	0 → 2	0 → 1
1.6377603	1.22E-21	A2 → A1	9 → 10	0 → 2	0 → 2	0 → 1
	7.86E-22	A2 → A1	9 → 10	0 → 2	0 → 2	0 → 1
1.6377694	1.22E-21	F2 → F1	9 → 10	0 → 2	0 → 2	0 → 1
	7.87E-22	F2 → F1	9 → 10	0 → 2	0 → 2	0 → 1
1.6377802	1.21E-21	F1 → F2	9 → 10	0 → 2	0 → 2	0 → 1
	7.79E-22	F1 → F2	9 → 10	0 → 2	0 → 2	0 → 1
1.6378206	1.25E-21	A1 → A2	9 → 10	0 → 2	0 → 2	0 → 1
	8.10E-22	A1 → A2	9 → 10	0 → 2	0 → 2	0 → 1
1.6378374	1.23E-21	F1 → F2	9 → 10	0 → 2	0 → 2	0 → 1
	7.94E-22	F1 → F2	9 → 10	0 → 2	0 → 2	0 → 1
1.6378437	1.25E-21	E → E	9 → 10	0 → 2	0 → 2	0 → 1
	8.04E-22	E → E	9 → 10	0 → 2	0 → 2	0 → 1
1.6379511	1.32E-21	F2 → F1	9 → 10	0 → 2	0 → 2	0 → 1
	8.53E-22	F2 → F1	9 → 10	0 → 2	0 → 2	0 → 1
1.6379555	1.33E-21	F1 → F2	9 → 10	0 → 2	0 → 2	0 → 1
	8.57E-22	F1 → F2	9 → 10	0 → 2	0 → 2	0 → 1
1.6403431	1.69E-21	F2 → F1	8 → 9	0 → 2	0 → 2	0 → 1
	1.00E-21	F2 → F1	8 → 9	0 → 2	0 → 2	0 → 1
1.6403485	1.70E-21	E → E	8 → 9	0 → 2	0 → 2	0 → 1
	1.00E-21	E → E	8 → 9	0 → 2	0 → 2	0 → 1
1.6403658	1.69E-21	F1 → F2	8 → 9	0 → 2	0 → 2	0 → 1
	1.00E-21	F1 → F2	8 → 9	0 → 2	0 → 2	0 → 1
1.6403891	1.72E-21	F2 → F1	8 → 9	0 → 2	0 → 2	0 → 1
	1.01E-21	F2 → F1	8 → 9	0 → 2	0 → 2	0 → 1
1.6404457	1.72E-21	E → E	8 → 9	0 → 2	0 → 2	0 → 1

Continued on next page

Table A2 – Continued from previous page

λ (μm)	Intensity (cm MOL^{-1})	$\Delta\Gamma$	ΔJ	$\Delta\nu_3$	ΔL3	ΔM3
	1.01E-21	E → E	8 → 9	0 → 2	0 → 2	0 → 1
1.6404488	1.72E-21	F1 → F2	8 → 9	0 → 2	0 → 2	0 → 1
	1.02E-21	F1 → F2	8 → 9	0 → 2	0 → 2	0 → 1
1.6404538	1.73E-21	A1 → A2	8 → 9	0 → 2	0 → 2	0 → 1
	1.02E-21	A1 → A2	8 → 9	0 → 2	0 → 2	0 → 1
1.6429176	2.12E-21	F1 → F2	7 → 8	0 → 2	0 → 2	0 → 1
	1.16E-21	F1 → F2	7 → 8	0 → 2	0 → 2	0 → 1
1.6429279	2.12E-21	E → E	7 → 8	0 → 2	0 → 2	0 → 1
	1.16E-21	E → E	7 → 8	0 → 2	0 → 2	0 → 1
1.6429353	2.12E-21	F2 → F1	7 → 8	0 → 2	0 → 2	0 → 1
	1.16E-21	F2 → F1	7 → 8	0 → 2	0 → 2	0 → 1
1.6429508	2.14E-21	A2 → A1	7 → 8	0 → 2	0 → 2	0 → 1
	1.17E-21	A2 → A1	7 → 8	0 → 2	0 → 2	0 → 1
1.6429864	2.14E-21	F2 → F1	7 → 8	0 → 2	0 → 2	0 → 1
	1.16E-21	F2 → F1	7 → 8	0 → 2	0 → 2	0 → 1
1.6429927	2.15E-21	F1 → F2	7 → 8	0 → 2	0 → 2	0 → 1
	1.17E-21	F1 → F2	7 → 8	0 → 2	0 → 2	0 → 1
1.6455325	2.55E-21	A1 → A2	6 → 7	0 → 2	0 → 2	0 → 1
	1.30E-21	A1 → A2	6 → 7	0 → 2	0 → 2	0 → 1
1.6455387	2.56E-21	F1 → F2	6 → 7	0 → 2	0 → 2	0 → 1
	1.30E-21	F1 → F2	6 → 7	0 → 2	0 → 2	0 → 1
1.6455462	2.56E-21	F2 → F1	6 → 7	0 → 2	0 → 2	0 → 1
	1.30E-21	F2 → F1	6 → 7	0 → 2	0 → 2	0 → 1
1.6455727	2.55E-21	A2 → A1	6 → 7	0 → 2	0 → 2	0 → 1
	1.30E-21	A2 → A1	6 → 7	0 → 2	0 → 2	0 → 1
1.6455831	2.57E-21	F2 → F1	6 → 7	0 → 2	0 → 2	0 → 1
	1.31E-21	F2 → F1	6 → 7	0 → 2	0 → 2	0 → 1
1.6455864	2.58E-21	E → E	6 → 7	0 → 2	0 → 2	0 → 1
	1.31E-21	E → E	6 → 7	0 → 2	0 → 2	0 → 1
1.6482014	2.97E-21	F1 → F2	5 → 6	0 → 2	0 → 2	0 → 1
	1.42E-21	F1 → F2	5 → 6	0 → 2	0 → 2	0 → 1
1.6482053	2.98E-21	E → E	5 → 6	0 → 2	0 → 2	0 → 1

Continued on next page

Table A2 – Continued from previous page

λ (μm)	Intensity (cm MOL^{-1})	$\Delta\Gamma$	ΔJ	$\Delta\nu_3$	ΔL3	ΔM3
	1.42E-21	E $\rightarrow$ E	5 $\rightarrow$ 6	0 $\rightarrow$ 2	0 $\rightarrow$ 2	0 $\rightarrow$ 1
1.6482248	2.98E-21	F2 $\rightarrow$ F1	5 $\rightarrow$ 6	0 $\rightarrow$ 2	0 $\rightarrow$ 2	0 $\rightarrow$ 1
	1.42E-21	F2 $\rightarrow$ F1	5 $\rightarrow$ 6	0 $\rightarrow$ 2	0 $\rightarrow$ 2	0 $\rightarrow$ 1
1.6482343	3.00E-21	F1 $\rightarrow$ F2	5 $\rightarrow$ 6	0 $\rightarrow$ 2	0 $\rightarrow$ 2	0 $\rightarrow$ 1
	1.43E-21	F1 $\rightarrow$ F2	5 $\rightarrow$ 6	0 $\rightarrow$ 2	0 $\rightarrow$ 2	0 $\rightarrow$ 1
1.6509167	3.35E-21	F2 $\rightarrow$ F1	4 $\rightarrow$ 5	0 $\rightarrow$ 2	0 $\rightarrow$ 2	0 $\rightarrow$ 1
	1.52E-21	F2 $\rightarrow$ F1	4 $\rightarrow$ 5	0 $\rightarrow$ 2	0 $\rightarrow$ 2	0 $\rightarrow$ 1
1.6509284	3.35E-21	E $\rightarrow$ E	4 $\rightarrow$ 5	0 $\rightarrow$ 2	0 $\rightarrow$ 2	0 $\rightarrow$ 1
	1.52E-21	E $\rightarrow$ E	4 $\rightarrow$ 5	0 $\rightarrow$ 2	0 $\rightarrow$ 2	0 $\rightarrow$ 1
1.6509328	3.36E-21	F1 $\rightarrow$ F2	4 $\rightarrow$ 5	0 $\rightarrow$ 2	0 $\rightarrow$ 2	0 $\rightarrow$ 1
	1.53E-21	F1 $\rightarrow$ F2	4 $\rightarrow$ 5	0 $\rightarrow$ 2	0 $\rightarrow$ 2	0 $\rightarrow$ 1
1.6509393	3.37E-21	A1 $\rightarrow$ A2	4 $\rightarrow$ 5	0 $\rightarrow$ 2	0 $\rightarrow$ 2	0 $\rightarrow$ 1
	1.53E-21	A1 $\rightarrow$ A2	4 $\rightarrow$ 5	0 $\rightarrow$ 2	0 $\rightarrow$ 2	0 $\rightarrow$ 1
1.6536827	3.65E-21	A2 $\rightarrow$ A1	3 $\rightarrow$ 4	0 $\rightarrow$ 2	0 $\rightarrow$ 2	0 $\rightarrow$ 1
	1.60E-21	A2 $\rightarrow$ A1	3 $\rightarrow$ 4	0 $\rightarrow$ 2	0 $\rightarrow$ 2	0 $\rightarrow$ 1
1.6536886	3.66E-21	F2 $\rightarrow$ F1	3 $\rightarrow$ 4	0 $\rightarrow$ 2	0 $\rightarrow$ 2	0 $\rightarrow$ 1
	1.60E-21	F2 $\rightarrow$ F1	3 $\rightarrow$ 4	0 $\rightarrow$ 2	0 $\rightarrow$ 2	0 $\rightarrow$ 1
1.6536937	3.66E-21	F1 $\rightarrow$ F2	3 $\rightarrow$ 4	0 $\rightarrow$ 2	0 $\rightarrow$ 2	0 $\rightarrow$ 1
	1.60E-21	F1 $\rightarrow$ F2	3 $\rightarrow$ 4	0 $\rightarrow$ 2	0 $\rightarrow$ 2	0 $\rightarrow$ 1
1.6565051	3.86E-21	F2 $\rightarrow$ F1	2 $\rightarrow$ 3	0 $\rightarrow$ 2	0 $\rightarrow$ 2	0 $\rightarrow$ 1
	1.64E-21	F2 $\rightarrow$ F1	2 $\rightarrow$ 3	0 $\rightarrow$ 2	0 $\rightarrow$ 2	0 $\rightarrow$ 1
1.6565072	3.87E-21	E $\rightarrow$ E	2 $\rightarrow$ 3	0 $\rightarrow$ 2	0 $\rightarrow$ 2	0 $\rightarrow$ 1
	1.64E-21	E $\rightarrow$ E	2 $\rightarrow$ 3	0 $\rightarrow$ 2	0 $\rightarrow$ 2	0 $\rightarrow$ 1
1.6622964	3.93E-21	A1 $\rightarrow$ A2	0 $\rightarrow$ 1	0 $\rightarrow$ 2	0 $\rightarrow$ 2	0 $\rightarrow$ 1
	1.62E-21	A1 $\rightarrow$ A2	0 $\rightarrow$ 1	0 $\rightarrow$ 2	0 $\rightarrow$ 2	0 $\rightarrow$ 1

Table A.3: Q-branch CH_4 ro-vibrational transition lines producing absorption features in the *H* band spectra of UGPS 0722 and 2MASS 0415 (shaded)

λ (μm)	Intensity (cm MOL^{-1})	$\Delta\Gamma$	ΔJ	$\Delta\nu_3$	ΔL3	ΔM3
1.6678339	1.97E-22	F2 → F1	12 → 12	0 → 2	0 → 2	0 → 1
	1.77E-22	F2 → F1	12 → 12	0 → 2	0 → 2	0 → 1
1.6677624	2.49E-22	A1 → A2	12 → 12	0 → 2	0 → 2	0 → 1
	2.24E-22	A1 → A2	12 → 12	0 → 2	0 → 2	0 → 1
1.6677392	2.11E-22	E → E	12 → 12	0 → 2	0 → 2	0 → 1
	1.90E-22	E → E	12 → 12	0 → 2	0 → 2	0 → 1
1.6676291	1.29E-22	F1 → F2	12 → 12	0 → 2	0 → 2	0 → 1
	1.16E-22	F1 → F2	12 → 12	0 → 2	0 → 2	0 → 1
1.6675407	3.93E-22	F1 → F2	11 → 11	0 → 2	0 → 2	0 → 1
	3.13E-22	F1 → F2	11 → 11	0 → 2	0 → 2	0 → 1
1.6675040	3.55E-22	E → E	11 → 11	0 → 2	0 → 2	0 → 1
	2.83E-22	E → E	11 → 11	0 → 2	0 → 2	0 → 1
1.6674878	3.66E-22	F2 → F1	11 → 11	0 → 2	0 → 2	0 → 1
	2.92E-22	F2 → F1	11 → 11	0 → 2	0 → 2	0 → 1
1.6674628	3.54E-22	A2 → A1	11 → 11	0 → 2	0 → 2	0 → 1
	2.82E-22	A2 → A1	11 → 11	0 → 2	0 → 2	0 → 1
1.6674453	2.17E-22	E → E	11 → 11	0 → 2	0 → 2	0 → 1
	1.73E-22	E → E	11 → 11	0 → 2	0 → 2	0 → 1
1.6674241	2.20E-22	F2 → F1	11 → 11	0 → 2	0 → 2	0 → 1
	1.75E-22	F2 → F1	11 → 11	0 → 2	0 → 2	0 → 1
1.6674079	1.21E-22	F1 → F2	11 → 11	0 → 2	0 → 2	0 → 1
	9.64E-23	F1 → F2	11 → 11	0 → 2	0 → 2	0 → 1
1.6673121	1.50E-22	F1 → F2	11 → 11	0 → 2	0 → 2	0 → 1
	1.20E-22	F1 → F2	11 → 11	0 → 2	0 → 2	0 → 1
1.6672999	3.51E-22	F2 → F1	11 → 11	0 → 2	0 → 2	0 → 1
	2.80E-22	F2 → F1	11 → 11	0 → 2	0 → 2	0 → 1
1.6672636	6.94E-22	F2 → F1	10 → 10	0 → 2	0 → 2	0 → 1
	4.96E-22	F2 → F1	10 → 10	0 → 2	0 → 2	0 → 1
1.6672515	6.82E-22	E → E	10 → 10	0 → 2	0 → 2	0 → 1
	4.87E-22	E → E	10 → 10	0 → 2	0 → 2	0 → 1
1.6672504	1.98E-22	F1 → F2	11 → 11	0 → 2	0 → 2	0 → 1

Continued on next page

Table A3 – Continued from previous page

λ (μm)	Intensity (cm MOL^{-1})	ΔΓ	ΔJ	Δν_3	ΔL3	ΔM3
	1.58E-22	F1 → F2	11 → 11	0 → 2	0 → 2	0 → 1
1.6672405	6.71E-22	F1 → F2	10 → 10	0 → 2	0 → 2	0 → 1
	4.79E-22	F1 → F2	10 → 10	0 → 2	0 → 2	0 → 1
1.6672103	6.50E-22	A1 → A2	10 → 10	0 → 2	0 → 2	0 → 1
	4.64E-22	A1 → A2	10 → 10	0 → 2	0 → 2	0 → 1
1.6671727	6.13E-22	F1 → F2	10 → 10	0 → 2	0 → 2	0 → 1
	4.38E-22	F1 → F2	10 → 10	0 → 2	0 → 2	0 → 1
1.6671634	6.14E-22	F2 → F1	10 → 10	0 → 2	0 → 2	0 → 1
	4.39E-22	F2 → F1	10 → 10	0 → 2	0 → 2	0 → 1
1.6670153	5.78E-22	A2 → A1	10 → 10	0 → 2	0 → 2	0 → 1
	4.12E-22	A2 → A1	10 → 10	0 → 2	0 → 2	0 → 1
1.6670143	5.79E-22	F2 → F1	10 → 10	0 → 2	0 → 2	0 → 1
	4.14E-22	F2 → F1	10 → 10	0 → 2	0 → 2	0 → 1
1.6670137	5.80E-22	E → E	10 → 10	0 → 2	0 → 2	0 → 1
	4.14E-22	E → E	10 → 10	0 → 2	0 → 2	0 → 1
1.6669060	9.65E-22	A2 → A1	9 → 9	0 → 2	0 → 2	0 → 1
	6.23E-22	A2 → A1	9 → 9	0 → 2	0 → 2	0 → 1
1.6668977	9.55E-22	F2 → F1	9 → 9	0 → 2	0 → 2	0 → 1
	6.17E-22	F2 → F1	9 → 9	0 → 2	0 → 2	0 → 1
1.6668871	9.41E-22	F1 → F2	9 → 9	0 → 2	0 → 2	0 → 1
	6.08E-22	F1 → F2	9 → 9	0 → 2	0 → 2	0 → 1
1.6668587	9.10E-22	A1 → A2	9 → 9	0 → 2	0 → 2	0 → 1
	5.88E-22	A1 → A2	9 → 9	0 → 2	0 → 2	0 → 1
1.6668347	8.89E-22	F1 → F2	9 → 9	0 → 2	0 → 2	0 → 1
	5.74E-22	F1 → F2	9 → 9	0 → 2	0 → 2	0 → 1
1.6668283	8.85E-22	E → E	9 → 9	0 → 2	0 → 2	0 → 1
	5.72E-22	E → E	9 → 9	0 → 2	0 → 2	0 → 1
1.6667096	8.36E-22	F2 → F1	9 → 9	0 → 2	0 → 2	0 → 1
	5.40E-22	F2 → F1	9 → 9	0 → 2	0 → 2	0 → 1
1.6667061	8.34E-22	F1 → F2	9 → 9	0 → 2	0 → 2	0 → 1
	5.39E-22	F1 → F2	9 → 9	0 → 2	0 → 2	0 → 1
1.6665685	1.27E-21	F2 → F1	8 → 8	0 → 2	0 → 2	0 → 1

Continued on next page

Table A3 – Continued from previous page

λ (μm)	Intensity (cm MOL^{-1})	ΔΓ	ΔJ	$\Delta\nu_3$	ΔL3	ΔM3
	7.48E-22	F2 → F1	8 → 8	0 → 2	0 → 2	0 → 1
1.6665622	1.26E-21	E → E	8 → 8	0 → 2	0 → 2	0 → 1
	7.42E-22	E → E	8 → 8	0 → 2	0 → 2	0 → 1
1.6665382	1.22E-21	F1 → F2	8 → 8	0 → 2	0 → 2	0 → 1
	7.23E-22	F1 → F2	8 → 8	0 → 2	0 → 2	0 → 1
1.6665154	1.20E-21	F2 → F1	8 → 8	0 → 2	0 → 2	0 → 1
	7.08E-22	F2 → F1	8 → 8	0 → 2	0 → 2	0 → 1
1.6664221	1.14E-21	E → E	8 → 8	0 → 2	0 → 2	0 → 1
	6.74E-22	E → E	8 → 8	0 → 2	0 → 2	0 → 1
1.6664196	1.14E-21	F1 → F2	→ 8	0 → 2	0 → 2	0 → 1
	6.74E-22	F1 → F2	8 → 8	0 → 2	0 → 2	0 → 1
1.6664150	1.14E-21	A1 → A2	8 → 8	0 → 2	0 → 2	0 → 1
	6.73E-22	A1 → A2	8 → 8	0 → 2	0 → 2	0 → 1
1.6662744	1.62E-21	F1 → F2	7 → 7	0 → 2	0 → 2	0 → 1
	8.83E-22	F1 → F2	7 → 7	0 → 2	0 → 2	0 → 1
1.6662583	1.59E-21	E → E	7 → 7	0 → 2	0 → 2	0 → 1
	8.68E-22	E → E	7 → 7	0 → 2	0 → 2	0 → 1
1.6662487	1.58E-21	F2 → F1	7 → 7	0 → 2	0 → 2	0 → 1
	8.58E-22	F2 → F1	7 → 7	0 → 2	0 → 2	0 → 1
1.6662319	1.55E-21	A2 → A1	7 → 7	0 → 2	0 → 2	0 → 1
	8.47E-22	A2 → A1	7 → 7	0 → 2	0 → 2	0 → 1
1.6661644	1.50E-21	F2 → F1	7 → 7	0 → 2	0 → 2	0 → 1
	8.17E-22	F2 → F1	7 → 7	0 → 2	0 → 2	0 → 1
1.6661579	1.50E-21	F1 → F2	7 → 7	0 → 2	0 → 2	0 → 1
	8.17E-22	F1 → F2	7 → 7	0 → 2	0 → 2	0 → 1
1.6660217	2.01E-21	A1 → A2	6 → 6	0 → 2	0 → 2	0 → 1
	1.02E-21	A1 → A2	6 → 6	0 → 2	0 → 2	0 → 1
1.6660116	1.99E-21	F1 → F2	6 → 6	0 → 2	0 → 2	0 → 1
	1.01E-21	F1 → F2	6 → 6	0 → 2	0 → 2	0 → 1
1.6660004	1.97E-21	F2 → F1	6 → 6	0 → 2	0 → 2	0 → 1
	1.00E-21	F2 → F1	6 → 6	0 → 2	0 → 2	0 → 1
1.6659467	1.91E-21	A2 → A1	6 → 6	0 → 2	0 → 2	0 → 1

Continued on next page

Table A3 – Continued from previous page

λ (μm)	Intensity (cm MOL^{-1})	$\Delta\Gamma$	ΔJ	$\Delta\nu_3$	ΔL3	ΔM3
	9.72E-22	A2 → A1	6 → 6	0 → 2	0 → 2	0 → 1
1.6659354	1.90E-21	F2 → F1	6 → 6	0 → 2	0 → 2	0 → 1
	9.64E-22	F2 → F1	6 → 6	0 → 2	0 → 2	0 → 1
1.6659313	1.90E-21	E → E	7 → 6	0 → 2	0 → 2	0 → 1
	9.64E-22	E → E	7 → 6	0 → 2	0 → 2	0 → 1
1.6657990	2.40E-21	F1 → F2	5 → 5	0 → 2	0 → 2	0 → 1
	1.15E-21	F1 → F2	5 → 5	0 → 2	0 → 2	0 → 1
1.6657929	2.39E-21	E → E	5 → 5	0 → 2	0 → 2	0 → 1
	1.14E-21	E → E	5 → 5	0 → 2	0 → 2	0 → 1
1.6657515	2.33E-21	F2 → F1	5 → 5	0 → 2	0 → 2	0 → 1
	1.12E-21	F2 → F1	5 → 5	0 → 2	0 → 2	0 → 1
1.6657385	2.32E-21	F1 → F2	5 → 5	0 → 2	0 → 2	0 → 1
	1.11E-21	F1 → F2	5 → 5	0 → 2	0 → 2	0 → 1
1.6656219	2.80E-21	F2 → F1	4 → 4	0 → 2	0 → 2	0 → 1
	1.27E-21	F2 → F1	4 → 4	0 → 2	0 → 2	0 → 1
1.6655948	2.75E-21	E → E	4 → 4	0 → 2	0 → 2	0 → 1
	1.25E-21	E → E	4 → 4	0 → 2	0 → 2	0 → 1
1.6655870	2.74E-21	F1 → F2	4 → 4	0 → 2	0 → 2	0 → 1
	1.25E-21	F1 → F2	4 → 4	0 → 2	0 → 2	0 → 1
1.6655757	2.73E-21	A1 → A2	4 → 4	0 → 2	0 → 2	0 → 1
	1.24E-21	A1 → A2	4 → 4	0 → 2	0 → 2	0 → 1
1.6654837	3.17E-21	A2 → A1	3 → 3	0 → 2	0 → 2	0 → 1
	1.38E-21	A2 → A1	3 → 3	0 → 2	0 → 2	0 → 1
1.6654686	3.14E-21	F2 → F1	3 → 3	0 → 2	0 → 2	0 → 1
	1.37E-21	F2 → F1	3 → 3	0 → 2	0 → 2	0 → 1
1.6654570	3.12E-21	F1 → F2	3 → 3	0 → 2	0 → 2	0 → 1
	1.36E-21	F1 → F2	3 → 3	0 → 2	0 → 2	0 → 1
1.6653696	3.45E-21	F2 → F1	2 → 2	0 → 2	0 → 2	0 → 1
	1.46E-21	F2 → F1	2 → 2	0 → 2	0 → 2	0 → 1
1.6653637	3.44E-21	E → E	2 → 2	0 → 2	0 → 2	0 → 1
	1.46E-21	E → E	2 → 2	0 → 2	0 → 2	0 → 1
1.6653022	3.67E-21	F1 → F2	1 → 1	0 → 2	0 → 2	0 → 1

Continued on next page

Table A3 – Continued from previous page

λ (μm)	Intensity (cm MOL^{-1})	$\Delta\Gamma$	ΔJ	$\Delta\nu_3$	ΔL3	ΔM3
	1.52E-21	F1 → F2	1 → 1	0 → 2	0 → 2	0 → 1

Table A.4: P-branch CH$_4$ ro-vibrational transition lines producing absorption features in the H band spectra of UGPS 0722 and 2MASS 0415 (shaded)

λ (μm)	Intensity (cm MOL^{-1})	$\Delta\Gamma$	ΔJ	$\Delta\nu_3$	ΔL3	ΔM3
1.6776510	2.38E-21	F2 → F1	4 → 3	0 → 2	0 → 2	0 → 1
	1.08E-21	F2 → F1	4 → 3	0 → 2	0 → 2	0 → 1
1.6776680	2.41E-21	E → E	4 → 3	0 → 2	0 → 2	0 → 1
	1.10E-21	E → E	4 → 3	0 → 2	0 → 2	0 → 1
1.6776742	2.42E-21	F1 → F2	4 → 3	0 → 2	0 → 2	0 → 1
	1.10E-21	F1 → F2	4 → 3	0 → 2	0 → 2	0 → 1
1.6776825	2.43E-21	A1 → A2	4 → 3	0 → 2	0 → 2	0 → 1
	1.10E-21	A1 → A2	4 → 3	0 → 2	0 → 2	0 → 1
1.6808647	1.97E-21	F1 → F2	5 → 4	0 → 2	0 → 2	0 → 1
	9.40E-22	F1 → F2	5 → 4	0 → 2	0 → 2	0 → 1
1.6808701	1.97E-21	E → E	5 → 4	0 → 2	0 → 2	0 → 1
	9.42E-22	E → E	5 → 4	0 → 2	0 → 2	0 → 1
1.6808938	2.00E-21	F2 → F1	5 → 4	0 → 2	0 → 2	0 → 1
	9.56E-22	F2 → F1	5 → 4	0 → 2	0 → 2	0 → 1
1.6809050	2.01E-21	F1 → F2	5 → 4	0 → 2	0 → 2	0 → 1
	9.61E-22	F1 → F2	5 → 4	0 → 2	0 → 2	0 → 1
1.6841156	1.57E-21	A1 → A2	6 → 5	0 → 2	0 → 2	0 → 1
	7.96E-22	A1 → A2	6 → 5	0 → 2	0 → 2	0 → 1
1.6841237	1.57E-21	F1 → F2	6 → 5	0 → 2	0 → 2	0 → 1
	7.99E-22	F1 → F2	6 → 5	0 → 2	0 → 2	0 → 1
1.6841332	1.58E-21	F2 → F1	6 → 5	0 → 2	0 → 2	0 → 1
	8.00E-22	F2 → F1	6 → 5	0 → 2	0 → 2	0 → 1
1.6841616	1.61E-21	A2 → A1	6 → 5	0 → 2	0 → 2	0 → 1
	8.16E-22	A2 → A1	6 → 5	0 → 2	0 → 2	0 → 1
1.6841737	1.61E-21	F2 → F1	6 → 5	0 → 2	0 → 2	0 → 1
	8.19E-22	F2 → F1	6 → 5	0 → 2	0 → 2	0 → 1
1.6841771	1.62E-21	E → E	6 → 5	0 → 2	0 → 2	0 → 1
	8.22E-22	E → E	6 → 5	0 → 2	0 → 2	0 → 1
1.6874142	1.21E-21	F1 → F2	7 → 6	0 → 2	0 → 2	0 → 1
	6.60E-22	F1 → F2	7 → 6	0 → 2	0 → 2	0 → 1
1.6874262	1.22E-21	E → E	7 → 6	0 → 2	0 → 2	0 → 1

Continued on next page

Table A4 – Continued from previous page

λ (μm)	Intensity (cm MOL^{-1})	ΔΓ	ΔJ	$\Delta\nu_3$	ΔL3	ΔM3
	6.64E-22	E → E	7 → 6	0 → 2	0 → 2	0 → 1
1.6874356	1.22E-21	F2 → F1	7 → 6	0 → 2	0 → 2	0 → 1
	6.64E-22	F2 → F1	7 → 6	0 → 2	0 → 2	0 → 1
1.6874561	1.23E-21	A2 → A1	7 → 6	0 → 2	0 → 2	0 → 1
	6.72E-22	A2 → A1	7 → 6	0 → 2	0 → 2	0 → 1
1.6874884	1.25E-21	F2 → F1	7 → 6	0 → 2	0 → 2	0 → 1
	6.83E-22	F2 → F1	7 → 6	0 → 2	0 → 2	0 → 1
1.6874951	1.26E-21	F1 → F2	7 → 6	0 → 2	0 → 2	0 → 1
	6.88E-22	F1 → F2	7 → 6	0 → 2	0 → 2	0 → 1
1.6907476	9.06E-22	F2 → F1	8 → 7	0 → 2	0 → 2	0 → 1
	5.35E-22	F2 → F1	8 → 7	0 → 2	0 → 2	0 → 1
1.6907544	9.07E-22	E → E	8 → 7	0 → 2	0 → 2	0 → 1
	5.36E-22	E → E	8 → 7	0 → 2	0 → 2	0 → 1
1.6907712	9.15E-22	F1 → F2	8 → 7	0 → 2	0 → 2	0 → 1
	5.40E-22	F1 → F2	8 → 7	0 → 2	0 → 2	0 → 1
1.6908041	9.27E-22	F2 → F1	8 → 7	0 → 2	0 → 2	0 → 1
	5.47E-22	F2 → F1	8 → 7	0 → 2	0 → 2	0 → 1
1.6908512	9.52E-22	E → E	8 → 7	0 → 2	0 → 2	0 → 1
	5.62E-22	E → E	8 → 7	0 → 2	0 → 2	0 → 1
1.6908548	9.53E-22	F1 → F2	8 → 7	0 → 2	0 → 2	0 → 1
	5.62E-22	F1 → F2	8 → 7	0 → 2	0 → 2	0 → 1
1.6908604	9.57E-22	A1 → A2	8 → 7	0 → 2	0 → 2	0 → 1
	5.65E-22	A1 → A2	8 → 7	0 → 2	0 → 2	0 → 1
1.6941092	6.53E-22	A2 → A1	9 → 8	0 → 2	0 → 2	0 → 1
	4.22E-22	A2 → A1	9 → 8	0 → 2	0 → 2	0 → 1
1.6941171	6.55E-22	F2 → F1	9 → 8	0 → 2	0 → 2	0 → 1
	4.23E-22	F2 → F1	9 → 8	0 → 2	0 → 2	0 → 1
1.6941273	6.53E-22	F1 → F2	9 → 8	0 → 2	0 → 2	0 → 1
	4.22E-22	F1 → F2	9 → 8	0 → 2	0 → 2	0 → 1
1.6941449	6.65E-22	A1 → A2	9 → 8	0 → 2	0 → 2	0 → 1
	4.30E-22	A1 → A2	9 → 8	0 → 2	0 → 2	0 → 1
1.6941874	6.69E-22	F1 → F2	9 → 8	0 → 2	0 → 2	0 → 1

Continued on next page

Table A4 – Continued from previous page

λ (μm)	Intensity (cm MOL^{-1})	ΔΓ	ΔJ	$\Delta\nu_3$	ΔL3	ΔM3
	4.32E-22	F1 → F2	9 → 8	0 → 2	0 → 2	0 → 1
1.6941953	6.77E-22	E → E	9 → 8	0 → 2	0 → 2	0 → 1
	4.37E-22	E → E	9 → 8	0 → 2	0 → 2	0 → 1
1.6942568	1.70E-22	F2 → F1	9 → 8	0 → 2	0 → 2	0 → 1
	4.51E-22	F2 → F1	9 → 8	0 → 2	0 → 2	0 → 1
1.6942629	6.99E-22	F1 → F2	9 → 8	0 → 2	0 → 2	0 → 1
	4.52E-22	F1 → F2	9 → 8	0 → 2	0 → 2	0 → 1
1.6975048	4.54E-22	F2 → F1	10 → 9	0 → 2	0 → 2	0 → 1
	3.24E-22	F2 → F1	10 → 9	0 → 2	0 → 2	0 → 1
1.6975154	4.56E-22	E → E	10 → 9	0 → 2	0 → 2	0 → 1
	3.26E-22	E → E	10 → 9	0 → 2	0 → 2	0 → 1
1.6975263	4.54E-22	F1 → F2	10 → 9	0 → 2	0 → 2	0 → 1
	3.24E-22	F1 → F2	10 → 9	0 → 2	0 → 2	0 → 1
1.6975807	4.67E-22	A1 → A2	10 → 9	0 → 2	0 → 2	0 → 1
	3.33E-22	A1 → A2	10 → 9	0 → 2	0 → 2	0 → 1
1.6976059	4.68E-22	F1 → F2	10 → 9	0 → 2	0 → 2	0 → 1
	3.34E-22	F1 → F2	10 → 9	0 → 2	0 → 2	0 → 1
1.6976212	4.75E-22	F2 → F1	10 → 9	0 → 2	0 → 2	0 → 1
	3.39E-22	F2 → F1	10 → 9	0 → 2	0 → 2	0 → 1
1.6976998	4.96E-22	A2 → A1	10 → 9	0 → 2	0 → 2	0 → 1
	3.54E-22	A2 → A1	10 → 9	0 → 2	0 → 2	0 → 1
1.6977043	4.95E-22	F2 → F1	10 → 9	0 → 2	0 → 2	0 → 1
	3.54E-22	F2 → F1	10 → 9	0 → 2	0 → 2	0 → 1
1.6977062	4.95E-22	E → E	10 → 9	0 → 2	0 → 2	0 → 1
	3.54E-22	E → E	10 → 9	0 → 2	0 → 2	0 → 1
1.700923	3.03E-22	F1 → F2	11 → 10	0 → 2	0 → 2	0 → 1
	2.41E-22	F1 → F2	11 → 10	0 → 2	0 → 2	0 → 1
1.700928	3.02E-22	E → E	11 → 10	0 → 2	0 → 2	0 → 1
	2.41E-22	E → E	11 → 10	0 → 2	0 → 2	0 → 1
1.700940	3.04E-22	F2 → F1	11 → 10	0 → 2	0 → 2	0 → 1
		F2 → F1	11 → 10	0 → 2	0 → 2	0 → 1
1.701001	2.93E-22	F1 → F2	11 → 10	0 → 2	0 → 2	0 → 1

Continued on next page

Table A4 – Continued from previous page

λ (μm)	Intensity (cm MOL^{-1})	$\Delta\Gamma$	ΔJ	$\Delta\nu_3$	ΔL3	ΔM3
	2.33E-22	F1 → F2	11 → 10	0 → 2	0 → 2	0 → 1
1.701052	3.11E-22	E → E	11 → 10	0 → 2	0 → 2	0 → 1
	2.48E-2	E → E	11 → 10	0 → 2	0 → 2	0 → 1
1.701072	3.08E-22	F2 → F1	11 → 10	0 → 2	0 → 2	0 → 1
	2.46E-22	F2 → F1	11 → 10	0 → 2	0 → 2	0 → 1
1.701114	3.26E-22	A2 → A1	11 → 10	0 → 2	0 → 2	0 → 1
	2.60E-22	A2 → A1	11 → 10	0 → 2	0 → 2	0 → 1
1.701188	3.31E-22	F2 → F1	11 → 10	0 → 2	0 → 2	0 → 1
	2.64E-22	F2 → F1	11 → 10	0 → 2	0 → 2	0 → 1
1.701199	3.41E-22	F1 → F2	11 → 10	0 → 2	0 → 2	0 → 1
	2.71E-22	F1 → F2	11 → 10	0 → 2	0 → 2	0 → 1

Table A.5: R-branch CH_4 ro-vibrational transition lines producing absorption features in the *K* band spectra of UGPS 0722 and 2MASS 0415 (shaded)

λ (μm)	Intensity (cm MOL^{-1})	$\Delta\Gamma$	ΔJ	$\Delta\nu_2$	ΔL2	$\Delta\nu_3$	ΔL3	ΔM3
2.0974108	8.25E-24	A1 → A2	4 → 5	0 → 0	0 → 0	0 → 2	0 → 2	0 → 1
	1.28E-23	A1 → A2	4 → 5	0 → 0	0 → 0	0 → 2	0 → 2	0 → 1
2.0975031	7.15E-24	F1 → F2	4 → 5	0 → 0	0 → 0	0 → 2	0 → 2	0 → 1
	1.11E-23	F1 → F2	4 → 5	0 → 0	0 → 0	0 → 2	0 → 2	0 → 1
2.0975852	6.03E-24	F2 → F1	4 → 5	0 → 0	0 → 0	0 → 2	0 → 2	0 → 1
	9.38E-24	F2 → F1	4 → 5	0 → 0	0 → 0	0 → 2	0 → 2	0 → 1
2.1145514	7.90E-24	F2 → F1	17 → 18	0 → 1	0 → 1	0 → 1	0 → 1	0 → 1
	1.50E-23	F2 → F1	17 → 18	0 → 1	0 → 1	0 → 1	0 → 1	0 → 1
2.1145748	6.11E-24	E → E	17 → 18	0 → 1	0 → 1	0 → 1	0 → 1	0 → 1
	1.16E-23	E → E	17 → 18	0 → 1	0 → 1	0 → 1	0 → 1	0 → 1
2.1179486	1.21E-23	A1 → A2	16 → 17	0 → 1	0 → 1	0 → 1	0 → 1	0 → 1
	1.95E-23	A1 → A2	16 → 17	0 → 1	0 → 1	0 → 1	0 → 1	0 → 1
2.1179540	6.70E-24	F1 → F2	17 → 18	0 → 1	0 → 1	0 → 1	0 → 1	0 → 1
	1.27E-23	F1 → F2	17 → 18	0 → 1	0 → 1	0 → 1	0 → 1	0 → 1
2.1179633	8.90E-24	F1 → F2	16 → 17	0 → 1	0 → 1	0 → 1	0 → 1	0 → 1
	1.42E-23	F1 → F2	16 → 17	0 → 1	0 → 1	0 → 1	0 → 1	0 → 1
2.1179804	4.79E-24	F2 → F1	16 → 17	0 → 1	0 → 1	0 → 1	0 → 1	0 → 1
	7.64E-24	F2 → F1	16 → 17	0 → 1	0 → 1	0 → 1	0 → 1	0 → 1
2.1180379	7.26E-24	E → E	15 → 16	0 → 1	0 → 1	0 → 1	0 → 1	0 → 1
	9.87E-24	E → E	15 → 16	0 → 1	0 → 1	0 → 1	0 → 1	0 → 1
2.1190291	1.40E-23	F1 → F2	16 → 17	0 → 1	0 → 1	0 → 1	0 → 1	0 → 1
	2.25E-23	F1 → F2	16 → 17	0 → 1	0 → 1	0 → 1	0 → 1	0 → 1
2.1190398	9.16E-24	A2 → A1	16 → 17	0 → 1	0 → 1	0 → 1	0 → 1	0 → 1
	1.46E-23	A2 → A1	16 → 17	0 → 1	0 → 1	0 → 1	0 → 1	0 → 1
2.1228554	1.83E-23	F2 → F1	15 → 16	0 → 1	0 → 1	0 → 1	0 → 1	0 → 1
	2.49E-23	F2 → F1	15 → 16	0 → 1	0 → 1	0 → 1	0 → 1	0 → 1
2.1228613	2.29E-23	A2 → A1	15 → 16	0 → 1	0 → 1	0 → 1	0 → 1	0 → 1
	3.12E-23	A2 → A1	15 → 16	0 → 1	0 → 1	0 → 1	0 → 1	0 → 1
2.1236780	1.59E-23	F1 → F2	15 → 16	0 → 1	0 → 1	0 → 1	0 → 1	0 → 1
	2.17E-23	F1 → F2	15 → 16	0 → 1	0 → 1	0 → 1	0 → 1	0 → 1
2.1237360	1.84E-23	F2 → F1	16 → 17	0 → 1	0 → 1	0 → 1	0 → 1	0 → 1

Continued on next page

Table A5 – Continued from previous page

λ (μm)	Intensity (cm MOL^{-1})	$\Delta\Gamma$	ΔJ	$\Delta\nu_2$	ΔL2	$\Delta\nu_3$	ΔL3	ΔM3
	2.93E-23	F2 → F1	16 → 17	0 → 1	0 → 1	0 → 1	0 → 1	0 → 1
2.1237494	1.84E-23	F1 → F2	16 → 17	0 → 1	0 → 1	0 → 1	0 → 1	0 → 1
	2.94E-23	F1 → F2	16 → 17	0 → 1	0 → 1	0 → 1	0 → 1	0 → 1
2.1237690	8.16E-24	F2 → F1	15 → 16	0 → 1	0 → 1	0 → 1	0 → 1	0 → 1
	1.11E-23	F2 → F1	15 → 16	0 → 1	0 → 1	0 → 1	0 → 1	0 → 1
2.1251507	8.21E-24	F1 → F2	12 → 13	0 → 1	0 → 1	0 → 1	0 → 1	0 → 1
	7.35E-24	F1 → F2	12 → 13	0 → 1	0 → 1	0 → 1	0 → 1	0 → 1
2.1251679	5.88E-24	F2 → F1	12 → 13	0 → 1	0 → 1	0 → 1	0 → 1	0 → 1
	5.27E-24	F2 → F1	12 → 13	0 → 1	0 → 1	0 → 1	0 → 1	0 → 1
2.1251880	6.48E-24	F2 → F1	12 → 13	0 → 1	0 → 1	0 → 1	0 → 1	0 → 1
	5.80E-24	F2 → F1	12 → 13	0 → 1	0 → 1	0 → 1	0 → 1	0 → 1
2.1275404	2.84E-23	E → E	14 → 15	0 → 1	0 → 1	0 → 1	0 → 1	0 → 1
	3.34E-23	E → E	14 → 15	0 → 1	0 → 1	0 → 1	0 → 1	0 → 1
2.1281795	2.76E-23	A2 → A1	15 → 16	0 → 1	0 → 1	0 → 1	0 → 1	0 → 1
	3.77E-23	A2 → A1	15 → 16	0 → 1	0 → 1	0 → 1	0 → 1	0 → 1
2.1281906	2.74E-23	F2 → F1	15 → 16	0 → 1	0 → 1	0 → 1	0 → 1	0 → 1
	3.74E-23	F2 → F1	15 → 16	0 → 1	0 → 1	0 → 1	0 → 1	0 → 1
2.1281963	2.74E-23	E → E	15 → 16	0 → 1	0 → 1	0 → 1	0 → 1	0 → 1
	3.74E-23	E → E	15 → 16	0 → 1	0 → 1	0 → 1	0 → 1	0 → 1
2.1295685	4.31E-23	F1 → F2	15 → 16	0 → 1	0 → 1	0 → 1	0 → 1	0 → 1
	5.86E-23	F1 → F2	15 → 16	0 → 1	0 → 1	0 → 1	0 → 1	0 → 1
2.1295691	4.31E-23	F2 → F1	15 → 16	0 → 1	0 → 1	0 → 1	0 → 1	0 → 1
	5.86E-23	F2 → F1	15 → 16	0 → 1	0 → 1	0 → 1	0 → 1	0 → 1
2.1312381	3.27E-23	A2 → A1	11 → 12	0 → 1	0 → 1	0 → 1	0 → 1	0 → 1
	2.60E-23	A2 → A1	11 → 12	0 → 1	0 → 1	0 → 1	0 → 1	0 → 1
2.1322746	5.35E-23	A2 → A1	13 → 14	0 → 1	0 → 1	0 → 1	0 → 1	0 → 1
	5.47E-23	A2 → A1	13 → 14	0 → 1	0 → 1	0 → 1	0 → 1	0 → 1
2.1323225	6.15E-23	F1 → F2	13 → 14	0 → 1	0 → 1	0 → 1	0 → 1	0 → 1
	6.29E-23	F1 → F2	13 → 14	0 → 1	0 → 1	0 → 1	0 → 1	0 → 1
2.1324049	5.65E-23	E → E	13 → 14	0 → 1	0 → 1	0 → 1	0 → 1	0 → 1
	5.78E-23	E → E	13 → 14	0 → 1	0 → 1	0 → 1	0 → 1	0 → 1
2.1339494	6.31E-23	E → E	14 → 15	0 → 1	0 → 1	0 → 1	0 → 1	0 → 1

Continued on next page

Table A5 – Continued from previous page

λ (μm)	Intensity (cm MOL^{-1})	$\Delta\Gamma$	ΔJ	$\Delta\nu_2$	ΔL2	$\Delta\nu_3$	ΔL3	ΔM3
	7.41E-23	E → E	14 → 15	0 → 1	0 → 1	0 → 1	0 → 1	0 → 1
2.1339497	6.31E-23	F2 → F1	14 → 15	0 → 1	0 → 1	0 → 1	0 → 1	0 → 1
	7.41E-23	F2 → F1	14 → 15	0 → 1	0 → 1	0 → 1	0 → 1	0 → 1
2.1339503	6.31E-23	A2 → A1	14 → 15	0 → 1	0 → 1	0 → 1	0 → 1	0 → 1
	7.42E-23	A2 → A1	14 → 15	0 → 1	0 → 1	0 → 1	0 → 1	0 → 1
2.1371371	1.04E-22	A1 → A2	12 → 13	0 → 1	0 → 1	0 → 1	0 → 1	0 → 1
	9.37E-23	A1 → A2	12 → 13	0 → 1	0 → 1	0 → 1	0 → 1	0 → 1
2.1371678	9.52E-23	F1 → F2	12 → 13	0 → 1	0 → 1	0 → 1	0 → 1	0 → 1
	8.55E-23	F1 → F2	12 → 13	0 → 1	0 → 1	0 → 1	0 → 1	0 → 1
2.1375107	9.07E-23	A2 → A1	12 → 13	0 → 1	0 → 1	0 → 1	0 → 1	0 → 1
	8.15E-23	A2 → A1	12 → 13	0 → 1	0 → 1	0 → 1	0 → 1	0 → 1
2.1420368	1.46E-22	F1 → F2	11 → 12	0 → 1	0 → 1	0 → 1	0 → 1	0 → 1
	1.16E-22	F1 → F2	11 → 12	0 → 1	0 → 1	0 → 1	0 → 1	0 → 1
2.1420483	1.34E-22	E → E	11 → 12	0 → 1	0 → 1	0 → 1	0 → 1	0 → 1
	1.07E-22	E → E	11 → 12	0 → 1	0 → 1	0 → 1	0 → 1	0 → 1
2.1421104	1.00E-22	F1 → F2	11 → 12	0 → 1	0 → 1	0 → 1	0 → 1	0 → 1
	8.01E-23	F1 → F2	11 → 12	0 → 1	0 → 1	0 → 1	0 → 1	0 → 1
2.1421564	1.10E-22	F2 → F1	11 → 12	0 → 1	0 → 1	0 → 1	0 → 1	0 → 1
	8.73E-23	F2 → F1	11 → 12	0 → 1	0 → 1	0 → 1	0 → 1	0 → 1
2.1428230	1.22E-22	A1 → A2	12 → 13	0 → 1	0 → 1	0 → 1	0 → 1	0 → 1
	1.09E-22	A1 → A2	12 → 13	0 → 1	0 → 1	0 → 1	0 → 1	0 → 1
2.1428231	1.22E-22	F1 → F2	12 → 13	0 → 1	0 → 1	0 → 1	0 → 1	0 → 1
	1.09E-22	F1 → F2	12 → 13	0 → 1	0 → 1	0 → 1	0 → 1	0 → 1
2.1428231	1.21E-22	E → E	12 → 13	0 → 1	0 → 1	0 → 1	0 → 1	0 → 1
	1.09E-22	E → E	12 → 13	0 → 1	0 → 1	0 → 1	0 → 1	0 → 1
2.1429694	1.47E-22	F1 → F2	9 → 10	0 → 1	0 → 1	0 → 1	0 → 1	0 → 1
	9.47E-23	F1 → F2	9 → 10	0 → 1	0 → 1	0 → 1	0 → 1	0 → 1
2.1429694	1.45E-22	F2 → F1	9 → 10	0 → 1	0 → 1	0 → 1	0 → 1	0 → 1
	9.34E-23	F2 → F1	9 → 10	0 → 1	0 → 1	0 → 1	0 → 1	0 → 1
2.1433470	1.29E-22	E → E	9 → 10	0 → 1	0 → 1	0 → 1	0 → 1	0 → 1
	8.33E-23	E → E	9 → 10	0 → 1	0 → 1	0 → 1	0 → 1	0 → 1
2.1433577	1.20E-22	F1 → F2	9 → 10	0 → 1	0 → 1	0 → 1	0 → 1	0 → 1

Continued on next page

Table A5 – Continued from previous page

λ (μm)	Intensity ($\mathrm{cm\ MOL^{-1}}$)	$\Delta\Gamma$	ΔJ	$\Delta\nu_2$	ΔL2	$\Delta\nu_3$	ΔL3	ΔM3
	7.76E-23	F1 → F2	9 → 10	0 → 1	0 → 1	0 → 1	0 → 1	0 → 1
2.1433913	1.09E-22	A1 → A2	9 → 10	0 → 1	0 → 1	0 → 1	0 → 1	0 → 1
	7.03E-23	A1 → A2	9 → 10	0 → 1	0 → 1	0 → 1	0 → 1	0 → 1
2.1435411	1.00E-22	F1 → F2	9 → 10	0 → 1	0 → 1	0 → 1	0 → 1	0 → 1
	6.48E-23	F1 → F2	9 → 10	0 → 1	0 → 1	0 → 1	0 → 1	0 → 1
2.1435782	9.98E-23	F2 → F1	9 → 10	0 → 1	0 → 1	0 → 1	0 → 1	0 → 1
	6.45E-23	F2 → F1	9 → 10	0 → 1	0 → 1	0 → 1	0 → 1	0 → 1
2.1436131	9.70E-23	A2 → A1	9 → 10	0 → 1	0 → 1	0 → 1	0 → 1	0 → 1
	6.27E-23	A2 → A1	9 → 10	0 → 1	0 → 1	0 → 1	0 → 1	0 → 1
2.1463298	8.40E-23	E → E	11 → 12	0 → 1	0 → 1	0 → 1	0 → 1	0 → 1
	6.67E-23	E → E	11 → 12	0 → 1	0 → 1	0 → 1	0 → 1	0 → 1
2.1463307	8.68E-23	F2 → F1	11 → 12	0 → 1	0 → 1	0 → 1	0 → 1	0 → 1
	6.89E-23	F2 → F1	11 → 12	0 → 1	0 → 1	0 → 1	0 → 1	0 → 1
2.1463339	9.41E-23	A2 → A1	11 → 12	0 → 1	0 → 1	0 → 1	0 → 1	0 → 1
	7.47E-23	A2 → A1	11 → 12	0 → 1	0 → 1	0 → 1	0 → 1	0 → 1
2.1469945	2.06E-22	F2 → F1	10 → 11	0 → 1	0 → 1	0 → 1	0 → 1	0 → 1
	1.47E-22	F2 → F1	10 → 11	0 → 1	0 → 1	0 → 1	0 → 1	0 → 1
2.1470298	1.87E-22	E → E	10 → 11	0 → 1	0 → 1	0 → 1	0 → 1	0 → 1
	1.34E-22	E → E	10 → 11	0 → 1	0 → 1	0 → 1	0 → 1	0 → 1
2.1470451	1.56E-22	F1 → F2	10 → 11	0 → 1	0 → 1	0 → 1	0 → 1	0 → 1
	1.12E-22	F1 → F2	10 → 11	0 → 1	0 → 1	0 → 1	0 → 1	0 → 1
2.1470527	1.43E-22	A1 → A2	10 → 11	0 → 1	0 → 1	0 → 1	0 → 1	0 → 1
	1.02E-22	A1 → A2	10 → 11	0 → 1	0 → 1	0 → 1	0 → 1	0 → 1
2.1473142	1.59E-22	F1 → F2	11 → 12	0 → 1	0 → 1	0 → 1	0 → 1	0 → 1
	1.27E-22	F1 → F2	11 → 12	0 → 1	0 → 1	0 → 1	0 → 1	0 → 1
2.1473144	1.59E-22	F2 → F1	11 → 12	0 → 1	0 → 1	0 → 1	0 → 1	0 → 1
	1.27E-22	F2 → F1	11 → 12	0 → 1	0 → 1	0 → 1	0 → 1	0 → 1
2.1489780	2.58E-22	A1 → A2	8 → 9	0 → 1	0 → 1	0 → 1	0 → 1	0 → 1
	1.52E-22	A1 → A2	8 → 9	0 → 1	0 → 1	0 → 1	0 → 1	0 → 1
2.1489856	2.53E-22	F1 → F2	8 → 9	0 → 1	0 → 1	0 → 1	0 → 1	0 → 1
	1.49E-22	F1 → F2	8 → 9	0 → 1	0 → 1	0 → 1	0 → 1	0 → 1
2.1489898	2.51E-22	E → E	8 → 9	0 → 1	0 → 1	0 → 1	0 → 1	0 → 1

Continued on next page

Table A5 – Continued from previous page

λ (μm)	Intensity (cm MOL^{-1})	$\Delta\Gamma$	ΔJ	$\Delta\nu_2$	ΔL2	$\Delta\nu_3$	ΔL3	ΔM3
	1.48E-22	E → E	8 → 9	0 → 1	0 → 1	0 → 1	0 → 1	0 → 1
2.1493565	2.34E-22	F2 → F1	8 → 9	0 → 1	0 → 1	0 → 1	0 → 1	0 → 1
	1.38E-22	F2 → F1	8 → 9	0 → 1	0 → 1	0 → 1	0 → 1	0 → 1
2.1494333	2.13E-22	F1 → F2	8 → 9	0 → 1	0 → 1	0 → 1	0 → 1	0 → 1
	1.26E-22	F1 → F2	8 → 9	0 → 1	0 → 1	0 → 1	0 → 1	0 → 1
2.1495688	2.05E-22	E → E	8 → 9	0 → 1	0 → 1	0 → 1	0 → 1	0 → 1
	1.21E-22	E → E	8 → 9	0 → 1	0 → 1	0 → 1	0 → 1	0 → 1
2.1495996	2.01E-22	F2 → F1	8 → 9	0 → 1	0 → 1	0 → 1	0 → 1	0 → 1
	1.19E-22	F2 → F1	8 → 9	0 → 1	0 → 1	0 → 1	0 → 1	0 → 1
2.1518405	2.00E-22	E → E	10 → 11	0 → 1	0 → 1	0 → 1	0 → 1	0 → 1
	1.43E-22	E → E	10 → 11	0 → 1	0 → 1	0 → 1	0 → 1	0 → 1
2.1518410	2.00E-22	F2 → F1	10 → 11	0 → 1	0 → 1	0 → 1	0 → 1	0 → 1
	1.42E-22	F2 → F1	10 → 11	0 → 1	0 → 1	0 → 1	0 → 1	0 → 1
2.1518421	1.98E-22	A2 → A1	10 → 11	0 → 1	0 → 1	0 → 1	0 → 1	0 → 1
	1.42E-22	A2 → A1	10 → 11	0 → 1	0 → 1	0 → 1	0 → 1	0 → 1
2.1520304	1.90E-22	A1 → A2	9 → 10	0 → 1	0 → 1	0 → 1	0 → 1	0 → 1
	1.23E-22	A1 → A2	9 → 10	0 → 1	0 → 1	0 → 1	0 → 1	0 → 1
2.1520377	2.24E-22	F1 → F2	9 → 10	0 → 1	0 → 1	0 → 1	0 → 1	0 → 1
	1.45E-22	F1 → F2	9 → 10	0 → 1	0 → 1	0 → 1	0 → 1	0 → 1
2.1520406	2.51E-22	F2 → F1	9 → 10	0 → 1	0 → 1	0 → 1	0 → 1	0 → 1
	1.62E-22	F2 → F1	9 → 10	0 → 1	0 → 1	0 → 1	0 → 1	0 → 1
2.1520429	2.69E-22	A2 → A1	9 → 10	0 → 1	0 → 1	0 → 1	0 → 1	0 → 1
	1.74E-22	A2 → A1	9 → 10	0 → 1	0 → 1	0 → 1	0 → 1	0 → 1
2.1549660	4.22E-22	F1 → F2	7 → 8	0 → 1	0 → 1	0 → 1	0 → 1	0 → 1
	2.30E-22	F1 → F2	7 → 8	0 → 1	0 → 1	0 → 1	0 → 1	0 → 1
2.1549864	4.14E-22	F2 → F1	7 → 8	0 → 1	0 → 1	0 → 1	0 → 1	0 → 1
	2.25E-22	F2 → F1	7 → 8	0 → 1	0 → 1	0 → 1	0 → 1	0 → 1
2.1552967	4.04E-22	A2 → A1	7 → 8	0 → 1	0 → 1	0 → 1	0 → 1	0 → 1
	2.20E-22	A2 → A1	7 → 8	0 → 1	0 → 1	0 → 1	0 → 1	0 → 1
2.1553792	3.84E-22	F2 → F1	7 → 8	0 → 1	0 → 1	0 → 1	0 → 1	0 → 1
	2.09E-22	F2 → F1	7 → 8	0 → 1	0 → 1	0 → 1	0 → 1	0 → 1
2.1554313	3.77E-22	E → E	7 → 8	0 → 1	0 → 1	0 → 1	0 → 1	0 → 1

Continued on next page

Table A5 – Continued from previous page

λ (μm)	Intensity (cm MOL^{-1})	$\Delta\Gamma$	ΔJ	$\Delta\nu_2$	ΔL2	$\Delta\nu_3$	ΔL3	ΔM3
	2.05E-22	E → E	7 → 8	0 → 1	0 → 1	0 → 1	0 → 1	0 → 1
2.1555366	3.70E-22	F1 → F2	7 → 8	0 → 1	0 → 1	0 → 1	0 → 1	0 → 1
	2.02E-22	F1 → F2	7 → 8	0 → 1	0 → 1	0 → 1	0 → 1	0 → 1
2.1564008	2.41E-22	F1 → F2	9 → 10	0 → 1	0 → 1	0 → 1	0 → 1	0 → 1
	1.56E-22	F1 → F2	9 → 10	0 → 1	0 → 1	0 → 1	0 → 1	0 → 1
2.1564041	2.38E-22	F2 → F1	9 → 10	0 → 1	0 → 1	0 → 1	0 → 1	0 → 1
	1.53E-22	F2 → F1	9 → 10	0 → 1	0 → 1	0 → 1	0 → 1	0 → 1
2.1570157	2.13E-22	F1 → F2	8 → 9	0 → 1	0 → 1	0 → 1	0 → 1	0 → 1
	1.26E-22	F1 → F2	8 → 9	0 → 1	0 → 1	0 → 1	0 → 1	0 → 1
2.1570853	1.49E-22	E → E	8 → 9	0 → 1	0 → 1	0 → 1	0 → 1	0 → 1
	8.80E-23	E → E	8 → 9	0 → 1	0 → 1	0 → 1	0 → 1	0 → 1
2.1570911	1.69E-22	F2 → F1	8 → 9	0 → 1	0 → 1	0 → 1	0 → 1	0 → 1
	9.97E-23	F2 → F1	8 → 9	0 → 1	0 → 1	0 → 1	0 → 1	0 → 1
2.1571675	2.86E-22	F2 → F1	8 → 9	0 → 1	0 → 1	0 → 1	0 → 1	0 → 1
	1.69E-22	F2 → F1	8 → 9	0 → 1	0 → 1	0 → 1	0 → 1	0 → 1
2.1571993	1.27E-22	E → E	8 → 9	0 → 1	0 → 1	0 → 1	0 → 1	0 → 1
	7.48E-23	E → E	8 → 9	0 → 1	0 → 1	0 → 1	0 → 1	0 → 1
2.1609090	6.63E-22	E → E	6 → 7	0 → 1	0 → 1	0 → 1	0 → 1	0 → 1
	3.37E-22	E → E	6 → 7	0 → 1	0 → 1	0 → 1	0 → 1	0 → 1
2.1609263	6.58E-22	F2 → F1	6 → 7	0 → 1	0 → 1	0 → 1	0 → 1	0 → 1
	3.34E-22	F2 → F1	6 → 7	0 → 1	0 → 1	0 → 1	0 → 1	0 → 1
2.1609746	6.43E-22	A2 → A1	6 → 7	0 → 1	0 → 1	0 → 1	0 → 1	0 → 1
	3.27E-22	A2 → A1	6 → 7	0 → 1	0 → 1	0 → 1	0 → 1	0 → 1
2.1609906	2.82E-22	A1 → A2	8 → 9	0 → 1	0 → 1	0 → 1	0 → 1	0 → 1
	1.66E-22	A1 → A2	8 → 9	0 → 1	0 → 1	0 → 1	0 → 1	0 → 1
2.1609981	2.72E-22	F1 → F2	8 → 9	0 → 1	0 → 1	0 → 1	0 → 1	0 → 1
	1.60E-22	F1 → F2	8 → 9	0 → 1	0 → 1	0 → 1	0 → 1	0 → 1
2.1610019	2.68E-22	E → E	8 → 9	0 → 1	0 → 1	0 → 1	0 → 1	0 → 1
	1.58E-22	E → E	8 → 9	0 → 1	0 → 1	0 → 1	0 → 1	0 → 1
2.1612685	6.34E-22	F2 → F1	6 → 7	0 → 1	0 → 1	0 → 1	0 → 1	0 → 1
	3.22E-22	F2 → F1	6 → 7	0 → 1	0 → 1	0 → 1	0 → 1	0 → 1
2.1613420	6.28E-22	F1 → F2	6 → 7	0 → 1	0 → 1	0 → 1	0 → 1	0 → 1

Continued on next page

Table A5 – Continued from previous page

λ (μm)	Intensity (cm MOL^{-1})	ΔΓ	ΔJ	$\Delta\nu_2$	ΔL2	$\Delta\nu_3$	ΔL3	ΔM3
	3.19E-22	F1 → F2	6 → 7	0 → 1	0 → 1	0 → 1	0 → 1	0 → 1
2.1614151	6.23E-22	A1 → A2	6 → 7	0 → 1	0 → 1	0 → 1	0 → 1	0 → 1
	3.16E-22	A1 → A2	6 → 7	0 → 1	0 → 1	0 → 1	0 → 1	0 → 1
2.1621351	1.97E-22	A2 → A1	7 → 8	0 → 1	0 → 1	0 → 1	0 → 1	0 → 1
	1.07E-22	A2 → A1	7 → 8	0 → 1	0 → 1	0 → 1	0 → 1	0 → 1
2.1622398	2.39E-22	E → E	7 → 8	0 → 1	0 → 1	0 → 1	0 → 1	0 → 1
	1.30E-22	E → E	7 → 8	0 → 1	0 → 1	0 → 1	0 → 1	0 → 1
2.1622592	1.46E-22	F2 → F1	7 → 8	0 → 1	0 → 1	0 → 1	0 → 1	0 → 1
	7.94E-23	F2 → F1	7 → 8	0 → 1	0 → 1	0 → 1	0 → 1	0 → 1
2.1623588	2.54E-22	F1 → F2	7 → 8	0 → 1	0 → 1	0 → 1	0 → 1	0 → 1
	1.38E-22	F1 → F2	7 → 8	0 → 1	0 → 1	0 → 1	0 → 1	0 → 1
2.1648853	1.79E-22	A2 → A1	7 → 8	0 → 1	0 → 1	0 → 1	0 → 1	0 → 1
	9.72E-23	A2 → A1	7 → 8	0 → 1	0 → 1	0 → 1	0 → 1	0 → 1
2.1656349	2.82E-22	F2 → F1	7 → 8	0 → 1	0 → 1	0 → 1	0 → 1	0 → 1
	1.53E-22	F2 → F1	7 → 8	0 → 1	0 → 1	0 → 1	0 → 1	0 → 1
2.1656201	3.04E-22	F1 → F2	7 → 8	0 → 1	0 → 1	0 → 1	0 → 1	0 → 1
	1.65E-22	F1 → F2	7 → 8	0 → 1	0 → 1	0 → 1	0 → 1	0 → 1
2.1667977	9.95E-22	F1 → F2	5 → 6	0 → 1	0 → 1	0 → 1	0 → 1	0 → 1
	4.75E-22	F1 → F2	5 → 6	0 → 1	0 → 1	0 → 1	0 → 1	0 → 1
2.1668627	9.79E-22	F2 → F1	5 → 6	0 → 1	0 → 1	0 → 1	0 → 1	0 → 1
	4.68E-22	F2 → F1	5 → 6	0 → 1	0 → 1	0 → 1	0 → 1	0 → 1
2.1671108	9.83E-22	E → E	5 → 6	0 → 1	0 → 1	0 → 1	0 → 1	0 → 1
	4.70E-22	E → E	5 → 6	0 → 1	0 → 1	0 → 1	0 → 1	0 → 1
2.1671550	9.80E-22	F1 → F2	5 → 6	0 → 1	0 → 1	0 → 1	0 → 1	0 → 1
	4.68E-22	F1 → F2	5 → 6	0 → 1	0 → 1	0 → 1	0 → 1	0 → 1
2.1726015	1.43E-21	A1 → A2	4 → 5	0 → 1	0 → 1	0 → 1	0 → 1	0 → 1
	6.50E-22	A1 → A2	4 → 5	0 → 1	0 → 1	0 → 1	0 → 1	0 → 1
2.1726606	1.42E-21	F1 → F2	4 → 5	0 → 1	0 → 1	0 → 1	0 → 1	0 → 1
	6.46E-22	F1 → F2	4 → 5	0 → 1	0 → 1	0 → 1	0 → 1	0 → 1
2.1727046	1.41E-21	E → E	4 → 5	0 → 1	0 → 1	0 → 1	0 → 1	0 → 1
	6.43E-22	E → E	4 → 5	0 → 1	0 → 1	0 → 1	0 → 1	0 → 1
2.1728811	1.44E-21	F2 → F1	4 → 5	0 → 1	0 → 1	0 → 1	0 → 1	0 → 1

Continued on next page

Table A5 – Continued from previous page

λ (μm)	Intensity (cm MOL^{-1})	$\Delta\Gamma$	ΔJ	$\Delta\nu_2$	ΔL2	$\Delta\nu_3$	ΔL3	ΔM3
	6.54E-22	F2 → F1	4 → 5	0 → 1	0 → 1	0 → 1	0 → 1	0 → 1
2.1744354	9.89E-23	E → E	5 → 6	0 → 1	0 → 1	0 → 1	0 → 1	0 → 1
	1.14E-22	E → E	5 → 6	0 → 1	0 → 1	0 → 1	0 → 1	0 → 1
2.1749673	2.84E-22	F1 → F2	5 → 6	0 → 1	0 → 1	0 → 1	0 → 1	0 → 1
	3.29E-22	F1 → F2	5 → 6	0 → 1	0 → 1	0 → 1	0 → 1	0 → 1
2.1750052	2.53E-22	F2 → F1	5 → 6	0 → 1	0 → 1	0 → 1	0 → 1	0 → 1
	2.93E-22	F2 → F1	5 → 6	0 → 1	0 → 1	0 → 1	0 → 1	0 → 1
2.1783877	1.95E-21	F1 → F2	3 → 4	0 → 1	0 → 1	0 → 1	0 → 1	0 → 1
	2.07E-21	F1 → F2	3 → 4	0 → 1	0 → 1	0 → 1	0 → 1	0 → 1
2.1784535	1.96E-21	F2 → F1	3 → 4	0 → 1	0 → 1	0 → 1	0 → 1	0 → 1
	2.08E-21	F2 → F1	3 → 4	0 → 1	0 → 1	0 → 1	0 → 1	0 → 1
2.1785538	1.99E-21	A2 → A1	3 → 4	0 → 1	0 → 1	0 → 1	0 → 1	0 → 1
	2.12E-21	A2 → A1	3 → 4	0 → 1	0 → 1	0 → 1	0 → 1	0 → 1
2.1796382	3.30E-22	A1 → A2	4 → 5	0 → 1	0 → 1	0 → 1	0 → 1	0 → 1
	3.64E-22	A1 → A2	4 → 5	0 → 1	0 → 1	0 → 1	0 → 1	0 → 1
2.1797179	2.08E-22	F1 → F2	4 → 5	0 → 1	0 → 1	0 → 1	0 → 1	0 → 1
	2.30E-22	F1 → F2	4 → 5	0 → 1	0 → 1	0 → 1	0 → 1	0 → 1
2.1797424	1.90E-22	E → E	4 → 5	0 → 1	0 → 1	0 → 1	0 → 1	0 → 1
	2.10E-22	E → E	4 → 5	0 → 1	0 → 1	0 → 1	0 → 1	0 → 1
2.1840555	2.57E-21	E → E	2 → 3	0 → 1	0 → 1	0 → 1	0 → 1	0 → 1
	2.64E-21	E → E	2 → 3	0 → 1	0 → 1	0 → 1	0 → 1	0 → 1
2.1840863	2.58E-21	F2 → F1	2 → 3	0 → 1	0 → 1	0 → 1	0 → 1	0 → 1
	2.64E-21	F2 → F1	2 → 3	0 → 1	0 → 1	0 → 1	0 → 1	0 → 1

Appendix B

NH_3 ro-vibrational transition lines

Table B.1: P-branch NH_3 ro-vibrational transition lines producing absorption features in the *J* band spectra of UGPS 0722 and 2MASS 0415 (shaded)

λ (μm)	Intensity (cm MOL^{-1})	$\Delta\Gamma$	ΔJ	$\Delta\nu_1$	$\Delta\nu_2$	$\Delta\nu_3$	$\Delta\nu_4$
1.2247302	3.65E-23	A2″ → A2′	8 → 7	0 → 1	0 → 0	0 → 0	0 → 3
	2.83E-23	A2″ → A2′	8 → 7	0 → 1	0 → 0	0 → 0	0 → 3
1.2248914	3.49E-23	A2′ → A2″	8 → 7	0 → 1	0 → 0	0 → 0	0 → 3
	2.66E-23	A2′ → A2″	8 → 7	0 → 1	0 → 0	0 → 0	0 → 3
1.2249129	4.98E-23	A2″ → A2′	9 → 8	0 → 1	0 → 0	0 → 0	0 → 3
	3.99E-23	A2″ → A2′	9 → 8	0 → 1	0 → 0	0 → 0	0 → 3
1.2249557	5.81E-23	A2′ → A2″	9 → 8	0 → 1	0 → 0	0 → 0	0 → 3
	4.57E-23	A2′ → A″	9 → 8	0 → 1	0 → 0	0 → 0	0 → 3
1.2264149	3.49E-23	E′ → E″	10 → 9	0 → 1	0 → 0	0 → 0	0 → 3
	3.09E-23	E′ → E″	10 → 9	0 → 1	0 → 0	0 → 0	0 → 3
1.2264596	3.65E-23	E″ → E′	10 → 9	0 → 1	0 → 0	0 → 0	0 → 3
	3.29E-23	E″ → E′	10 → 9	0 → 1	0 → 0	0 → 0	0 → 3
1.2265591	2.32E-23	A2′ → A2″	10 → 9	0 → 1	0 → 0	0 → 0	0 → 3
	2.30E-23	A2′ → A2″	10 → 9	0 → 1	0 → 0	0 → 0	0 → 3
1.2283857	3.49E-23	A2′ → A2″	5 → 5	0 → 1	0 → 0	0 → 1	0 → 1
	2.06E-23	A2′ → A2″	5 → 5	0 → 1	0 → 0	0 → 1	0 → 1
1.2283999	9.13E-23	A2′ → A2″	3 → 2	0 → 1	0 → 0	0 → 1	0 → 1
	4.42E-23	A2′ → A2″	3 → 2	0 → 1	0 → 0	0 → 1	0 → 1
1.2284403	7.97E-23	A2″ → A2′	3 → 2	0 → 1	0 → 0	0 → 1	0 → 1

Continued on next page

Table B1– Continued from previous page

λ (μm)	Intensity (cm MOL^{-1})	$\Delta\Gamma$	ΔJ	$\Delta\nu_1$	$\Delta\nu_2$	$\Delta\nu_3$	$\Delta\nu_4$
	3.88E-23	A2″ → A2′	3 → 2	0 → 1	0 → 0	0 → 1	0 → 1
1.2299675	4.15E-23	A2″ → A2′	12 → 11	0 → 1	0 → 0	0 → 0	0 → 3
	4.94E-23	A2″ → A2′	12 → 11	0 → 1	0 → 0	0 → 0	0 → 3
1.2299811	4.32E-23	A2′ → A2″	12 → 11	0 → 1	0 → 0	0 → 0	0 → 3
	5.11E-23	A2′ → A2″	12 → 11	0 → 1	0 → 0	0 → 0	0 → 3
1.2300664	4.32E-23	E′ → E″	4 → 3	0 → 1	0 → 0	0 → 1	0 → 1
	2.24E-23	E′ → E″	4 → 3	0 → 1	0 → 0	0 → 1	0 → 1
1.2326398	2.66E-23	E′ → E″	5 → 4	0 → 1	0 → 0	0 → 1	0 → 1
	1.46E-23	E′ → E″	5 → 4	0 → 1	0 → 0	0 → 1	0 → 1
1.2326417	4.98E-23	A2′ → A2″	6 → 5	0 → 1	0 → 0	0 → 1	0 → 1
	2.90E-23	A2′ → A2″	6 → 5	0 → 1	0 → 0	0 → 1	0 → 1
1.2327083	7.31E-23	A2″ → A2′	6 → 5	0 → 1	0 → 0	0 → 1	0 → 1
	4.28E-23	A2″ → A2′	6 → 5	0 → 1	0 → 0	0 → 1	0 → 1
1.2327282	3.16E-23	A2′ → A2″	3 → 2	0 → 1	0 → 0	0 → 1	0 → 1
	1.59E-23	A2′ → A2″	3 → 2	0 → 1	0 → 0	0 → 1	0 → 1
1.2327877	3.32E-23	E″ → E′	5 → 4	0 → 1	0 → 0	0 → 1	0 → 1
	1.86E-23	E″ → E′	5 → 4	0 → 1	0 → 0	0 → 1	0 → 1
1.2340163	5.31E-23	A2′ → A2″	5 → 4	0 → 1	0 → 0	0 → 1	0 → 1
	3.10E-23	A2′ → A2″	5 → 4	0 → 1	0 → 0	0 → 1	0 → 1
1.2340977	4.15E-23	A2″ → A2′	6 → 5	0 → 1	0 → 0	0 → 0	0 → 3
	2.47E-23	A2″e → A2′	6 → 5	0 → 1	0 → 0	0 → 0	0 → 3
1.2377870	1.83E-23	E′ → E″	8 → 7	0 → 1	0 → 0	0 → 1	0 → 1
	1.41E-23	E′ → E″	8 → 7	0 → 1	0 → 0	0 → 1	0 → 1
1.2378322	5.31E-23	A2′ → A2″	9 → 8	0 → 1	0 → 0	0 → 1	0 → 1
	4.24E-23	A2′ → A2″	9 → 8	0 → 1	0 → 0	0 → 1	0 → 1
1.2379398	1.83E-23	A2′ → A2″	5 → 4	0 → 1	0 → 0	0 → 1	0 → 1
	1.09E-23	A2′ → A2″	5 → 4	0 → 1	0 → 0	0 → 1	0 → 1
1.2380673	4.82E-23	A2″ → A2′	9 → 8	0 → 1	0 → 0	0 → 1	0 → 1
	3.75E-23	A2″ → A2′	9 → 8	0 → 1	0 → 0	0 → 1	0 → 1
1.2437394	2.16E-23	A2′ → A2″	12 → 11	0 → 1	0 → 0	0 → 1	0 → 1
	2.62E-23	A2′ → A2″	12 → 11	0 → 1	0 → 0	0 → 1	0 → 1
1.2437880	2.66E-23	A2″ → A2′	12 → 11	0 → 1	0 → 0	0 → 1	0 → 1

Continued on next page

Table B1– Continued from previous page

λ (μm)	Intensity (cm MOL^{-1})	$\Delta\Gamma$	ΔJ	$\Delta\nu_1$	$\Delta\nu_2$	$\Delta\nu_3$	$\Delta\nu_4$
	3.05E-23	A2$''$ → A2$'$	12 → 11	0 → 1	0 → 0	0 → 1	0 → 1
1.2493775	1.16E-23	A2$'$ → A2$''$	9 → 8	0 → 1	0 → 0	0 → 1	0 → 1
	1.26E-23	A2$'$ → A2$''$	9 → 8	0 → 1	0 → 0	0 → 1	0 → 1
1.2494636	1.66E-23	A2$'$ → A2$''$	12 → 13	0 → 0	0 → 1	0 → 2	0 → 0
	1.93E-23	A2$'$ → A2$''$	12 → 13	0 → 0	0 → 1	0 → 2	0 → 0

Table B.2: R-branch NH_3 ro-vibrational transition lines producing absorption features in the *H*-band spectra of UGPS 0722 and 2MASS 0415 (shaded)

λ (μm)	Intensity (cm MOL^{-1})	$\Delta\Gamma$	ΔJ	$\Delta\nu_1$	$\Delta\nu_2$	$\Delta\nu_3$	$\Delta\nu_4$
1.4995246	1.07E-21	$E'' \rightarrow E'$	4 → 5	0 → 1	0 → 0	0 → 1	0 → 0
	5.49E-22	$E'' \rightarrow E'$	4 → 5	0 → 1	0 → 0	0 → 1	0 → 0
1.4994996	2.01E-22	$A2' \rightarrow A2''$	5 → 5	0 → 1	0 → 0	0 → 0	0 → 2
	1.19E-22	$A2' \rightarrow A2''$	5 → 5	0 → 1	0 → 0	0 → 0	0 → 2
1.5019192	1.83E-21	$A2'' \rightarrow A2'$	3 → 4	0 → 1	0 → 0	0 → 1	0 → 0
	8.90E-22	$A2'' \rightarrow A2'$	3 → 4	0 → 1	0 → 0	0 → 1	0 → 0
1.5020051	1.94E-21	$A2' \rightarrow A2''$	3 → 4	0 → 1	0 → 0	0 → 1	0 → 0
	9.42E-22	$A2' \rightarrow A2''$	3 → 4	0 → 1	0 → 0	0 → 1	0 → 0

Table B.3: Q-branch NH_3 ro-vibrational transition lines producing absorption features in the *H* band spectra of UGPS 0722 and 2MASS 0415 (shaded)

λ (μm)	Intensity (cm MOL^{-1})	ΔΓ	ΔJ	$\Delta\nu_1$	$\Delta\nu_2$	$\Delta\nu_3$	$\Delta\nu_4$
1.5086164	3.02E-22	A2′ → A2″	3 → 3	0 → 1	0 → 0	0 → 1	0 → 0
	1.47E-22	A2′ → A2″	3 → 3	0 → 1	0 → 0	0 → 1	0 → 0
1.5086397	1.79E-22	A2″ → A2′	8 → 8	0 → 1	0 → 0	0 → 1	0 → 0
	1.55E-22	A2″ → A2′	8 → 8	0 → 1	0 → 0	0 → 1	0 → 0
1.5086610	4.92E-22	A2″ → A2′	5 → 5	0 → 1	0 → 0	0 → 1	0 → 0
	2.83E-22	A2″ → A2′	5 → 5	0 → 1	0 → 0	0 → 1	0 → 0
1.5086724	3.37E-22	A2″ → A2′	3 → 3	0 → 1	0 → 0	0 → 1	0 → 0
	1.64E-22	A2″ → A2′	3 → 3	0 → 1	0 → 0	0 → 1	0 → 0
1.5140040	1.77E-21	A2″ → A2′	4 → 4	0 → 1	0 → 0	0 → 1	0 → 0
	9.59E-22	A2″ → A2′	4 → 4	0 → 1	0 → 0	0 → 1	0 → 0
1.5140142	1.02E-21	A2″ → A2′	6 → 6	0 → 1	0 → 0	0 → 1	0 → 0
	6.80E-22	A2″ → A2′	6 → 6	0 → 1	0 → 0	0 → 1	0 → 0
1.5151545	4.25E-22	A2″ → A2′	8 → 8	0 → 1	0 → 0	0 → 1	0 → 0
	3.76E-22	A2″ → A2′	8 → 8	0 → 1	0 → 0	0 → 1	0 → 0
1.5151655	8.00E-22	A2″ → A2′	6 → 5	0 → 0	0 → 2	0 → 0	0 → 3
	4.70E-22	A2″ → A2′	6 → 5	0 → 0	0 → 2	0 → 0	0 → 3
1.5151910	1.91E-22	A2′ → A2″	9 → 9	0 → 1	0 → 0	0 → 0	0 → 2
	1.95E-22	A′ → A2″	9 → 9	0 → 1	0 → 0	0 → 0	0 → 2
1.5152438	2.16E-22	A2′ → A2″	5 → 5	0 → 1	0 → 2	0 → 0	0 → 1
	1.28E-22	A2′ → A2″	5 → 5	0 → 1	0 → 2	0 → 0	0 → 1
1.5178560	2.31E-22	E′ → E″	5 → 5	0 → 1	0 → 0	0 → 1	0 → 0
	1.36E-22	E′ → E″	5 → 5	0 → 1	0 → 0	0 → 1	0 → 0
1.5178783	2.89E-22	A2′ → A2″	9 → 9	0 → 1	0 → 0	0 → 1	0 → 0
	3.03E-22	A2′ → A2″	9 → 9	0 → 1	0 → 0	0 → 1	0 → 0
1.5178897	2.31E-22	E′ → E″	7 → 6	0 → 1	0 → 0	0 → 0	0 → 2
	1.48E-22	E′ → E″	7 → 6	0 → 1	0 → 0	0 → 0	0 → 2
1.5179236	1.38E-22	E″ → E′	7 → 7	0 → 1	0 → 0	0 → 0	0 → 2
	1.04E-22	E″ → E′	7 → 7	0 → 1	0 → 0	0 → 0	0 → 2
1.5179910	3.19E-22	E′ → E″	4 → 4	0 → 1	0 → 0	0 → 1	0 → 0
	1.70E-22	E′ → E″	4 → 4	0 → 1	0 → 0	0 → 1	0 → 0
1.5180634	2.31E-22	E′ → E″	3 → 3	0 → 1	0 → 0	0 → 1	0 → 0

Continued on next page

Table B3 – Continued from previous page

λ (μm)	Intensity (cm MOL^{-1})	$\Delta\Gamma$	ΔJ	$\Delta\nu_1$	$\Delta\nu_2$	$\Delta\nu_3$	$\Delta\nu_4$
	1.15E-22	E′ → E″	3 → 3	0 → 1	0 → 0	0 → 1	0 → 0
1.5200393	4.02E-22	A2″ → A2′	7 → 6	0 → 0	0 → 2	0 → 0	0 → 3
	2.70E-22	A2″ → A2′	7 → 6	0 → 0	0 → 2	0 → 0	0 → 3
1.5200624	3.84E-22	A2″ → A2′	4 → 4	0 → 1	0 → 0	0 → 1	0 → 0
	2.01E-22	A2″ → A2′	4 → 4	0 → 1	0 → 0	0 → 1	0 → 0
1.5200956	2.01E-22	A2′ → A2″	7 → 7	0 → 1	0 → 0	0 → 0	0 → 2
	1.53E-22	A2′ → A″	7 → 7	0 → 1	0 → 0	0 → 0	0 → 2
1.5201413	4.12E-22	A2′ → A2″	4 → 4	0 → 1	0 → 0	0 → 1	0 → 0
	2.16E-22	A2′ → A2″	4 → 4	0 → 1	0 → 0	0 → 1	0 → 0

Table B.4: P-branch NH_3 ro-vibrational transition lines producing absorption features in the *H* band spectra of UGPS 0722 and 2MASS 0415 (shaded)

λ (μm)	Intensity (cm MOL^{-1})	$\Delta\Gamma$	ΔJ	$\Delta\nu_1$	$\Delta\nu_2$	$\Delta\nu_3$	$\Delta\nu_4$
1.5214707	2.08E-22	E″ → E′	2 → 1	0 → 1	0 → 0	0 → 1	0 → 0
	9.80E-23	E″ → E′	2 → 1	0 → 1	0 → 0	0 → 1	0 → 0
1.5215077	2.14E-22	E′ → E″	2 → 1	0 → 1	0 → 0	0 → 1	0 → 0
	1.01E-22	E′ → E″	2 → 1	0 → 1	0 → 0	0 → 1	0 → 0
1.5215312	2.57E-22	A2′ → A2″	5 → 4	0 → 1	0 → 0	0 → 0	0 → 2
	1.54E-22	A2′ → A2″	5 → 4	0 → 1	0 → 0	0 → 0	0 → 2
1.5215766	2.59E-22	A2″ → A2′	8 → 8	0 → 1	0 → 0	0 → 1	0 → 0
	2.23E-22	A2″ → A2′	8 → 8	0 → 1	0 → 0	0 → 1	0 → 0
1.5224293	1.05E-21	A2′ → A2″	3 → 2	0 → 1	0 → 0	0 → 1	0 → 0
	5.11E-22	A2′ → A2″	3 → 2	0 → 1	0 → 0	0 → 1	0 → 0
1.5224349	1.07E-21	A2″ → A2′	3 → 2	0 → 1	0 → 0	0 → 1	0 → 0
	5.19E-22	A2″ → A2′	3 → 2	0 → 1	0 → 0	0 → 1	0 → 0
1.5239753	3.70E-22	A2″ → A2′	6 → 5	0 → 1	0 → 0	0 → 0	0 → 2
	2.18E-22	A2″ → A2′	6 → 5	0 → 1	0 → 0	0 → 0	0 → 2
1.5240378	3.82E-22	A2′ → A2″	6 → 5	0 → 1	0 → 0	0 → 0	0 → 2
	2.25E-22	A2′ → A2″	6 → 5	0 → 1	0 → 0	0 → 0	0 → 2
1.5240477	5.45E-22	A2″ → A2′	9 → 8	0 → 1	0 → 0	0 → 0	0 → 2
	4.31E-22	A2″ → A2′	9 → 8	0 → 1	0 → 0	0 → 0	0 → 2
1.5259702	2.54E-22	A2″ → A2′	4 → 4	0 → 1	0 → 0	0 → 0	0 → 2
	1.38E-22	A2″ → A2′	4 → 4	0 → 1	0 → 0	0 → 0	0 → 2
1.5260083	1.73E-22	A2′ → A2″	8 → 8	0 → 1	0 → 0	0 → 1	0 → 0
	1.36E-22	A2′ → A2″	8 → 8	0 → 1	0 → 0	0 → 1	0 → 0
1.5260297	2.34E-22	E″ → E′	3 → 2	0 → 1	0 → 0	0 → 1	0 → 0
	1.17E-22	E″ → E′	3 → 2	0 → 1	0 → 0	0 → 1	0 → 0
1.5261075	2.44E-22	E′ → E″	3 → 2	0 → 1	0 → 0	0 → 1	0 → 0
	1.22E-22	E′ → E″	3 → 2	0 → 1	0 → 0	0 → 1	0 → 0
1.5269136	8.09E-22	A2′ → A2″	4 → 3	0 → 1	0 → 0	0 → 1	0 → 0
	4.24E-22	A2′ → A2″	4 → 3	0 → 1	0 → 0	0 → 1	0 → 0
1.5269699	2.14E-22	E′ → E″	10 → 9	0 → 1	0 → 0	0 → 0	0 → 2
	1.91E-22	E′ → E″	10 → 9	0 → 1	0 → 0	0 → 0	0 → 2
1.5269801	9.10E-22	A2″ → A2′	4 → 3	0 → 1	0 → 0	0 → 1	0 → 0

Continued on next page

Table B4 – Continued from previous page

λ (μm)	Intensity (cm MOL^{-1})	ΔΓ	ΔJ	$\Delta\nu_1$	$\Delta\nu_2$	$\Delta\nu_3$	$\Delta\nu_4$
	4.78E-22	A2″ → A2′	4 → 3	0 → 1	0 → 0	0 → 1	0 → 0
1.5282854	5.01E-22	E″ → E′	5 → 4	0 → 1	0 → 0	0 → 1	0 → 0
	2.74E-22	E″ → E′	5 → 4	0 → 1	0 → 0	0 → 1	0 → 0
1.5305726	2.21E-22	E″ → E′	4 → 3	0 → 1	0 → 0	0 → 1	0 → 0
	1.20E-22	E″ → E′	4 → 3	0 → 1	0 → 0	0 → 1	0 → 0
1.5307200	2.37E-22	E′ → E″	4 → 3	0 → 1	0 → 0	0 → 1	0 → 0
	1.28E-22	E′ → E″	4 → 3	0 → 1	0 → 0	0 → 1	0 → 0
1.5318288	6.51E-22	A2′ → A2″	5 → 4	0 → 1	0 → 0	0 → 1	0 → 0
	3.76E-22	A2′ → A2″	5 → 4	0 → 1	0 → 0	0 → 1	0 → 0
1.5326047	3.04E-22	A2″ → A2′	3 → 2	0 → 1	0 → 0	0 → 0	0 → 2
	1.47E-22	A2″ → A2′	3 → 2	0 → 1	0 → 0	0 → 0	0 → 2
1.5326105	3.72E-22	E″ → E′	6 → 5	0 → 1	0 → 0	0 → 1	0 → 0
	2.28E-22	E″ → E′	6 → 5	0 → 1	0 → 0	0 → 1	0 → 0
1.5327935	3.89E-22	E′ → E″	6 → 5	0 → 1	0 → 0	0 → 1	0 → 0
	2.37E-22	E′ → E″	6 → 5	0 → 1	0 → 0	0 → 1	0 → 0
1.5350255	4.73E-22	A2″ → A2′	9 → 8	0 → 1	0 → 0	0 → 1	0 → 0
	3.74E-22	A2″ → A2′	9 → 8	0 → 1	0 → 0	0 → 1	0 → 0
1.5350794	4.73E-22	A2′ → A2″	9 → 8	0 → 1	0 → 0	0 → 0	0 → 2
	3.74E-22	A2′ → A2″	9 → 8	0 → 1	0 → 0	0 → 0	0 → 2
1.5366815	2.92E-22	E″ → E′	5 → 4	0 → 1	0 → 0	0 → 0	0 → 2
	1.59E-22	E″ → E′	5 → 4	0 → 1	0 → 0	0 → 0	0 → 2
1.5367137	4.53E-22	A2′ → A2″	6 → 5	0 → 1	0 → 0	0 → 1	0 → 0
	2.94E-22	A2′ → A2″	6 → 5	0 → 1	0 → 0	0 → 1	0 → 0
1.5367442	3.16E-22	A2′ → A2″	4 → 3	0 → 1	0 → 0	0 → 0	0 → 2
	1.66E-22	A2′ → A2″	4 → 3	0 → 1	0 → 0	0 → 0	0 → 2
1.5367718	3.04E-22	A2″ → A2′	4 → 3	0 → 1	0 → 0	0 → 0	0 → 2
	1.59E-22	A2″ → A2′	4 → 3	0 → 1	0 → 0	0 → 0	0 → 2
1.5381836	2.99E-22	A2′ → A2″	6 → 5	0 → 1	0 → 0	0 → 0	0 → 2
	1.76E-22	A2′ → A2″	6 → 5	0 → 1	0 → 0	0 → 0	0 → 2
1.5382605	1.83E-22	E′ → E″	10 → 9	0 → 1	0 → 0	0 → 1	0 → 0
	1.63E-22	E′ → E″	10 → 9	0 → 1	0 → 0	0 → 1	0 → 0
1.5396001	2.24E-22	A2″ → A2′	6 → 5	0 → 2	0 → 0	0 → 0	0 → 0

Continued on next page

Table B4 – Continued from previous page

λ (μm)	Intensity (cm MOL^{-1})	ΔΓ	ΔJ	$\Delta\nu_1$	$\Delta\nu_2$	$\Delta\nu_3$	$\Delta\nu_4$
	1.32E-22	A2″ → A2′	6 → 5	0 → 2	0 → 0	0 → 0	0 → 0
1.5396664	2.84E-22	A2′ → A2″	8 → 7	0 → 1	0 → 0	0 → 1	0 → 0
	2.22E-22	A2′ → A2″	8 → 7	0 → 1	0 → 0	0 → 1	0 → 0
1.5408852	2.77E-22	A2′ → A2″	5 → 4	0 → 1	0 → 0	0 → 0	0 → 2
	1.60E-22	A2′ → A2″	5 → 4	0 → 1	0 → 0	0 → 0	0 → 2
1.5409306	2.94E-22	A2″ → A2′	5 → 4	0 → 1	0 → 0	0 → 0	0 → 2
	1.70E-22	A2″ → A2′	5 → 4	0 → 1	0 → 0	0 → 0	0 → 2
1.5426358	1.73E-22	E′ → E″	6 → 5	0 → 1	0 → 0	0 → 0	0 → 2
	1.09E-22	E′ → E″	6 → 5	0 → 1	0 → 0	0 → 0	0 → 2
1.5426426	5.43E-22	A2″ → A2′	6 → 5	0 → 1	0 → 0	0 → 1	0 → 0
	3.63E-22	A2″ → A2′	6 → 5	0 → 1	0 → 0	0 → 1	0 → 0
1.5427689	1.66E-22	E″ → E′	6 → 5	0 → 1	0 → 0	0 → 0	0 → 2
	1.05E-22	E″ → E′	6 → 5	0 → 1	0 → 0	0 → 0	0 → 2
1.5439872	1.79E-22	E′ → E″	8 → 7	0 → 1	0 → 0	0 → 0	0 → 2
	1.27E-22	E′ → E″	8 → 7	0 → 1	0 → 0	0 → 0	0 → 2
1.5440214	3.87E-22	E″ → E′	8 → 7	0 → 1	0 → 0	0 → 0	0 → 2
	2.74E-22	E″ → E′	8 → 7	0 → 1	0 → 0	0 → 0	0 → 2
1.5442200	2.11E-22	E′ → E″	8 → 7	0 → 1	0 → 0	0 → 0	0 → 2
	1.50E-22	E′ → E″	8 → 7	0 → 1	0 → 0	0 → 0	0 → 2
1.5460370	2.47E-22	E″ → E′	8 → 7	0 → 1	0 → 0	0 → 0	0 → 2
	1.85E-22	E″ → E′	8 → 7	0 → 1	0 → 0	0 → 0	0 → 2
1.5460891	2.76E-22	A2″ → A2′	8 → 7	0 → 1	0 → 0	0 → 0	0 → 2
	2.16E-22	A2″ → A2′	8 → 7	0 → 1	0 → 0	0 → 0	0 → 2
1.5461195	3.57E-22	A2′ → A2″	8 → 7	0 → 1	0 → 0	0 → 0	0 → 2
	2.79E-22	A2′ → A2″	8 → 7	0 → 1	0 → 0	0 → 0	0 → 2
1.5479982	3.49E-22	A2′ → A2″	7 → 6	0 → 1	0 → 0	0 → 1	0 → 0
	2.65E-22	A2′ → A2″	7 → 6	0 → 1	0 → 0	0 → 1	0 → 0
1.5504098	1.96E-22	A2″ → A2′	9 → 8	0 → 1	0 → 0	0 → 0	0 → 2
	1.82E-22	A2″ → A2′	9 → 8	0 → 1	0 → 0	0 → 0	0 → 2
1.5532507	1.62E-22	E″ → E′	10 → 9	0 → 1	0 → 0	0 → 0 0 → 2	
	1.64E-22	E″ → E′	10 → 9	0 → 1	0 → 0	0 → 0 0 → 2	
1.5533022	1.59E-22	A2′ → A2″	12 → 11	0 → 1	0 → 0	0 → 0	0 → 2

Continued on next page

Table B4 – Continued from previous page

λ (μm)	Intensity (cm MOL^{-1})	$\Delta\Gamma$	ΔJ	$\Delta\nu_1$	$\Delta\nu_2$	$\Delta\nu_3$	$\Delta\nu_4$
	1.88E-22	A2′ → A2″	12 → 11	0 → 1	0 → 0	0 → 0	0 → 2
1.5533409	1.49E-22	A2″ → A2′	12 → 11	0 → 1	0 → 0	0 → 0	0 → 2
	1.77E-22	A2″ → A2′	12 → 11	0 → 1	0 → 0	0 → 0	0 → 2
1.5533705	1.94E-22	A2″ → A2′	8 → 7	0 → 1	0 → 0	0 → 1	0 → 0
	1.73E-22	A2″ → A2′	8 → 7	0 → 1	0 → 0	0 → 1	0 → 0
1.5544681	1.48E-22	E′ → E″	11 → 10	0 → 1	0 → 0	0 → 0	0 → 2
	1.63E-22	E′ → E″	11 → 10	0 → 1	0 → 0	0 → 0	0 → 2
1.5545022	8.80E-23	A2″ → A2′	8 → 7	0 → 1	0 → 0	0 → 1	0 → 0
	7.73E-23	A2″ → A2′	8 → 7	0 → 1	0 → 0	0 → 1	0 → 0
1.5545891	9.47E-23	E′ → E″	9 → 8	0 → 1	0 → 0	0 → 0	0 → 2
	9.33E-23	E′ → E″	9 → 8	0 → 1	0 → 0	0 → 0	0 → 2
1.5546618	8.80E-23	E″ → E′	9 → 8	0 → 1	0 → 0	0 → 0	0 → 2
	8.72E-23	E″ → E′	9 → 8	0 → 1	0 → 0	0 → 0	0 → 2
1.5606256	2.49E-23	E″ → E′	11 → 10	0 → 1	0 → 0	0 → 1	0 → 0
	3.26E-23	E″ → E′	11 → 10	0 → 1	0 → 0	0 → 1	0 → 0
1.5606434	1.99E-23	E′ → E″	11 → 10	0 → 0	0 → 6	0 → 0	0 → 0
	2.93E-23	E′ → E″	11 → 10	0 → 0	0 → 6	0 → 0	0 → 0
1.5606584	2.49E-23	E″e → E′	11 → 10	0 → 1	0 → 0	0 → 1	0 → 0
	3.30E-23	E″ → E′	11 → 10	0 → 1	0 → 0	0 → 1	0 → 0
1.5606818	6.64E-23	A2″ → A2′	10 → 9	0 → 1	0 → 0	0 → 0	0 → 2
	8.08E-23	A2″ → A2′	10 → 9	0 → 1	0 → 0	0 → 0	0 → 2
1.5657048	2.99E-23	E″ → E′	9 → 8	0 → 1	0 → 0	0 → 0	0 → 2
	3.09E-23	E″ → E′	9 → 8	0 → 1	0 → 0	0 → 0	0 → 2
1.5657826	8.30E-23	A2′ → A2″	9 → 8	0 → 1	0 → 0	0 → 0	0 → 2
	8.68E-23	A2′ → A2″	9 → 8	0 → 1	0 → 0	0 → 0	0 → 2
1.5657926	1.83E-23	E″ → E′	15 → 14	0 → 1	0 → 0	0 → 0	0 → 2
	4.18E-23	E″ → E′	15 → 14	0 → 1	0 → 0	0 → 0	0 → 2
1.5686759	6.48E-23	A2″ → A2′	10 → 9	0 → 1	0 → 0	0 → 1	0 → 0
	8.05E-23	A2″ → A2′	10 → 9	0 → 1	0 → 0	0 → 1	0 → 0
1.5734597	1.66E-23	E″ → E′	11 → 10	0 → 1	0 → 2	0 → 0	0 → 1
	2.66E-23	E″ → E′	11 → 10	0 → 1	0 → 2	0 → 0	0 → 1
1.5734728	3.82E-23	E′ → E″	11 → 10	0 → 1	0 → 0	0 → 1	0 → 0

Continued on next page

Table B4 – Continued from previous page

λ (μm)	Intensity (cm MOL^{-1})	$\Delta\Gamma$	ΔJ	$\Delta\nu_1$	$\Delta\nu_2$	$\Delta\nu_3$	$\Delta\nu_4$
	5.92E-23	E′ → E″	11 → 10	0 → 1	0 → 0	0 → 1	0 → 0
1.5734975	2.99E-23	A2″ → A2′	11 → 10	0 → 1	0 → 0	0 → 1	0 → 0
	4.49E-23	A2″ → A2′	11 → 10	0 → 1	0 → 0	0 → 1	0 → 0
1.5735244	1.99E-23	A2′ → A2″	11 → 10	0 → 1	0 → 0	0 → 0	0 → 2
	3.02E-23	A2′ → A2″	11 → 10	0 → 1	0 → 0	0 → 0	0 → 2
1.5735331	4.65E-23	E″ → E′	11 → 10	0 → 1	0 → 0	0 → 1	0 → 0
	7.24E-23	E″ → E′	11 → 10	0 → 1	0 → 0	0 → 1	0 → 0
1.5735477	1.66E-23	A2″ → A2′	18 → 17	0 → 1	0 → 0	0 → 0	0 → 2
	6.16E-23	A2″ → A2′	18 → 17	0 → 1	0 → 0	0 → 0	0 → 2
1.5802442	4.15E-23	A2′ → A2″	12 → 11	0 → 1	0 → 0	0 → 1	0 → 0
	7.96E-23	A2′ → A2″	12 → 11	0 → 1	0 → 0	0 → 1	0 → 0
1.5902833	9.96E-24	A2″ → A2′	6 → 5	0 → 0	0 → 0	0 → 0	0 → 4
	6.79E-24	A2″ → A2′	6 → 5	0 → 0	0 → 0	0 → 0	0 → 4
1.5903468	9.96E-24	A2′ → A2″	11 → 10	0 → 2	0 → 0	0 → 0	0 → 0
	1.09E-23	A2′ → A2″	11 → 10	0 → 2	0 → 0	0 → 0	0 → 0
1.5903955	1.99E-23	A2′ → A2″	3 → 2	0 → 0	0 → 3	0 → 1	0 → 0
	9.30E-24	A2′ → A2″	3 → 2	0 → 0	0 → 3	0 → 1	0 → 0
1.5905922	2.99E-23	A2″ → A2′	9 → 8	0 → 0	0 → 0	0 → 0	0 → 4
	2.30E-23	A2″ → A2′	9 → 8	0 → 0	0 → 0	0 → 0	0 → 4
1.5999721	2.66E-23	A2″ → A2′	6 → 5	0 → 0	0 → 3	0 → 1	0 → 0
	1.60E-23	A2″ → A2′	6 → 5	0 → 0	0 → 3	0 → 1	0 → 0

Table B.5: Q-branch NH_3 ro-vibrational transition lines producing absorption lines in the K band spectra of UGPS 0722 and 2MASS 0415 (shaded)

λ (μm)	Intensity (cm MOL^{-1})	$\Delta\Gamma$	ΔJ	$\Delta\nu_1$	$\Delta\nu_2$	$\Delta\nu_3$	$\Delta\nu_4$
1.9667023	2.26E-21	E″ → E′	2 → 3	0 → 1	0 → 0	0 → 0	0 → 1
	1.06E-21	″ → E′	2 → 3	0 → 1	0 → 0	0 → 0	0 → 1
1.9698319	1.65E-21	A2″ → A2′	4 → 4	0 → 1	0 → 0	0 → 0	0 → 1
	8.63E-22	A2″ → A2′	4 → 4	0 → 1	0 → 0	0 → 0	0 → 1
1.9698457	2.05E-21	A′ → A2″	4 → 4	0 → 1	0 → 0	0 → 0	0 → 1
	1.08E-21	A2′ → A2″	4 → 4	0 → 1	0 → 0	0 → 0	0 → 1
1.9699059	1.48E-21	A2′ → A2″	3 → 3	0 → 1	0 → 0	0 → 0	0 → 1
	7.18E-22	A2′ → A2″	3 → 3	0 → 1	0 → 0	0 → 0	0 → 1
1.9700253	1.44E-21	A2″ → A2′	7 → 7	0 → 1	0 → 0	0 → 0	0 → 1
	1.06E-21	A2″ → A2′	7 → 7	0 → 1	0 → 0	0 → 0	0 → 1
1.9736627	7.79E-22	E′ → E″	2 → 2	0 → 1	0 → 0	0 → 0	0 → 1
	3.64E-22	E′ → E″	2 → 2	0 → 1	0 → 0	0 → 0	0 → 1
1.9737128	8.87E-22	E″ → E′	3 → 3	0 → 1	0 → 0	0 → 0	0 → 1
	4.39E-22	E″ → E′	3 → 3	0 → 1	0 → 0	0 → 0	0 → 1
1.9737639	7.67E-22	E″ → E′	2 → 2	0 → 1	0 → 0	0 → 0	0 → 1
	3.59E-22	E″ → E′	2 → 2	0 → 1	0 → 0	0 → 0	0 → 1
1.9740311	2.11E-21	A2″ → A2′	0 → 1	0 → 1	0 → 0	0 → 0	0 → 1
	9.45E-22	A2″ → A2′	0 → 1	0 → 1	0 → 0	0 → 0	0 → 1
1.9777502	1.12E-21	E′ → E″	2 → 2	0 → 1	0 → 0	0 → 0	0 → 1
	5.27E-22	E′ → E″	2 → 2	0 → 1	0 → 0	0 → 0	0 → 1
1.9777654	7.62E-22	E′ → E″	1 → 1	0 → 1	0 → 0	0 → 0	0 → 1
	3.47E-22	E′ → E″	1 → 1	0 → 1	0 → 0	0 → 0	0 → 1
1.9777834	1.15E-21	E′ → E″	3 → 3	0 → 1	0 → 0	0 → 0	0 → 1
	5.77E-22	E′ → E″	3 → 3	0 → 1	0 → 0	0 → 0	0 → 1
1.9777991	1.03E-22	E″ → E′	11 → 11	0 → 1	0 → 0	0 → 0	0 → 1
	1.59E-22	E″ → E′	11 → 11	0 → 1	0 → 0	0 → 0	0 → 1
1.9778023	9.85E-22	E″ → E′	4 → 4	0 → 1	0 → 0	0 → 0	0 → 1
	5.32E-22	E″ → E′	4 → 4	0 → 1	0 → 0	0 → 0	0 → 1
1.9778160	1.07E-21	A2″ → A2′	8 → 8	0 → 1	0 → 0	0 → 0	0 → 1
	9.50E-22	A2″ → A2′	8 → 8	0 → 1	0 → 0	0 → 0	0 → 1
1.9778896	1.14E-21	E′ → E″	4 → 4	0 → 1	0 → 0	0 → 0	0 → 1

Continued on next page

Table B5 – Continued from previous page

λ (μm)	Intensity (cm MOL^{-1})	$\Delta\Gamma$	ΔJ	$\Delta\nu_1$	$\Delta\nu_2$	$\Delta\nu_3$	$\Delta\nu_4$
	6.13E-22	E′ → E″	4 → 4	0 → 1	0 → 0	0 → 0	0 → 1
1.9780305	8.42E-22	E″ → E′	5 → 5	0 → 1	0 → 0	0 → 0	0 → 1
	4.99E-22	E″ → E′	5 → 5	0 → 1	0 → 0	0 → 0	0 → 1
1.9780984	8.40E-22	E′ → ″	5 → 5	0 → 1	0 → 0	0 → 0	0 → 1
	4.99E-22	E′ → E″	5 → 5	0 → 1	0 → 0	0 → 0	0 → 1
1.9781406	6.38E-22	E″ → E′	6 → 6	0 → 1	0 → 0	0 → 0	0 → 1
	4.23E-22	E″ → E′	6 → 6	0 → 1	0 → 0	0 → 0	0 → 1
1.9782424	7.34E-22	E′ → E″	6 → 6	0 → 1	0 → 0	0 → 0	0 → 1
	4.88E-22	E′ → E″	6 → 6	0 → 1	0 → 0	0 → 0	0 → 1
1.9784734	1.69E-21	A2′ → A2″	7 → 7	0 → 1	0 → 0	0 → 0	0 → 1
	1.29E-21	A2′ → A2″	7 → 7	0 → 1	0 → 0	0 → 0	0 → 1
1.9834031	1.36E-21	A2′ → A2″	5 → 5	0 → 0	0 → 0	0 → 1	0 → 1
	8.13E-22	A2′ → A2″	5 → 5	0 → 0	0 → 0	0 → 1	0 → 1
1.9834432	6.16E-22	A2″ → A2′	6 → 6	0 → 1	0 → 0	0 → 0	0 → 1
	4.11E-22	A2″ → A2′	6 → 6	0 → 1	0 → 0	0 → 0	0 → 1
1.9855316	1.18E-21	E″ → E′	4 → 4	0 → 1	0 → 0	0 → 0	0 → 1
	6.35E-22	E″ → E′	4 → 4	0 → 1	0 → 0	0 → 0	0 → 1
1.9856694	1.17E-21	E′ → E″	4 → 4	0 → 1	0 → 0	0 → 0	0 → 1
	6.29E-22	E′ → E″	4 → 4	0 → 1	0 → 0	0 → 0	0 → 1
1.9857268	1.09E-21	E″ → E′	3 → 3	0 → 1	0 → 0	0 → 0	0 → 1
	5.44E-22	E″ → E′	3 → 3	0 → 1	0 → 0	0 → 0	0 → 1
1.9858207	1.08E-21	E′ → E″	3 → 3	0 → 1	0 → 0	0 → 0	0 → 1
	5.40E-22	E′ → E″	3 → 3	0 → 1	0 → 0	0 → 0	0 → 1
1.9858881	7.37E-22	E′ → E″	2 → 2	0 → 1	0 → 0	0 → 0	0 → 1
	3.48E-22	E′ → E″	2 → 2	0 → 1	0 → 0	0 → 0	0 → 1
1.9899619	6.68E-22	E′ → E″	3 → 3	0 → 1	0 → 0	0 → 0	0 → 1
	3.30E-22	E′ → E″	3 → 3	0 → 1	0 → 0	0 → 0	0 → 1
1.9900275	6.63E-22	E″ → E′	3 → 3	0 → 1	0 → 0	0 → 0	0 → 1
	3.28E-22	E″ → E′	3 → 3	0 → 1	0 → 0	0 → 0	0 → 1

Table B.6: P-branch NH_3 ro-vibrational transition lines producing absorption features in the *K* band spectra of UGPS 0722 and 2MASS 0415 (shaded)

λ (μm)	Intensity (cm MOL^{-1})	$\Delta\Gamma$	ΔJ	$\Delta\nu_1$	$\Delta\nu_2$	$\Delta\nu_3$	$\Delta\nu_4$
1.9933051	4.27E-21	A2′ → A2″	3 → 2	0 → 1	0 → 0	0 → 0	0 → 1
	2.08E-21	A2′ → A2″	3 → 2	0 → 1	0 → 0	0 → 0	0 → 1
1.9971614	2.60E-21	E′ → E″	4 → 3	0 → 1	0 → 0	0 → 0	0 → 1
	1.33E-21	E′ → E″	4 → 3	0 → 1	0 → 0	0 → 0	0 → 1
1.9971660	1.32E-21	E′ → E″	3 → 2	0 → 1	0 → 0	0 → 0	0 → 1
	6.53E-22	E′ → E″	3 → 2	0 → 1	0 → 0	0 → 0	0 → 1
1.9972077	4.32E-22	E′ → E″	8 → 8	0 → 1	0 → 0	0 → 0	0 → 1
	3.62E-22	E′ → E″	8 → 8	0 → 1	0 → 0	0 → 0	0 → 1
1.9972565	2.59E-21	E″ → E′	4 → 3	0 → 1	0 → 0	0 → 0	0 → 1
	1.33E-21	E′ → E′	4 → 3	0 → 1	0 → 0	0 → 0	0 → 1
2.0011576	2.80E-21	E″ → E′	5 → 4	0 → 1	0 → 0	0 → 0	0 → 1
	1.53E-21	E″ → E′	5 → 4	0 → 1	0 → 0	0 → 0	0 → 1
2.0052060	5.03E-21	A2′ → A2″	6 → 5	0 → 1	0 → 0	0 → 0	0 → 1
	2.96E-21	A2′ → A2″	6 → 5	0 → 1	0 → 0	0 → 0	0 → 1
2.0053250	5.50E-21	A2″ → A2′	6 → 5	0 → 1	0 → 0	0 → 0	0 → 1
	3.23E-21	A2″ → A2′	6 → 5	0 → 1	0 → 0	0 → 0	0 → 1
2.0090814	2.69E-21	A2′ → A2″	5 → 4	0 → 1	0 → 0	0 → 0	0 → 1
	1.55E-21	A2′ → A2″	5 → 4	0 → 1	0 → 0	0 → 0	0 → 1
2.0090858	2.00E-21	A2″ → A2′	5 → 4	0 → 1	0 → 0	0 → 0	0 → 1
	1.16E-21	A2″ → A2′	5 → 4	0 → 1	0 → 0	0 → 0	0 → 1
2.0091443	1.98E-21	E′ → E″	6 → 5	0 → 1	0 → 0	0 → 0	0 → 1
	1.21E-21	E′ → E″	6 → 5	0 → 1	0 → 0	0 → 0	0 → 1
2.0091937	5.83E-22	E″ → E′	4 → 3	0 → 1	0 → 0	0 → 0	0 → 1
	3.14E-22	E″ → E′	4 → 3	0 → 1	0 → 0	0 → 0	0 → 1
2.0130727	3.61E-21	A2′ → A2″	7 → 6	0 → 1	0 → 0	0 → 0	0 → 1
	2.42E-21	A2′ → A2″	7 → 6	0 → 1	0 → 0	0 → 0	0 → 1
2.0130956	1.41E-21	E″ → E′	6 → 5	0 → 1	0 → 0	0 → 0	0 → 1
	8.93E-22	E″ → E′	6 → 5	0 → 1	0 → 0	0 → 0	0 → 1
2.0131948	7.94E-22	E′ → E″	8 → 7	0 → 0	0 → 4	0 → 0	0 → 1
	5.61E-22	E′ → E″	8 → 7	0 → 0	0 → 4	0 → 0	0 → 1
2.0132054	3.67E-21	A2″ → A2′	7 → 6	0 → 1	0 → 0	0 → 0	0 → 1

Continued on next page

Table B6– Continued from previous page

λ (μm)	Intensity (cm MOL^{-1})	$\Delta\Gamma$	ΔJ	$\Delta\nu_1$	$\Delta\nu_2$	$\Delta\nu_3$	$\Delta\nu_4$
	2.46E-21	$A2'' \rightarrow A2'$	$7 \rightarrow 6$	$0 \rightarrow 1$	$0 \rightarrow 0$	$0 \rightarrow 0$	$0 \rightarrow 1$
2.0176909	3.61E-21	$A2'' \rightarrow A2'$	$9 \rightarrow 8$	$0 \rightarrow 1$	$0 \rightarrow 0$	$0 \rightarrow 0$	$0 \rightarrow 1$
	2.85E-21	$A2'' \rightarrow A2'$	$9 \rightarrow 8$	$0 \rightarrow 1$	$0 \rightarrow 0$	$0 \rightarrow 0$	$0 \rightarrow 1$
2.0178703	3.60E-21	$A2' \rightarrow A2''$	$9 \rightarrow 8$	$0 \rightarrow 1$	$0 \rightarrow 0$	$0 \rightarrow 0$	$0 \rightarrow 1$
	2.85E-21	$A2' \rightarrow A2''$	$9 \rightarrow 8$	$0 \rightarrow 1$	$0 \rightarrow 0$	$0 \rightarrow 0$	$0 \rightarrow 1$
2.0209868	2.33E-21	$A2' \rightarrow A2''$	$8 \rightarrow 7$	$0 \rightarrow 1$	$0 \rightarrow 0$	$0 \rightarrow 0$	$0 \rightarrow 1$
	1.82E-21	$A2' \rightarrow A2''$	$8 \rightarrow 7$	$0 \rightarrow 1$	$0 \rightarrow 0$	$0 \rightarrow 0$	$0 \rightarrow 1$
2.0211593	2.31E-21	$A2'' \rightarrow A2'$	$8 \rightarrow 7$	$0 \rightarrow 1$	$0 \rightarrow 0$	$0 \rightarrow 0$	$0 \rightarrow 1$
	1.81E-21	$A2'' \rightarrow A2'$	$8 \rightarrow 7$	$0 \rightarrow 1$	$0 \rightarrow 0$	$0 \rightarrow 0$	$0 \rightarrow 1$
2.0257054	1.99E-21	$A2' \rightarrow A2''$	$10 \rightarrow 9$	$0 \rightarrow 1$	$0 \rightarrow 0$	$0 \rightarrow 0$	$0 \rightarrow 1$
	1.90E-21	$A2' \rightarrow A2''$	$10 \rightarrow 9$	$0 \rightarrow 1$	$0 \rightarrow 0$	$0 \rightarrow 0$	$0 \rightarrow 1$
2.0263273	1.06E-21	$E'' \rightarrow E'$	$11 \rightarrow 10$	$0 \rightarrow 1$	$0 \rightarrow 0$	$0 \rightarrow 0$	$0 \rightarrow 1$
	1.08E-21	$E'' \rightarrow E'$	$11 \rightarrow 10$	$0 \rightarrow 1$	$0 \rightarrow 0$	$0 \rightarrow 0$	$0 \rightarrow 1$
2.0290052	1.35E-21	$A2' \rightarrow A2''$	$9 \rightarrow 8$	$0 \rightarrow 1$	$0 \rightarrow 0$	$0 \rightarrow 0$	$0 \rightarrow 1$
	1.25E-21	$A2' \rightarrow A2''$	$9 \rightarrow 8$	$0 \rightarrow 1$	$0 \rightarrow 0$	$0 \rightarrow 0$	$0 \rightarrow 1$
2.0292219	1.36E-21	$A2'' \rightarrow A2'$	$9 \rightarrow 8$	$0 \rightarrow 1$	$0 \rightarrow 0$	$0 \rightarrow 0$	$0 \rightarrow 1$
	1.27E-21	$A2'' \rightarrow A2'$	$9 \rightarrow 8$	$0 \rightarrow 1$	$0 \rightarrow 0$	$0 \rightarrow 0$	$0 \rightarrow 1$
2.0350128	6.66E-22	$A2' \rightarrow A2''$	$7 \rightarrow 6$	$0 \rightarrow 1$	$0 \rightarrow 0$	$0 \rightarrow 0$	$0 \rightarrow 1$
	5.07E-22	$A2' \rightarrow A2''$	$7 \rightarrow 6$	$0 \rightarrow 1$	$0 \rightarrow 0$	$0 \rightarrow 0$	$0 \rightarrow 1$
2.0374324	3.62E-22	$E' \rightarrow E''$	$9 \rightarrow 8$	$0 \rightarrow 1$	$0 \rightarrow 0$	$0 \rightarrow 0$	$0 \rightarrow 1$
	3.60E-22	$E' \rightarrow E''$	$9 \rightarrow 8$	$0 \rightarrow 1$	$0 \rightarrow 0$	$0 \rightarrow 0$	$0 \rightarrow 1$
2.0374558	3.52E-22	$E''e \rightarrow E'$	$9 \rightarrow 8$	$0 \rightarrow 1$	$0 \rightarrow 0$	$0 \rightarrow 0$	$0 \rightarrow 1$
	3.50E-22	$E'' \rightarrow E'$	$9 \rightarrow 8$	$0 \rightarrow 1$	$0 \rightarrow 0$	$0 \rightarrow 0$	$0 \rightarrow 1$
2.0374909	3.72E-22	$E'' \rightarrow E'$	$11 \rightarrow 10$	$0 \rightarrow 1$	$0 \rightarrow 0$	$0 \rightarrow 0$	$0 \rightarrow 1$
	4.65E-22	$E'' \rightarrow E'$	$11 \rightarrow 10$	$0 \rightarrow 1$	$0 \rightarrow 0$	$0 \rightarrow 0$	$0 \rightarrow 1$
2.0375446	3.24E-22	$E' \rightarrow E''$	$12 \rightarrow 11$	$0 \rightarrow 1$	$0 \rightarrow 0$	$0 \rightarrow 0$	$0 \rightarrow 1$
	4.47E-22	$E' \rightarrow E''$	$12 \rightarrow 11$	$0 \rightarrow 1$	$0 \rightarrow 0$	$0 \rightarrow 0$	$0 \rightarrow 1$
2.0386534	6.26E-22	$A2'' \rightarrow A2'$	$13 \rightarrow 12$	$0 \rightarrow 1$	$0 \rightarrow 0$	$0 \rightarrow 0$	$0 \rightarrow 1$
	9.47E-22	$A2'' \rightarrow A2'$	$13 \rightarrow 12$	$0 \rightarrow 1$	$0 \rightarrow 0$	$0 \rightarrow 0$	$0 \rightarrow 1$
2.0387969	3.19E-22	$A2' \rightarrow A2''$	$13 \rightarrow 12$	$0 \rightarrow 1$	$0 \rightarrow 0$	$0 \rightarrow 0$	$0 \rightarrow 1$
	4.81E-22	$A2' \rightarrow A2''$	$13 \rightarrow 12$	$0 \rightarrow 1$	$0 \rightarrow 0$	$0 \rightarrow 0$	$0 \rightarrow 1$
2.0413738	5.13E-22	$A2'' \rightarrow A2'$	$12 \rightarrow 11$	$0 \rightarrow 1$	$0 \rightarrow 0$	$0 \rightarrow 0$	$0 \rightarrow 1$

Continued on next page

Table B6– Continued from previous page

λ (μm)	Intensity (cm MOL^{-1})	ΔΓ	ΔJ	$\Delta\nu_1$	$\Delta\nu_2$	$\Delta\nu_3$	$\Delta\nu_4$
	7.56E-22	A2″ → A2′	12 → 11	0 → 1	0 → 0	0 → 0	0 → 1
2.0413793	2.81E-22	E″ → E′	10 → 9	0 → 1	0 → 0	0 → 0	0 → 1
	3.26E-22	E″ → E′	10 → 9	0 → 1	0 → 0	0 → 0	0 → 1
2.0414177	2.76E-22	E′ → E″	10 → 9	0 → 1	0 → 0	0 → 0	0 → 1
	3.21E-22	E′ → E″	10 → 9	0 → 1	0 → 0	0 → 0	0 → 1
2.0414248	2.04E-22	E′ → E″	11 → 10	0 → 1	0 → 0	0 → 0	0 → 1
	2.69E-22	E′ → E″	11 → 10	0 → 1	0 → 0	0 → 0	0 → 1
2.0414375	2.66E-22	A2′ → A2″	9 → 8	0 → 1	0 → 0	0 → 0	0 → 1
	2.70E-22	A2′ → A2″	9 → 8	0 → 1	0 → 0	0 → 0	0 → 1
2.0415579	2.92E-22	A2′ → A2″	9 → 8	0 → 1	0 → 0	0 → 0	0 → 1
	2.97E-22	A2′ → A2″	9 → 8	0 → 1	0 → 0	0 → 0	0 → 1
2.0416804	5.05E-22	A2′ → A2″	12 → 11	0 → 1	0 → 0	0 → 0	0 → 1
	7.45E-22	A2′ → A2″	12 → 11	0 → 1	0 → 0	0 → 0	0 → 1
2.0424475	3.16E-22	A2″ → A2′	9 → 8	0 → 1	0 → 0	0 → 0	0 → 1
	3.21E-22	A2″ → A2′	9 → 8	0 → 1	0 → 0	0 → 0	0 → 1
2.0425366	1.93E-22	E″ → E′	14 → 13	0 → 1	0 → 0	0 → 0	0 → 1
	3.47E-22	E″ → E′	14 → 13	0 → 1	0 → 0	0 → 0	0 → 1
2.0453569	3.17E-22	A2″ → A2′	11 → 10	0 → 1	0 → 0	0 → 0	0 → 1
	4.36E-22	A2″ → A2′	11 → 10	0 → 1	0 → 0	0 → 0	0 → 1
2.0454034	3.87E-22	A2′ → A2″	11 → 10	0 → 1	0 → 0	0 → 0	0 → 1
	5.33E-22	A2′ → A2″	11 → 10	0 → 1	0 → 0	0 → 0	0 → 1
2.0454100	3.22E-22	A2′ → A2″	15 → 14	0 → 1	0 → 0	0 → 0	0 → 1
	6.34E-22	A2′ → A2″	15 → 14	0 → 1	0 → 0	0 → 0	0 → 1
2.0455159	1.98E-22	A2″ → A2′	15 → 14	0 → 1	0 → 0	0 → 0	0 → 1
	3.89E-22	A2″ → A2′	15 → 14	0 → 1	0 → 0	0 → 0	0 → 1
2.0497800	3.01E-22	A2″ → A2′	10 → 9	0 → 1	0 → 0	0 → 0	0 → 1
	3.69E-22	A2″ → A2′	10 → 9	0 → 1	0 → 0	0 → 0	0 → 1